THÈSE

Pour obtenir le grade de

DOCTEUR DE L'UNIVERSITÉ GRENOBLE ALPES

Spécialité : Chimie Physique Moléculaire et Structurale

Arrêté ministériel : 25 mai 2016

Présentée par

Saumya BADONI

Thèse dirigée par **Gael DE PAEPE**
et co-encadrée par **Daniel LEE**

préparée au sein du **Laboratoire Modélisation et Exploration des Matériaux**
dans **l'École Doctorale Chimie et Sciences du Vivant**

Développement de la RMN hyperpolarisée par DNP pour la détermination structurale de nanoparticules de ZnO stabilisées par des ligands

Development of DNP hyperpolarized NMR for structural determination of ligand-stabilized ZnO nanoparticles

Thèse soutenue publiquement le **22 juillet 2021**,
devant le jury composé de :

Monsieur Gaël DE PAEPE
INGENIEUR HDR, CEA Grenoble, Directeur de thèse
Madame Myrtil KAHN
DIRECTRICE DE RECHERCHE, CNRS délégation Occitanie Ouest, Rapporteure
Monsieur Olivier LAFON
PROFESSEUR DES UNIVERSITES, Université de Lille, Rapporteur
Monsieur Peter REISS
INGENIEUR HDR, CEA Grenoble, Examinateur
Monsieur Thibault CHARPENTIER
INGENIEUR HDR, CEA Paris-Saclay, Examinateur
Madame Sabine HEDIGER
DIRECTRICE DE RECHERCHE, CNRS délégation Alpes, Présidente
Monsieur Daniel LEE
PROFESSEUR ASSISTANT, University of Manchester, Invité

Acknowledgments

In the three years and eight months of my PhD project, I have learned the joy of problem-solving and made many valuable acquaintances, experiences, and memories. For that, I want to thank all the people who have made this possible.

Firstly, I thank my supervisors Dr Daniel Lee and Dr Gaël De Paëpe, for their guidance and support throughout my PhD project. I want to thank Dr Daniel Lee for his patient guidance in teaching me DNP NMR instrumentation and theory, intriguing scientific discussions, and enthusiastic encouragement throughout my PhD. I am thankful to Dr. Gaël De Paëpe for his constructive critique of my work and the stimulating scientific discussions. Alongside my supervisors, I want to thank Dr Sabine Hediger for the scientific discussions, valuable insights into challenging scientific problems, and her contagious good nature and energy.

I also want to thank Dr Myrtil Kahn, Prof Olivier Lafon, Dr Peter Reiss, Dr Thibault Charpentier, and Dr Sabine Hediger for agreeing to be members of my PhD jury and for the stimulating discussion and valuable insights into the various aspects of my PhD project.

I am indebted to Prof. Janusz Lewinski's group at Warsaw University of Technology and the Polish Academy of Sciences for synthesizing ZnO NPs on which I could subsequently perform characterization. Also, Michał Terłecki for preparing the ZnO nanoplatelet samples discussed in Chapters 3 and 4, and Małgorzata Wolska-Pietkiewicz for preparing the samples presented in Chapter 2 and Chapter 5 and also for helping me understand ZnO NP chemistry.

The many past and present lab members have contributed to making my PhD a memorable and learning experience. In particular, Dr Adam Smith helped me with the practical aspects of DNP NMR at the beginning of my PhD, Dr Diego Gauto kindly gave me time to run my DFT calculations on his account on the cluster while I was

going through the long process of having my account and also for his valuable suggestions regarding the same, and Dr Wing Ying Chow provided helpful insights on good scientific writing and presentations. I also want to thank all other lab members, including Dr Subhradip Paul, Arisa Komatsubara, Dr Yao Fu, Dr Akshay Kumar, Rania Harrabi, Ons Dakhlaoui, Dr Katharina Märker, and Natalia Olejnik-Feher along with all other lab members, for their presence, the shared laughter and stimulating discussions during coffee breaks, and for facilitating my over-all growth as a PhD student.

I want to thank Rahul for supporting me throughout my PhD, from being a comrade in our travels across Europe, to being a good practice audience for the day before an important presentation, and for keeping me updated with the latest technology-trends required for a smart PhD. I want to thank all the friends I made during my PhD and my friends back in India for being there for me in happy and sad times.

Finally, I want to thank my family for their constant love and support through all my years of education. My brother Shashwat for making me a very proud and happy big sister. And my mother and father for their endless love and patience in my pursuits away from home.

Abstract

The nanoparticle-ligand interface plays a key role in the unique physicochemical properties of nanoparticles (NPs). Thus, a deep understanding of surface properties such as intimate interactions on NP surfaces, the surface ligand dynamics, ligand packing density, and their binding mode and affinity is required to fine-tune materials for desired applications. In this work, novel applications of dynamic nuclear polarization (DNP) enhanced solid-state nuclear magnetic resonance (ssNMR) spectroscopy for the characterization of ligand shells on zinc oxide (ZnO) NPs have been presented. The ability of DNP-enhanced ssNMR to characterize the ligand shell of NPs has been demonstrated in three key areas concerning ZnO NPs. These include a comparison between the ligand shell arrangement and stability of ZnO NPs synthesized using two different synthetic approaches, understanding the role of ligand in the growth and stabilization of hexagonal ZnO nanoplatelets, and studying the ligand shell morphology (namely, Janus, patchy, stripe-like, and random) of mixed ligand shell NPs.

Firstly, DNP enhanced ssNMR was used to study the surface ligand binding and arrangement on ZnO NPs prepared by a sol-gel and by an organometallic approach. It was shown that the ligand shell on NPs prepared by the **o**ne-pot **s**elf-**s**upporting **o**rgano**m**etallic (OSSOM) approach was more stable and uniform compared to that produced through sol-gel methodology, which shows a time-dependent surface restructuring process with a displacement of the majority of the ligands from the surface. Moreover, the study revealed stable μ_2 and μ_3 coordination modes of ligands that pair up on polar surfaces.

In order to deepen our understanding of ZnO interfaces, size-controlled ZnO nanoplatelets (NPLs) produced by OSSOM-II, a modified version of the OSSOM approach, were studied. The crystal structure and morphology of the NPLs were analyzed using powder X-ray diffraction (PXRD) and high-resolution transmission

electron microscopy (HRTEM) analysis. The multi-faceted system was investigated to understand the role of benzamidine ligands in its growth and stabilization. Therefore, binding modes and atomic-scale arrangements of ligands on the ZnO surfaces were analyzed using DNP-enhanced solid-state NMR. Bimodal binding of benzamidine was observed, with different binding strengths being related to the polar and non-polar facets of these NPLs. The assignments of NMR peaks were confirmed using density functional theory (DFT) calculations. Moreover, insights into the role of ligand in the growth of these NPLs were provided.

Lastly, DNP-enhanced ssNMR was used to investigate NPs capped with mixed ligands. Mixed ligand shells on NPs are known to improve NP properties such as solvability, catalysis, and cation capturing ability. Several recent reports have presented methods for the characterization of mixed ligand shell morphologies, namely Janus, random, and stripe-like, however, a generally applicable method is still lacking. In this work, a quantitative analysis of neighboring ligands based on the well-known transferred echo double resonance (TEDOR) experiment, which is used here for the measurement of hetero-ligand proximities, is presented. DNP enhancements allowed the acquisition of multiple data points for $^{13}C\{^{31}P\}$ TEDOR at natural isotopic abundance (NA) for ligands present on the NP surfaces.

In this work, the enhancements provided by DNP have made possible the measurement of NMR spectra for nuclei with low NA and low gyromagnetic ratio, and inter-ligand long-range distance measurements on the surface of ZnO NPs. Using this information, detailed pictures of ligand shell morphologies on ZnO NP surfaces have been provided. The methods presented in this work for surface ligand characterization can be extended to other hybrid materials with an internal crystalline core and surface species.

Résumé

L'interface nanoparticule-ligand joue un rôle clé dans les propriétés physico-chimiques uniques des nanoparticules (NPs). Ainsi, une compréhension approfondie des propriétés de surface telles que les interactions des ligands avec la surface des NPs, la dynamique des ligands de surface, la densité des ligands présents à la surface, et leur mode de liaison et affinité est nécessaire pour optimiser les matériaux pour les applications souhaitées. Dans ce travail, nous présentons de nouveaux développements en spectroscopie de résonance magnétique nucléaire à l'état solide (RMN solide) hyperpolarisée par polarisation nucléaire dynamique (DNP) pour la caractérisation des enveloppes de ligands sur les NPs d'oxyde de zinc (ZnO). La capacité de la RMN-DNP solide à caractériser l'enveloppe des ligands des NPs à l'échelle atomique a été illustrée au travers de trois questions clés permettant d'améliorer notre compréhension de ces systèmes. Nous avons tout d'abord comparer l'arrangement et la stabilité de l'enveloppe de ligand pour deux approches synthétiques, puis questionner le rôle du ligand dans la croissance et la stabilisation des nanoplaquettes de ZnO hexagonaux, pour enfin étudier la morphologie de l'enveloppe de ligand dans le cas d'une enveloppe à ligand mixte.

Tout d'abord, la RMN-DNP solide a été utilisée pour étudier la liaison et l'arrangement du ligand de surface sur les NPs de ZnO préparées par une approche sol-gel et organométallique. Il a été montré que l'enveloppe de ligands sur les NPs préparées par l'approche "**o**ne-pot **s**elf-**s**upporting **o**rgano**m**etallic" (OSSOM) était plus stable et uniforme comparée à celle produite par la méthodologie sol-gel, qui montre un processus de restructuration de la surface dépendant du temps avec un détachement de la majorité des ligands de la surface. En outre, l'étude a révélé des modes de coordination μ_2 et μ_3 stables des ligands qui s'associent sur des surfaces polaires.

Afin d'approfondir notre compréhension des interfaces de ZnO, des nanoplaquettes de ZnO de taille contrôlée (NPL) produites par OSSOM-II, une version modifiée de

l'approche OSSOM, ont été étudiées. La structure cristalline et la morphologie des NPL ont été analysées par diffraction des rayons X sur poudre (PXRD) et par microscopie électronique à transmission à haute résolution (HRTEM). Ce système à multiples facettes a aussi été étudié en détail par RMN-DNP pour comprendre le rôle des ligands benzamidine dans sa croissance et sa stabilisation. Les modes de liaison et les arrangements à l'échelle atomique des ligands sur les surfaces de ZnO ont notamment été résolues par des expériences de RMN-DNP multidimensionnelles et le recours à des calculs DFT. Une liaison bimodale de la benzamidine a ainsi été mise en évidence en fonction de la polarité des facettes.

Enfin, la RMN-DNP solide a été utilisée pour étudier les NPs recouvertes de ligands mixtes. Les enveloppes de ligands mixtes sur les NPs sont connues pour améliorer les propriétés des NPs telles que la solvabilité, la catalyse et la capacité de capture des cations. Plusieurs rapports récents ont présenté des méthodes de caractérisation des morphologies d'enveloppe de ligands mixtes, à savoir Janus, aléatoire et en forme de bande, mais il n'existe toujours pas de méthode généralement applicable. Dans ce travail, nous présentons une approche nouvelle permettant une analyse quantitative de la proximité des hétéro-ligands en surface des NPs de ZnO. Ce travail est notamment basé sur l'utilisation d'une séquence de RMN appelé TEDOR, qui permet de transférer l'aimantation d'un ligand aux ligands voisins. L'augmentation de la sensibilité obtenue par DNP a permis l'acquisition de suffisamment de données de transfert d'aimantation $^{13}C\{^{31}P\}$ TEDOR en abondance isotopique naturelle (NA) pour fournir des contraintes permettant de modéliser l'enveloppe de ligands.

Dans ce travail, les améliorations apportées par la DNP ont rendu possible la mesure de spectres RMN pour des noyaux à faible NA et à faible rapport gyromagnétique, ainsi que des mesures de distance inter-ligands à longue portée à la surface des NPs de ZnO. Ces informations ont permis d'obtenir des images détaillées de la structure des ligands sur les surfaces des NPs de ZnO. Les méthodes présentées dans ce travail pour la caractérisation des ligands de surface peuvent être étendues à d'autres matériaux hybrides.

LIST OF PUBLICATIONS

Part of this thesis is based on the following publications:

- Chapter 2

  Lee, D.†, Wolska-Pietkiewicz, M.†, **Badoni, S.**, Grala, A., Lewiński, J., & De Paëpe, G. (2019). Disclosing Interfaces of ZnO Nanocrystals Using Dynamic Nuclear Polarization: Sol-Gel versus Organometallic Approach. Angewandte Chemie International Edition, 58(48), 17163-17168.

Other publications include:

- Chapter 3

  Terlecki, M.†, **Badoni, S.**†, Leszczyński, M. K., Gierlotka, S., Justyniak, I., Okuno, H., Wolska-Pietkiewicz M., Lee D., De Paëpe, G., and Lewiński, J. (2021). ZnO Nanoplatelets with Controlled Thickness: Atomic Insight into Facet-Specific Bimodal Ligand Binding Using DNP NMR. Advanced Functional Materials, 2105318.
- Chapter 4

  Badoni S., Terlecki, M., Gauto D., Carret S., Poisson J., Charpentier T., Hanako Okuno, Wolska-Pietkiewicz M., Lee D., Lewiński J., De Paëpe G. Benzamidine supported ZnO nanoplatelets: insight into surface termination, ligand structure and growth mechanism from Dynamic Nuclear Polarization and HRTEM. (**In preparation**)
- Chapter 5

  Badoni S.†, Wolska-Pietkiewicz M.†, Lee D., Lewiński J., De Paëpe G. Unravelling mixed ligand shell morphology on ZnO nanoparticles using Dynamic Nuclear Polarization enhanced solid-state NMR. (**In preparation**)

† = these authors contributed equally to the work

Table of Contents

Acknowledgments i

Abstract iii

Resume v

List of publications vii

Table of contents

CHAPTER 1 INTRODUCTION **1**

1.1 CHAPTER OVERVIEW 1

1.2 ZNO NPS 3

1.2.1 Applications and synthetic methods *3*

1.2.2 Mechanism of growth *5*

1.2.3 Potential of NMR for characterization of ZnO NPs *6*

1.3 MAS-DNP ENHANCED SOLID-STATE NMR 8

1.3.1 Solid-state NMR *8*

1.3.2 Need for MAS-DNP *10*

1.3.3 DNP setup *11*

1.3.4 Cross-effect: mechanism and associated polarizing agents *12*

1.3.5 Advantages of working at natural isotopic abundance *14*

1.3.6 DNP for surface studies *15*

1.3.7 Density Functional Theory *17*

1.3.8 Plane-wave pseudopotential formalism *17*

1.3.9 The GIPAW method *18*

1.4 THESIS OUTLINE 19

CHAPTER 2 SOL-GEL VERSUS OSSOM APPROACH **23**

2.1 INTRODUCTION 23

2.2 RESULTS AND DISCUSSIONS 24

2.2.1 Standard sample characterization. *24*

2.2.2 Effect of competing ligand studied using NMR spectroscopy *25*

2.2.3 Disclosing interfaces using Dynamic Nuclear Polarization *31*
2.3 CONCLUSION 37
2.4 MATERIALS AND METHODS 37
2.4.1 General considerations *37*
2.4.2 Standard sample characterization. *38*
2.4.3 Synthesis of $[EtZn(X)]_n$ (where X = DPP) and its transformation to OM NCs: *39*
2.4.4 Preparation of OM NCs *39*
2.4.5 Preparation of SG NCs: *40*
2.4.6 Sample Characterization *40*
2.4.7 DNP-enhanced solid-state NMR. *44*

CHAPTER 3 AN ORGANOMETALLIC APPROACH TO LIGAND-COATED ZNO NANOPLATELETS WITH CONTROLLED THICKNESS: ATOMIC INSIGHT INTO BIMODAL FACET-SPECIFIC INTERFACES USING DNP NMR 47

3.1 INTRODUCTION 47
3.2 RESULTS AND DISCUSSION 51
3.2.1 Synthetic approaches to bza ligand-coated ZnO nanoparticles and nanoplatelets. *51*
3.2.2 Characterization of ZnO NPLs *53*
3.2.3 Elucidation of bimodal facet-specific ligand binding using DNP-enhanced ssNMR. *57*
3.3 CONCLUSION 62
3.4 MATERIALS AND METHODS 62
3.4.1 Synthetic procedures *62*
3.4.2 Characterization *63*

CHAPTER 4 PROBING BENZAMIDINE LIGAND COORDINATION CHEMISTRY ON MULTI-FACETED ZNO NANOPLATELET SURFACES USING DNP-NMR SPECTROSCOPY 85

4.1 INTRODUCTION 85
4.1.1 ZnO NPLs *85*
4.2 RESULTS AND DISCUSSIONS 87
4.2.1 ZnO NPLs: Synthesis and ZnO core structure information *87*
4.2.2 Experiments at ^{13}C (~1.1%) and ^{15}N (~0.4%) natural isotopic abundance: DNP sample preparation and signal enhancement *88*
4.2.3 Zn terminated (0001) and (000$\bar{1}$) facets *89*
4.2.4 Hydrogen-bonding interactions of ligands on the (10$\bar{1}$0) non-polar and (0001) polar surfaces *91*
4.2.5 Determining the 'other' anionic form of BA ligand *94*
4.2.6 Assignment confirmation by ^{15}N labeling of surface ligand *101*
4.2.7 Effect of polar protic solvent addition on NPL-1: insight into transition from molecular complexes to NPLs *103*

4.2.8 Presence of neutral ligand on NPL-1 (10$\bar{1}$0) facets: Gauging ligand proximities on the surface at ^{13}C natural isotopic abundance *105*
4.2.9 Insight into the role of ligand in the growth of NPLs *111*
4.3 CONCLUSION 111
4.4 MATERIALS AND METHODS 112
4.4.1 DNP NMR spectroscopy *112*
4.4.2 ^{15}N labelling *113*
CHAPTER 5 MIXED LIGAND SHELL NANOPARTICLES 115
5.1 INTRODUCTION 115
5.1.1 Mixed ligand shell nanoparticles *115*
5.1.2 The strategy *116*
5.2 SYNTHESIS AND CORE STRUCTURE ANALYSIS 122
5.2.1 General synthesis of mixed ligand shell ZnO NPs using modified OSSOM approach *122*
5.2.2 Transmission electron microscopy (TEM) *123*
..... *123*
5.3 SPECTRAL ASSIGNMENT AND AN INITIAL UNDERSTANDING OF THE LIGAND-SHELL 123
5.3.1 ^{13}C and ^{31}P peak assignment *123*
5.3.2 Comparison between RT, 100 K, and DNP-NMR spectra *126*
5.3.3 Quantitative measurements – multiCP experiments *127*
5.4 QUANTITATIVE ANALYSIS OF THE MIXED LIGAND SHELL 129
5.4.1 Spin echo and TEDOR measurements *129*
5.4.2 Buildup analysis *131*
5.4.3 Distance estimates *132*
5.4.4 Quantification *133*
5.4.5 Percentage inter-ligand boundaries in the mixed ligand shell *137*
5.4.6 Important considerations *140*
5.5 CONCLUSION 140
5.6 MATERIALS AND METHODS 141
5.6.1 DNP NMR spectroscopy *141*
CONCLUSIONS AND OUTLOOK 143

Chapter 1
Introduction

1.1 Chapter overview

Colloidal semiconductor nanoparticles (NPs) are the foundation of nanoscience and nanotechnology. They have attracted considerable attention in recent decades for their unique photophysical and electronic properties, making them interesting for many applications[1–6]. These nano-sized objects have a high surface to bulk ratio, and hence the surface plays a crucial role in their physical and chemical properties[7–9]. Thus, it is crucial to analyze the surface of these nano-objects at an atomic scale. To modulate surface properties for such NPs and to also control NP growth, organic capping ligands are employed. Common ligand types based on number of electrons donated from ligand to metal are a) L-type (donates two electrons and forms coordinate bond with the metal center), b) X-type (accepts one electron from metal center and donates one electron to the metal center forming normal covalent bond) and c) Z-type (accepts two electrons from the metal center and forms coordinate bond). Chemical nature and size of ligands and their interactions with NP determines the NP functionality, size, morphology, and stability[10,11]. Therefore, an understanding of intricate interfacial NP-ligand interactions will improve the control of synthetic procedures and thus lead to nano-systems with optimized structures and properties.

Among the various semiconductor NPs, zinc oxide (ZnO) is attractive due to its low toxicity and unique catalytic and electro-optical characteristics[12–15]. Among many other applications, ZnO NPs have found utility in medicine[16], sensors[17–19], and light-emitting diodes (LED)[20] industries, and for their photocatalytic properties[21]. In this work, ZnO NPs prepared by the **o**ne-pot **s**elf-**s**upporting **o**rgano**m**etallic (OSSOM) approach have

been studied[22–31]. The OSSOM approach uses controlled transformations of an organozinc [EtZn(X)]-type precursor by exposure to atmospheric air (where H_2O and O_2 act simultaneously as a source of oxygen, X – monoanionic organic ligand) at room temperature. The X-type ligand tailors the organometallic precursor's reactivity, supports the nucleation and growth process, and effectively stabilizes the surface of the resulting NPs. As-synthesized NPs possess a highly organized interface structure, which gives them unique properties such as high stability[24,27,31], biosafety[28], and ultra-long-lived luminescence[29].

Additionally, the nanocrystal-ligand interface plays a vital role in the unique physicochemical properties of ZnO. Thus, information on ligand binding and arrangement on the surface is crucial. This work focuses on analyzing the ligand coordination chemistry on the surface of ZnO NPs produced by the OSSOM approach using Dynamic Nuclear Polarization (DNP)-enhanced solid-state nuclear magnetic resonance (ssNMR). Complementary techniques such as density functional theory (DFT) calculations, powder X-ray diffraction (PXRD), and high-resolution transmission electron microscopy (HRTEM) were used to gain further insights into these systems. For this work, I am indebted to the group of Prof. Janusz Lewinski at the Polish Academy of Sciences and Warsaw University of Technology, Poland, for the synthesis and standard characterization of the exciting NP systems that have been discussed in this thesis. The rest of the analysis, including the DNP-NMR analysis and DFT calculations were performed by the doctoral candidate, and the HRTEM in collaboration with Dr. Hanako Okuno, at CEA Grenoble.

In the following sections, various aspects of ZnO nanoparticles and DNP-enhanced solid-state NMR are discussed in detail, along with a brief introduction to the calculation of NMR parameters using DFT. In particular, methods commonly used for organometallic synthesis of ZnO nanoparticles and the corresponding growth mechanisms are described. Moreover, relevant studies on ZnO nanoparticles using solid-state NMR have been summarized. In the DNP-enhanced solid-state NMR section, specific details about the technique, required instrumentation, involved mechanisms, and advantages of using DNP (over conventional solid-state NMR) are discussed. Furthermore, relevant studies of nanoparticle surface characterization using the enhanced sensitivities provided by DNP have also been highlighted.

1.2 ZnO NPs

1.2.1 Applications and synthetic methods

ZnO nanoparticles (NPs) have attracted significant research efforts owing to their versatility, with applications in numerous fields including catalysis[32], semiconductors[33], in paint and rubber industries, as well as for their antimicrobial activity[34]. These excellent semiconductor NPs possess a wide bandgap of ~3.37 eV, a high exciton binding energy of 60 meV, and high electrical conductivity. Moreover, their additional advantages, such as chemical stability, non-toxicity, and biocompatibility[35], make them promising for industrial and medical applications. The shape, size, core composition, and ligand capping of these nanoparticles determine their suitability for a particular application[36–39]. All these properties are highly affected or determined by the synthetic approach used to prepare ZnO NPs. Therefore, much attention has been paid to the development of suitable synthetic methods. In the following discussion, commonly used organometallic approaches for the synthesis of ZnO NPs have been described briefly.

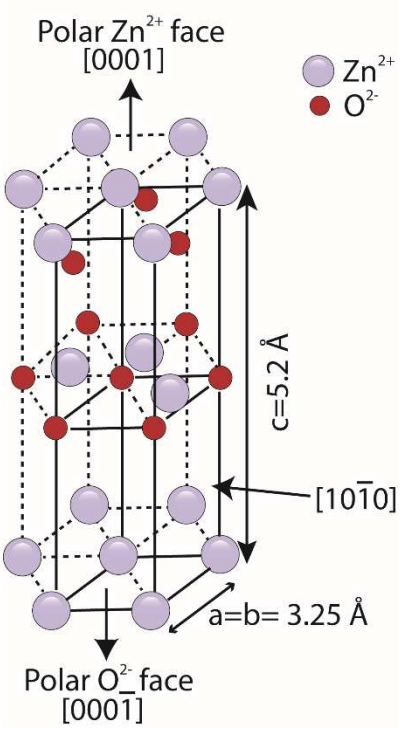

Figure 1-1. ZnO wurtzite unit cell with positions of Zn^{2+} and O^{2-} ions, showing various crystal planes of ZnO wurtzite structure.

In this work, ZnO has been found to have a wurtzite-type core structure where one (Zn^{2+}/ O^{2-}) ion is surrounded by four (O^{2-}/ Zn^{2+}) counter ion species, forming a tetrahedron. This wurtzite-type structure has hexagonal space group P63mc and lattice parameters of a = b = 3.2499 and c = 5.2066 Å[40] containing two formula units of ZnO per unit cell Figure 1-1.

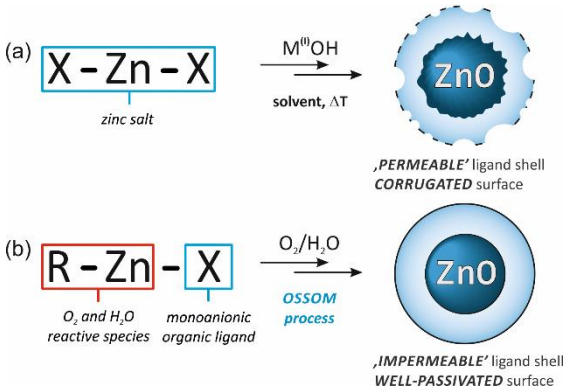

Figure 1-2. Schematic showing the sol-gel method and OSSOM approach for the synthesis of zinc oxide nanoparticles.

As mentioned earlier, this work focuses on the detailed characterization of organic ligand shells on the surface of ZnO NPs prepared by the OSSOM method[22,24,26,28,41] and its modified version OSSOM-II wet-organometallic approach discussed in Chapter 2. Chaudret and co-workers pioneered organometallic approach-based synthesis of ZnO NPs[42]. They have used di-cyclohexyl zinc precursors along with long-chain amines to prepare L-type ligand capped ZnO NPs. These organometallic approaches presented an alternative to the commonly used sol-gel method (Figure 1-2). Even though versatile, the reproducibility of NPs produced by the sol-gel method could not be regulated and hence posited a need for a different synthesis method. In 2012, Orchard et al.[43] reported another efficient organometallic route that involved the hydrolysis of a mixture of a dialkylzinc (ZnR_2) and zinc carboxylate ($Zn(O_2CR')_2$) or zinc phosphinates. This reaction was carried out at an ambient temperature and without post-synthesis refinement. More recently, the OSSOM[22,24,26,28,41] procedure was reported. It is based on the controlled exposure of [EtZn(X)]-type precursor (X = monoanionic organic ligand) to air, leading to ZnO NPs capped with an organic shell composed of surface-anchored X-type ligands[22–31]. The OSSOM approach is thermodynamically controlled and produces ZnO NPs stable[24,27,31], bio-safe[28] and well-passivated with ultra-long-lived luminescence[29].

1.2.2 Mechanism of growth

In order to produce NPs with desired applications, it is important to understand the underlying synthesis mechanism. The mechanism can vary depending on the synthetic method used, i.e., on the reagents and the specific reaction conditions. Thus, there is no generalized rule behind the intricate growth of NPs. However, if reactions proceed under similar conditions, some similarities in the reaction mechanisms can be expected. In the following discussion, mechanism of growth for NPs prepared by the sol-gel method and some organometallic approaches are discussed.

The growth of NPs via the classical sol-gel approach is kinetically controlled. Hence, non-uniform particle morphology and particle-ligand interfaces are obtained due to a lack of control over the fast growth at the NC formation stage[44,45].

The mechanism of growth of nanoparticles, specifically oxides, has been described by Jolivet[46] as involving three steps: nucleation, growth, and ripening. The first report about an organometallic synthesis of ZnO NPs by Kahn et al.[42] explained the NP growth based on this widely accepted account. NMR analysis showed ligand coordination throughout NP synthesis and evidenced dynamic exchange between surface-bound and free ligand in solution. Moreover, low precursor concentrations associated with homogeneous particles were attributed to the 'nucleation' stage. In contrast, inhomogeneous particles associated with higher precursor concentrations were attributed to the nanoparticles' 'growth' stage. The third stage, ripening, is when changes in the size of particles can be observed in absence of free zinc precursor. In Ostwald ripening[47,48], an increase in the mean size of particles is observed where larger particles are formed through the dissolution of smaller ones. It was observed that no more zinc precursor was present after 24 h of exposure to moisture when the reaction was performed in the presence of a solvent. However, in the absence of solvent, the precursor was consumed in 1 h. This observation was found to be in line with Ostwald ripening. Finally, it was concluded that mass transport (where the ligand plays an active role in the growth of particles by favoring the growth of a particular facet) of individual atoms was responsible for the anisotropic growth of particles, for instance, in the case of rods, rather than "oriented attachment," i.e., coalescence of two particles to form bigger aggregates.

In another more detailed mechanistic study of an organometallic synthesis, Pike et al.[49] investigated the exact role of the ligand in the growth process for the applied synthetic method. It thus provided a fresh insight into the growth of these NPs. The synthetic method involved hydrolysis of dialkylzinc and organozinc precursor at ambient temperatures; in this particular case, phosphinate ligands were used in the organozinc precursor. The approach takes advantage of the absence of excess free ligand and the fact that progress of the reaction can be controlled by the amount of water added to the reaction mixture. Therefore, to the starting precursor, one equivalent of water was added in 8 steps, and the progress of the reaction was studied at each step using ^{31}P NMR. From the analysis, it was found that ligands form cluster species and stay as 'ligand reservoirs' in solution while nucleation occurs and get consumed only at the end of the reaction. Moreover, performing the same synthesis in the absence of ligands gave a particle size of 3.5 nm, which was similar to the size obtained in the presence of di-octylphosphinate ligands (2-3 nm). Thus, contrary to the widely accepted idea that the ligand is always involved in the growth of NPs and cluster compounds are the building units of NPs, in this work, the ligand was not necessary for particle size control. However, they are essential to produce well-dispersed and soluble particles as they prevent further aggregation.

1.2.3 Potential of NMR for characterization of ZnO NPs

The nanocrystal-ligand interface plays a crucial role in the unique physicochemical properties of ZnO. NPs have a large surface to bulk atom ratio, because of which the organic-inorganic interface is a crucial factor controlling their properties. The ligand shell on NPs provides control over the nucleation and growth of NPs. Also, depending on the choice of ligand, NPs can have several applications[50]. Thus, a deeper understanding of the atomic-level surface chemistry of NPs is required to produce functional materials with desired applications. Solid-state NMR, a common spectroscopic technique, provides rich site-specific information concerning atomic environments and details about short-range order. Hence, this technique is ideal for understanding the nature of interactions at surface sites[51]. In recent times, some reports have aimed to characterize the surface and bulk of ZnO using NMR spectroscopy[52–56]. Consequently, NMR in the context of ZnO-based studies has been used in various ways to perform a detailed study of defects, understand the surface ligand chemistry,

elucidate the mechanism of growth, study the stability of NPs, and be used as a tool to identify the facets.

For example, defect engineering is essential for the fabrication of electronic and optical devices, and so the electronic and diffusion properties of hydrogen in ZnO have been widely investigated[57,58]. Since ^{1}H NMR is a powerful method for quantification, ^{1}H chemical shifts of surface hydroxyls, interstitial protons, and protons substituting for oxygen ions have been widely studied and debated[59–61]. Another use of NMR has been to elucidate the mechanism of growth of NPs, as discussed in the previous section.

In particular, the work of Kahn and co-workers has improved the understanding of ZnO NPs. Long-term stability of nanoparticles is crucial but is compromised by environmental factors affecting the chemical and structural aspects of NCs. Water being an essential environmental factor, it is critical to understand its effect on the sample. An exciting application of ^{17}O NMR was shown by Champouret et al.[62] to determine the dynamics of ZnO ^{17}O atoms on the surface and, interestingly, in the core of the NPs. For this purpose, anisotropic nanorods and isotropic ZnO NPs were exposed to ^{17}O-enriched water, and the changes in the ^{17}O spectra of the sample were studied over time using 1D T_1-filtered ^{17}O NMR spectra. Consequently, three observed ^{17}O NMR contributions were assigned to the core O atoms, surface O atoms and hydroxyl O and O atoms from the first sublayers. Among other things, it was found that ^{17}O exchanges not only with the more accessible surface sites but also with the sites located in ZnO core.

Coppel et al.[52] performed a detailed analysis of the ligand shell formed by long-chain amines on the surface of ZnO NPs using solution NMR techniques. It was found that ligands on the surface of these NPs are present in three forms in equilibrium with free amines. The three forms were characterized using ^{1}H, pulsed-field gradient spin-echo-NMR, diffusion-filtered ^{1}H NMR, NOESY, and ROESY, and found to be ligands bound to the surface with different interaction strengths. In another study, using multinuclear ^{1}H, ^{2}H, ^{13}C, ^{15}N, ^{17}O, and ^{67}Zn magic angle spinning (MAS)-NMR spectroscopies, Spataro et al.[63] studied the organic shell and the inorganic core of ZnO NPs.

^{31}P NMR of trimethyl phosphine (TMP) was used as a probe to map ZnO surfaces qualitatively and quantitatively. TMP has been extensively used for acidity characterization of acid catalysts by means of ^{31}P MAS-NMR experiments[64]. ^{31}P is 100% abundant and has a wide chemical shift range, and is therefore a sensitive probe for the various sites[65]. It was shown that TMP with its lone pair could bind to surface cationic sites (Lewis acidic sites) and form TMP-Lewis acid adduct, and downfield ^{31}P chemical shifts were observed for stronger TMP-Lewis acid-binding. Thus, information about the nature of possible binding sites could be obtained.

1.3 MAS-DNP enhanced solid-state NMR

1.3.1 Solid-state NMR

Solid-state NMR is a well-known spectroscopic technique and has been widely used for the atomic-scale characterization of materials[66–68] and biomolecules[69–71]. It is based on the interaction of the nuclear spin magnetic moment with applied external magnetic fields. The Hamiltonian $\hat{H}$ for a spin under a static field applied along the z-direction is:

$$\hat{H} = -\hat{\mu}_z . B_0 \qquad 1.3.1$$

This interaction is referred to as Zeeman interaction. $\hat{\mu}_z$ is the nuclear magnetic moment operator along the z-direction, and B_0 is the applied static magnetic field. $\hat{\mu}_z$ can be written as:

$$\hat{\mu}_z = \gamma \hbar \hat{I}_z \qquad 1.3.2$$

Where $\hat{I}$ is the nuclear spin operator, and γ is the gyromagnetic ratio characteristic of the nuclide. Thus, the Hamiltonian can be rewritten as:

$$\hat{H} = -\gamma \hbar \hat{I}_z . B_0 \qquad 1.3.3$$

The Eigenvalue can be obtained by operating $\hat{H}$ on the spin wavefunction, $\Psi_{I,m}$:

$$\hat{H}\Psi_{I,m} = E\Psi_{I,m} \quad 1.3.4$$

The eigenvalue of $\hat{I}_z$ operating on $\Psi_{I,m}$ is m, i.e.:

$$\hat{I}_z\Psi_{I,m} = m\Psi_{I,m} \quad 1.3.5$$

Thus, combining equations 1.3.3, 1.3.4 and 1.3.5, we have:

$$E = -\gamma\hbar B_0 m \quad 1.3.6$$

For spin I nuclei, values of m vary between $I, I-1, I-2\ldots, -I$. In this thesis, only spin-½ nuclei are dealt with, and the values of m corresponding to I= ½ are $m = \pm\frac{1}{2}$. Therefore, in the presence of an applied magnetic field B_0, the energy level of spin-½ nuclei split into two levels of energy $E_{+1/2} = -\frac{1}{2}\gamma\hbar B_0$ *and* $E_{-1/2} = \frac{1}{2}\gamma\hbar B_0$. Hence, the transition energy required for excitation between the two states is $\Delta E = \gamma\hbar B_0$ where $\gamma B_0 = \omega_0$ (the nuclear Larmor angular frequency). In terms of the vector model, a radiofrequency pulse is applied to make the transition occur, which introduces an oscillating magnetic field B_1(t) of angular frequency ω_{rf} perpendicular to B_0. This situation can be analyzed in a rotating frame of reference that rotates at angular frequency ω_{rf} about B_0, removing the time dependence of B_1. If the frequency of oscillations of this applied pulse is on resonance with the frequency of nuclear precession about B_0, i.e., $\omega_{rf} = \omega_0$, the static field along z appears to be zero, and the magnetization vector consequently precesses about the weak magnetic field B_1. At room temperature, the ratio of the population of the higher energy state $P_{-1/2}$ to the lower energy state $P_{+1/2}$ is given by:

$$\frac{P_{-1/2}}{P_{+1/2}} = e^{-\Delta E/k_B T} = e^{-\gamma\hbar B_0/k_B T}$$

Here k_B is Boltzmann's constant, 1.3806 x10^{-23} J/K, and T is the temperature in Kelvin. Hence, higher nuclear gyromagnetic ratio, higher applied external magnetic field, and lower experimental temperatures lead to more difference in population between the two energy states. This is directly related to the intensity of the NMR signal.

Following excitation, these spins are manipulated under a series of carefully chosen sequences of pulses to study interactions of these spins with their surroundings.

Broadly, nuclei experience two kinds of interactions: 1) external interactions which include Zeeman interaction with static magnetic field (B_0) and the interaction with magnetic field of radiofrequency pulses (B_1), and 2) internal interactions which include chemical shift interaction, through-bond j-coupling interactions, through-space dipolar coupling interactions and quadrupolar coupling interactions for nuclei with spin > ½.

1.3.2 Need for MAS-DNP

In Section 1.2.3, several interesting applications of NMR for the characterization of ZnO nanoparticles were shown. However, generally further applications, such as measuring internuclear distances between unreceptive nuclei, whose intrinsic low thermal population differences and natural isotopic abundance (NA) prevent recording multiple experiments because of the unreasonably long experiment times. This issue is aggravated when looking at NP surfaces, where the number of atoms is much less than in bulk. This lack of sensitivity can be overcome by hyperpolarization techniques that provide significantly higher sensitivity. These include spin-exchange optical pumping (SEOP)[72], para-hydrogen induced polarization (PHIP)[73], chemically-induced dynamic nuclear polarization (CIDNP)[74], and dynamic nuclear polarization (DNP)[75,76]. Among these, dynamic nuclear polarization (DNP), is known to provide significant nuclear hyperpolarization at high magnetic fields under MAS conditions.

The concept of DNP was introduced by Overhauser[75], followed by an experimental demonstration on metals by Carver and Slichter[76]. DNP involves transferring the much larger electron spin polarization to nearby nuclei using microwave irradiation at or near electron paramagnetic resonance (EPR) frequency. This transfer of polarization can be described mainly by four mechanisms: the solid-effect, the cross effect, the Overhauser effect, and thermal mixing, a mechanism closely related to the cross effect. Among these, the cross effect has the broadest applicability due to efficient proton hyperpolarization at moderate magnetic fields (5-14 T) and temperatures (~100 K). The cross-effect mechanism can describe all the DNP experiments performed in this work, and hence it will be discussed in more detail in Section 1.3.4 along with the radicals used as polarization sources.

1.3.3 DNP setup

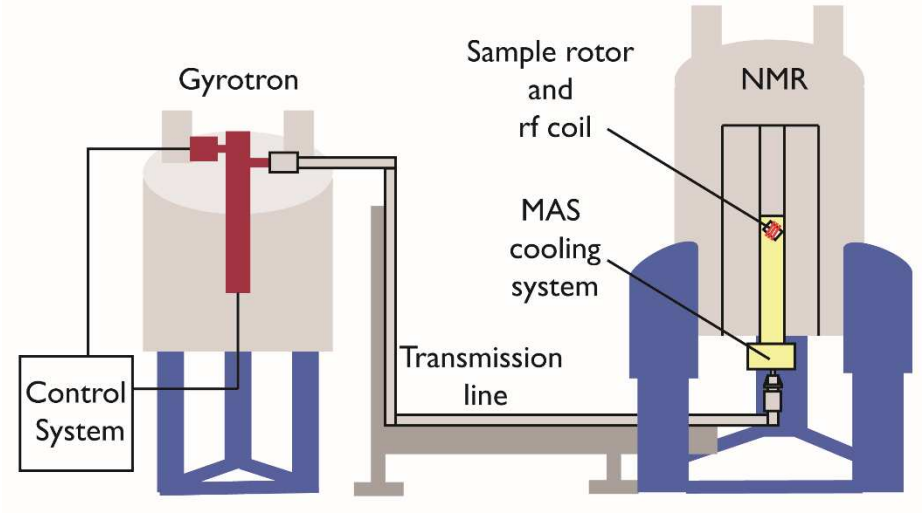

Figure 1-3. Schematic showing solid-state DNP NMR setup showing gyrotron, gyrotron tube in red, microwave transmission line, and low-temperature NMR probe (yellow) containing the sample rotor and rf coil.

Pioneering work[77–80] by the Griffin group at Massachusetts Institute of Technology (MIT) has laid the foundation for now widespread advanced MAS-DNP instrumentation. Their work has contributed significantly to the progress and the accessibility of new applications in the field. Figure 1-3 shows a solid-state DNP NMR setup containing an NMR magnet (NMR console and work station not shown), a gyrotron tube as a microwave source (shown in red) with a magnet and control unit with a high voltage power supply, a transmission line, DNP NMR probe (yellow) containing the sample rotor and rf coil, and cooling unit to provide cryogenic gases for sample cooling. A detailed description of the various aspects of MAS-DNP instrumentation has been given by Barnes et al.[81] and Rosay et al.[82]. The majority of DNP NMR experiments are performed at temperatures below 120 K, mainly due to the prolonged electron spin relaxation times at these temperatures, which are required for high DNP enhancements.

In order to transfer high purity gaussian beams from the gyrotron output to the NMR probe and minimize losses, a corrugated waveguide is used as transmission line[83]. Subsequently, the microwave beam arrives at the bottom of the probe and is reflected 90 degrees via a miter bend and propagates through a taper, cylindrical waveguide and one or two miter bends to reach the sample in the MAS system finally. Significant engineering challenges were overcome to build DNP probes and equipment for efficient

cooling of samples at cryogenic temperatures under MAS. For sample spinning at cryogenic temperatures, gas flow rates 30-100 L/min are required[82]. The heat exchanger currently used for the purpose is an improvement on the design proposed by Allen at al.[84]. A closed-loop cryogenic helium spinning system is even more promising for DNP applications allowing experiments at ultra-low temperatures[85,86] and providing much higher MAS speeds than previously possible with cryogenic nitrogen[87,88].

1.3.4 Cross-effect: mechanism and associated polarizing agents

The cross-effect mechanism dominates when the EPR spectral width Δ (generally through inhomogeneous broadening) is greater than the nuclear Larmor frequency ω_n[89,90]. The minimal model requires a two-electron and one nucleus system with significant coupling between electron spins and a mutually coupled nuclear spin. The polarization equilibration of this system occurs in two steps. First, irradiation at the Larmor frequency of one of the electrons ω_{e1} creates a substantial polarization difference between the two electrons. Second, the difference in Larmor frequency of the two electrons matches the nuclear Larmor frequency ($|\omega_{e1}-\omega_{e2}|=|\omega_n|$), and hence the three spins can flip with energy conservation. These three spin flips over the ensemble of spins present in the analyte make the polarization of the nuclear spins equal to the polarization difference between the two electrons.

Under MAS conditions, other aspects need to be considered to understand the cross-effect mechanism. The mechanism for the cross effect under MAS was simultaneously proposed by Vega and co-workers[91] and Thurber and Tycko[92]. Under MAS, there is a dynamic modulation of the eight energy levels formed by an electron-electron-nucleus (e-e-n) spin system. Unlike the static case where the correct simultaneous orientation of the e-e-n spin-system is required, under MAS the dynamic modulation of energy levels facilitates the presence of correct relative orientations for discrete three-spin systems. Under continuous sample rotation, these occurrences collectively lead to a build-up in polarization for individual spin systems. Thus, significantly improved polarization gains are obtained under MAS compared to the static case.

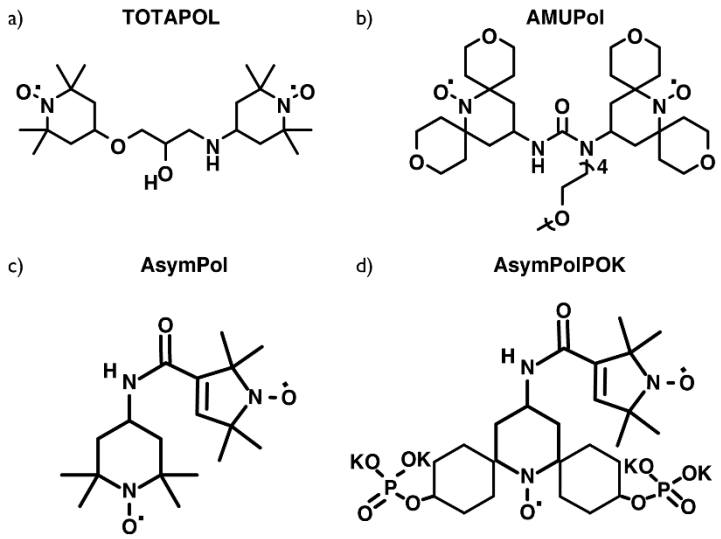

Figure 1-4. Chemical structure of a) TOTAPOL, b) AMUPol, c) AsymPol, and d) AsymPolPOK biradicals.

As mentioned above, the cross-effect requires coupled electrons for which the difference in Larmor frequency of the two electrons is equal to the nuclear Larmor frequency. This is generally achieved by using tailored biradicals that can act as efficient polarization sources; important examples include bis-nitroxides TOTAPOL[93] (Figure 1-4a), AMUPol[94] (Figure 1-4b), and bTbK[95]. Moreover, the use of asymmetric biradicals like the nitroxide-based AsymPol[96] family (Figure 1-4c and d) or nitroxide with trityl[97]/BDPA[98] has led to notable improvements.

Upon microwave irradiation, large polarization transfer from electrons can occur either directly to the nucleus under study or to protons and then to the nucleus via cross-polarization. The former is helpful for cases for which the surrounding of the nucleus under study is devoid of protons[99]. However, the latter is the more commonly used method as it leads to higher enhancement factors and shorter recycle delays. This work's most common sample preparation involves a 10 mM bi-radical in 6:3:1 volume ratio d_8-glycerol/D_2O/H_2O solution. This sample preparation is required to maintain optimum proton concentration for hyperpolarization while allowing efficient spin-diffusion uniformly throughout the sample. Moreover, the glycerol/water matrix forms a glass at low temperatures and hence avoids the formation of crystalline domains that create high electron density areas, consequently leading to shortening of relaxation times and reducing DNP efficiency.

1.3.5 Advantages of working at natural isotopic abundance

Distance measurements between spin-1/2 nuclei (such as ^{13}C, ^{15}N, etc.) in solid-state MAS-NMR can be performed using a sequence of carefully chosen radiofrequency pulses; a technique referred to as dipolar recoupling[100]. The dipolar coupling between two nuclei can be extracted from the plot of polarization transfer between these nuclei as a function of recoupling time. Since the dipolar coupling between two nuclei is inversely proportional to the distance cubed between them, it can help extract distance information. Thus, strong dipolar couplings are observed for nuclei close in space, whereas weak couplings are observed for these same nuclei farther apart.

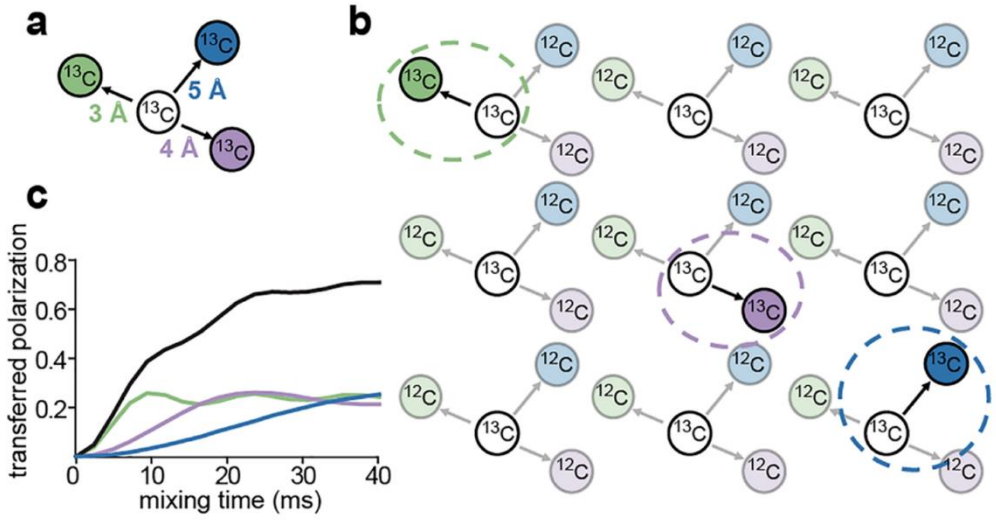

Figure 1-5. (a) Isotopically enriched ^{13}C spin system with different distances between nuclei. (b) The same spin system (a) was diluted at natural isotopic abundance (NA) and showing coupling only between individual spin pairs from the system. (c) Characteristic build-up curves for ^{13}C–^{13}C spin pairs at 3, 4, and 5 Å (green, purple, and blue curves, respectively) and the resulting superposition of build-up curves for the three distances that can be expected for a sample at NA, as in (b) (black). Reprinted (adapted) with permission from [101] Copyright (2019) American Chemical Society.

For isotopically enriched samples, measurement of long distances (present simultaneously with shorter distances) is complex as the densely populated NMR active nuclei have a strong network of through-space dipolar couplings or through bond j-couplings which interfere with weaker dipolar couplings associated with long distances[102–106]. This effect where the dipolar coupling of distant spins gets attenuated by stronger couplings to closer spins is known as truncation. At NA, this problem is simplified for nuclei like ^{13}C (NA 1.1 %) and ^{15}N (NA 0.37%) with low NA. Due to the dilute concentrations of these nuclei, each spin pair is virtually isolated, and hence the build-up can be treated as a sum of these discrete spin-pair interactions. Figure 1-5

demonstrates a system with ^{13}Cs and the corresponding homonuclear dipolar polarization build-up curves obtained at NA, showing that each spin pair can be treated separately. However, as described earlier, solid-state NMR suffers from low sensitivity, which makes recording some experiments impractical. MAS-DNP[101] can overcome this drastically reduced sensitivity from working with NA samples. For instance, Märker et al.[107] recorded ^{13}C homonuclear dipolar recoupling experiments using DNP-enhanced solid-state NMR and showed long-distance (>3 Å) polarization transfer can be recorded due to reduced dipolar truncation effects.

1.3.6 DNP for surface studies

As described earlier, DNP uses the large electron spin polarization to enhance the signal of nearby nuclei and hence improves the sensitivity compared to conventional ssNMR. Thus, for DNP sample preparation, tailored radicals are added to the sample as paramagnetic sources. Generally, due to relative proximity between these exogenous radicals and the surface of materials, the surface gets selectively more enhanced compared to the bulk[108–111]. In 2010, Lesage et al. showed the first fifty-fold selective surface enhancement on hybrid organic-inorganic silica-based materials. This approach for enhancing the surface signals by DNP was termed as DNP surface-enhanced NMR spectroscopy (SENS)[108]. Therefore, DNP provides an added advantage when probing the surface of materials and has been used to study the surface of various nanoparticles. Some of those studies relevant to this thesis are discussed below.

In 2016, Berruyer et al.[112] showed the use of DNP NMR in combination with Extended X-ray Absorption Fine Structure (EXAFS) to perform detailed structure determination of an organometallic complex present on an amorphous silica surface with a 0.7 Å precision. For this purpose, structural constraints were obtained from DNP SENS ^{13}C-{^{15}N} and ^{29}Si-{^{15}N} rotational echo double resonance (REDOR)[113,114] experiments for various sites. Thus, they were able to determine a single well-defined structure that is not very disordered.

DNP sample preparation is key to obtaining good signal enhancements on the samples, and hence studies have been performed to optimize the sample preparation for various NPs. In 2015, Piveteau et al.[115] used DNP SENS to selectively enhance the surface sites

of organic/ inorganic surface ligand capped InP, W-CdSe, ZB-CdSe, PbSe, PbTe, CdTe NPs and presented a general technique to characterize these nanoparticles. In order to avoid precipitation of NPs, which was required to perform solid-state NMR experiments, a new sample preparation using mesoporous silica (meso-SiO_2) was presented, which allowed experiments on colloidal dispersions of NPs. Moreover, the enhancements obtained on the nanoparticles allowed the acquisition of DNP enhanced 1D and 2D experiments, which enabled distinguishing between surface and bulk and provided bonding motifs between the NP surfaces and capping ligands. Subsequently, in 2019, Hanrahan et al.[116] presented another sample preparation using hexagonal boron nitride (h-BN), which reportedly doubled the DNP enhancements and absolute sensitivity obtained compared to meso-SiO_2.

Many nanoparticles have a composition containing a quadrupolar nucleus; for example, oxide-based nanoparticles have ^{17}O, a spin-5/2 nucleus. Thus, the NMR of these quadrupolar sites can provide information about the structure of these materials. In 2017, Hope et al.[117] showed the first surface-selective direct ^{17}O DNP spectra on ceria (CeO_2) nanoparticles. It was found that the polarization build-up by DNP on ^{17}O of surface and sub-surface species was faster than the bulk. They performed experiments with notable surface selectivity and consequently differentiated between the first three layers of CeO_2 NPs with high selectivity. In 2020, Nagashima et al.[118] presented a novel NMR approach to enhance the ability of indirect MAS-DNP to probe quadrupolar nuclei. Unlike the phase-shifted recoupling effects smooth transfer of order (PRESTO) or direct DNP approaches, which are preferred for studying quadrupolar nuclei, this method significantly improved the sensitivity of these nuclei, especially ones near the surface and having low gyromagnetic ratios. This approach was presented on hydrated titania-supported MoO_3 and aluminum-doped ZnO nanoparticles and showed indirect DNP-enhanced spectra of ^{95}Mo, $^{47,49}Ti$, ^{67}Zn, ^{17}O, and ^{27}Al quadrupolar nuclei. DFT calculations.

1.3.7 Density Functional Theory

In recent times, Density Functional Theory (DFT) calculations have become an indispensable tool for many analytic techniques to find a link between the experimental data and the corresponding structural models. Briefly, DFT calculations can be used to calculate the ground state energy of a system. In 1964, Hohenberg and Kohn[119] showed that the total ground state energy $E_0[n_0(r)]$ of a system could be found using electron density $n_0(r)$ information. $E_0[n_0(r)]$ can, in turn, be used to measure other fundamental properties of the system. Kohn and Sham[120] noted that the many-body problem could be alternatively written as a set of non-interacting one-electron orbitals $\Psi_i(r)$ whose electron density is the same as that of the real system. Thus, from Schrödinger-like Kohn–Sham equations:

$$\{\tfrac{1}{2}\left(\vec{\nabla}\right)^2 + V_H[n_0(\mathrm{r})] + V_{EXT}(r) + V_{XC}[n_0(\mathrm{r})]\}\Psi_i(r) = \varepsilon_i\Psi_i(r) \qquad 1.3.7$$

With,

$$n_0(r) = \sum_{OCC}|\Psi_i(r)|^2 \qquad 1.3.8$$

In Equation 1.4.1, the four terms within curly brackets represent the kinetic energy of non-interacting electrons, the Hartree potential accounting for electron-electron repulsion, the external potential accounting for electron nuclei interactions, and the exchange-correlation (XC) potential, respectively. While the first three terms can be calculated precisely, the XC represents the all-electron correlation effects, and its true form is unknown. Thus, to account for XC, several approximations have been proposed. Among them, the Generalized Gradient Approximation from Perdew–Bruker–Ernzerhof (GGA- PBE)[121] has been most widely used to calculate NMR parameters. At the start, an approximate value of $n_0(r)$ in Equation 1.4.1 is used, which is iteratively solved until self-consistency is achieved for $n_0(r)$ or the total energy E_0 converges to a user-defined precision.

1.3.8 Plane-wave pseudopotential formalism

For computational purposes, the Kohn-Sham orbitals are expanded using basis functions obtained from Bloch's Theorem:

$$\Psi_j(\boldsymbol{r}) = \sum_k e^{-ik.r} u_{j,k}(\boldsymbol{r}) \quad 1.3.9$$

here *k* represents a reciprocal lattice vector, generally inputted as an equidistant mesh in the first Brillouin zone. $u_{j,k}(r)$ is a periodic function in the unit cell with respect to real space lattice vectors and can subsequently be expanded as plane-wave, as:

$$u_{j,k}(\boldsymbol{r}) = \sum_G c_{j,k}(G) e^{-iGr} \quad 1.3.10$$

where *G* is a set of reciprocal lattice vectors. To truncate this plane-wave basis set in Equation 1.4.4, the summation is performed for a set of reciprocal lattice vectors present within a sphere whose radius depends on the cut-off energy, E_{cut}:

$$\frac{1}{2}|k + G|^2 \leq E_{cut} \quad 1.3.11$$

This systematically controllable parameter is the key strength of using the plane-wave basis set. However, in this method, high cut-off energy is required to represent the highly electron-dense core. In order to reduce the computational time, only the valence electrons are treated explicitly while the core is considered to be frozen, and the core-valence interactions are replaced by an effective potential known as a pseudopotential. The most widely used pseudopotential is based on the Martin–Troullier recipe[122].

1.3.9 The GIPAW method

The popularity of this tool to complement solid-state NMR experiments was renewed in 2001 when Mauri and Pickard[123] pioneered the now well-established gauge including projected augmented wave (GIPAW) method, which allowed the calculation of NMR parameters in solids under periodic boundary conditions with all-electron accuracy. This method is rooted in DFT, a plane-wave basis set, pseudopotentials, and PAW and allows calculating accurate NMR parameters for solids. A detailed description of the use of this method has been provided by Charpentier[124] and Bonhomme et al.[125]

In NMR, as discussed in section 1.3.1, the Zeeman interaction between an external magnetic field and a spin-½ nucleus is given by:

$$H = -\gamma\hbar\hat{I}(1-\overleftrightarrow{\sigma})B_0 \quad 1.3.12$$

Where $\overleftrightarrow{\sigma}$ is the magnetic shielding tensor and is defined by the response of electrons around a nucleus to the applied external magnetic field as follows:

$$\vec{B}_{ind}(r) = -\overleftrightarrow{\sigma}(r).\overrightarrow{B_0} \quad 1.3.13$$

In a diamagnet, the applied field induces orbital currents $j^{(1)}(r')$. The current leads to an induced field as:

$$\vec{B}_{ind}(r) = \frac{1}{c}\int d^3r' j^{(1)}(\boldsymbol{r'}) \times \frac{\boldsymbol{r}-\boldsymbol{r'}}{|\boldsymbol{r}-\boldsymbol{r'}|^3} \quad 1.3.14$$

The expression for the induced current $j^{(1)}(\boldsymbol{r'})$ is as follows:

$$j^{(1)}(\boldsymbol{r'}) = -\sum_{j}^{OCC}\left(\Psi_j^{(0)}(r)\vec{\nabla}\Psi_j^{(1)}(r) + \Psi_j^{(1)}(r)\vec{\nabla}\Psi_j^{(0)}(r)\right) - \frac{1}{2c}n_0(\mathrm{r})\vec{\boldsymbol{B}}_{\boldsymbol{0}} \times (\boldsymbol{r}-\boldsymbol{r_0})$$

$$= \boldsymbol{j_p^{(1)}}(\boldsymbol{r}) + \boldsymbol{j_d^{(1)}}(\boldsymbol{r}) \quad 1.3.15$$

Thus, the induced current is a sum of paramagnetic $\boldsymbol{j_p^{(1)}}(\boldsymbol{r})$and diamagnetic $\boldsymbol{j_d^{(1)}}(\boldsymbol{r})$ terms. $\boldsymbol{r_0}$ is the gauge origin, and $\Psi_j^{(0)}$ and $\Psi_j^{(1)}$ represent the unperturbed and perturbed Kohn-Sham orbitals, respectively.

The isotropic chemical shift δ_{iso} can be calculated from the magnetic shielding σ_{iso} as follows:

$$\delta_{iso} = \frac{\sigma_{iso}(ref)-\sigma_{iso}(sample)}{1-\sigma_{iso}(ref)} \quad 1.3.16$$

Except for very heavy elements, the $|\sigma_{ref}| << 1$, hence:

$$\delta \approx \sigma_{iso}(ref) - \sigma_{iso}(sample) \quad 1.3.17$$

1.4 Thesis outline

This thesis focuses on the characterization of the ligand shell surrounding the surface of ZnO NPs prepared by the OSSOM approach, using DNP-enhanced ssNMR combined with other complementary techniques, in broadly three different contexts/applications. These include comparing two synthetic approaches in terms of stability and uniformity of produced NPs, understanding the formation of a hexagonal

nanoplatelet (NPL) morphology, and characterizing the ligand shell of mixed ligand ZnO NPs, all using an understanding of the ligand shell obtained from DNP-enhanced ssNMR. The approaches used in this work can be extended to hybrid materials with an internal crystalline core and surface species.

Chapter 2 studies the arrangement of diphenyl phosphate capping ligands on polar surfaces of NPs prepared by the one-pot self-supporting organometallic (OSSOM) approach and a sol-gel methodology, determined using DNP-enhanced ssNMR. Using this information from the inorganic-organic interface showed that the structure of ZnO nanoparticles, and therefore the properties, depend on the employed synthetic method. In particular, the OSSOM approach produced more stable and consistent nanocrystals compared to the traditional sol-gel methodology.

Chapter 3 discusses a novel organometallic approach to produce ZnO NPLs with controlled thickness and long-term colloidal stability in polar aprotic (THF, DMSO) and protic (MeOH) solvents. The NPLs are ultra-thin, ranging in thickness from 3.2 nm for the smallest to 7.5 nm for the largest, making them attractive for various applications. These NPLs were characterized through a combination of various classical analytical techniques, as well as HRTEM and DNP-enhanced ssNMR. This study reveals that the NPLs are hexagonal and well-faceted, with a bimodal binding of facet-specific ligands on the polar (0001) and non-polar ($10\bar{1}0$) facets of the wurtzite ZnO.

In Chapter 4, a more detailed analysis will be discussed for the ultra-thin ZnO NPLs whose synthesis was shown in Chapter 3. DNP-enhanced ssNMR combined with DFT calculations, and HAADF STEM was used to analyze the surfaces. More specifically, DNP-enhanced ^{13}C homonuclear dipolar correlation spectra for ^{13}C from surface ligands were studied at NA. These were used to study ligand proximity and arrangement of ligands on the ZnO surface. Also, DNP-enhanced ^{13}C and ^{15}N MAS NMR spectra and ^{1}H-^{15}N heteronuclear correlations recorded at NA were analyzed. These spectra evidenced the presence of various ligand-binding sites at the inorganic interface associated with different facets. Based on the NMR observations, insights have been provided into the role of ligand in the growth of these NPLs.

Chapter 5 describes an in-depth analysis of the mixed-ligand shell of ZnO NPs prepared by the modified OSSOM approach. Mixed ligand shells on nanoparticles (NPs) have been extensively studied, as these are found to improve NP properties such as solubility, wettability, catalysis, cation capturing ability and are used for their bioapplications. Thus, there is a need to have a technique to determine the ligand shell composition and morphology. In this work, a method has been presented to analyze the percentage of heteroligands in the vicinity to each other quantitatively. Therefore, for the mixed ligand shell NPs, an exciting application of DNP-enhanced NMR to potentially determine the mixed-ligand shell morphology on the surface of ZnO NPs is presented.

Finally, a conclusion and outlook section will bring the work together and provide a vision for the future applications of the approaches presented herein.

Chapter 2
Sol-gel versus OSSOM approach

2.1 Introduction

Zinc oxide (ZnO) is a versatile material of long-standing interest due to its unique catalytic and electro-optical characteristics[12,14,126–128]. The inherent and distinctive physicochemical properties of ZnO nanocrystals (NCs) are dependent on a variety of factors that are largely determined by the applied synthetic procedure and the character of the resulting nanocrystal-ligand interface including intimate interactions on NC surfaces, the surface ligand dynamics, ligand packing density, and their binding mode and/or affinity. In this regard, classical wet-inorganic sol-gel methodology has played a key role in advancing ZnO NC science by providing access to a multitude of tailored nanostructures[44,129–132]. While this process is versatile, it showcased some significant drawbacks[129,133–137]. For instance, the reproducibility of this method can be hardly regulated as the formation of quantum-sized ZnO NC is kinetically controlled. The lack of direct control over the fast NC formation at the stage of quantum-sized crystals[44,129] likely inhibits both the uniformity of particle morphology and nanocrystal-ligand interface composition, including the density and homogeneity of any ligand shell[53,138–142]. It could also be related with an inherently highly-defected and corrugated surface structure, and an unstable resulting nanocrystal-ligand interface (e.g., Gong et al. demonstrated that sol-gel derived ZnO NCs with a stable surface structure could be achieved after a one-month aging process[142]). An alternative to the omnipresent sol-gel method are highly promising wet-organometallic approaches[42,43,52,143,144]. In this regard, Chaudret and co-workers pioneered the preparation of ZnO NCs, utilizing dicyclohexylzinc as the precursor in the presence of long-chain amines acting as L-type ligands[42,52,143,144], where the resulting amine-stabilizing layer has the *'dynamic*

structure'[52,62]. More recently, the one-pot self-supporting organometallic (OSSOM) procedure was introduced, it is based on the controlled exposition of a [EtZn(X)]-type precursor (X = monoanionic organic ligand) to air leading to ZnO NCs coated with an organic shell composed of surface-anchored X-type ligands[22,24,26,28,41]. The OSSOM process is thermodynamically controlled and affords stable, bio-safe[28] and well-passivated ZnO NCs with ultra-long-lived luminescence[28,29].

To gain a better understanding of how the interface between the inorganic core and the organic shell relates to observed synthetic procedure-driven properties, ZnO NCs coated with monoanionic diphenyl phosphate (DPP) ligands were prepared by both the OSSOM and sol-gel methods as representative nanosystems (abbreviated as OM NCs and SG NCs, respectively; for experimental details see the materials and methods section). The diorganophosphate anchoring ligand was chosen due to intriguing structural properties and the 100 % naturally abundant NMR-active nucleus of phosphorus, ^{31}P. Then, 9.4 T solid-state NMR combined with magic angle sample spinning and dynamic nuclear polarization (MAS-DNP)[145,146] was applied, which has recently proven invaluable for specialized surface studies[108–110], including for quantum dots[115,147]. In addition, to test the stability of the ZnO NCs toward chemical environment, a solvent matrix containing glycerol was chosen for the MAS-DNP experiments.

2.2 Results and Discussions

2.2.1 Standard sample characterization.

STEM micrographs and DLS analysis of the OM NCs show well-dispersed and nearly spherically shaped particles with a core mean diameter of 4.8±0.5 nm (the average NC's size calculated from PXRD is equal to 4.4±1 nm) and a hydrodynamic diameter of 9.6 nm (PDI = 0.083) (see Figure 2-13 and Figure 2-14 in the materials and methods section). In contrast, the standard sol-gel method provided significantly larger NCs with a core size of 10-12 nm (10±1.8 nm calculated from PXRD), though their aggregation and irregular shape prevented a more exact size distribution analysis (note that the

aggregation and formation of a colloidal suspension of the SG NCs prevented reliable DLS measurements).

The PXRD patterns for OM and SG NCs are consistent with a hexagonal wurtzite-type ZnO phase (see Figure 2-15). Both sets of NCs revealed a broad absorption in the UV region and emission maxima centered at 525 and 555 nm, respectively (Figure 2-16 and Figure 2-17). The FTIR spectra confirm that DPP passivating moieties are deprotonated (see Figure 2-18), which corroborate the thermogravimetric analysis (see Figure 2-19). In the TGA profile of the OM NCs only one main decomposition step in the range from 0°C to 500°C is present. On the contrary, the SG system shows a significantly more complex decomposition path. This observation substantiates the different nanocrystal-ligand interfaces for NCs derived from the OSSOM and sol-gel methods, and indicates a more complex structure of organic ligand shell for the SG NCs. The TGA-determined surface coverage of OM and SG NCs were ca. 4-5 ligands/nm^2 and 12 ligands/nm^2, respectively[148]. A comparison of the characteristic properties of the OM and SG NCs is presented in Figure 2-20 in materials and methods section.

2.2.2 Effect of competing ligand studied using NMR spectroscopy

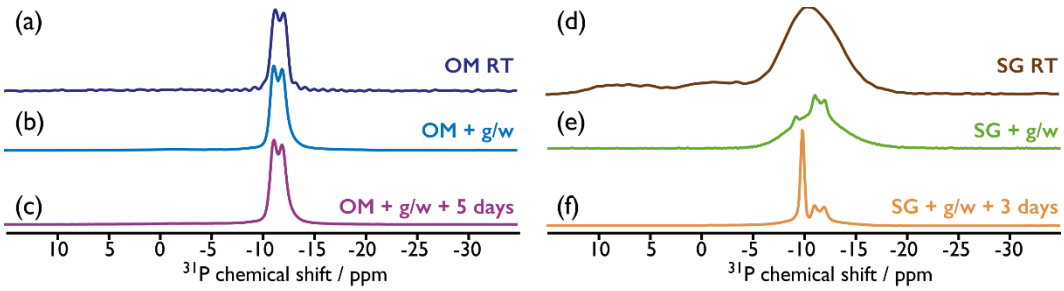

Figure 2-1. Time-dependent room temperature (a, d) and 105 K DNP-enhanced (b, c, e, f) {1H-}31P CPMAS NMR spectra of (a, b, c) organometallic and (d, e, f) sol-gel derived ZnO NCs. (b, e) Spectra recorded within 30 minutes of addition of glycerol/water (g/w) solution and (c, f) after storage at -18 °C.

The structures of the organic ligand shells were compared using NMR spectroscopy, which has recently been shown to be particularly powerful in this regard[149,150]. Figure 2-1 shows the {^{1}H-}^{31}P cross-polarization (CP) MAS NMR spectra of OM and SG NCs (Figure 2-1a and d) and corresponding DNP-enhanced spectra recorded for freshly wetted samples (Figure 2-1b and e) as well as after sample storage at -18 °C for 5 and 3 days, respectively (Figure 2-1c and f). The NMR spectra highlight that the surface of

the OM NCs is indeed functionalized by monoanionic diphenyl phosphate ligands, evidenced by ^{31}P NMR signals at $\delta\{^{31}P\} \approx$ -11 and -12 ppm (F.W.H.M. ~120 Hz) that are *inconsistent* with pure DPP-H (see Figure 2-3a), whereas they are *consistent* with the chemical shift of bridging DPP, as observed in model organozinc molecular complexes[151]. The relatively narrow linewidth of the two ^{31}P peaks indicates a rather ordered structure at the surface. In addition, the time-dependent spectra show that the OM NCs remain stable (Figure 2-1b and c), which indicates that the resulting nanocrystal-ligand interface is robust.

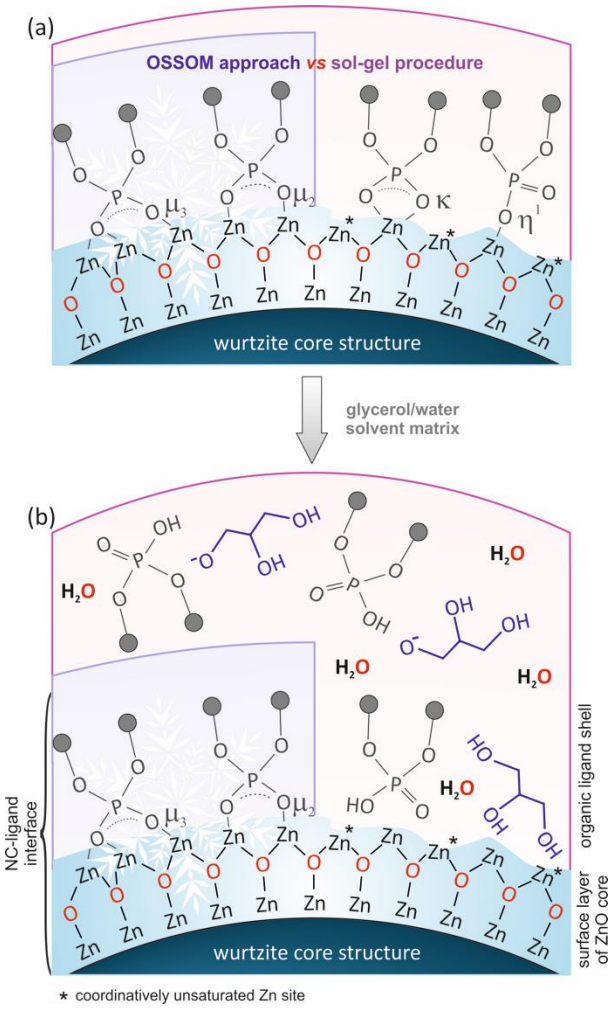

Figure 2-2. Schematic representation of the organic ligand shell of OM and SG NCs before (a) and after (b) wetting and aging with a glycerol-based matrix. The snowflake represents a surface portion with an ordered and stable ligand arrangement (i.e. stable μ_2- and μ_3- DPP-bridging-ligand pairs), termed here as *cold spots*. Residual acetate moieties present on the surface of SG NCs are omitted for clarity.

In contrast, the respective spectrum of the SG NCs (Figure 2-1d) is far more complex and consists of broad signals ranging from approximately 15 to -15 ppm, indicating a

dramatically different organic-inorganic interface to that in OM NCs. The ^{31}P NMR spectrum of the "just-wetted" SG NCs (Figure 2-1e) consists of remaining broad contributions (ranging from $\delta\{^{31}P\} \approx$ -5 to -15 ppm) and also the emergence of narrow peaks. After 3 days' storage at -18 ºC, the spectrum has evolved to leave the narrow signals at $\delta\{^{31}P\} \approx$ -11 and -12 ppm (minor intensities) and to produce a separate intense signal at ≈ -10 ppm (Figure 2-1f). The first two signals correspond to those observed for the OM NCs, while the signal at $\delta\{^{31}P\} \approx$ -10 ppm is associated with the solvent-matrix-induced release of DPP species from the surface of the SG NCs in the protonated form as DPP-H (Figure 2-2), resulting in the same $\delta\{^{31}P\}$ as observed for pure pro-ligand (see Figure 2-3a). The relatively narrow linewidth of the signal at $\delta\{^{31}P\} \approx$ -10 ppm suggests that although the ligand has been detached from the surface, it is in an ordered environment. A broad peak would be expected for a less-ordered environment, such as found in pure DPP-H or for a DPP-H solution (see Figure 2-3a). A large range of ^{31}P chemical shifts and the observed changes in the time-dependent $\{^{1}H\text{-}\}^{31}P$ cross-polarization (CP) MAS NMR spectra data clearly indicate that SG NCs possess a corrugated NC surface structure composed of islands and ridges with variously coordinated, and potentially multi-layered, organic ligands (Figure 2-2). Moreover, the data demonstrate that the organic-inorganic interface of these NCs is not stable toward chemical environment and a ligand exchange process takes place between DPP ligands and glycerol molecules (see Figure 2-2)[152,153]. Possible hydrogen-bond formation between the resulting anionic glycerol species and DPP-H molecules as well as between glycerol and the residual DPP ligands present on the surface could force some short-range order. The next- and second next-neighboring molecules probably also align similarly, leading to the formation of a multi-layered structure described previously as a *'swollen'* shell (i.e. the organic shell is not built up by a closely-packed monolayer of DPP molecules but is rather a swollen coating composed of DPP and solvent molecules).[4e] Moreover, for the time-evolved SG NCs, the small relative intensities of the narrow signals from the remaining surface-bound DPP ligands compared to the signal from the surface-detached DPP-H moieties suggests that the ZnO surface produced from the sol-gel synthesis is characterized by the presence of only very limited and randomly distributed robust surface islands with an ordered and stable ligand arrangement, which were termed as *"cold spots"*. These sparse and relatively

stable spots then have a similar local structure to that of the entire surface of the ZnO NCs derived from the OSSOM approach (Figure 2-2). An estimation of the amount of detached DPP-H molecules can be obtained from the ^{31}P NMR spectrum of Figure 2-1f (assuming that the CP dynamics are similar for surface-bound and free ligand moieties). This analysis (see Figure 2-4) shows that approximately one quarter of the ligands remain surface-bound, half are in the ordered swollen shell, and the remaining quarter are randomly distributed in the solvent.

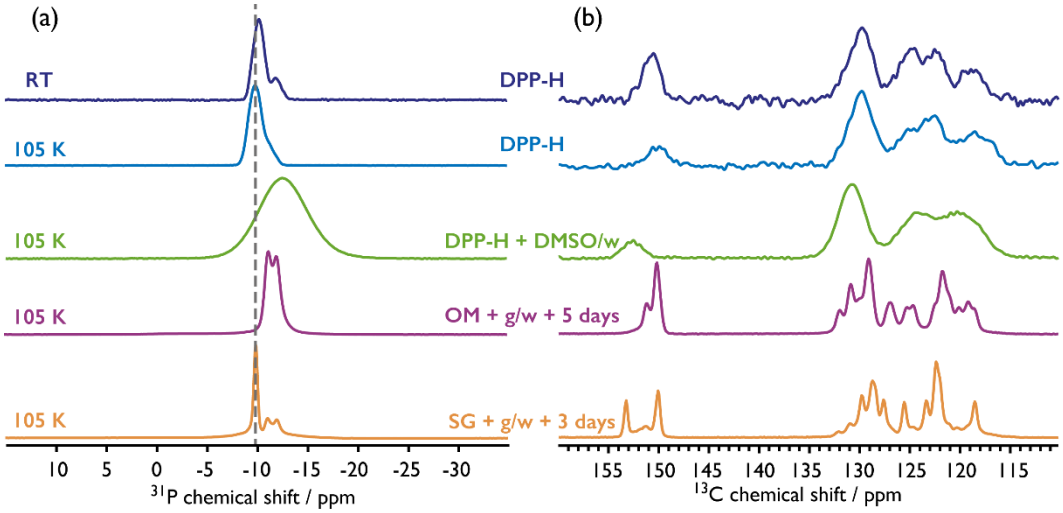

Figure 2-3 (a) {^{1}H-}^{31}P and (b) {^{1}H-}^{13}C CPMAS NMR spectra of diphenyl phosphate (DPP-H) powder (as received and not recrystallized), recorded at room temperature (RT) and compared to corresponding spectra recorded at 105 K for DPP-H powder and DNP-enhanced spectra of 0.5 M DPP-H DMSO-D_6/D_2O/H_2O (24/3/1; v/v; denoted DMSO/w) frozen solution and organometallic and sol-gel derived ZnO NCs impregnated with glycerol-D_8/D_2O/H_2O (6/3/1; v/v; denoted g/w).

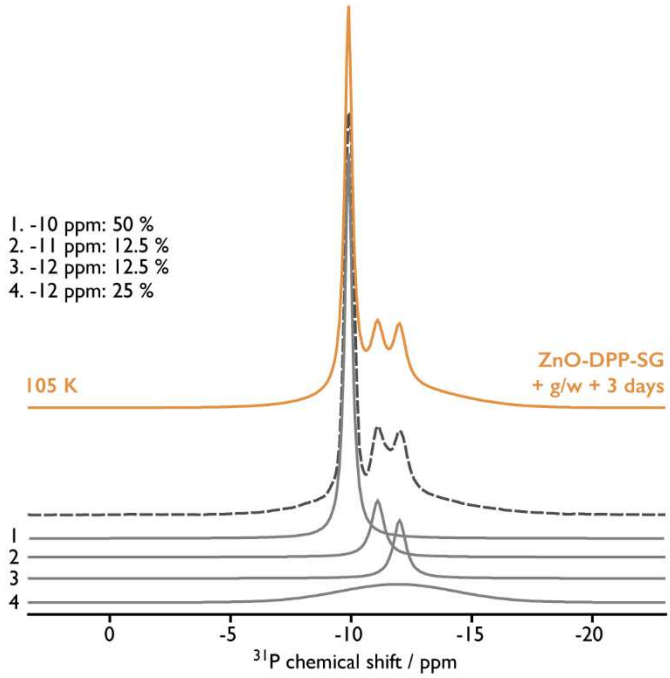

Figure 2-4 DNP-enhanced $\{^1H\text{-}\}^{31}P$ CPMAS NMR spectrum of the aged SG NCs (orange), associated deconvolution into four components (grey), and the resulting summation of the components (grey dashed line). Also shown are the relative integrated intensities of each component and their approximate chemical shifts. Note that the 4th component has the same lineshape and chemical shift as a 0.5 M DPP-H DMSO-D_6/D_2O/H_2O frozen solution (see Figure 2-3a) and is thus attributed to dissolved and randomly distributed DPP-H in the glycerol/water matrix.

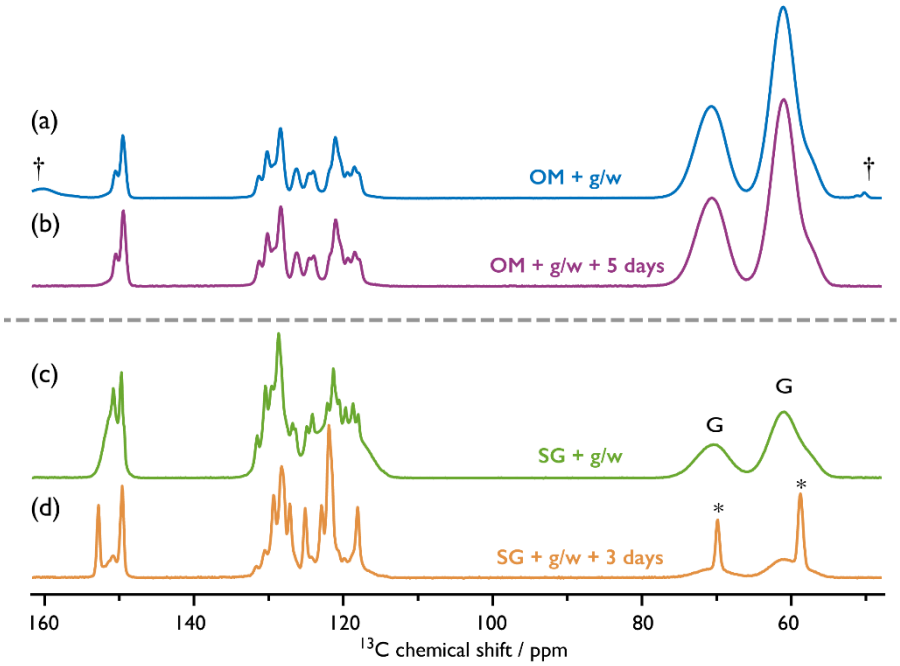

Figure 2-5. Time-dependent 105 K DNP-enhanced $\{^1H\text{-}\}^{13}C$ CPMAS NMR spectra. (a, b) Organometallic and (c, d) sol-gel derived ZnO NCs. "G" and "*" denote signals from amorphous and crystalline glycerol, respectively, and "†" denotes spinning side bands. The MAS frequency for (a) was 10 kHz, whereas 13.889 kHz was used for (b-d).

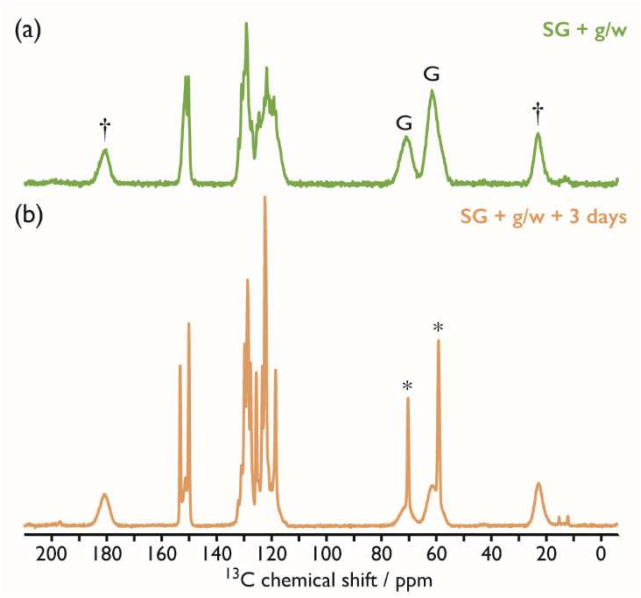

Figure 2-6. Time-dependent 105 K DNP-enhanced {^{1}H-}^{13}C CPMAS NMR spectra of the SG NCs impregnated with glycerol-D_8/D_2O/H_2O (6/3/1; v/v; denoted g/w). "G" and "*" denote signals from amorphous and crystalline glycerol, respectively, and "†" denotes signals from acetate moieties.

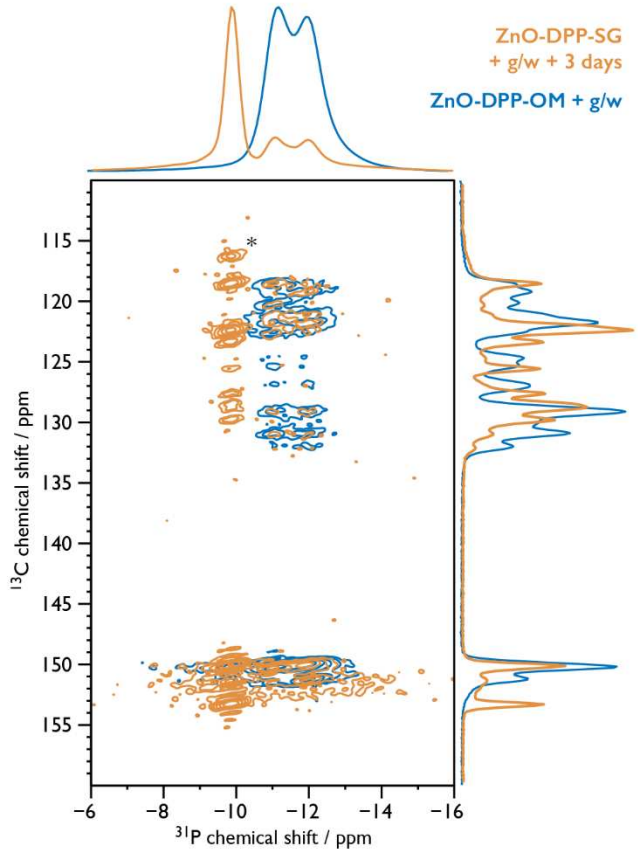

Figure 2-7. DNP-enhanced ^{13}C–^{31}P dipolar correlation (DCP-HETCOR) spectra of the OM (blue) and aged SG (orange) NCs, recorded with a ^{13}C–^{31}P CP mixing time of 5 ms. The total experiment time was approximately 9 hours for each. The asterisks denote aliased cross peaks from the ^{13}C resonances ($\delta\{^{13}C\}$

= 59 (*) and 70 (*') ppm) of the crystalline glycerol. Also shown, corresponding 1D DNP-enhanced {^{1}H-}^{31}P (top) and {^{1}H-}^{13}C (right) CPMAS NMR spectra.

2.2.3 Disclosing interfaces using Dynamic Nuclear Polarization

To further characterize the effect of the glycerol/water solvent matrix on the DPP ligand shell in the SG and OM NCs, time-dependent DNP-enhanced {^{1}H-}^{13}C CPMAS NMR spectra (Figure 2-5 and Figure 2-6) along with DNP-enhanced 2D ^{13}C–^{31}P correlation spectra (Figure 2-7) were acquired. The ^{13}C NMR data (Figure 2-5) indicate that the OM sample remained unaffected during sample storage and the surface-bound DPP ligands are highly ordered, with at least 20 ^{13}C resonances for the DPP moieties of OM NCs (suggesting more than one DPP environment, see Figure 2-5). In contrast, the respective spectra of the SG NCs (Figure 2-1d) are far more complex. There is a change in the ^{13}C NMR signals stemming from glycerol for the SG sample with time (Figure 2-5c and d). Two narrow peaks (denoted by asterisks on Figure 2-5) are observed to evolve from the broad peaks typical of a glycerol/water glassy matrix. These narrow peaks together with the pattern characteristic for DPP-H molecules (particularly when compared to pure pro-ligand, see Figure 2-3b infer the presence of an ordered system within a *'swollen'* shell around SG NCs. Furthermore, a close proximity is detected between ^{31}P from surface-detached DPP-H moieties ($\delta\{^{31}P\} \approx$ -10 ppm) and ^{13}C of ordered glycerol in 2D ^{13}C–^{31}P correlation spectra (see Figure 2-7) but this is not the case for surface-bound DPP species, which strongly supports this concept of a *'swollen'* organic shell[141] surrounding SG NCs. Strikingly, the ^{13}C NMR data also shows that the sol-gel approach, which used zinc acetate as a precursor, results in residual acetate as well as DPP ligands on the surface of ZnO NCs (see Figure 2-6). The DPP ligands occupy the anticipated *cold spot* and residual acetates are likely encapsulated in niches on corrugated surface structures of the SG NCs. The latter observation corroborates earlier studies reported by Peukert et al.[139] in which it was evidenced that acetate moieties could be continuously detached from organic coatings upon purification and only a small amount of coordinated acetate remains at ZnO NC surfaces.

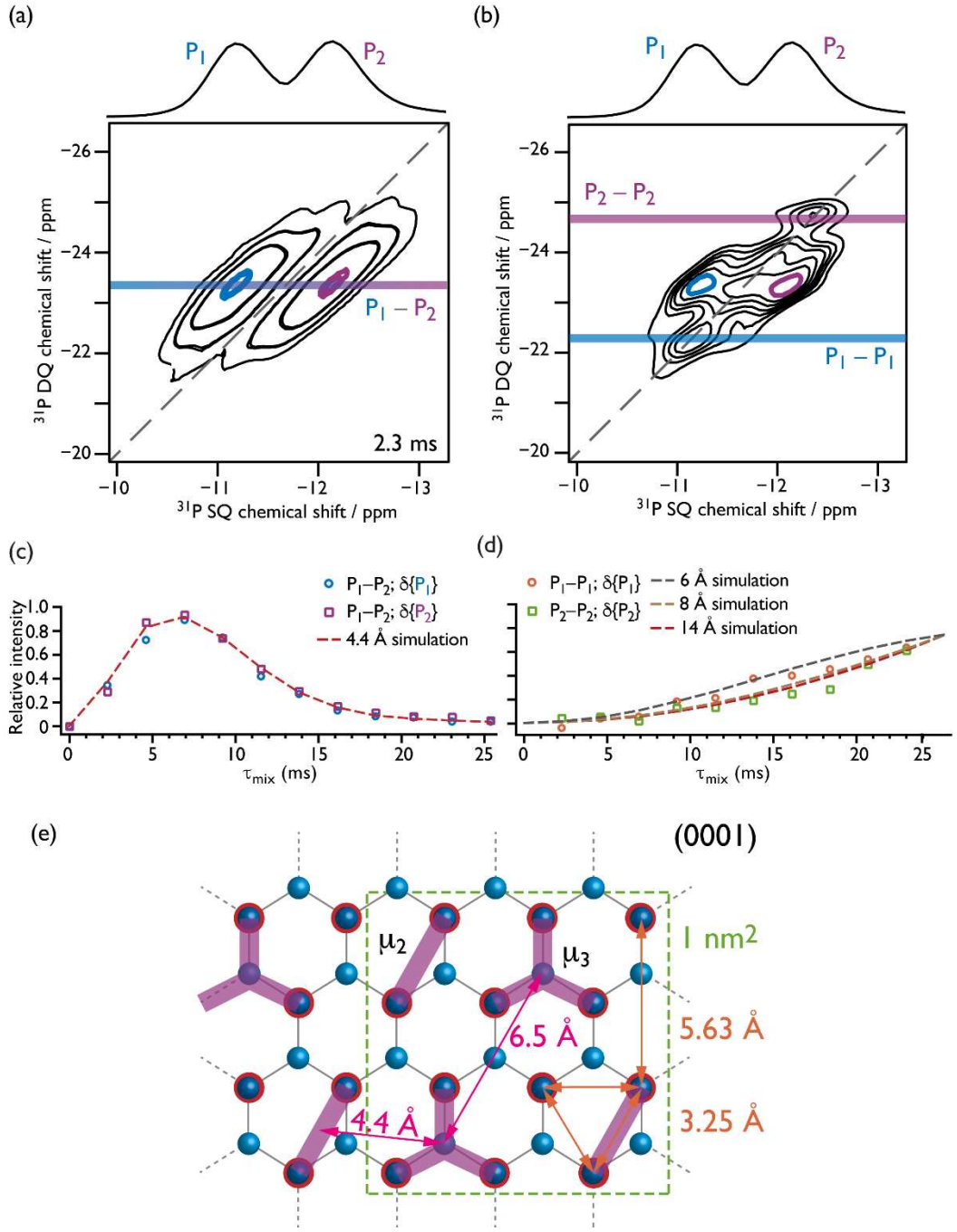

Figure 2-8. Representative DNP-enhanced ^{31}P–^{31}P S3 dipolar correlation spectra recorded with a total S3 recoupling time, τ_{mix}, of (a) 2.3 ms and (b) 23 ms, along with (c) a plot showing the relative intensities of P1–P2 and P1–P1 and P2–P2 correlations peaks as a function of τ_{mix}, with corresponding SPINEVOLUTION simulations (dashed lines) based on the internuclear distances given and on the schematic wurtzite (0001) surface structure shown in (d).

The intimate interactions between organic ligands and NC surfaces (binding mode and/or affinity etc.) are crucial for the structure-property relationship of ZnO NCs. Thus, for a more detailed study of the organic ligand shell, 2D NMR spectroscopy was employed. Figure 2-8 shows DNP-enhanced 2D ^{31}P homonuclear dipolar correlation

spectra of the wetted and aged OM NCs, recorded using the S_3 recoupling sequence[154,155] with short (Figure 2-8 a) and long (Figure 2-8 b) dipolar recoupling times. This experiment produces peaks that share a common frequency (or double-quantum (DQ) chemical shift) in the horizontal dimension for nuclei that are spatially close to one another. Interestingly, a short recoupling time (Figure 2-8 a) shows that the two ^{31}P signals with $\delta\{^{31}P\} \approx$ -11 and -12 ppm stem from two discrete but adjacent DPP bridging ligands, denoted here as P_1 and P_2. Moreover, there is no evidence in this spectrum of these sites showing autocorrelation peaks, i.e., surface-bound DPP is not spatially close to another DPP moiety with the same conformational environment (and thus chemical shift). Therefore, surface-bound DPP is only spatially very close to a second DPP moiety that has a different conformation, likely resulting from pairs on polar facets of the NCs. At longer recoupling times (Figure 2-8 b) connections between P_1 and another P_1 site as well as P_2 and other P_2 sites become present. This means that there is some proximity between P_1/P_2 and other P_1/P_2 environments but that P_1 environments are much closer to dissimilar P_2 environments.

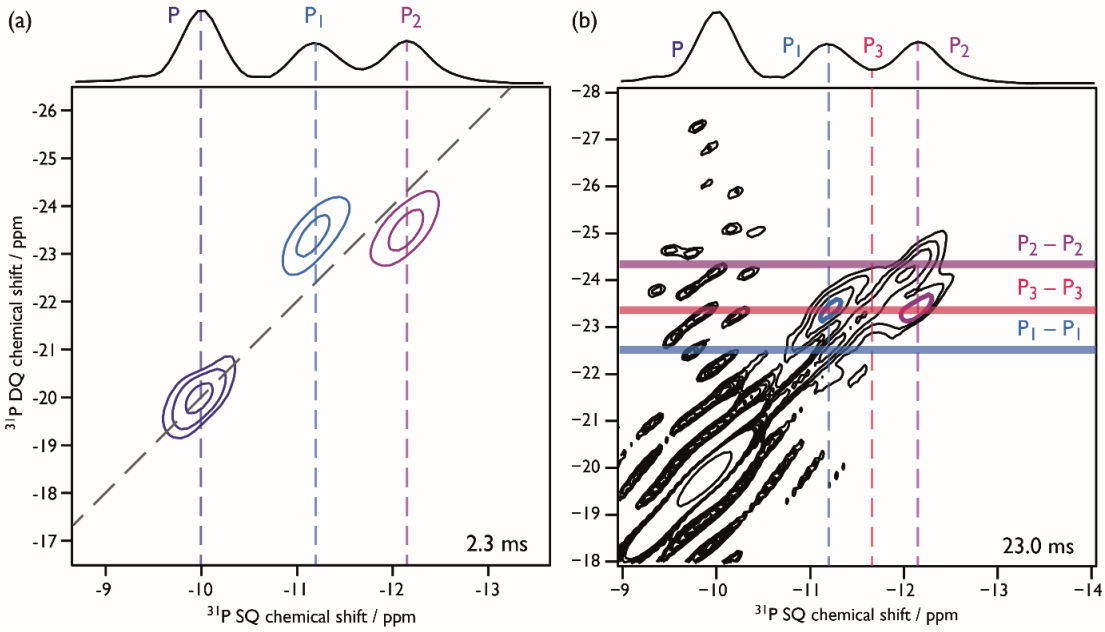

Figure 2-9. DNP-enhanced ^{31}P–^{31}P S3 dipolar correlation spectra of the aged SG NCs, recorded with total recoupling times of 2.3 ms (a) and 23.0 ms (b). The total experiment time was approximately 1.5 hours for each.

Comparative 2D ^{31}P homonuclear dipolar correlation spectra for the SG NCs (*i*) show that the surface-dissociated (solvated or *swollen* shell) DPP-H moieties with $\delta\{^{31}P\}$ = -10 ppm display an autocorrelation peak (at $\delta\{^{31}P_{DQ}\}$ = -20 ppm, see Figure 2-9) arising from a proximity between these released molecules and (*ii*) exhibit P_1–P_2 connections at short recoupling times as well as P_1–P_1 and P_2–P_2 connections at longer recoupling times, as found for the OM NCs. This latter observation substantiates the conclusion of sparse *cold spots* on the surface of the SG NCs having the same stable ligand arrangement as the ZnO NC surfaces produced from the OSSOM approach. Note that a third DPP binding environment is observed, with a chemical shift $\delta\{^{31}P\}$ = -11.7 ppm (denoted P_3) that is in between that of P_1 ($\delta\{^{31}P\}$ = -11.3 ppm) and P_2 ($\delta\{^{31}P\}$ = -12.1 ppm), clearly visible in Figure 2-9b and also in Figure 2-8b. This P_3 site does not share connections with dissimilar P sites (i.e., P_1 or P_2), only other P_3 sites. Since this P_3 environment is not observed in the 2D experiments recorded using a short recoupling time (Figure 2-9a and Figure 2-8a), it can be concluded that these surface P_3 sites are discrete and separated from their nearest neighbor P_3 site by a distance greater than that between P_1 and P_2, and could relate to DPP ligands located on a different polar facet (to P_1 and P_2) or at the edges between facets of the NC. P_3–P_3 distances cannot be estimated reliably due to the lack of resolution of the corresponding correlation peak. P_3 only appears at longer recoupling times, like P_1–P_1 or P_2–P_2.

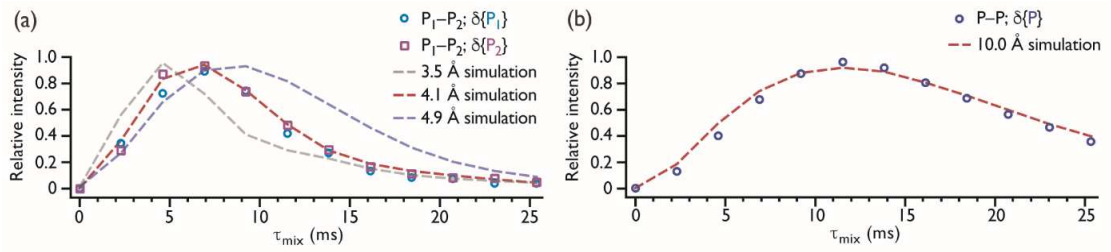

Figure 2-10. Plots showing the relative intensity of correlation peaks from DNP-enhanced ^{31}P–^{31}P S3 dipolar correlation spectra of aged OM (a) and SG (b) NCs as a function of total S3 recoupling time, τ_{mix}. Also shown are corresponding SPINEVOLUTION[156] simulations (dashed lines are used as a guide between simulated data points) based on the internuclear distances given; for both, a 2-^{31}P-spin system was employed.

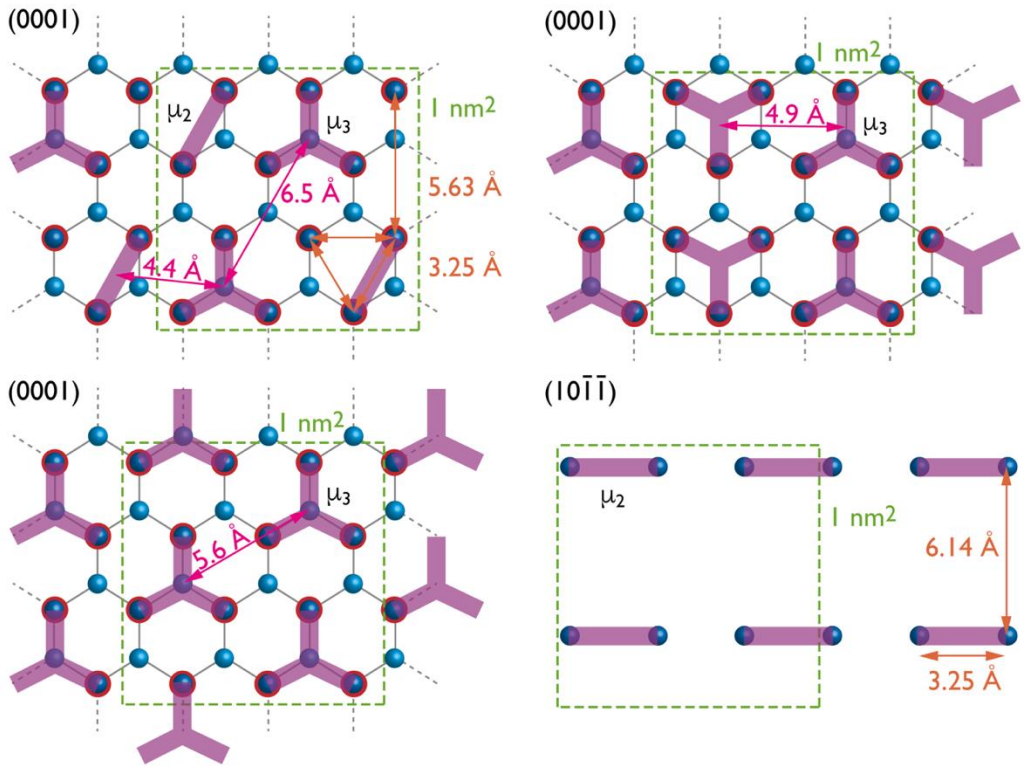

Figure 2-11. Schematic showing possible surface arrangement of DPP ligands on polar wurtzite ZnO facets.

For the estimation of distances between ^{31}P nuclei, and thus between DPP moieties, multiple 2D ^{31}P homonuclear dipolar correlation experiments were performed with varying dipolar recoupling times (τ_{mix}). Plotting the intensity of the OM NC P_1–P_2 correlation peaks (at $\delta\{^{31}P_{DQ}\}$ = -23.4 ppm) as a function of τ_{mix} and comparing the resulting curve to numerical simulations using SPINEVOLUTION[156] software gives a good fit for a discrete internuclear *P*–*P* distance of 4.1±0.2 Å (see Figure 2-10a). The presence of surface dianionic tetraphenyl pyrophosphate moieties (resulting from a condensation reaction between two DPP-H pro-ligands) can be ruled out since this would result in a ^{31}P–^{31}P internuclear distance of approximately 3 Å. The presence of monoanionic ligands, either monodentate or bidentate (κ, μ_2-η^1:η^1 or μ_3-μ_2:η^1 bridging coordination modes), would result in ^{31}P internuclear distances either <3.5 or >4.9 Å between DPP ligands on wurtzite NCs, except if pairs of μ_2–μ_3 ligands are formed on wurtzite (0001) surfaces (see Figure 2-11). Therefore, with the estimated P_1–P_2 distance of ~4.1 Å, some surface DPP moieties *must* be arranged close together, forming these μ_2–μ_3 pairs (on wurtzite (0001) surfaces), possibly stabilized through π–

π interactions of the DPP aromatic rings. Accordingly, P_1 and P_2 must be from μ_2-η^1:η^1 and μ_3-μ_2:η^1 ligands (not necessarily respectively). Taking this surface structure, depicted in Figure 2-8e, for the numerical simulations (rather than simple *P–P* pairs) results in a revised estimate for the $P_{\mu3}$–$P_{\mu2}$ internuclear distance, giving 4.4±0.2 Å (see Figure 2-8 c). A P_1–P_1 (or P_2–P_2) distance from the proposed wurtzite (0001) ZnO-DPP surface configuration would be >6 Å and from other polar surfaces (such as $(10\bar{1}\bar{1})$, see Figure 2-11) it would be at least 5 Å. This is what is found from comparing numerical simulations to experimental data (see Figure 2-8c and d), using a similar correlation peak analysis as above. This surface characterization indicates that a very compact coverage is possible for the OM NCs, in agreement with the TGA analysis that gives 4–5 ligands per nm^2. It could thus be proposed that the thermodynamically-controlled OSSOM approach and the utility of monoanionic stabilizing ligands, which could strongly and formation-selectively adsorb to the polar (0001) face, allow for the lower aspect-ratio (i.e., quasi-spherically shaped) ZnO NCs with significantly more [0001] planes present. This is consistent with the literature[157] and the observed relatively high surface coverage of ZnO NCs derived from the organometallic approach.

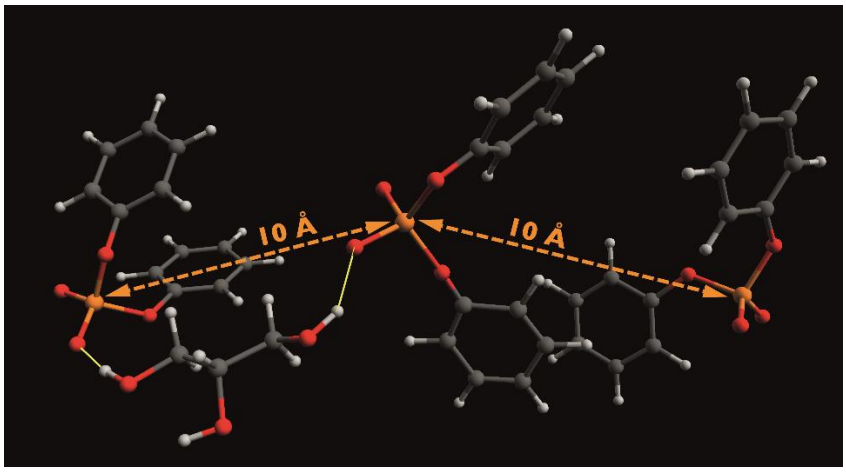

Figure 2-12 Schematic showing a glycerol molecule hydrogen bonded between DPP moieties.

The same correlation peak analysis was also performed for the surface-detached DPP-H observed for the SG NCs, which indicates one large internuclear P–P distance of ~10 Å (see Figure 2-10b). This is consistent with an ordered *swollen* shell containing glycerol molecules hydrogen-bonded between DPP molecules (see schematic in Figure

2-12). It should be noted that no interactions between detached and surface-bound species were observed. The surface characterization of the wetted SG NCs then indicates that a mixture of sparse, randomly distributed surface *cold spots* containing stable μ_2- and μ_3-DPP-bridging-ligand pairs, and above-surface ordered DPP-H molecules in probable multi-layers, consistent with the TGA analysis that gives the large number of 12 ligands per nm^2 of NC surface.

2.3 Conclusion

In conclusion, DNP-enhanced solid-state NMR spectroscopy proves extremely pertinent for detailed characterization of nanocrystal-ligand interfaces, here highlighting large differences between DPP-coated ZnO NCs prepared by the organometallic approach and the traditional sol-gel procedure. It has been shown that the OSSOM approach provides ZnO NCs with a highly-ordered surface ligand arrangement of μ_2-η^1:η^1-DPP_1 and μ_3–μ_2:η^1-DPP_2 bridging ligands, which are paired-up on the surface and which remain unaffected during sample storage and even in the presence of glycerol as a highly competitive capping ligand. In contrast, ZnO NCs produced via the sol-gel method exhibit variously-coordinated DPP ligands and a time-dependent surface restructuring process with a displacement of the majority of the ligands from the surface, creating an ordered *swollen shell* containing DPP-H and solvent molecules, signifying a corrugated surface morphology of these NCs and substantially labile surface-ligand interactions. Moreover, in the case of SG NCs, the presence of randomly distributed robust surface islands with an ordered and stable ligand arrangement were evidenced.

2.4 Materials and methods

2.4.1 General considerations

All manipulations connected with the synthesis of organozinc compounds were conducted under dry, oxygen-free nitrogen atmosphere in carefully dried glassware using standard Schlenk techniques. All other reagents were purchased from commercial

vendors and used as received. Tetrahydrofuran was dried and distilled from sodium-potassium alloy and benzophenone prior to use.

2.4.2 Standard sample characterization.

Liquid-state NMR spectra of organozinc precursor were acquired on Bruker 300 MHz spectrometer at 298 K. FTIR spectra were measured with a Bruker Vertex 80V spectrometer. Size and morphology of the ZnO NCs were imaged using a C_s corrected Scanning Transmission Electron Microscope (STEM, HITACHI HD2700, 200 kV). Nanocrystal samples were drop-cast (THF solution) onto 300-mesh, holey carbon-coated copper grids (Quantifoil). Afterward, the excess solvent evaporated at room temperature. The observations were carry on in two modes: SE (images used to study morphology) and HRTEM (images showing the atomic structure). The size of ZnO NCs was calculated by image analyses, using ImageJ2x computer software. For image analyses a population of at least 100 particles was used for each sample. Powder XRD data were collected on an Empyrean diffractometer (PANalytical). Measurements employed Ni-filtered Cu Kα radiation of a copper sealed tube charged with 40 kV voltage and 40 mA current and Bragg-Brentano geometry with beam divergence of 1 deg. in the scattering plane. Diffraction patterns were measured in the range of 20-80 degrees of scattering angle by step scanning with step of 0.008 degree. Thermogravimetric analysis (TGA) was carried out using a TA Instruments Q600 under a flow of artificial air, to max 800°C, at a heating rate of $5°C \cdot min^{-1}$ (flow rate of 100 mL/min). Open alumina crucibles with 5 mm in diagonal were used. Hydrodynamic diameter of ZnO NCs was determined by Dynamic Light Scattering (DLS) performed on Malvern Zetasizer Nano Z. A THF solution of ZnO NCs was filtered before the analysis through a 0.2 micron filter to remove any dust particles. Optical absorption (UV-Vis) spectra for ZnO NP colloidal solutions or suspensions in THF were collected on a Hitachi U-2910 spectrophotometer. A standard quartz cell (Hellma) with a 10 mm path length was used and rinsed with proper solvent before each run. Photoluminescence (PL) measurements were carried out using a HITACHI Fluorescence Spectrophotometer F-7000.

2.4.3 Synthesis of $[EtZn(X)]_n$ (where X = DPP) and its transformation to OM NCs:

$[EtZn(DPP)]_n$: An appropriate amount of diphenyl phosphate (0.250 g, 1 mmol) was dissolved in THF (5 mL) and the solution was cooled to -78°C under N_2 atmosphere. $ZnEt_2$ (0.5 mL of a 2 M solution in hexane, 1 mmol) was then added dropwise under vigorous stirring. After a few minutes, the reaction mixture was allowed to gradually warm to room temperature and stirred for 6 h. ^{1}H NMR (THF-d_8, 300 MHz, 298 K): δ = 0.04 (q, 2H, CH_3CH_2-Zn, $^3J_{H,H}$ = 8,1 Hz); 1.13 (t, 3H, CH_3CH_2-Zn, $^3J_{H,H}$ = 8,1 Hz); 7-7.3 (m, 10H, -CH_{Ar}-) ppm.^{31}P NMR (THF-d_8, 121 MHz, 298 K): δ = - 17.53 (s, 1P, $(PhO)_2P$(O)OZn-) ppm. IR (ATR): 2962 (vw), 2942 (vw), 2929 (vw), 2907 (vw), 2892 (vw), 2854 (vw), 1590 (w), 1488 (s), 1455 (vw), 1261 (vw), 1192 (vs), 1161 (m), 1101 (m), 1066 (vs), 1025 (m), 1009 (s), 982 (w), 958 (vs), 945 (vs), 935 (vs), 902 (m), 801 (w), 777 (s), 754 (vs), 730 (w), 687 (vs), 615 (m), 570 (m), 560 (s), 537 (s), 520 (vs), 499 (s) cm^{-1}.

2.4.4 Preparation of OM NCs

The synthetic protocol for preparing ZnO NCs with the surface passivated by phosphate ligands involves two steps conducted in a one-pot manner. In the first step, organozinc precursor $[EtZn(DPP)]_n$ was synthesized *in situ* through the equimolar reaction of $ZnEt_2$ and the selected pro-ligand (DPP-H). $ZnEt_2$ in hexane (0.5 mL of a 2 M solution in hexane, 1 mmol) was added dropwise at to solution of 1.0 mmol of diphenyl phosphate (250 mg) in −78°C in THF (10 mL), and then the reaction mixture was allowed to warm to room temperature and stirred for 3 h. In the second step, a solution of the $[EtZn(DPP)]_n$ precursor in THF was exposed to air to initiate transformations and stirred for 5 days in a room temperature. Subsequently, the liquid residual was evaporated *in vacuo*. Then the OM NCs were redispersed in THF and were precipitated using hexane, centrifuged, and washed again with hexane. The as-prepared OM NCs were dried under vacuum and characterized. IR (ATR): 3327 (vw), 3066 (vw), 2954 (vw), 2930 (vw), 2877 (vw), 1778 (vw), 1728 (vw), 1592 (m), 1488 (m), 1456 (vw), 1440 (vw), 1367 (vw), 1346 (vw), 1226 (m), 1197 (s), 1164 (w), 1101 (vs),

1070 (m), 1027 (m), 1008 (m), 932 (vs), 907 (m), 778 (m), 768 (m), 755 (m), 670 (s), 622 (w), 582 (w), 535 (s), 521 (s), 503 (s), 465 (s), 410 (m) cm^{-1}.

2.4.5 Preparation of SG NCs:

ZnO NCs were synthesized according to the literature procedure[129,158]. In a typical experiment, 2 mmol of $Zn(OAc)_2 \cdot 2H_2O$ (439 mg) and 4 mmol of $LiOH \cdot H_2O$ (168 mg) were dissolved in 50 mL of absolute ethanol. Then diphenylphosphate (4 mmol, 1000.76 mg) was added. The solution was stirred at 70°C for 2 h and then cooled to room temperature. Subsequently the solvent was evaporated under vacuum. Then, the precipitate was washed with ethanol, dried under vacuum and characterized. IR (ATR): 2965 (vw), 1576 (m), 1558 (m), 1542 (w), 1523 (w), 1508 (w), 1489 (m), 1457 (w), 1417 (m), 1398 (m), 1339 (w), 1286 (vw), 1259 (m), 1232 (w), 1206 (m), 1163 (vw), 1098 (m), 1074 (m), 1048 (vw), 1025 (m), 923 (m), 797(w), 778 (m), 756 (m), 720 (w), 688 (m), 670 (m), 659 (w), 618 (w), 523 (w), 442 (vs), 420 (vs) cm^{-1}.

2.4.6 Sample Characterization

STEM characterization

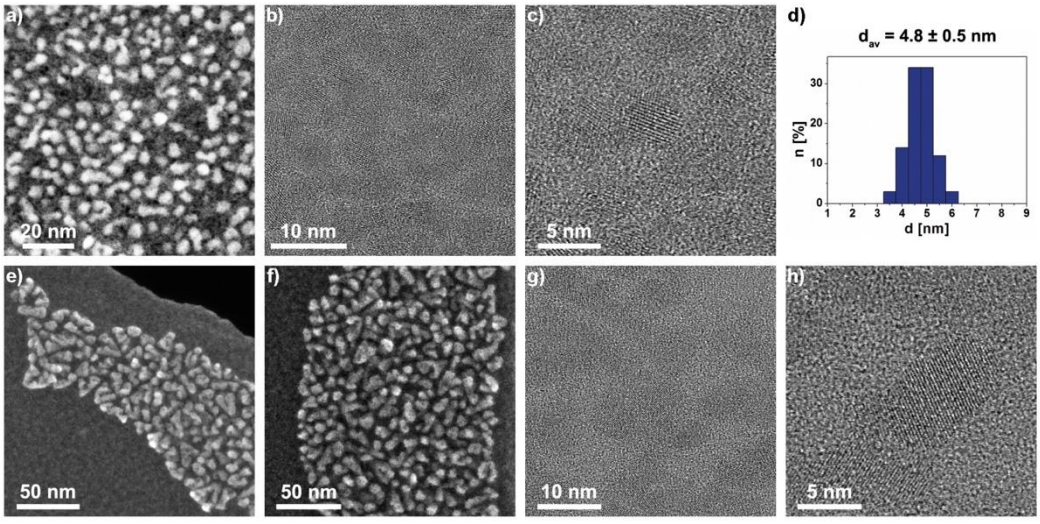

Figure 2-13. Representative STEM micrographs of OM (a-d) and SG (e-h) NCs in SE and HRTEM modes.

Dynamic Light Scattering analysis

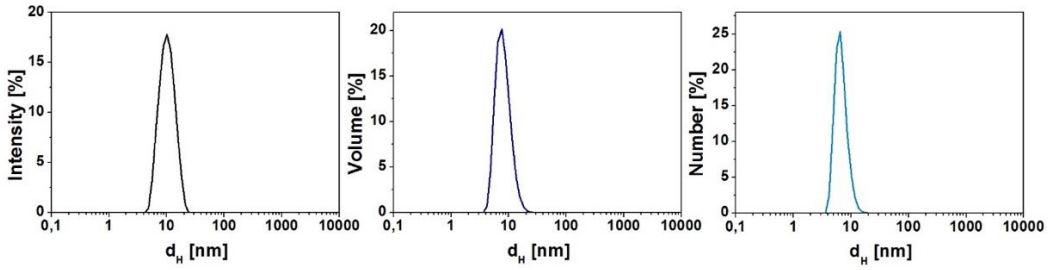

Figure 2-14. Particle size distribution of OM NCs dispersed in THF solutions based on DLS measurements.

Powder X-ray Diffraction analysis

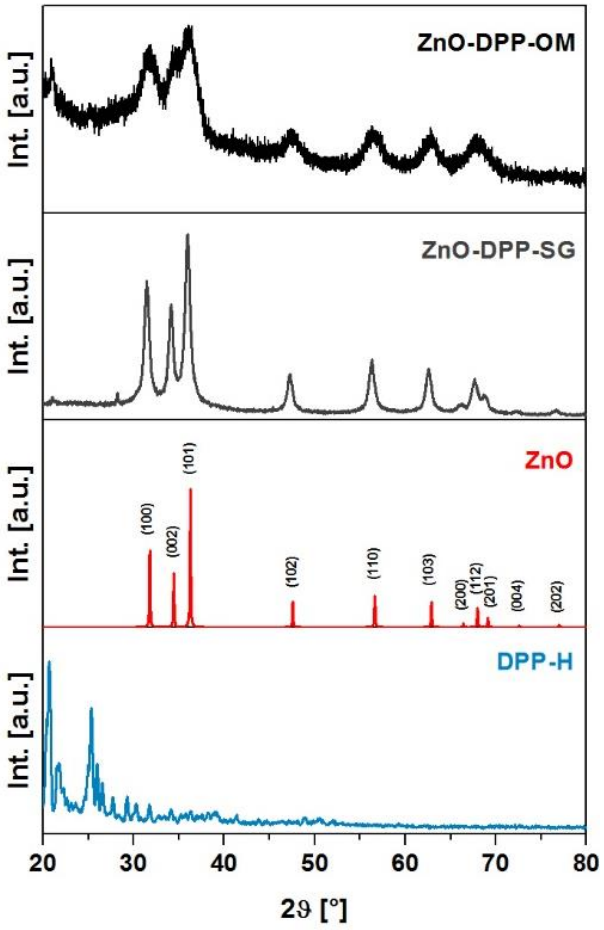

Figure 2-15. Powder X-ray diffraction pattern of OM and SG NCs confirming ZnO wurtzite crystalline structure. The observed changes in both intensity and width of the diffraction peak are related to the OM and SG NCs core sizes. Note that in X-ray physics the crystallite size is inversely proportional to the full width at half maximum of the diffraction peak (i.e. Scherrer's formula), hence smaller NCs generally produce broader peaks of lower intensity.

UV-Vis and PL spectroscopy

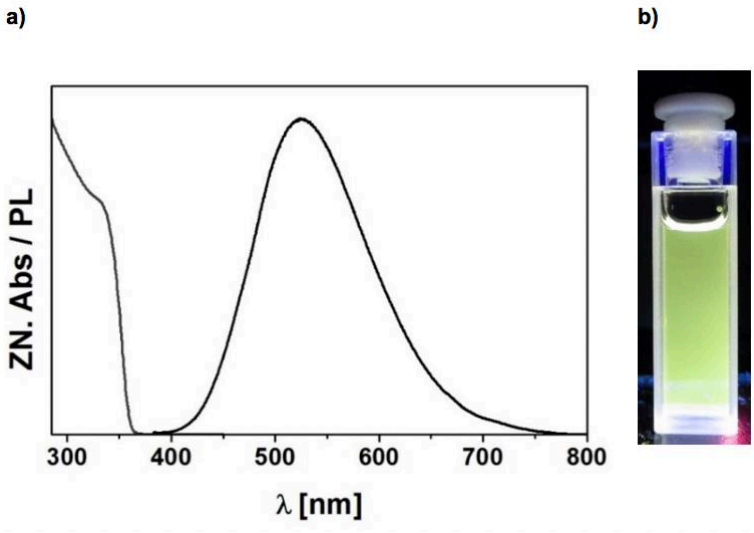

Figure 2-16. a) Absorption and emission spectra of as-prepared OM NCs collected in THF and b) UV light images of OM NCs in THF.

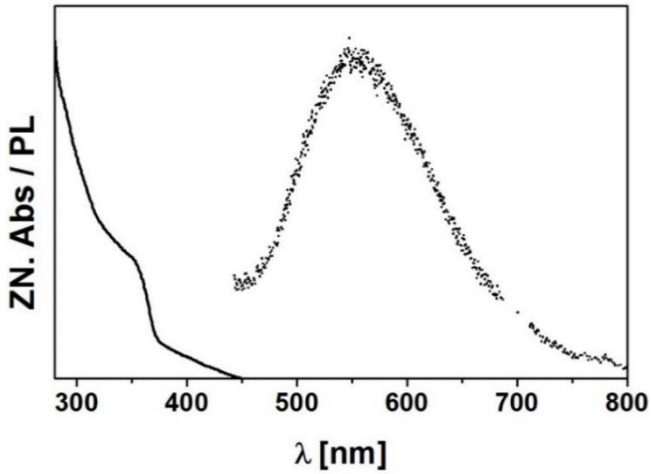

Figure 2-17. Absorption and emission spectra of as-prepared SG NCs collected in THF.

FTIR analysis

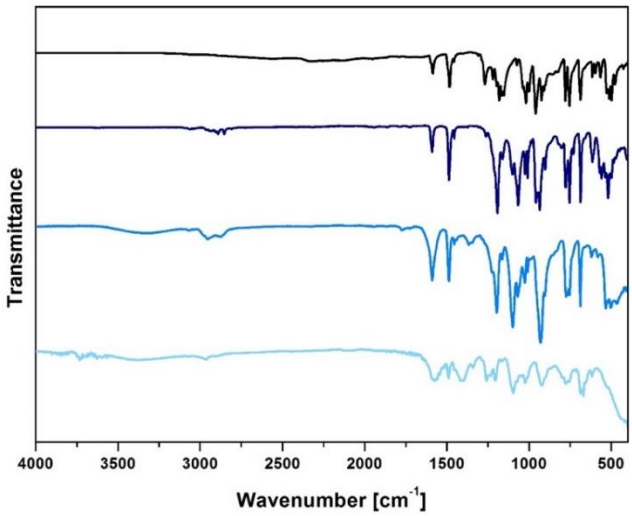

Figure 2-18. FTIR spectra of SG NCs (light blue), OM NCs (blue), organometallic precursor (dark blue) and pure DPP-H pro-ligand (black line).

Thermogravimetric analysis

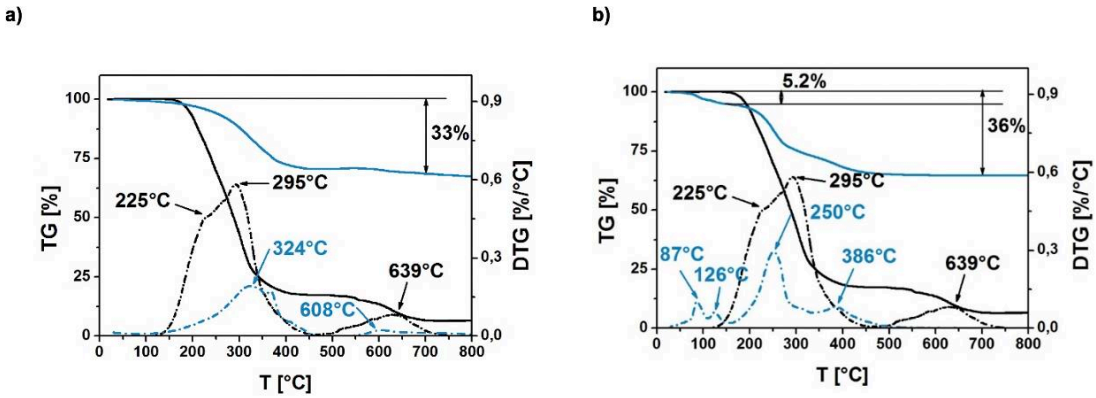

Figure 2-19. The TGA and derivative thermogravimetric analysis (DTG) traces showing the decomposition of a) OM and b) SG NCs in an air atmosphere.

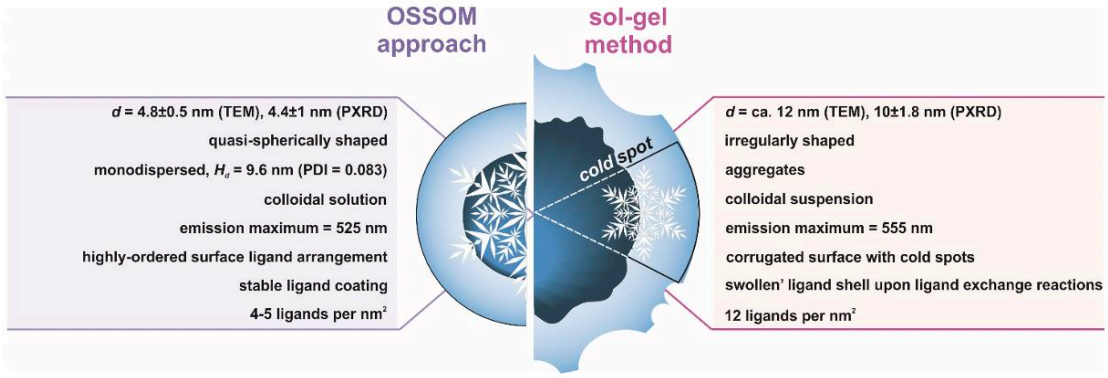

Figure 2-20. Comparison between the inorganic core / organic shell of the quantum-sized ZnO NCs prepared by a classical sol–gel process and by the OSSOM approach.

2.4.7 DNP-enhanced solid-state NMR.

In preparation for the DNP experiments, the NC powder was wetted with a glass-forming solvent matrix of glycerol-d_8/D_2O/H_2O (60/30/10; v/v) containing 10 mM AMUPol biradical polarizing agent[94]. The 'DNP-ready' sample was inserted into a triple-resonance ($^{1}H/^{31}P/^{13}C$) 3.2 ßmm low-temperature MAS NMR probe and pneumatically spun at a desired rate of 13889 Hz, with a sample temperature of ≈105 K, within a static magnetic field of 9.4 T. Hyperpolarization of ^{1}H nuclei through DNP from unpaired electrons is achieved via high-power (≈5 W) microwave irradiation of the sample at a suitable frequency, close to the Larmor frequency of these bis-nitroxide radicals, ≈264 GHz. The sensitivity gain under these conditions can be obtained through the absolute sensitivity ratio (ASR)[159], which compares the sensitivity achieved with a DNP experiment to that of an NMR experiment recorded under conventional conditions (room temperature, pure sample etc.). Here, the measured ASR was approximately 50 for both samples. This large value results from positive contributions from the DNP enhancement (intensity ratio of the analyte signals measured with and without microwave irradiation, $^{1H}\varepsilon_{on/off}$ ~10) and the increased Boltzmann polarization and reduced thermal noise as well as the longer nuclear coherence times at low temperature. This ASR corresponds to an experimental time saving factor of 2500. So an experiment that would take 3.5 hours to acquire here with DNP would require 1 year with conventional NMR.

Further experimental details: The $^{2}H_2O$ and [$^{2}H_8$] glycerol were purchased from Sigma-Aldrich and were both used without further purification. The AMUPol biradical was purchased from Cortecnet. The experiments recorded under conditions suitable for DNP were performed on a Bruker DNP-SSNMR AVANCE III 9.4 T 400 MHz spectrometer equipped with a gyrotron and transmission line capable of providing ~5 W of 264 GHz microwave irradiation at the sample and a low-temperature 3.2 mm MAS probe suitable for spinning rates of up to 15 kHz and sample temperatures of ~105 K.

Experiments were acquired using a MAS rate of 13.889 kHz (unless otherwise stated), ^{1}H $\pi/2$ pulses of 100 kHz, ^{31}P $\pi/2$ pulses of 50 kHz, ^{31}P and ^{13}C CP spin-locking at ~50 kHz was applied for 4 and 5 ms, respectively, with corresponding ramped (50-100 %) ^{1}H CP at ~85 kHz. 100 kHz of SPINAL-64[160] heteronuclear ^{1}H decoupling was used throughout the 20 and 40 ms signal detection periods for ^{31}P and ^{13}C CP experiments, respectively, with direct spectral widths of 50 kHz. These low temperature (~110 K) experiments used optimized experimental repetition delays of 4.8 and 11.6 s, for the OM and SG NCs, respectively. ^{13}C-^{31}P DCP-HETCOR[161] spectra (see Figure 2-7) were recorded using the same parameters as for the ^{31}P and ^{13}C CP experiments but with a ^{13}C–^{31}P CP mixing time of 5 ms for ^{31}P spin-locking at ~59 kHz with corresponding ramped (80-100 %) ^{13}C at 50 kHz. The indirect dimensions used spectral widths of 4.63 kHz and total evolution times of 17.3 ms. 16 transients were co-added for each t_1 increment. 100 kHz of SPINAL-64 heteronuclear ^{1}H decoupling was used throughout the indirect and direct detection periods. S_3[154,155] recoupling was used for the through-space (dipolar) two-dimensional ^{31}P homonuclear correlation experiments. The indirect dimensions used spectral widths of 6.944 kHz and total evolution times of 9.2 ms. 8 transients were co-added for each t_1 increment. 100 kHz of SPINAL-64 heteronuclear ^{1}H decoupling was used throughout the indirect and direct detection periods, whereas 100 kHz of CW Lee-Goldburg decoupling[162] was used during the S_3 recoupling periods.

Chapter 3
An organometallic approach to ligand-coated ZnO nanoplatelets with controlled thickness: Atomic insight into bimodal facet-specific interfaces using DNP NMR

3.1 Introduction

Colloidal semiconductor nanocrystals (NCs) are the foundation of nanoscience and nanotechnology. They have attracted considerable attention in recent decades for their unique optoelectronic/optical properties, making them interesting for a wide range of applications[1–6]. The NCs' properties depend strongly on their composition, size, and morphology, among other inherent characteristics[163,164]. Today, it is possible to synthesize a wide array of colloidal semiconductor NCs with precise control of their size and shape[165–167].

In recent years, colloidal nanoplatelets (NPLs) and nanosheets with a uniform thickness have emerged as an exciting new class of quantum-sized nanomaterials with substantially improved optical properties compared to zero-dimensional (0D) quantum dots (QDs)[168–170]. While 0D QDs induce strong quantum confinement in all dimensions, anisotropic 2D NPLs induce quantum confinement in only one direction, which is the key factor for their unique optoelectronic properties. Hence, these types of nanocrystals are considered prime candidates for new generation optoelectronic devices like light-emitting diodes, lasers, field-effect transistors, and photodetectors[168,169,171–174].

Moreover, semiconductor nanocrystals' 2D morphology may also positively affect their photocatalytic properties[15,175,176]. Therefore, the development of new synthetic approaches to control the thickness of NPLs with atomic precision has become an emerging field of research, and various strategies to induce anisotropic growth of nanocrystals have been developed based on a templating environment[177], kinetic control over lateral growth[178–180], and facet-specific surface–ligand binding[181,182].

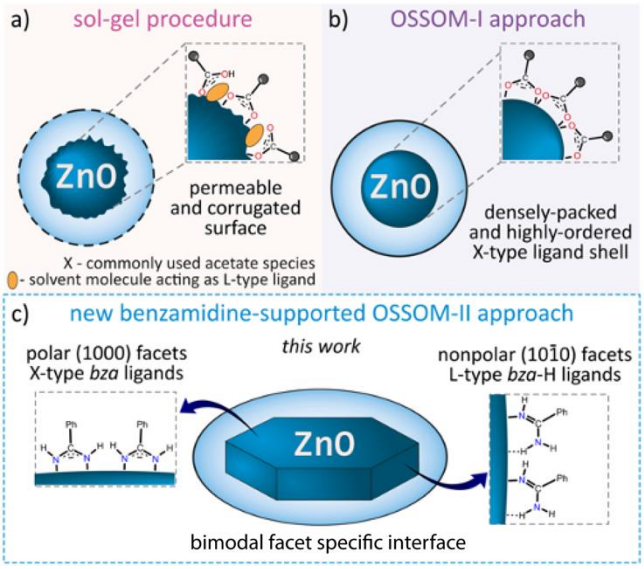

Figure 3-1. Composition of the organic-inorganic interface of ZnO NCs obtained using various synthetic approaches.

The classic example of anisotropic colloidal 2D semiconductor nanostructures is cadmium chalcogenide NPLs (CdX, X = Se, S, Te), leaving other types of semiconductors in the shadows[169,179,180,183–185]. However, unlike their Cd-based counterparts, the research field of Zn-chalcogenide-based NPLs is essentially strongly undeveloped, although it is an interesting target for heavy-metal-free quantum-confined nanostructures. For example, very recent reports have shown that the synthesis of hexagonal NPLs of ZnS or ZnSe is challenging to achieve by direct wet synthetic approaches[186,187]. It is also striking that there is no synthetic method to ensure a high level of control of colloidal zinc oxide (ZnO)-based NPLs with uniform atomic thickness. To date, a number of ZnO NPLs have been prepared using a solvothermal approach involving controlled growth on a suitable substrate[175,188–193] or by ultrasound-supported[194] and electrochemical synthesis[195]. The resulting NPLs generally have a thickness of approximately 10-20 nm and lateral dimensions approaching the

submicrometer or micrometer scale and are usually highly aggregated. Notably, their surface coordination chemistry or the potential role of supporting organic ligands in the anisotropic growth have not been investigated in detail. The properties of nanocrystals are considerably influenced by the composition of both their surface and interface, which is why a deeper understanding of their structure at the atomic level is crucial for the rational development of new nanomaterials with desired functionality.

ZnO is a versatile material of long-standing interest due to its low toxicity and unique catalytic and electro-optical characteristics[12–15]. Wet inorganic procedures are commonly used to synthesize ZnO nanostructures, but they provide low control over the nucleation and growth of NCs in the quantum-size regime, which results in low reproducibility and lack of uniformity of the inorganic core–organic shell interface[31] (Figure 3-1a). Only recently OSSOM (one-pot self-supporting organometallic, hereafter referred OSSOM-I) procedure was developed by Lewinski and co-workers for the fabrication of a vast array of unprecedented high-quality colloidal isotropic 0D QDs[22–31]. The OSSOM approach uses controlled transformations of an organozinc [EtZn(X)]-type precursor by exposure to atmospheric air (where H_2O and O_2 act simultaneously as a source of oxygen) at room temperature. The X-type ligand tailors the organometallic precursor's reactivity, supports the nucleation and growth process and effectively stabilizes the surface of the resulting QDs. As-synthesized QDs possess a highly organized interface structure, which gives them unique properties such as high stability[24,27,31], biosafety[28], and ultra-long-lived luminescence[29] (Figure 3-1b). In particular, the proper selection of organic ligands allows the size-control of QDs by modulating the strength and mode of ligand-surface interaction[25,26]. Furthermore, the ligand shell's appropriate functionalization affects solubility and self-organization processes since it directly impacts post-synthetic functionalization[22–24,27,30].

In the course of investigations on the development of efficient organometallic strategies for the preparation of high-quality ZnO nanocrystalline materials, a vast array of organozinc precursors incorporating monoanionic O,O'- and N,O'-bidentate ligands like carboxylates[22–24,27,28], phosphinates[25], phosphates[31], amides,[196] urea,[197] and bidentate functional subunits, essentially isostructural in terms of coordination bifunctional aminoalkoxides[26], were tested. Subsequently, benzamidinate (bza) ligands

were studied that possess an N,N'- mode compared to the carboxylate and amidate ligands used so far. It was pondered whether an organic ligand with much less acidic character (benzamidine is a strong N-base, pKa=26.7[198]) than the previously reported O,O'-ligands might exhibit both X- and L-type character acting as an effective growth modulator for ZnO nanostructures fabricated in an organometallic process.

In this work, a first synthesis of highly-stable and thickness-controlled ZnO NPLs with a bimodal facet-specific interface involving the polar (0001) and non-polar ($10\bar{1}0$) surfaces stabilized by monoanionic bza and neutral bza-H ligands, respectively (Figure 3-1c) has been described. The latter is evidenced by a combination of advanced characterization techniques such as high-resolution transmission electron microscopy (HRTEM) and dynamic nuclear polarization (DNP)-enhanced solid-state ^{15}N NMR, which reveals that the nanoplatelets are well-faceted, and that the benzamidine ligands exhibit different modes of binding to the polar and non-polar ZnO facets, acting as an X-type or L-type ligand, respectively. This likely differentiates the surface energy on individual facets, yielding the formation of hexagonal nanoplatelets. The developed synthetic procedure is scalable and does not use harsh conditions (like temperature, high pressure, and reagents). The amount of water used in the synthesis directly controls the thickness and lateral dimensions of the NPLs.

3.2 Results and Discussion

3.2.1 Synthetic approaches to *bza* ligand-coated ZnO nanoparticles and nanoplatelets.

OSSOM-I approach to bza ligand-coated ZnO NCs.

Initially, benzamidine (*bza*-H) was probed as the proligand in the recently developed OSSOM-I approach, which involves a two-step procedure conducted in a one-pot manner[22–31]. Briefly, an ethylzinc derivative of benzamidine, [EtZn(*bza*)], as an organometallic precursor, was generated *in situ* by an equimolar reaction of commercially available $ZnEt_2$ and *bza*-H in a THF solution and then exposed to atmospheric air for a few days at ambient temperature.

However, all attempts resulted in the formation of amorphic white product(s) insoluble in common organic solvents instead of the expected ZnO NCs coated by a benzamidinate ligand shell (for details, see 'Optimization of the transformation of ethylzinc benzamidate precursor', materials and methods section). This result was unexpected at first in light of the above-mentioned reports on the OSSOM procedure. Nevertheless, there are possible explanations that can be envisioned. The exposition to air entails the engagement of both H_2O and O_2 molecules as an oxygen source, and the organozinc precursor is subjected to two different processing events, i.e., the hydrolysis and oxygenation reactions. While controlled hydrolysis is a straightforward way to form zinc-oxo clusters entrapped by the parent organometallic precursor's organic counterparts[199]. the oxygenation reaction can lead either to the zinc oxo peroxide or alkoxide species[200–205]. It seems reasonable to assume that these divergent reaction pathways make the nucleation process much more difficult due to the formation of insoluble zinc oxo(alkoxide) aggregates. Hence, as a next step, water was used exclusively as an oxygen source in a transformation process of the [EtZn(*bza*)] precursor towards ZnO nanostructures, and this variant of the self-supporting organometallic approach is termed OSSOM-II.

Hydrolytic OSSOM-II approach to ZnO NPLs with a bimodal facet-specific interface. The new synthetic protocol involves dropwise addition of a specific amount of water to an *in-situ* generated THF solution of [EtZn(*bza*)] at room temperature, which first induces slight turbidity of the reaction mixture. The addition of 1 or 2 equivalents of H_2O per [EtZn(*bza*)] leads to the formation of a zinc-oxo [$Zn_4(\mu_4$-O)(*bza*)$_6$] (**1**) cluster as the major isolable product (for details, see Optimization of the transformation of ethylzinc benzamidate precursor, materials and methods section). It is also interesting to note that the formation of tetranuclear zinc-oxo clusters was previously observed for other related organozinc systems[49,199,206–208].

Remarkably, it was found that the use of higher amounts of water paves the way for wurtzite-type ZnO NPLs. Using 3 to 10 equivalents of water, the reaction mixture was stirred for 2-3 days at room temperature, which finally resulted in a cloudy and luminescent suspension composed of the unprecedented wurtzite-type ZnO NPLs. The NPLs were separated from the post-reaction mixture as a white and air-stable crystalline material using anti-solvent, viz. hexane, washed twice with a THF/hexane (3:1 *v*/*v*) mixture, and dried under vacuum. Systematic investigations on optimizing the reaction conditions revealed that the organometallic precursor's concentration (in the range of 0.2 to 0.8 M) does not significantly affect the reaction outcome, and room temperature (ca. 24°C) is optimal for the transformation process (for details, see 'Optimization of the transformation of ethylzinc benzamidate precursor', materials and methods section). Notably, the amount of added water has appeared to be a pivotal factor affecting both the thickness and the basal plane dimension of NPLs. More specifically, the thickness increased gradually from 3.2 nm to about 7.5 nm with the increasing molar ratio of H_2O (for detailed characterization *vide infra*). The individual nanomaterials are hereafter termed as NPL-Y, where Y = 1, 2 … 8 and corresponds to 3, 4 … 10 equivalents of added H_2O, respectively (Figure 3-2 a). All isolated NPLs, from NPL-1 to NPL-8 featuring a bimodal facet-specific interface stabilized by monoanionic *bza* and neutral *bza*-H ligands (*vide infra*), can be easily re-dispersed in THF, DMSO, or MeOH to form luminescent colloidal solutions over a wide range of concentrations. The NPLs are stable for months without aggregation or particle growth (Figure 3-26 and Figure 3-27, materials and methods section).

3.2.2 Characterization of ZnO NPLs

The inherent and distinctive physicochemical properties of semiconductor nanocrystals are strongly dependent on a variety of factors such as size and particle morphology, chemical composition, and the character of the resulting nanocrystal-ligand interface, including the binding mode and packing density of the coating ligand and other intimate interactions on the NC surface. To gain in-depth insight into the structure-function relationship, the physicochemical properties of the resulting series of NPLs were characterized using high-field solid-state NMR combined with magic angle spinning and dynamic nuclear polarization (MAS-DNP), along with various classical analytical techniques like scanning transmission electron microscopy (STEM), powder X-ray diffraction (PXRD), thermogravimetric analysis (TGA), Fourier-transform infrared spectroscopy (FTIR), UV-Vis absorption and photoluminescence (PL) spectroscopy.

Shape and size distribution of faceted hexagonal ZnO NPLs.

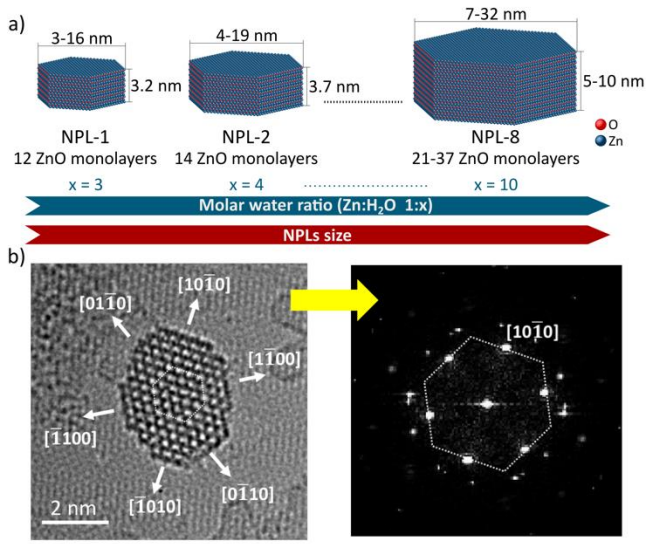

Figure 3-2. a) Schematic representation of NPL1-8 and b) representative HRTEM image of NPL-1 and the corresponding fast Fourier transform (FFT).

The analysis of NPL-1 to NPL-8 by PXRD indicates the presence of pure wurtzite (ZnO) phase and highlights a strong anisotropy corresponding to platelet-shaped nanocrystals (Figure 3-3). In addition, advanced powder pattern inspection using pattern decomposition into individual peaks and peak shape analysis, which allowed estimation of the size distribution of NPLs in particular directions were performed (for

more details, see PXRD analysis, materials and methods section). Using a hexagonal platelet model, the thickness and width of the platelets along crystallographic directions *a* and *c* based on reflections (100) and (002), respectively (Figure 3-10), were determined. The results show that the NPLs exhibit a narrow distribution in thickness, ranging from 3.2 nm for NPL-1 to about 7.5 nm for NPL-8, depending on the water-to-zinc molar ratio used in the synthesis (Figure 3-2 a and Table 3-2). The distribution along lateral dimensions is much broader, with mean values ranging from 9.1 nm for NPL-1 to 19.7 nm for NPL-8 (Figure 3-11 b, and Table 3-2). It is essential to highlight that for the smallest nanoplatelets NPL-1 and NPL-2, monodisperse thickness values of 3.2 and 3.7 nm were found, respectively, corresponding to 12 and 14 ZnO monolayers or 6 and 7 ZnO unit cells (Figure 3-2 a).

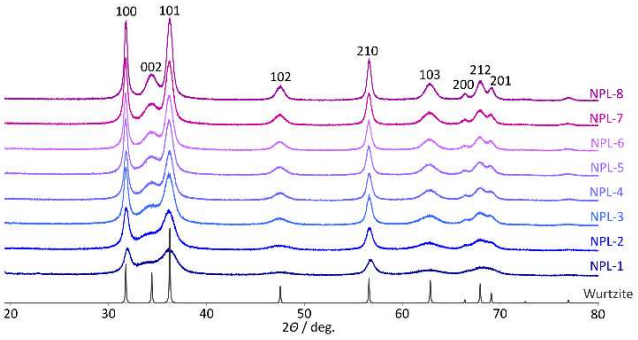

Figure 3-3. Powder XRD patterns of NPL1-8 and for wurtzite ZnO phase.

The hexagonal shape of NPLs was further confirmed by HRTEM (Figure 3-2b). On the HRTEM images, the NPLs are well-faceted and mostly observed along the [0001] direction. The analysis also demonstrates the formation of ZnO platelets with varying lateral dimensions from 3-16 nm to 7-32 nm for NPL-1 and NPL-8, respectively (Figure 3-11, and Figure 3-12). The tendency of the NPLs to lay flat on the basal plane greatly reduces the possibility to measure the platelet thicknesses.

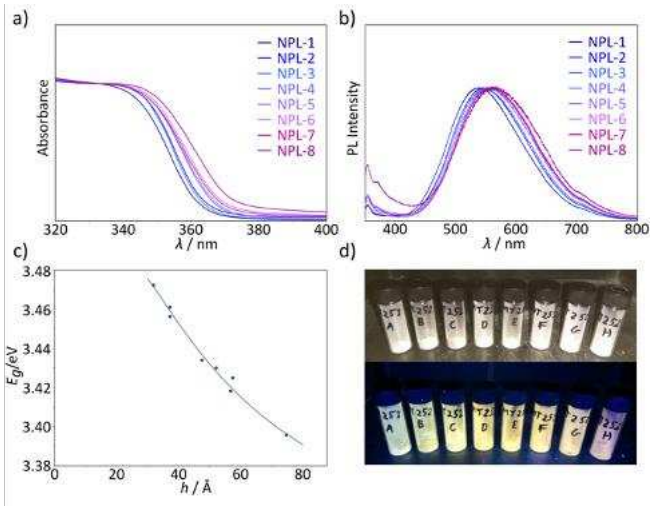

Figure 3-4. a,b) Absorption and PL spectra of NPL-1-8 in MeOH (λ_{ex} = 320 nm); c) Estimated band gap energy dependence on the thickness; d) NPL-1-8 samples under visible and UV (365 nm) light.

Optical properties and shelf-life stability of ZnO NPLs.

From UV/vis spectroscopy, the absorption and emission maxima for NPL-1 to NPL-8 were found in the ranges 334 – 342 nm and 538 – 565 nm (for an excitation wavelength λ_{ex} = 320 nm, FWHM ca. 160-170 nm), respectively (Figure 3-4 a, b and Table 3-5). Interestingly, the estimated band-gap energy using Tauc plots is in the range 3.47-3.40, which correlates with the average thickness of the NPLs (Figure 3-3 c, Figure 3-22, Table 3-5). Remarkably, the PL emission spectra recorded after approximately four years of storage in air remained virtually unchanged with respect to those collected for freshly-prepared NPLs (Figure 3-27). The morphology and the homogeneity of NPL solutions also remained virtually unaffected during storage and no precipitation was observed.

Initial assessment of the inorganic-organic interface of ZnO NPLs using TGA and FTIR analysis.

All TGA profiles of the ZnO NPLs (Figure 3-14) exhibit complex decomposition pathways, involving four main steps with a maximum decomposition rate in the ranges 50-110°C (~ 2%), 110-220°C (~ 2-3%), 220-370°C (~ 3-8%) and 370-470°C (~ 3-5%), respectively. The whole thermolysis is completed at about 600°C with a total weight loss of ~ 11-18%, decreasing with increasing size of the NPLs. The mass decrease observed up to 220°C (3-5%) can probably be attributed to continuous physical

desorption of both solvent and possible residual free benzamidine impurities. At higher temperatures, one can observe two additional steps in the 220-370°C and 370-470°C range, likely corresponding to the decomposition of *bza*-H and *bza*, bonded to the non-polar and polar NPLs' surfaces, respectively. Indeed, the later decomposition should occur at a higher temperature because *bza* anions are expected to interact more strongly with the NPL surface. The relative content of both forms of ligand was estimated based on the overall weight loss in both temperature ranges, and it nicely correlates with the results of the PXRD analysis in terms of polar/non-polar surface ratio (for details, see TGA analysis, materials and methods section). Interestingly, combining these results with the hexagonal NPL models obtained from PXRD analysis, an area per ligand, which is similar on both types of NPLs' surfaces of about 0.25 nm^2 was estimated.

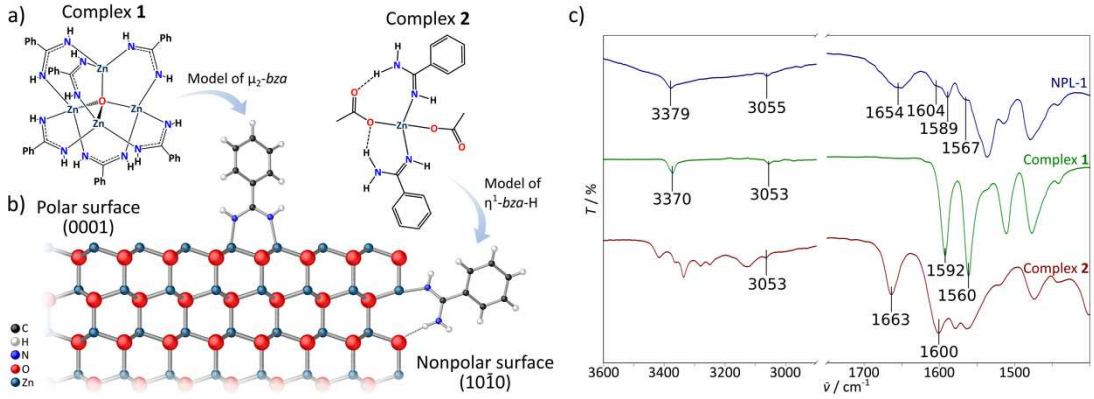

Figure 3-5. a) Schematic representation of the model zinc complexes (top) and b) the proposed coordination modes of neutral bza-H and monoanionic bza ligands on the surface of NPLs (bottom); c) the FTIR spectra of NPL-1 and complexes 1 and 2.

The FTIR spectra of the ZnO NPLs were compared to the ones obtained on model zinc complexes $[OZn_4(bza)_6]$ (**1**)[208] and $[Zn(AcO)_2(bza\text{-}H)_2]$ (**2**) (Figure 3-5). The two selected model complexes comprise monoanionic and neutral benzamidine ligands of various coordination modes (see ref. [208]and materials and methods section for details on the synthesis and characterization of compounds **1** and **2)**. The FTIR spectra of NPL-1-8 are very similar, displaying characteristic bands for ZnO vibrations in the range of 390-400 cm^{-1} and complex patterns associated with the organic ligand shell (Figure 3-5c and Figure 3-21). Multiple broad and diffusive bands at 3100-3500 cm^{-1} and two signals at 3379 and 3055 cm^{-1} may be attributed to the ν(NH) and ν(CH) stretching vibrations of the organic ligands. Furthermore, a detailed analysis of the 1700-1500

cm^{-1} region indicates the presence of two ligand forms, i.e., neutral *bza*-H and monoanionic *bza*. For instance, the NPL spectra comprise signals at 1589 cm^{-1} and 1654 cm^{-1}, similar to the ν(C=N) stretching bands observed in the spectra of **1** and **2**, respectively. Note that the latter resonance is significantly red-shifted for the NPLs, which might be the result of differences in the energy of Zn-ligand interactions (more details, see FTIR spectroscopy in materials and methods section).

3.2.3 Elucidation of bimodal facet-specific ligand binding using DNP-enhanced ssNMR.

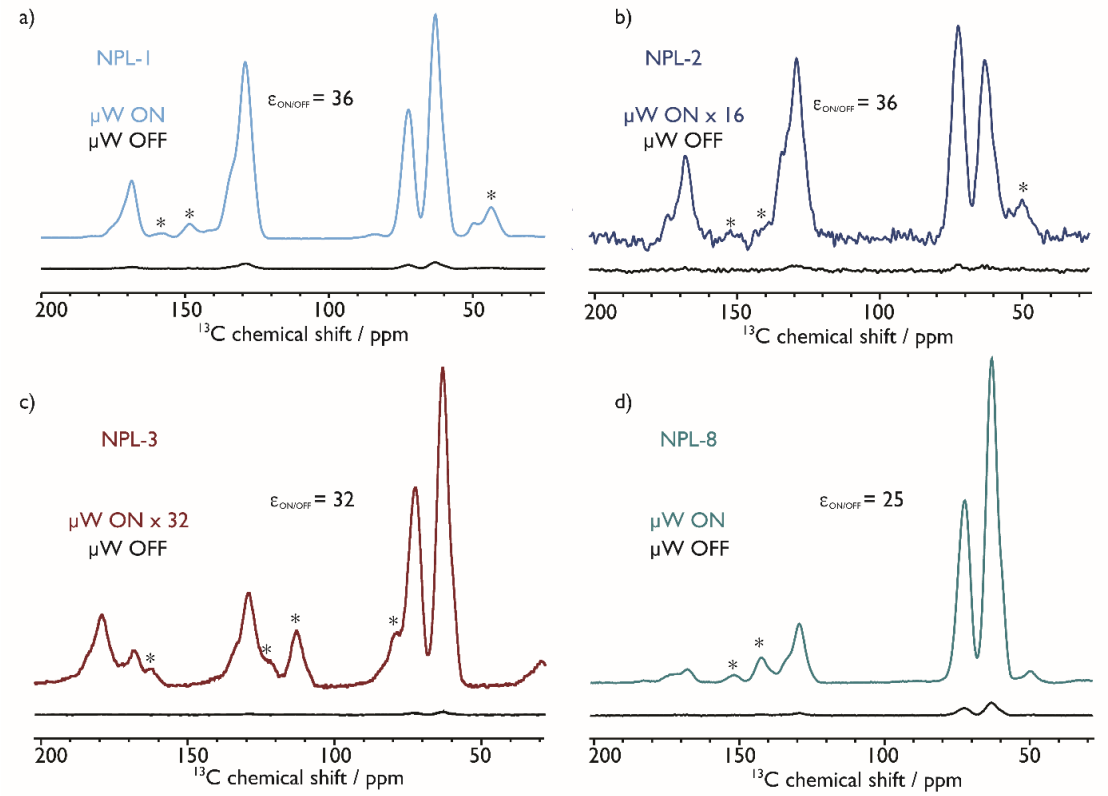

Figure 3-6. {^{1}H-}^{13}C CPMAS NMR spectra of (a) NPL-1, (b) NPL-2, (c) NPL-3, and (d) NPL-8, recorded at ~105 K, 9.4 T, and at a MAS frequency of 8.6, 8, 5 and 8 kHz for ZnO-BA-NPL-1,2,3,8 respectively, with and without microwave (μW) irradiation suitable for DNP. "*" denotes signals from spinning sidebands. The multiplicative factor next to μW ON is to normalize the number of scans recorded for μW ON with respect to μW OFF.

The revealed high propensity of the reported modified organometallic synthesis protocol for forming anisotropic 2D ZnO NPLs is likely associated with individual facets of different surface energy and the suspected facet-specific bimodal stabilization by organic ligands, which calls for an in-depth study of the nanoplatelet surface

chemistry. Solid-state NMR is a well-known spectroscopic technique that provides rich site-specific information concerning atomic environments and details about their short-range order. Thus, this technique is ideal for understanding the nature of interactions at surface sites.[51] However, solid-state NMR often suffers from low sensitivity, especially at interfaces, where the relative number of atoms is less than the bulk. Dynamic nuclear polarization (DNP), a technique that uses the large polarization of electron spins to enhance the signal of surrounding nuclei,[75,209,210] can be used to selectively enhance the surface sites of nano-objects.[108–110,211] Thus, to gain insights into the specific-binding of *bza* and *bza*-H ligands on the surface of the NPLs, the respective nanomaterials were analyzed using DNP-enhanced solid-state NMR spectroscopy. DNP enhancement factors, $^{1H,CP}\varepsilon_{on/off}$, were measured on NMR signals from the NPLs and compared to those from the solvent. The $^{1H,CP}\varepsilon_{on/off}$ factor, defined as the ratio of the signal intensities returned from ^{1}H cross-polarization (CP) experiments recorded with and without microwave irradiation suitable for DNP, was found to be 36, 31, 30, and 26 for $\{^{1}H\text{-}\}^{13}C$ CPMAS NMR spectra of NPL-1,2,3, and 8, respectively (Figure 3-6 and Figure 3-7). The same $^{1H,CP}\varepsilon_{on/off}$ factors were found for ^{13}C signals of glycerol, which is used as a glass-forming agent in the DNP matrix in DNP-ready samples (Figure 3-6). This uniform enhancement throughout the sample highlights a homogeneous mixing of the polarizing agent around the NPLs. These enhancements allowed the acquisition of $\{^{1}H\text{-}\}^{15}N$ CPMAS spectra at ^{15}N natural isotopic abundance (0.4%) for benzamidine ligands on the surface of NPLs.

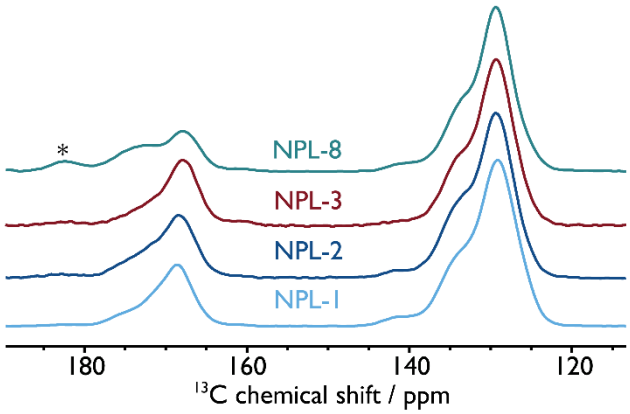

Figure 3-7. DNP-enhanced $\{^{1}H\text{-}\}^{13}C$ CPMAS NMR spectra of (a) NPL-1, (b) NPL-2, (c) NPL-3, and (d) NPL-8, recorded at ~105 K, 9.4 T, and at a MAS frequency of 12 kHz for NPL-8, and 13.333 kHz for NPL-1,2,3. "*" denotes signals from spinning sidebands.

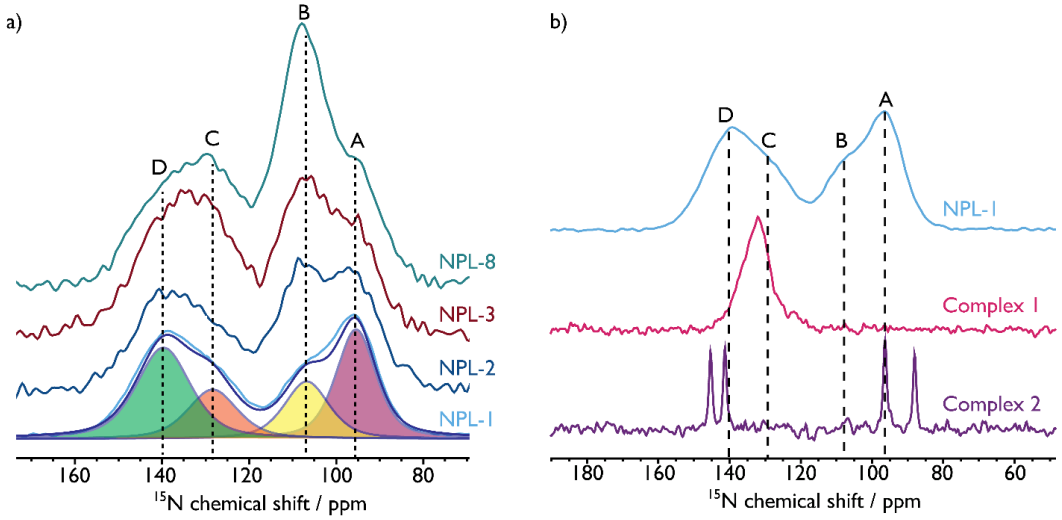

Figure 3-8. a) DNP-enhanced $\{^1H\text{-}\}^{15}N$ CPMAS NMR spectra of NPL-1,2,3,8 showing deconvolution of the peaks, recorded using a MAS frequency of 8 kHz and 12 kHz for NPL-1,8 and NPL-2,3 respectively at ~100 K and 9.4 T; b) Comparison of $\{^1H\text{-}\}^{15}N$ CPMAS NMR spectra of model complexes recorded at room temperature, and a DNP-enhanced $\{^1H\text{-}\}^{15}N$ CPMAS NMR spectrum of NPL-1 recorded at ~100 K.

Table 3-1. Isotropic chemical shift (σ/ppm) and relative intensities for peaks A, B, C and D obtained from deconvolution of DNP-enhanced $\{^1H\text{-}\}^{15}N$ CPMAS NMR spectra of NPL-1, NPL-2, NPL-3, and NPL-8.

	Peak D		Peak C		Peak B		Peak A	
	σ/ppm	Rel. amount	σ/ppm	Rel. amount	σ/ppm	Rel. amount	σ/ppm	Rel. amount
NPL-1	**140.9**	**1.13**	**129.4**	**0.56**	**107.6**	**0.58**	**96.4**	**1**
NPL-2	**140.6**	**1.16**	**128.7**	**0.5**	**108.2**	**1.22**	**96.5**	**1**
NPL-3	**142.0**	**0.94**	**131.5**	**1.51**	**109.5**	**1.35**	**97.3**	**1**
NPL-8	**141.2**	**0.89**	**129.5**	**1.41**	**108.3**	**2.72**	**95.8**	**1**

The investigation of nitrogen environments is crucial for an in-depth understanding of the facet-specific bimodal stabilization of the nanocrystals' surface by the monoanionic and neutral forms of the organic ligand. It seems reasonable to assume that the non-polar surface facets of the NPLs are terminated by the neutral *bza*-H ligands (L-type) and thus should have two distinct ^{15}N NMR chemical shifts corresponding to the imino and amino nitrogen atoms. Whereas, to establish local charge balance, Zn-rich polar (0001) facets are likely to be capped by the anionic form (X-type) of the *bza* ligands, possibly through binding of two surface Zn (+0.5)'s to each benzamidinate anion (-1). Thus, on these polar facets, due to the resonance hybrid structure of the anionic *bza* ligand, the two nitrogen atoms should be spectroscopically equivalent and produce only one ^{15}N NMR chemical shift.

The DNP-enhanced {^{1}H-}^{15}N CPMAS NMR spectra for NPL-1,2,3 and 8, shown in Figure 3-8 a, can be deconvoluted into at least four broad peaks, and the relative intensity of each contribution can be observed to vary across the various NPLs (see Table 3-1). On comparing these ^{15}N NMR spectra, it can be noted that the intensity ratio of peaks A ($\delta\{^{15}N\}$ = 96.4 ppm) and D ($\delta\{^{15}N\}$ = 140.9 ppm) is similar for all NPLs. This constant ratio indicates that these signals belong to nitrogen atoms within one molecule, and thus A and D likely result from the two amidine nitrogen atoms of the neutral form of the ligand. The higher-shifted peak D then corresponds to the imino nitrogen atom and peak A to the amino nitrogen atom of the amidine functional group of the *bza*-H ligand. It is also worth highlighting that the ^{15}N NMR chemical shifts of the amine and imine at $\delta\{^{15}N\}$ = 96.4 and 140.9 ppm, respectively, are expected to appear at $\delta\{^{15}N\}$ = 92 and 181 ppm for a free *bza*-H proligand at 100 K (see Figure 3-9).

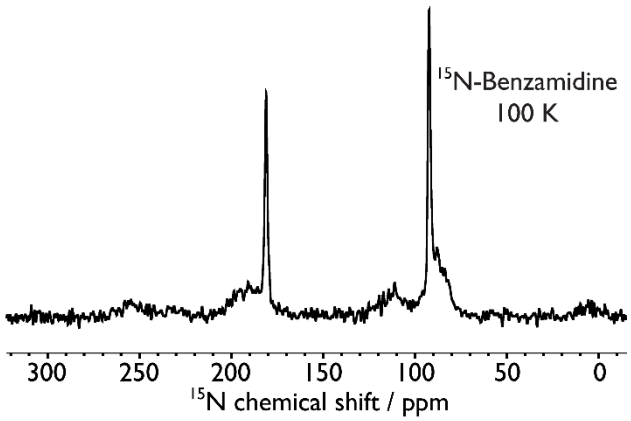

Figure 3-9. {^{1}H-}^{15}N CPMAS NMR spectrum of ^{15}N labeled benzamidine ligand recorded at 100 K, 9.4 T, and a MAS frequency of 12 kHz.

Interestingly, imino nitrogen chemical shifts have previously been observed to be shielded upon protonation. While protonation of amines leads to a moderate downfield ^{15}N NMR chemical shift, the same for sp^2 hybridized imino nitrogens leads to a significant upfield protonation shielding. This observation was explained by a change in the contribution of the sp^2 hybridized lone pair of imino groups upon protonation.[212] Thus, the significant (~40 ppm) lowering of the imino nitrogen's chemical shift can be considered analogous to the effect of protonation and indicates that benzamidine

proligand binds to surface Zn(0.5+) sites through its more basic imino nitrogen. This effect confirms that the ligand is surface-bound. Here neutral benzamidine acts as an L-type ligand forming a dative bond by donating a lone pair to zinc on the non-polar facet. A few articles exploring ligand capping on ZnO nanoparticles have observed a secondary shell of free ligand near the surface.[53,56] Here, no ^{15}N NMR chemical shifts corresponding to free benzamidine ligand were observed, and hence this shows that a secondary shell of ligand around the nanoplatelets was absent in this case.

Assuming that the ligand density on any particular facet does not change drastically across the platelets, the amount of ligand associated with a particular facet should increase if the relative proportion of that facet grows. This assumption is justified because an excess of ligand was used for the synthesis of all the nanoplatelets. The PXRD data show an increasing ratio of polar (0001) to non-polar $(10\bar{1}0)$ facets going from NPL-1 to NPL-8, and consistently the TGA data report a relative increase of the anionic to neutral ligand ratio (*vide supra*). Interestingly, the ^{15}N NMR spectra show that the intensity of peaks B ($\delta\{^{15}N\}$ = 107.6 ppm) and C ($\delta\{^{15}N\}$ = 129.4 ppm) increases relative to the A-D pair (Figure 3-8 a). This trend implies that B and C signals are from nitrogen atoms of ligands capping polar (0001) Zn-terminated facets. Furthermore, the relative growth of peaks B and C across NPLs is independent of other peaks and each other, which indicates the presence of two different forms of anionic *bza* ligands.

The $\{^{1}H\text{-}\}^{15}N$ CPMAS NMR spectra of the model complexes **1** and **2** were recorded using conventional solid-state NMR at room temperature (Figure 3-8 b). The selected complexes **1** and **2** may serve as model systems for the μ_2 coordination mode of the monoanionic *bza* and the N-H···O hydrogen bond supported κ^1 coordination of the neutral *bza*-H, respectively (Figure 3-5 a). Comparison of the respective spectra of model complexes and NPL-1 (in Figure 3-8 b) confirms that peaks A and D correspond to the amino and imino nitrogen atoms of the surface-bound neutral form of the ligand, whereas peak C is associated with the μ_2 *bza* anions. However, peak B from the spectra of the NPLs, which has the largest intensity increase with the relative growth of the polar basal plane, cannot be assigned definitively using the selected molecular

complexes. Further studies to investigate the nature of its origin are discussed in the following chapter.

3.3 Conclusion

The development of new synthetic methods to control the thickness of NPLs with atomic precision has become an emerging field in nanoscience. In this work, a novel organometallic approach to produce ZnO NPLs with controlled thickness and long-term colloidal stability in polar aprotic (THF, DMSO) and protic (MeOH) solvents was presented. While a contemporary sol-gel method produces platelets typically between 10 and 20 nm thick with poor reproducibility, the nanoplatelets produced by the modified OSSOM-II approach are much smaller, with excellent reproducibility. The NPLs are ultra-thin, ranging in thickness from 3.2 nm for the smallest to 7.5 nm for the largest, making them attractive for a range of applications.[168,169,171–174] These NPLs were characterized through a combination of various classical analytical techniques, as well as HRTEM and DNP-enhanced solid-state NMR. This study reveals that the NPLs are hexagonal and well-faceted, with an original bimodal binding of facet-specific ligands on polar (0001) and non-polar ($10\bar{1}0$) facets of wurtzite ZnO. On the polar facets, the ligand's anionic form was found to bind in a μ_2 coordination mode, whereas on the non-polar facets the neutral ligand binds to the surface Zn through its imine nitrogen lone pair. Further investigation of the interactions and arrangement of ligands at these interfaces will be discussed in Chapter 4. Such atomic-scale structural information of the organic-inorganic interfaces of ZnO NPLs will facilitate the synthesis of stable and size-controlled colloidal suspensions by design.

3.4 Materials and methods

3.4.1 Synthetic procedures

General remarks: All manipulations connected with the synthesis and hydrolysis of the organometallic compounds were conducted under a dry, oxygen-free nitrogen atmosphere using standard Schlenk techniques. Reagents were purchased from

commercial vendors and used as received: benzamidine (Sigma Aldrich), $ZnEt_2$ (ABCR), $Zn(OAc)_2 \cdot 2H_2O$ (Sigma Aldrich). THF was purified and dried using MBraun Solvent Purification System (SPS).

OSSOM approach to bza ligand-coated ZnO NCs: A hexane solution of $ZnEt_2$ (2 M, 1 ml, 2 mmol) was added to a solution of *bza*-H (0.240 g, 2 mmol) in THF (5 mL) at -78°C. The reaction mixture was allowed to warm to room temperature and stirred overnight. Then the reaction mixture was exposed to air. After stirring for six days, the product was isolated as a white powder by filtration and dried under vacuum.

General OSSOM-II procedure for ZnO NPLs: A hexane solution of $ZnEt_2$ (2 M, 1 ml, 2 mmol) was added to a solution of *bza*-H (0.240 g, 2 mmol) in THF (5 mL) at -78°C. The reaction mixture was allowed to warm to room temperature and stirred overnight. The specified amount of water (2 M solution in THF, molar ratio Zn: H_2O 1:x, where x = 3-10 for NPL1-8, accordingly) was then added dropwise to the reaction mixture at room temperature, which caused slight turbidity of the solution. After stirring for three days, 3 ml of hexane was added to precipitate the product. The suspension was separated by centrifugation, and as-synthesized ZnO NPLs were purified by dissolution in THF and precipitating with hexane twice (THF: hexane 3:1 *v*/*v*). After drying under vacuum, 160-180 mg of the pure product was obtained in the form of a white powder exhibiting a yellow luminescence under UV (365 nm) irradiation.

3.4.2 Characterization

PXRD analysis

Powder XRD data were collected with an Empyrean diffractometer (PANalytical) by employing Ni-filtered CuKa radiation from a copper sealed tube charged with 40 kV voltage and 40 mA current in Bragg-Brentano geometry with a beam divergence of 1° in the scattering plane. Diffraction patterns were decomposed into individual peaks using the Pawley method[213]. In the method, the peak positions are constrained by the lattice parameters, and the peak shapes and intensities are freely refinable. Additionally, the shapes of the 100, 210, and 200 peaks were linked together since those peaks describe the same in-plane direction. The formula for the peak shapes reported by

Wejrzanowski et al.[214], which contains the average particle size and the breadth of the size distribution as refinable parameters was used. The values listed in Table 3-2 for the platelet height h are those obtained for the 002 diffraction peak, and for the platelet width d are those obtained for the 100, 210, and 200 group of peaks.

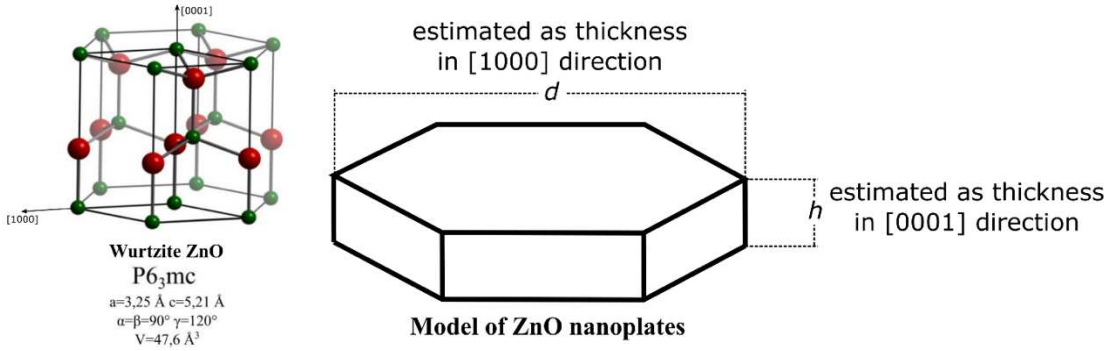

Figure 3-10. Wurtzite ZnO lattice and hexagonal plate model.

Table 3-2 Dimensions of ZnO NPLs estimated from PXRD diffractograms.

Sample	O:Zn molar ratio	NPLs thickness [Å]		Layers of wurtzite ZnO*	NPLs width [Å]	
		h	d*h*		*d*	d*d*
NPL-1	**3**	**32**	**± 0**	**6**	**91**	**± 67**
NPL-2	**4**	**37**	**± 0**	**7**	**116**	**± 80**
NPL-3	**5**	**37**	**± 16**	**7**	**140**	**± 95**
NPL-4	**6**	**48**	**± 21**	**9**	**147**	**± 95**
NPL-5	**7**	**52**	**± 21**	**10**	**157**	**± 98**
NPL-6	**8**	**57**	**± 21**	**10**	**164**	**± 104**
NPL-7	**9**	**57**	**± 21**	**11**	**163**	**± 101**
NPL-8	**10**	**75**	**± 25**	**14**	**197**	**± 126**

*** h divided by 5.21 Å i.e. parameter c of the wurtzite ZnO unit cell**

HRTEM.

HRTEM images in Section 3.2.2:

Samples for atomic resolution images were prepared by drop-casting a suspension of the material onto a C-flat carbon membrane-coated copper grid with 2 μm holes. For background free observation of nanometer size crystals, a graphene monolayer was pre-transferred on the grid before the drop-casting. Aberration corrected TEM imaging was done using a Thermofisher Titan Ultimate performing at 80 kV in monochromated mode with CS <1 μm, Cc = 1.2 mm and an electron energy spread = 0.25 eV giving a focal spread = 1.2 nm.

HRTEM images given below:

Samples for HRTEM were prepared by drop-casting a suspension of the material onto 300-mesh, holey carbon-coated copper grids (Quantifoil). The characterization of size, shape, and morphology was carried out on a high-resolution Scanning Transmission Electron Microscope (FEI TECNAI G2 F20 S-TWIN) with the following optical parameters: CS = 1.2 mm, Cc = 1.2 mm, electron energy spread = 0.7 eV, beam divergence semi-angle = 1 mrad. Particle size distributions were calculated by counting the diameters of more than 100 particles.

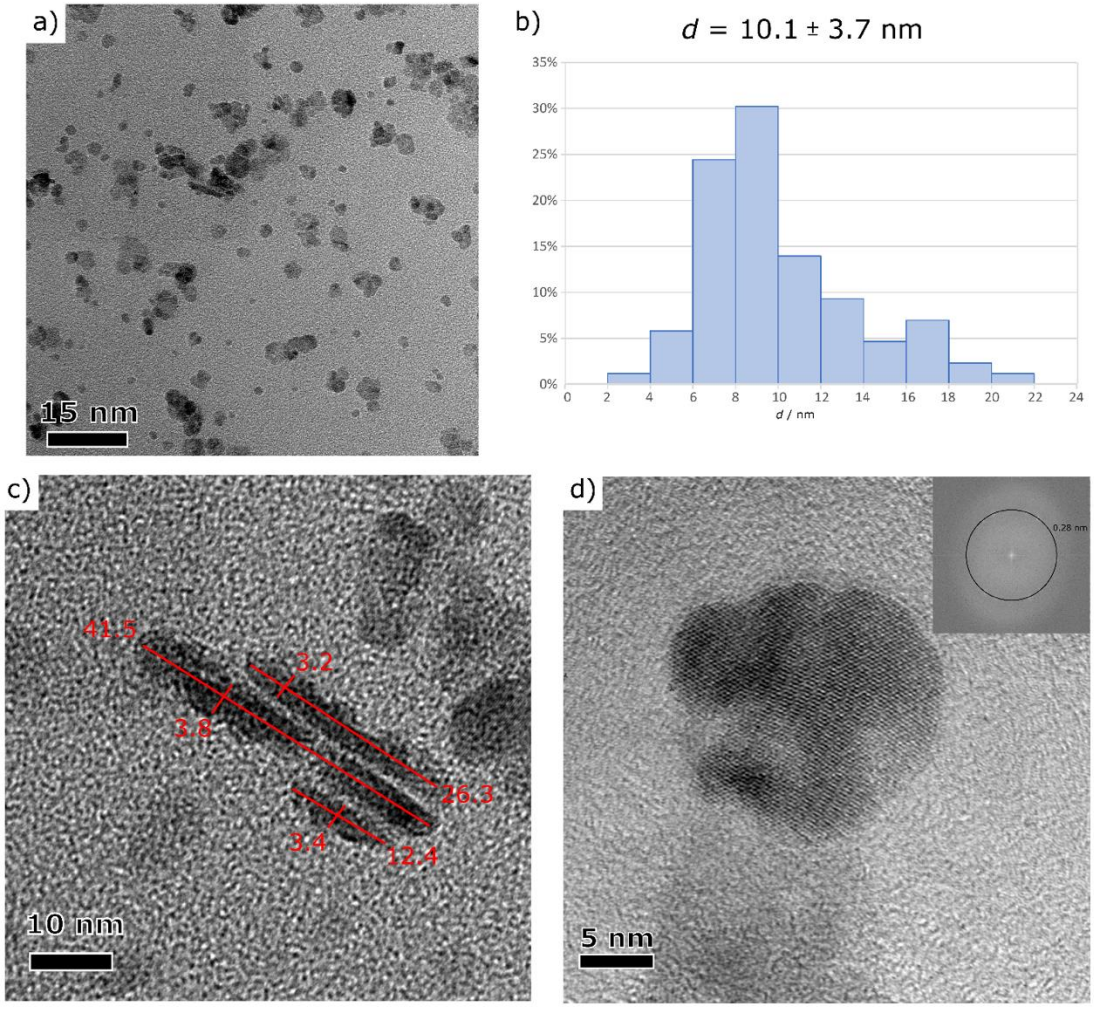

Figure 3-11. HRTEM images and size distribution analysis of NPL-1.

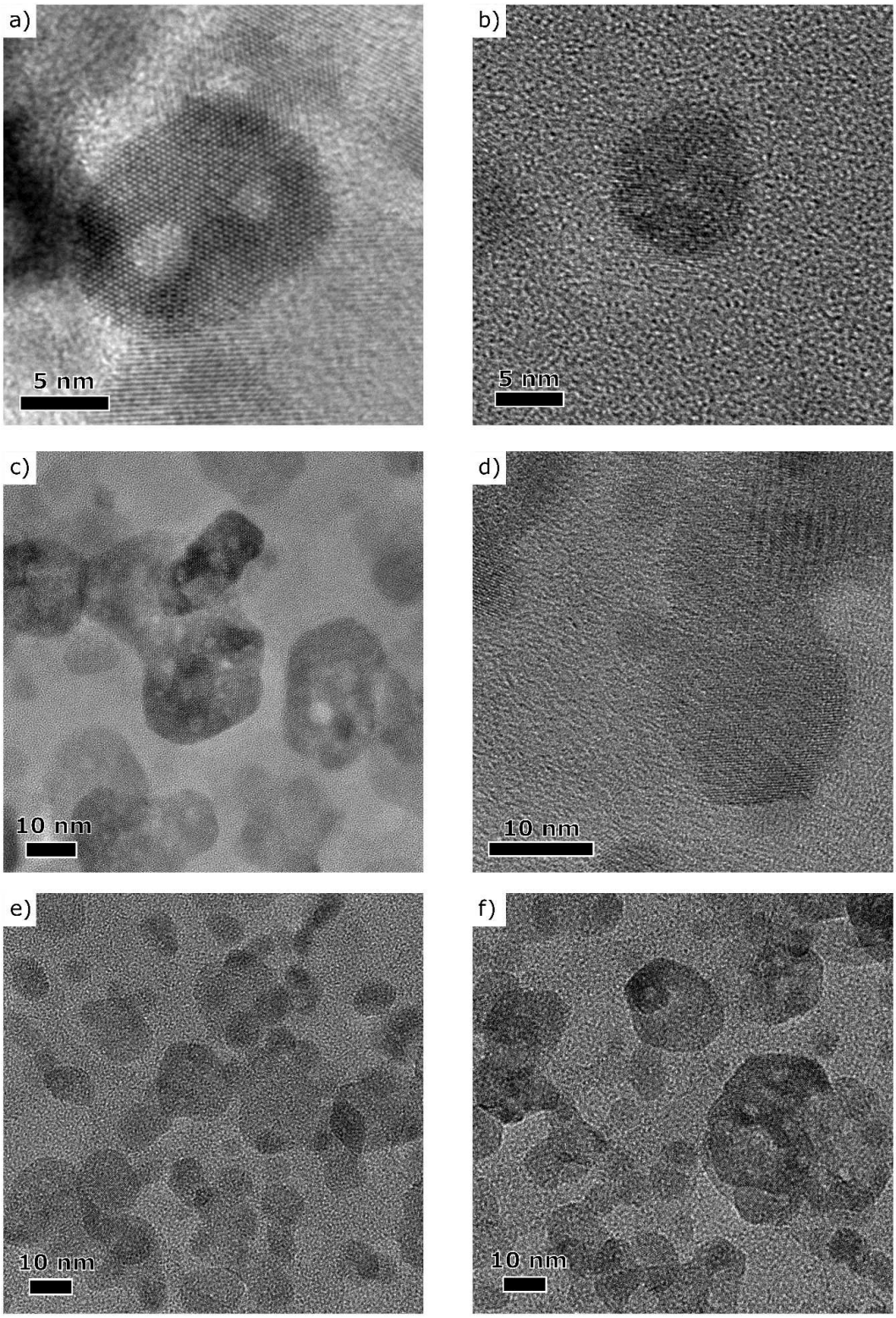

Figure 3-12. HRTEM images of NPL-2 (a), NPL-4 (b), NPL-5 (c), NPL-6 (d), NPL-7 (e), and NPL-8 (f).

TGA analysis.

TGA was carried out with a TA Instruments Q600 instrument under an airflow (flow rate of 100 ml·min^{-1}) to 600 °C at a heating rate of 5 °C·min^{-1}. Open alumina crucibles of 5 mm in diagonal were used.

TGA analysis of NPLs-1-6 performed in an air flow shows complex thermal decomposition pathways, involving four main steps with a maximum decomposition rate in the ranges 50-110°C (~ 2%), 110-220°C (~ 2-3%), 220-325°C (~ 3-6%) and 325-450°C (~ 4-8%), respectively (Figure 3-13). The mass decrease observed up to 220°C (4-6 %) has been assigned to physical desorption of both solvent and possible residual free benzamidine impurities from the surface along with their thermal degradation. At higher temperatures, one can observe two additional steps in the 220-325°C and 325-450°C range, likely corresponding to the decomposition of two forms of ligand, i.e., *bza*-H and *bza*. For a more insightful analysis of two-component ligand sphere of NPLs the reduced values of individual steps of mass decrease have been calculated assuming mass at 220°C as weight of pure ligand coated ZnO NPLs (Table 3-3). Organic ligands content decreases monotonically from c.a. 14% for NPL-1 to c.a. 7% for NPL-6 (Figure 3-15). A mass ratio of *bza* to *bza*-H ligands has been estimated based on two individual steps of decomposition at 325-450°C and 220-325°C, respectively, assuming stronger interaction of the anionic form of ligand with the polar ZnO surface, and thus the dissociation/decomposition at higher temperatures. The obtained values change non-monotonically for individual NPLs first increasing from c.a. 1.3 and reaching the maximum of c.a. 1.9 for NPL-4, then decreasing and stabilizing at c.a. 1.7 (Figure 3-16). Interestingly, *bza*/*bza*-H ligand ratio well correlate with basal to lateral (A_b/A_s) surface area ratio calculated for model of hexagonal NPLs estimated from PXRD analysis (note that, the divergence for the bigger NPLs is likely due to the high distribution of the dimensions). Finally, based on the combined results from TGA and PXRD analysis for NPL-1 as the most precise and well-defined model an estimated area per ligand on the surface of NPLs has been calculated, which are similar for both types of ligands (Table 3-4).

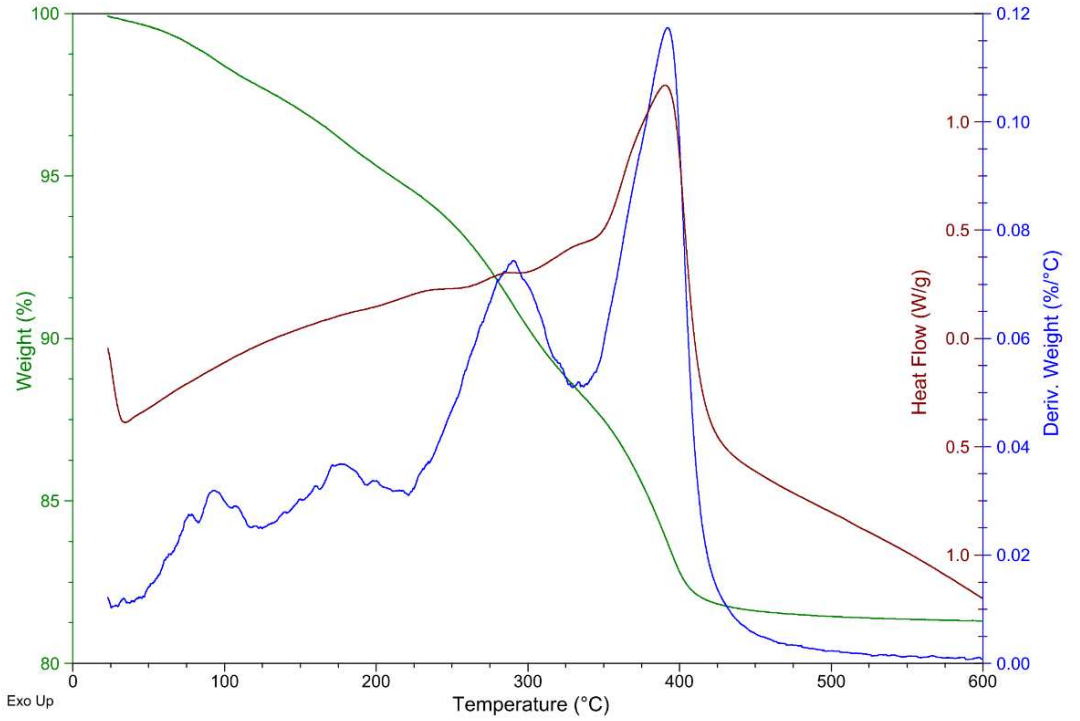

Figure 3-13. Thermogravimetric and differential scanning calorimetric curves of NPL-1.

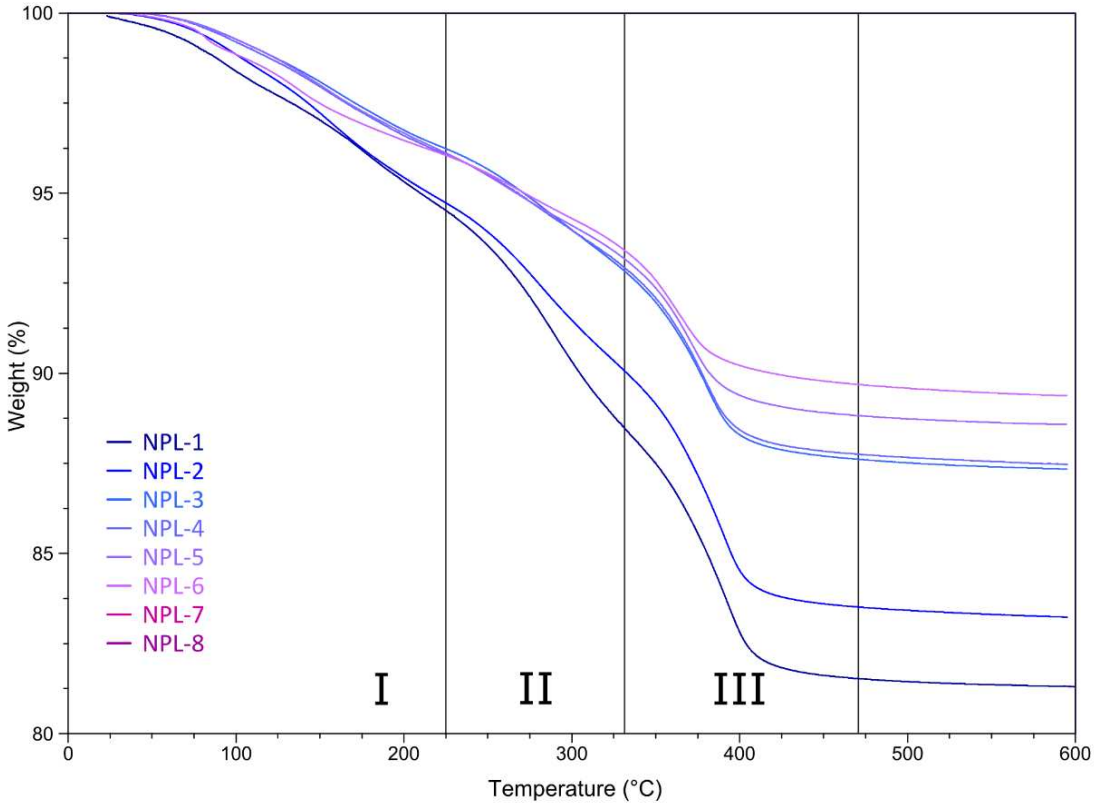

Figure 3-14. Thermogravimetric curves of NPL-1 to NPL-6.

Table 3-3. Quantitative analysis of individual steps of the thermal decomposition of samples NPL-1-6 and the comparison of *bza*/*bza*-H ligand ratio with the lateral to basal area ratio for individual NPLs.

Sample	Mass decrease (%)			$\%_m$ ZnO	Reduced mass decrease (%)*		Reduced % ZnO*	*bza*/*bza*-H ratio III'/I'	Facets area ratio A_b/A_s**
	I (<220°C)	II (220-325°C)	III (>325°C)		II' (220-325°C)	III' (>325°C)			
NPL-1	5.32	5.87	7.45	81.36	6.20	7.87	85.93	1.27	1.23
NPL-2	5.13	4.52	7.04	83.31	4.76	7.42	87.81	1.56	1.35
NPL-3	3.67	3.24	5.68	87.41	3.36	5.90	90.74	1.75	1.63
NPL-4	3.82	3.01	5.62	87.55	3.13	5.84	91.03	1.87	1.34
NPL-5	3.77	2.83	4.76	88.64	2.94	4.95	92.11	1.68	1.31
NPL-6	3.87	2.50	4.17	89.46	2.60	4.34	93.06	1.67	1.25

*** calculated omitting mass decrease associated with impurities bellow 220°C**

**** basal (A_b) to lateral (A_s) surface area ratio was calculated based on model of hexagonal NPLs estimated from PXRD analysis**

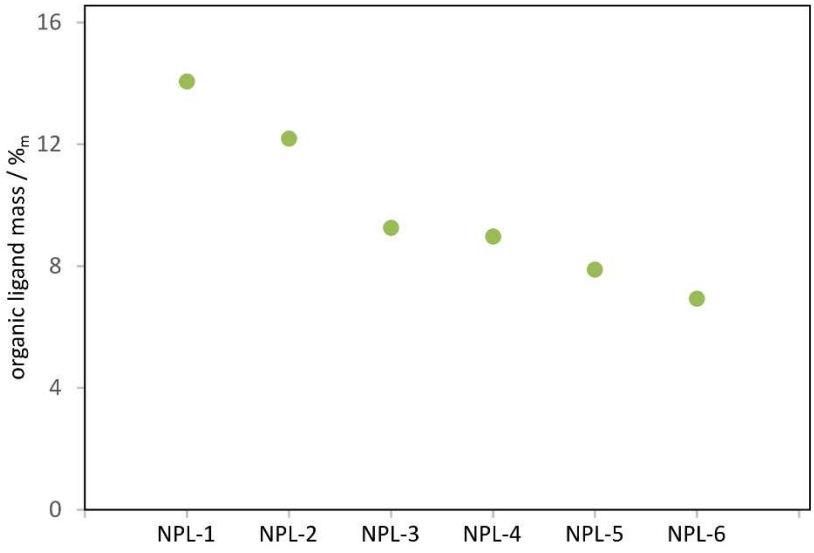

Figure 3-15. Organic ligand content in NPL-1 to NPL-6.

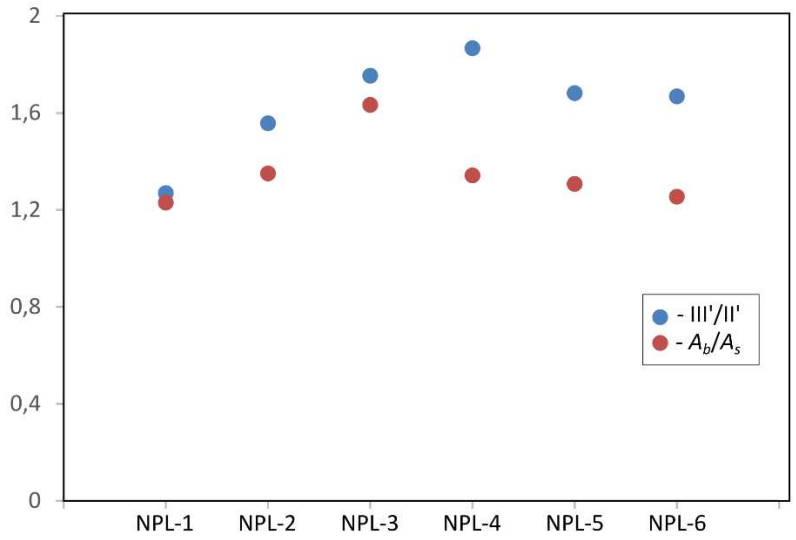

Figure 3-16. *bza*/*bza*-H ligand ratio (as III'/II' mass decrease ratio) and lateral to basal area ratio (A_b/A_s calculated based on PXRD) for NPL-1 to NPL-6.

Table 3-4. Calculation of the area per ligand for NPL-1.

h [Å]	d [Å]	A_b [Å^2]	A_s [Å^2]	V [Å^3]	d_{ZnO} [g·cm^{-1}]	m_{core} [·10^{-19} g]
32	91	10650	8650	170 000	5.606*	9.5
$\%_m$ ZnO	**m_{ligand} [·10^{-19} g]**	***bza*/*bza*-H ratio**	**n_{bza}**	**$n_{bza\text{-}H}$**	***A*$_b$ per *bza* [nm^2]**	***A*$_s$ per *bza*-H [nm^2]**
85.93	1.6	1.27	440	340	0.24	0.25

*** Haynes WM, ed. (2011). CRC Handbook of Chemistry and Physics (92nd ed.). CRC Press. ISBN 978-1439855119.**

FTIR spectroscopy.

FTIR spectra were measured with a Bruker Tensor II spectrometer equipped with an ATR (attenuated total reflection) accessory.

***bza*-H:** FTIR spectrum of *bza*-H shows bands characteristic for amidinate functional group and aromatic backbone. In the range of 3100-3500 cm^{-1} are multiple broad signals form ν(N-H) stretching of -NH_2 and =NH groups involved in the formation of hydrogen bonds (see crystal structure of *bza*-H; CCDC 128021). At 3070 cm^{-1} is band associated with the ν(C-H) stretching of sp^2 CH moieties and signals at 785 and 695 cm^{-1} are characteristic for the monosubstituted aromatic ring. Bands at 1640 and 1597 cm^{-1} come from ν(C=N) stretching and wagging NH_2 vibrations of the amidine group, respectively. Intensive band at 1560 cm^{-1} is probably related with ν(C=C) stretching in the aromatic ring as similar signal is observed in all herein characterized compounds.

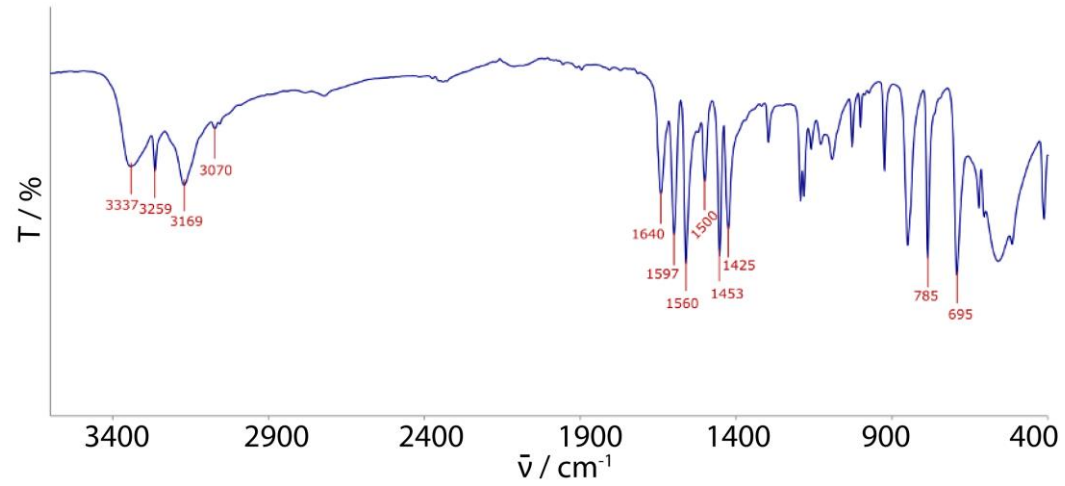

Figure 3-17. FTIR spectrum of *bza*-H.

Complex 1: In the complex **1** *bza* ligands are in a monoanionic form. Thus, on the FTIR spectrum there are no signals characteristic for NH_2 moieties, and only one simple signal form *v*(N-H) stretching is observed at 3370 cm^{-1}. Like in Bza-H spectrum, there are bands at 3053, 1560, 786 and 695 cm^{-1} characteristic for the monosubstituted aromatic ring. Two signals at 1592 and 1510 cm^{-1} are associated with v_{sym}(C=N) and v_{asym}(C=N) stretching of the anionic amidine group.

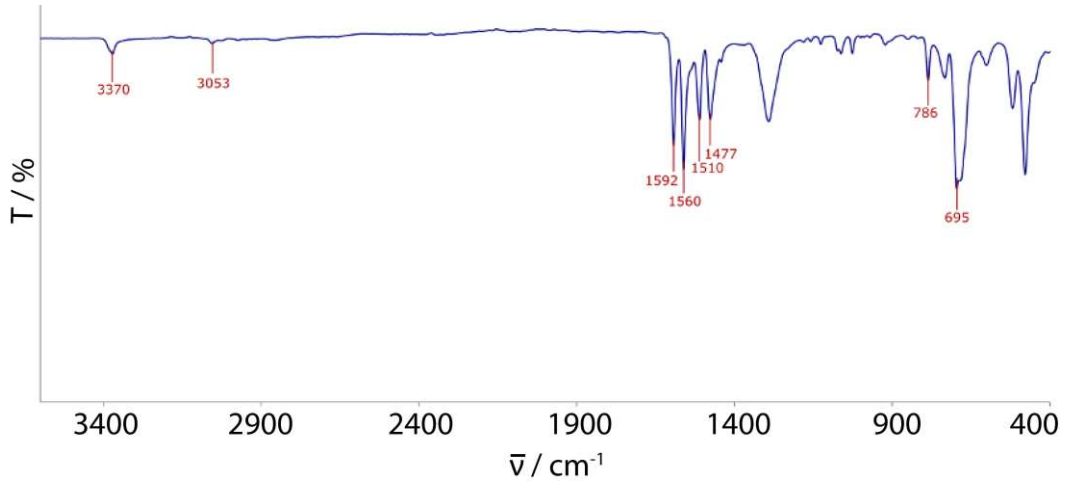

Figure 3-18. FTIR spectrum of complex **1**.

Complex 2: In complex 2 the -NH2 and =NH groups are involved in the formation of numerous intra- and intermolecular hydrogen bonds (see the crystal structure), which results in multiple bands form ν(N-H) stretching in the range of 3100-3500 cm^{-1}. Bands at 3063, 1562, 789 and 693 cm^{-1} are associated with the presence of the monosubstituted aromatic ring. In comparison with Bza-H, signal from ν(C=N) stretching at 1663 cm^{-1}

is red shifted due to the coordination to Zn center, while the signal form wagging NH2 vibrations is in the similar range at 1600 cm^{-1}. The additional band at 1579 cm-1 comes from ν(C=O) stretching of acetate group present in **2**.

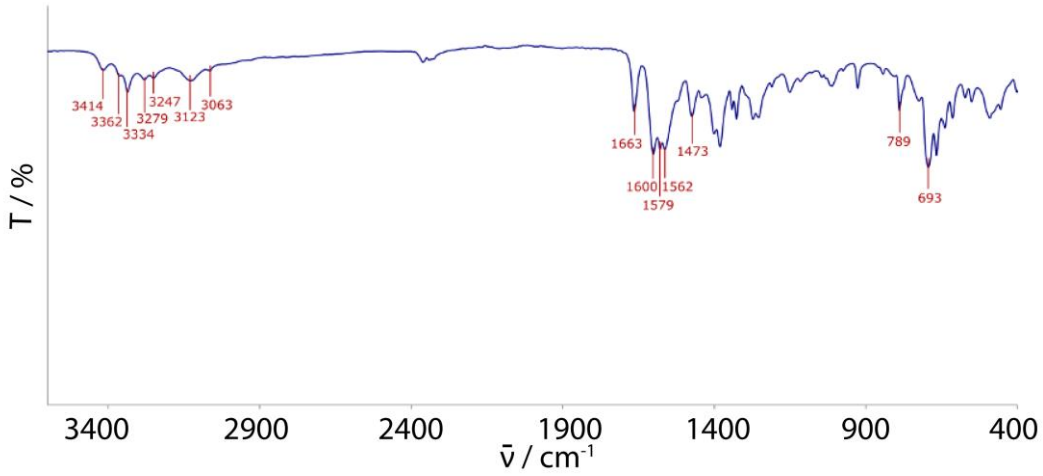

Figure 3-19. FTIR spectrum of complex **2**.

ZnO-Bza NPls: On the FTIR spectrum of purified ZnO-Bza NPLs besides the intensive band from ZnO around 400 cm^{-1} there are signals, which may be assigned to the organic ligand on the surface of NPLs. Comparative analysis revieled that these signals remind bands presence on the spectra of both model complexes **1** and **2**, which may imply the presence of bimodal coordination of Bza ligands on the surface. Especially, the signals at 1654 and 1604 cm^{-1} on the spectrum of ZnO-Bza NPLs match well with ν(C=N) stretching and wagging NH_2 vibrations of amidine group in 2 and bands at 1589 and 1513 cm^{-1} are similar to ν_{sym}(C=N) and ν_{asym}(C=N) stretching of the anionic amidine group in 1. Additional broad intensive band at 1536 cm-1 may be associated with the presence of other groups on the surface like OH or carbonate moieties. Furthermore, the signals at 3055, 1567, 787 and 695 cm^{-1} belongs to the monosubstituted aromatic ring of Bza ligands and band at 3379 cm^{-1} and clear broadening in the range of 3100-3500 cm^{-1} may be assigned the N-H groups with various bonding.

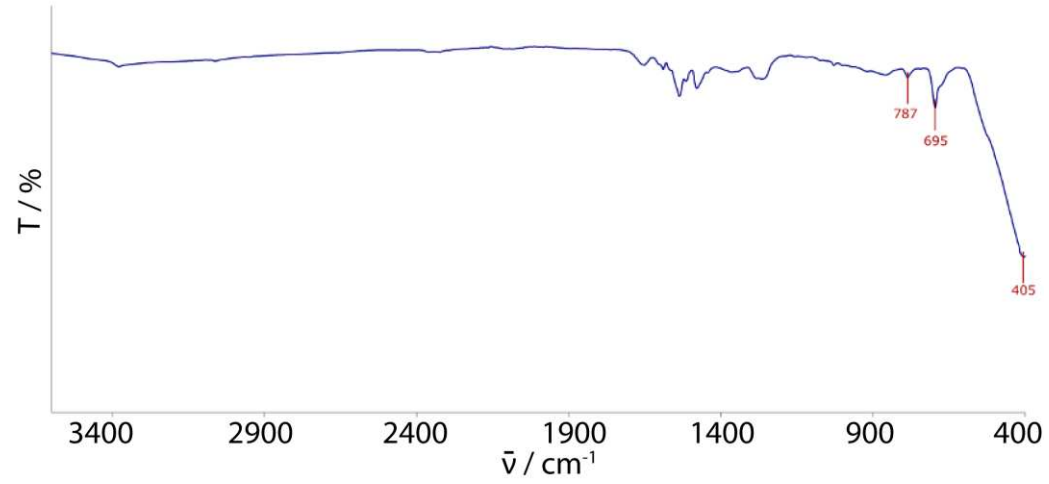

Figure 3-20. FTIR spectrum of NPL-1.

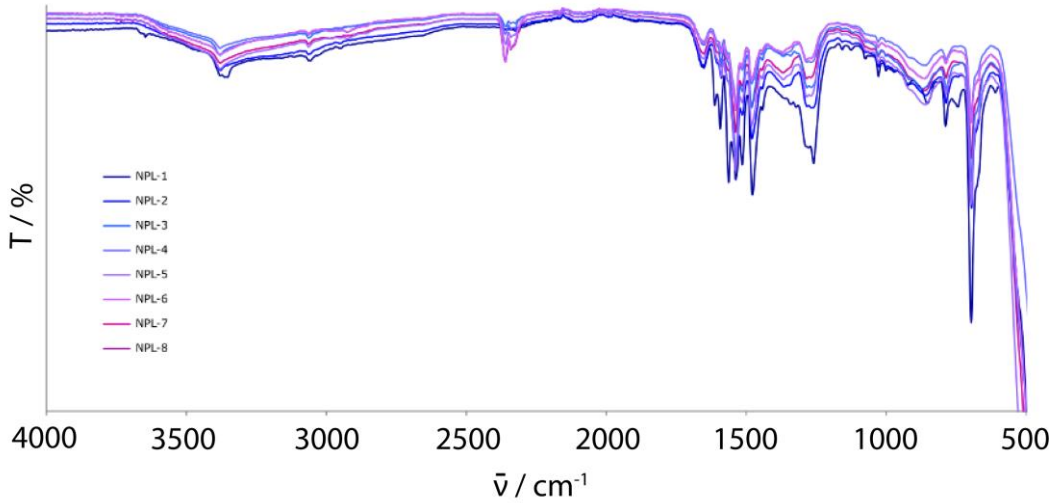

Figure 3-21. FTIR spectra of NPL-1 to NPL-8.

UV/vis and PL spectroscopy.

Optical absorption (UV/Vis) spectra of ZnO NCs in methanol colloidal solutions were collected with a Hitachi U-2910 spectrophotometer. A standard quartz cell (Hellma) with a 10 mm path length was used and rinsed with the appropriate solvent before each run. PL measurements were carried out with a Hitachi F-7000 fluorescence spectrophotometer. Optical band-gap energies of ZnO NPLs have been estimated using Tauc plots.

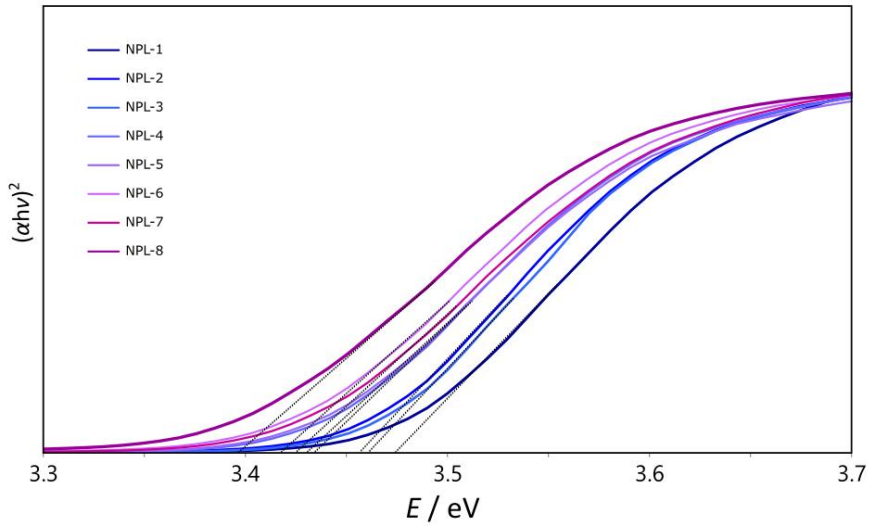

Figure 3-22. Tauc plots for NPL-1 to NPL-8.

Table 3-5. Estimated optical band-gap energies and PL maxima of ZnO NPLs.

Sample	Zn:O molar ratio	E_g [eV]	PL maxima [nm]
NPL-1	**3**	**3.472**	**538**
NPL-2	**4**	**3.456**	**549**
NPL-3	**5**	**3.461**	**549**
NPL-4	**6**	**3.434**	**554**
NPL-5	**7**	**3.430**	**558**
NPL-6	**8**	**3.418**	**560**
NPL-7	**9**	**3.425**	**561**
NPL-8	**10**	**3.396**	**565**

DNP NMR spectroscopy

The experiments were performed on a Bruker DNP-SSNMR AVANCE III 9.4 T 400 MHz spectrometer equipped with a gyrotron and transmission line capable of providing ~5 W of 264 GHz microwave irradiation at the sample. These experiments were performed on a low-temperature 3.2 mm MAS probe at sample temperatures of ~105 K or at room temperature (RT), as stated in the corresponding figure caption. Experiments were acquired using ^{1}H $\pi/2$ pulses of 100 kHz, ^{13}C $\pi/2$ pulses of 50 kHz,

^{15}N π/2 pulses of ~40 kHz, ^{15}N and ^{13}C CP spin-locking at ~40 kHz and ~50 kHz, respectively. 100 kHz of SPINAL-64 heteronuclear ^{1}H decoupling was used throughout the 10 and 15 ms signal detection periods for ^{13}C and ^{15}N CP experiments, respectively, with direct spectral widths of 40 kHz. These low temperature (~105 K) experiments used optimized experimental repetition delays of 3.4 s, 1.5 s, 3 s and 3.7 s for NPL-1,2,3,8, respectively.

DNP sample preparation.

The "DNP-ready" sample was prepared by adding 40 μL of 10 mM AsymPolPOK polarizing agent[96] d_8-glycerol:D_2O:H_2O (6:3:1; v:v) solution to 1 mL of the colloidal NPL-methanol solution (containing 60 mg of NPLs) with stirring and subsequent evaporation of the volatile solvent. The resulting damp powder was fully packed (~100 mg) into a thin-wall 3.2 mm outer-diameter zirconia magic angle spinning (MAS) rotor, which was subsequently inserted into a cold (~ 100 K) NMR probe within a 9.4 T magnet and rapidly spun pneumatically with cold nitrogen gas about the magic angle.

Optimization of the transformation of ethylzinc benzamidate precursor

Transformation conditions. The transformation of a generated in-situ THF solution of ethylzinc benzamidate towards ZnO nanostructures was optimized in terms of O source (air or water), water excess (1:3 to 1:10 Zn:O molar ratio), temperature (-20°C to 50°C), and precursor concentration (0.2 to 0.8 M). Strikingly, the transformation on air according to the OSSOM procedure resulted in amorphic product, while the control hydrolysis using 3 or more molar excess of water (compared to Zn) gives a nanocrystalline ZnO phase with clear shape anisotropy (Figure 3-23). Interestingly, the size of nanocrystals highly depends on the molar excess of water. The higher temperature has no significant effect on the product of the transformation (Figure 3-24). However, low temperature during the hydrolysis gives unidentified crystal phase. Therefore, room temperature (ca. 24°C) was chosen as optimal for the synthesis of ZnO NPls. The precursor concentration in the range of 0.2-0.8 M has no significant influence on the product of the hydrolysis (Figure 3-25).

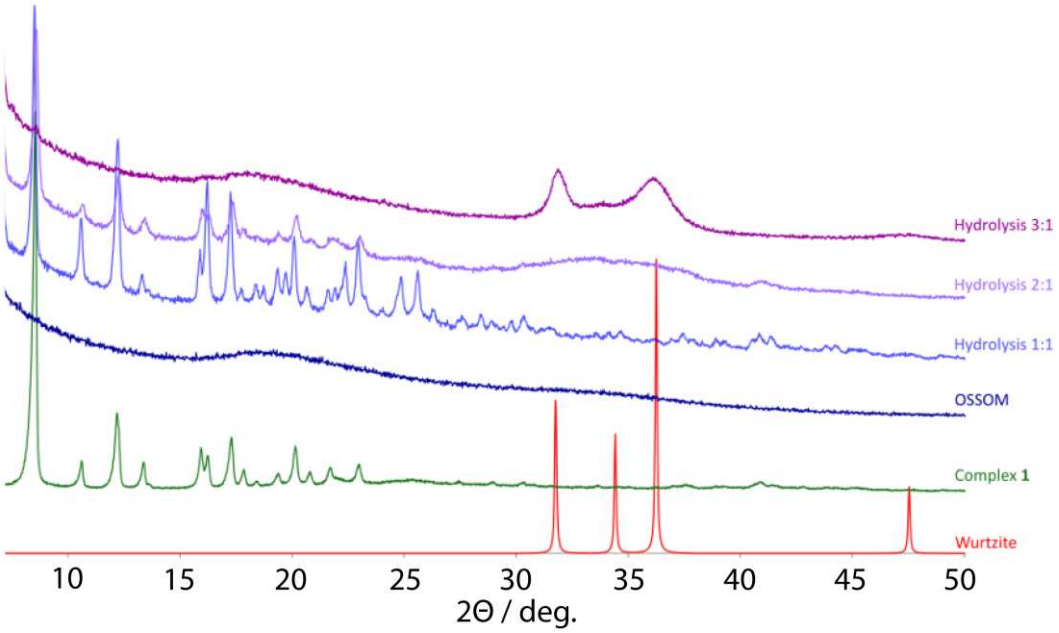

Figure 3-23. Powder patterns generated for wurtzite ZnO structure (a) and measured for complex **1** (b), and products of the transformation of ethylzinc benzamidate using OSSOM approach (c) and hydrolysis with 1:1 (d), 2:1 (e), and 3:1 (f) H_2O:Zn molar ratio.

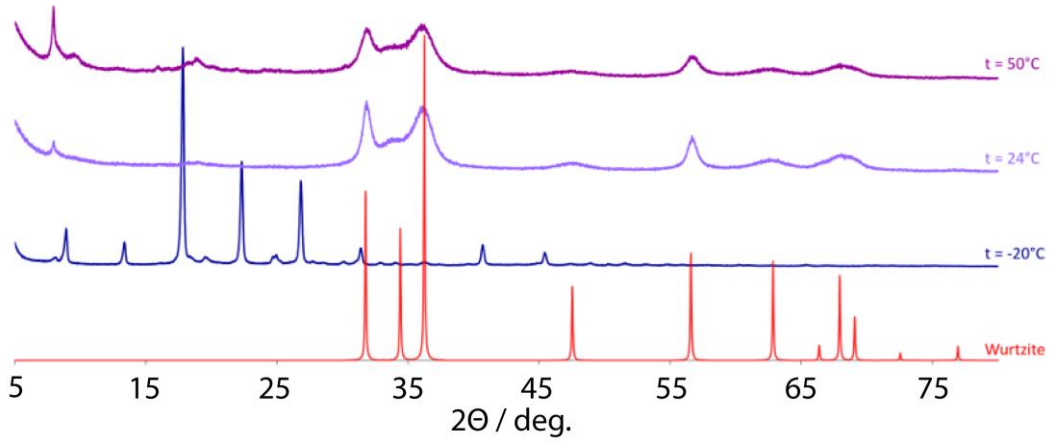

Figure 3-24. Powder patterns generated for wurtzite ZnO structure (a) and measured for the products of the hydrolysis in various temperatures with 3:1 H_2O:Zn molar ratio.

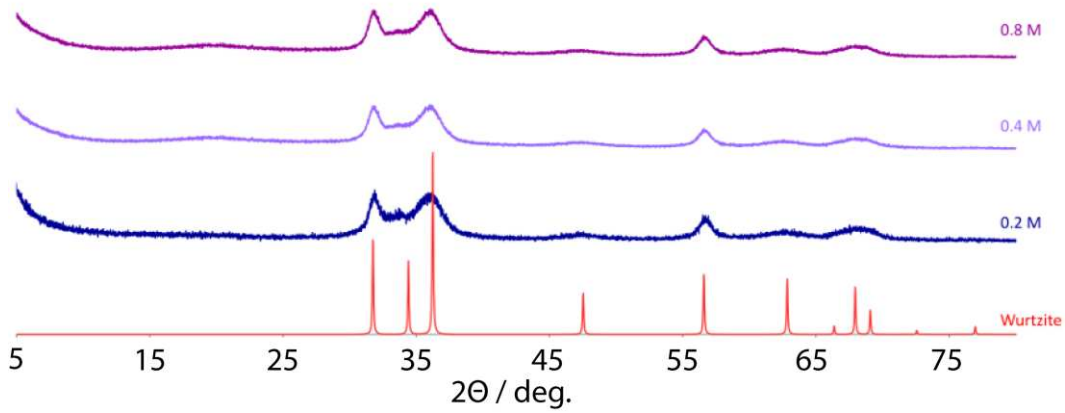

Figure 3-25. Powder patterns generated for wurtzite ZnO structure (a) and measured for the products of the hydrolysis with various precursor concentration with 3:1 H_2O:Zn molar ratio.

Stability

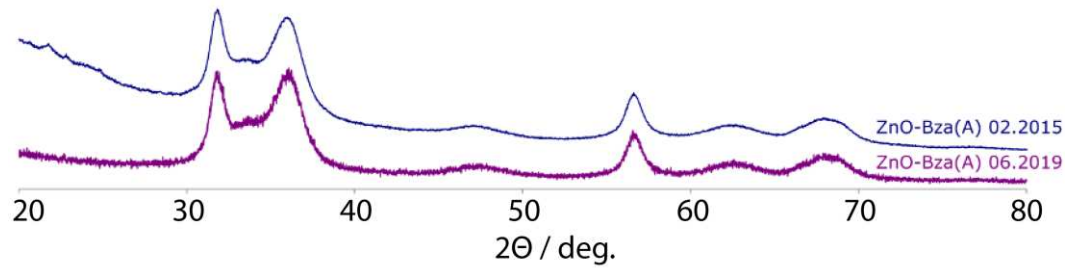

Figure 3-26. Powder patterns of the same sample of NPL-1 stored on air by about 4 years.

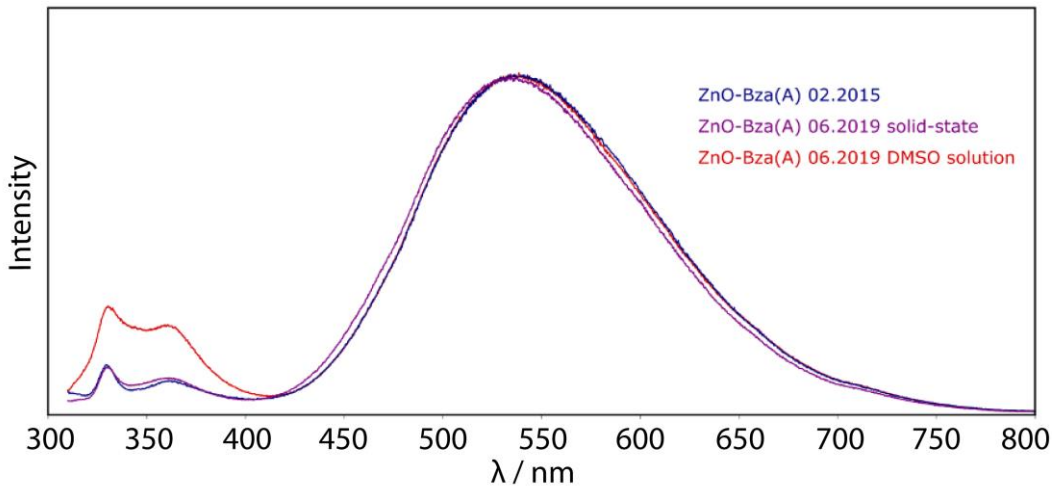

Figure 3-27. PL spectra of the same sample of NPL-1 stored on air by about 4 years as powder and in DMSO solution.

Synthesis and structural characterization of selected model complexes

Amidines are frequently used as common neutral donor or anionic ligands in coordination chemistry. However, the corresponding zinc complexes incorporating benzamidine ligand still represent a highly unexplored field. In **1** bza ligand adopts classic μ_2 coordination mode observed commonly for X-type O,O'-bidentate ligands on the surface of ZnO nanocrystals. Therefore, complex 1 was used as model compound for the most likely expected mode of interaction between ZnO and bza (Figure 3-28). Simultaneously, as strong N-base bza-H may efficiently act as the neutral donor ligand. To demonstrate the tendency of bza-H for the formation of cooperative hydrogen bonding and donor-acceptor interactions a new simple complex $[Zn(AcO)_2(bza\text{-}H)_2]$ (**2**), which is simple adduct of neutral *bza*-H to zinc acetate, we designed, synthesized, and fully characterized. In **2** benzamidine acts as strong N-donor ligand and its monodentate κ^1 coordination mode is supported by extended network of intra- and intermolecular N-H···O hydrogen bonds. Compound **2** servs us further as model of L-type H-bond supported interaction of ligands in the surface of ZnO NPls (Figure 3-29).

FTIR spectra were measured with a Brucker Tensor II spectrometer equipped with ATR (attenuated total reflection) accessory. ^1H and ^{13}C NMR spectra were acquired on Varian Mercury (400 MHz) spectrometer. Elemental analyses were performed on Elementar VarioMicro Cube analyzer.

Complex 1

Synthesis of [OZn4(bza)6]·0.5THF (1·0.5THF): Complex was synthesized according to the previously reported procedure[215]. $ZnEt_2$ (2 M in hexane, 0.5 ml, 1 mmol) was added to a solution of bza-H (180 mg, 1.5 mmol) in 5 ml of THF at -78°C. The reaction mixture was allowed to warm to room temperature and stirred overnight. Next, the stoichiometric amount of H_2O was added (1 M in THF, 0.25 ml, 0.25 mmol), and the reaction was stirred overnight. Then, the solvent was removed under vacuum and complex 1 was collected as white crystalline powder in almost quantitative yield. The purity of the product was confirmed spectroscopically and by elemental analysis. ^1H NMR (d8-THF, 400 MHz): δ [ppm] = 7.59 (m, 12H, Ar), 7.28 (m, 18H, Ar), 4.71 (s, 12H, NH); 13C NMR (d8-THF, 100 MHz): δ [ppm] = 174.64, 144.79, 129.49, 128.99,

126.86; FTIR (ATR): ν [cm-1] = 3366 (m), 3058 (w), 2970(w), 2857 (w), 1593 (s), 1560 (s), 1512 (s), 1477 (s), 1442 (m), 1290 (s), 1061 (m), 1027 (m), 905 (w), 785 (m), 732 (m), 698 (s), 682 (s), 518 (m), 478 (s); elemental analysis calcd (%) for 1·0.5THF ($C_{44}H_{46}Zn_4O_{1.5}N_{12}$): C 51.39, H 4.50, N 16.34; found: C 50.11, H 4.59, N 15.22.

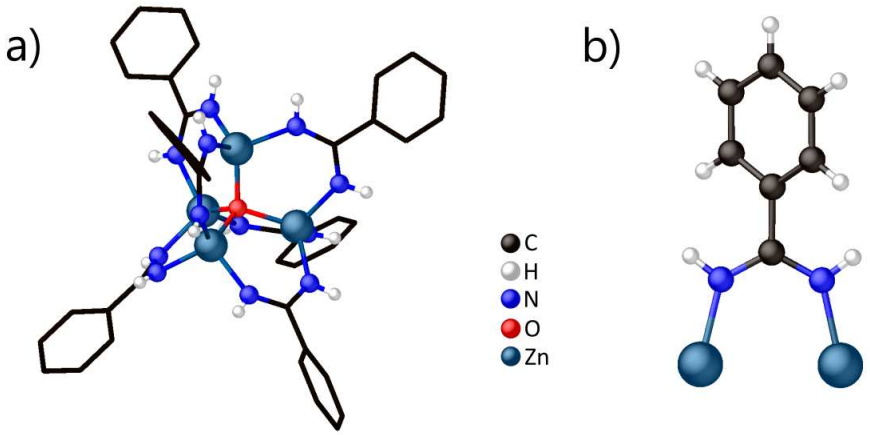

Figure 3-28. Molecular structure (a) and bza coordination mode (b) in 1.

Complex 2

Synthesis of $[Zn(OAc)_2(bza\text{-}H)_2]$ (2): $Zn(OAc)_2{\cdot}2H_2O$ (0.110 g, 0.5 mmol) and *bza*-H (0.120 g, 1 mmol), were dissolved in 10 ml THF at 60°C. Slow cooling of the solution to room temperature resulted in colorless crystals of 2. Alternatively, the solvent was removed under vacuum after 2 hours of stirring, yielding a quantitative amount of 2 in the form of white powder. The product was characterized by SC-XRD, NMR and FTIR spectroscopy, and elemental analysis. 1H NMR (d8-THF, 400 MHz): δ [ppm] = 7.64 (m, 4H, Ar), 7.42 (m, 6H, Ar), 7.54 (d, 4H, Ar), 2.53 (bs, 6H, NH), 1.88 (s, 6H, Me); 13C NMR (d8-THF, 100 MHz): δ [ppm] = 194.7, 169.3, 131.8, 129.3, 127.2, 30.5; FTIR (ATR): ν [cm-1] = 3414 (w), 3362 (w), 3334 (m), 3279 (w), 3247 (w), 3123 (w), 3063 (w), 1663 (m), 1600 (s), 1579 (s), 1562 (s), 1518 (m), 1473 (m), 1330 (m), 1326 (m), 1273 (m), 1253 (m), 789 (m), 693 (s), 667 (s); elemental analysis calcd (%) for $C_{18}H_{22}N_4O_4Zn$: C 51.02, H 5.20, N 13.23; found: C 51.10, H 5.28, N 13.12.

Single Crystal X-Ray analysis:

The molecular structure of **2** comprise a single Zn center with a tetragonal coordination sphere built by two N atoms and two O atoms of two *bza*-H and two acetate ligands, respectively. Each benzamidine form a single donor-acceptor bond with Zn acting as L-type ligands utilizing the imine N atoms with N-Zn bond length in the range of 1.988-2.013 Å. The monodentate κ^1 coordination mode of both *bza*-H (Figure 3-29a) is cooperatively stabilized by intramolecular hydrogen bonds in the proximal secondary coordination sphere formed between the amine groups of both *bza*-H and two oxygen atoms of one acetate anion (Figure 3-29a). The second acetate anion is involved in the formation of two intermolecular hydrogen interactions with the two imine hydrogen atoms from the second molecule of **2**. The resulted H-bonded supramolecular dimers (Figure 3-29c) are further self-assembled *via* extensive network of intermolecular hydrogen bonds into 2D supramolecular layers (Figure 3-29d). The respective O···H lengths are in the range of 2.000-2.306 Å and each *bza*-H and OAc ligand form three hydrogen bonds utilizing maximum number of possible H-donor and H-acceptor sites, respectively.

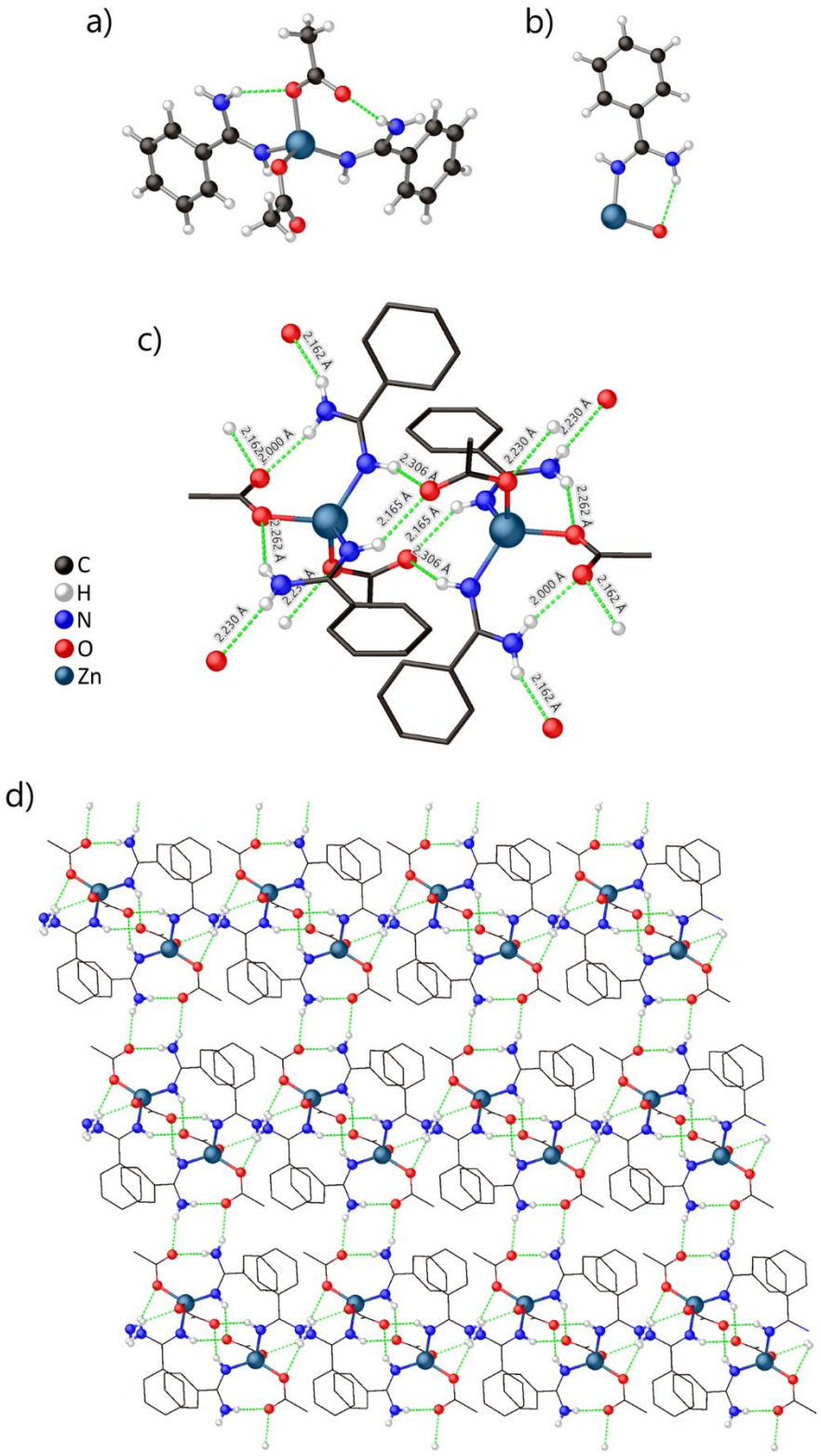

Figure 3-29. Molecular structure (a) and *bza*-H coordination mode (b) in **2**. H-bond mediated dimers (c) and 2D supramolecular layers (d) of **2**.

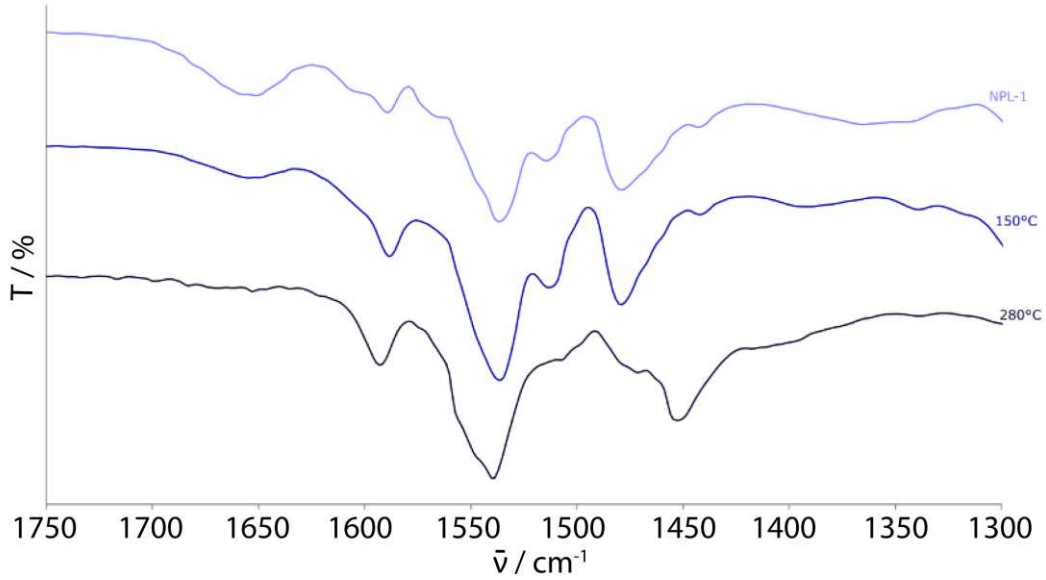

Figure 3-30. FTIR spectra of NPL-1 after heating to 150°C and 280°C.

Calcination experiment

Thermogravimetric analysis indicates binary character of organic coatings in ZnO-Bza NPls, and that it can be removed gradually by the calcination. The influence of heating on the composition and morphology of the nanomaterial was analyzed. To this aim, the samples of ZnO-Bza(A) were heated to 200°C and 300°C under vacuum and then characterized by PXRD and FTIR spectroscopy. Heating ZnO-Bza NPls up to 250°C does not cause any visible changes to the nanomaterial. Above this temperature the sample begins to turn brown, which is most likely caused by the pyrolysis of the organic ligand and deposition of amorphous carbon impurities. However, PXRD analysis shows that there is no change in the morphology of the sample heated up to 300°C and on the diffractograms no changes in crystallite sizes or formation of new crystalline products were observed. The FTIR spectra shows no significant changes in organic ligands up to 200°C. After heating to 300°C there is a loss of signals at 1654 and 1604 cm^{-1} likely caused by dissociation or pyrolysis of one form of organic ligands. There is also a new band at 1451 cm^{-1}, which may by associated to carbon impurities in the sample.

Chapter 4
Probing benzamidine ligand coordination chemistry on multi-faceted ZnO nanoplatelet surfaces using DNP-NMR spectroscopy

4.1 Introduction

4.1.1 ZnO NPLs

Colloidal 2D quantum dots are an exciting new class of nanomaterials that find tremendous applications for their optoelectronic properties[1–6]. Hence, significant research effort has been dedicated to producing uniform nanoplatelets (NPLs) with atomic-level size control[168–170]. ZnO is especially promising among the semiconductor nanomaterials used because of its low toxicity and unique catalytic and opto-electronic properties but remains relatively understudied[12–15]. Until recently, solvo-thermal synthesis has been the most commonly used method for the production of ZnO NPLs[175,188–195]. However, the produced platelets are generally 10-20 nm thick with sub-micrometer or micrometer range lateral dimensions and are highly aggregated. In Chapter 3, the synthesis of highly stable size-controlled ZnO NPLs with the thickness of the smallest NPLs reaching dimensions less than 5 nm and lateral dimensions of about 15 nm was discussed. The applied organometallic approach OSSOM-II is a modified version of the recently reported one-pot self-supporting organometallic (OSSOM) approach which uses controlled exposure of organometallic precursor to atmospheric air to produce high-quality 0D QDs[22–24,26–30,41,216,217]. Instead of exposure

to air, the method applied here uses water as a control parameter to obtain NPLs of different sizes. An in-depth understanding of the atomic-level structure of these unique NPLs is still required to understand its formation.

QDs have a large surface to bulk atom ratio, because of which the organic-inorganic interface is a crucial factor controlling their properties. Ligand shell on QDs provides control over the nucleation and growth of nanocrystals (NCs). Also, depending on the choice of ligand, QDs can have several applications. Thus, a deep understanding of the atomic-level surface chemistry of NCs is required to produce functional materials with desired applications. Solid-state nuclear magnetic resonance (ssNMR), a common spectroscopic technique, provides rich site-specific information concerning atomic environments and details about short-range order. Thus, this technique is ideal for understanding the nature of interactions at surface sites[51]. In recent times, some reports have been aimed at the characterization of the surface and bulk of ZnO using NMR spectroscopy[52–56]. However, ssNMR often suffers from low sensitivity, especially at interfaces, where the relative number of atoms is less compared to the bulk. This drawback is overcome by dynamic nuclear polarization (DNP), a technique that uses the large electron spin polarization to enhance the signal from surrounding nuclei[75,79,209], and thus can be used to selectively enhance the surface sites of nano-objects[108–111] . For ZnO NCs, in Chapter 2 it was shown that the arrangement of diphenyl phosphate capping ligands on polar surfaces could be determined using DNP-enhanced ssNMR[31]. Using this information from the inorganic-organic interface, it was proven that the structure of ZnO NCs, and therefore the properties, depends on the employed synthetic method. In particular, the one-pot self-supporting organometallic (OSSOM) approach[22,24,28,41,216] produced more stable and consistent nanocrystals compared to traditional sol-gel methodology.

An important aspect for growing NCs of specific morphology is facet stabilization. Stable facets are truncated crystal planes that are created by cutting only through bonds and not through atoms. It is well known that during the synthesis of NCs, higher energy facets grow faster, governing the resulting aspect ratio of these NCs[182]. Relative facet energy can be managed via the addition of suitable ligands that selectively bind to desired facets. ZnO wurtzite structure has four stable facets which are (0001) and

$(000\bar{1})$ polar facets, and $(10\bar{1}0)$ and $(2\bar{1}\bar{1}0)$ non-polar facets[218]. For hexagonal wurtzite NPLs, polar facets generally constitute (0001) Zn-rich top and $(000\bar{1})$ O-rich bottom because these are formed by severing only one out of four bonds for the surface atoms[219]. In this work, observations from HRTEM images of side facets of NPLs combined with TGA data highlight divergence in the structure of $(000\bar{1})$ polar facets from the expected O-rich terminations.

The NC-ligand interface plays a key role in the unique physicochemical properties of ZnO. Thus, information on ligand binding and arrangement on the surface is crucial. In this work, the surface chemistry of novel size-controlled ZnO NPLs produced by the OSSOM-II approach using DNP-enhanced ssNMR will be analyzed and discussed. For this purpose, the smallest and the largest NPLs in the group were analyzed. ^{1}H-^{15}N heteronuclear dipolar correlation NMR spectroscopy experiments (HETCOR) and ^{15}N-^{13}C heteronuclear dipolar correlation experiments, specifically transferred echo double resonance (TEDOR) experiments were performed to elucidate the binding of benzamidine ligand on the polar and non-polar facets of these unique NPLs. Moreover, performing ^{13}C-^{13}C dipolar correlation NMR experiments on the smallest NPLs at ^{13}C natural isotopic abundance (NA 1.1%), the average ligand distribution on the $(10\bar{1}0)$ facets was studied. Finally, changes in the NMR spectra of the smallest platelets upon water addition provided insights into the role of ligands in the growth of these NPLs. Understanding the mechanism of growth allows optimization of the synthetic process, thus this study will enable controlled production of future designer nano-objects.

4.2 Results and Discussions

4.2.1 ZnO NPLs: Synthesis and ZnO core structure information

Hexagonal ZnO NPLs were synthesized by OSSOM-II, an organometallic approach (described in Chapter 3). For this, a specific amount of water (3 up to 10 equivalents as a THF solution) was added dropwise to an *in-situ* generated [EtZn(*bza*)] solution in THF at room temperature (RT). The reaction mixture was stirred for 2-3 days at RT which finally resulted in a cloudy and luminescent suspension composed of wurtzite-

type ZnO NPLs. In this way, NPLs of different sizes were obtained depending on the amount of water that was added to the reaction mixture. The addition of 3 up to 10 equivalents of water led to the formation of NPL-1 to NPL-8, respectively, whereas the addition of 1 or 2 equivalents of water formed molecular complexes capped by anionic benzamidinate species. In general, the increase in size along the basal plane was more pronounced compared to the rise along with the height. PXRD scherrer analysis (Chapter 3, PXRD analysis, materials and methods section) results showed that the NPLs exhibit a very narrow distribution of thickness, which changes from 3.2 to about 7.5 nm, and high distribution of lateral dimensions with mean values ranging from about 9.1 to 19.7 nm for samples NPL-1 to NPL-8, respectively. The thickness of the smallest NPLs NPL-1 is exactly 3.2 Å (i.e., showing mono-disperse distribution along the *c* direction), which corresponds to 12 monolayers of ZnO (thickness of 6 wurtzite unit cells).

4.2.2 Experiments at ^{13}C (~1.1%) and ^{15}N (~0.4%) natural isotopic abundance: DNP sample preparation and signal enhancement

The surface ligand binding on the smallest and biggest platelets, i.e., NPL-1 and NPL-8, were analyzed using DNP enhanced solid-state NMR to understand these materials' interface. DNP sample preparation is key to obtaining substantial NMR signal enhancements and overall experimental sensitivity[159,220–222]. The method involved forming a colloidal solution in a suitable volatile solvent (in this particular case, methanol) that is also miscible with the solution containing the hyperpolarizing agent, thus facilitating a homogeneous mixture of NPLs. The $^{1H,\,CP}\varepsilon_{on/off}$ factor, defined as the ratio of the signal intensities returned from ^{1}H CP experiments recorded with and without microwave irradiation suitable for DNP, was found to be 36, and 26 for $\{^{1}H\text{-}\}^{13}C$ CPMAS NMR spectra of NPL-1 and 8, respectively. The same $^{1H,\,CP}\varepsilon_{on/off}$ factor was found for ^{13}C signals of glycerol, which is used as a glass-forming agent in the DNP matrix in DNP-ready samples. This uniform enhancement throughout the sample highlights a homogeneous mixing of the polarizing agent around the NPLs. Moreover, owing to the minor depolarization effects with AsymPolPOK[96] combined with the

benefits of working at low temperatures (~100 K)[223], absolute sensitivity ratios (ASRs)[159] of 97.5 (see Figure 4-1) were obtained for NPL-1 when compared with similar experiments recorded using conventional RT ssNMR. This converts to experimental time-savings of a factor ~9500, i.e., an experiment that would require a week of signal-averaging with conventional ssNMR can be recorded in ~1 minute using DNP. This substantial sensitivity gain, using DNP at low temperatures, allowed the acquisition of $\{^{1}H\text{-}\}^{15}N$ CPMAS NMR, $^{1}H\text{-}^{15}N$ heteronuclear dipolar correlation, and ^{13}C homonuclear dipolar correlation experiments for surface bound ligands without ^{15}N or ^{13}C isotopic enrichment for NPL-1.

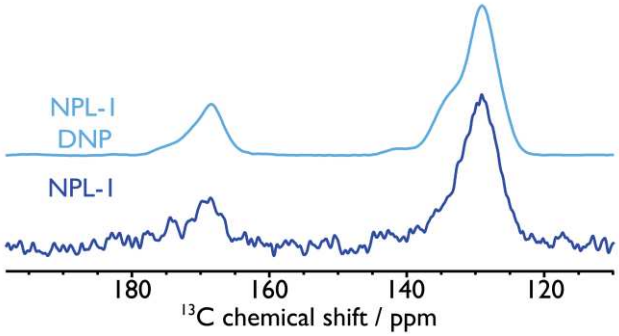

Figure 4-1. $\{^{1}H\text{-}\}^{13}C$ CPMAS NMR spectra of NPL-1 recorded with DNP at low temperature (105 K, 16 scans) and its comparison to NPL-1 (suspended in methanol, followed by complete evaporation of methanol) recorded at RT (1024 scans) at MAS frequency of 13.333 kHz and 9.4 T.

4.2.3 Zn terminated (0001) and (000$\bar{1}$) facets

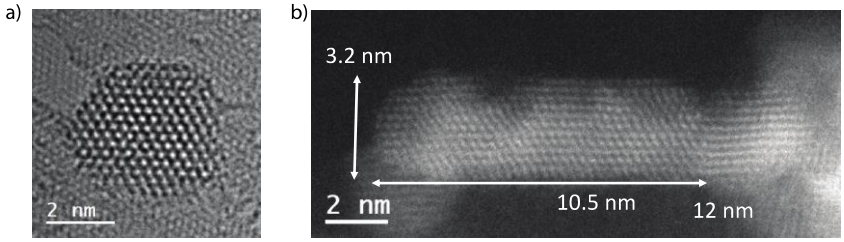

Figure 4-2. a) Monochromate TEM image of basal plane on graphene and b) STEM HAADF image of cross-sectional observation on carbon nanotubes (CNT) for NPL-1.

TEM images of NPLs were recorded and these showed that NPLs tend to fall flat on the basal plane. When suspended on graphene, majority of the observed surfaces are (0001) and (000$\bar{1}$) polar facets. To observe the sides of the NPLs, they were mixed with carbon nanotubes (CNT) and subsequently high-angle annular dark-field scanning

transmission electron microscopy (HAADF-STEM) image was obtained as shown in Figure 4-2. When observed from the side, the majority of NPLs were observed to have one polar facet termination that was flat and appeared as if it had been prepared by deposition, while the other appeared to be corrugated. TGA data (Chapter 3, materials and methods section) shows that assuming anionic ligands are present only on the (0001) Zn-terminated surfaces, 4 ligands/5 Zn's are present. However, the maximum possible coverage of these surfaces is 2.5 ligands/ 5 Zn's. This indicates that there might be some anionic ligand capped Zn terminations on the $(000\overline{1})$ facets as well. ZnO polar surfaces are generally flat even when bare, thus the flat polar facet termination must be the (0001) Zn rich facet. Whereas, the $(000\overline{1})$ facets if terminated by Zn would have three dangling bonds in contrast to one for the (0001) facet Zn's. Thus, the presence of Zn terminations on $(000\overline{1})$ facets could be the cause of corrugation on this polar facet. Generally, hexagonal wurtzite ZnO NPLs have a (0001) Zn-rich top and $(000\overline{1})$ O-rich bottom because these facets are formed by severing only one out of four bonds for the surface formation. However, from the observations described here-in it can be deduced that there might be some Zn atoms terminating the $(000\overline{1})$ facets as well. From the STEM HAADF and HRTEM images of the NPLs, it is clear that mainly the non-polar surface facets are composed of $(10\overline{1}0)$. Whereas, the polar facets constitute (0001) Zn terminated facets which are observed to be flat, and the $(000\overline{1})$ possibly Zn and O terminated bottom facets which are found to be corrugated.

4.2.4 Hydrogen-bonding interactions of ligands on the $(10\bar{1}0)$ non-polar and (0001) polar surfaces

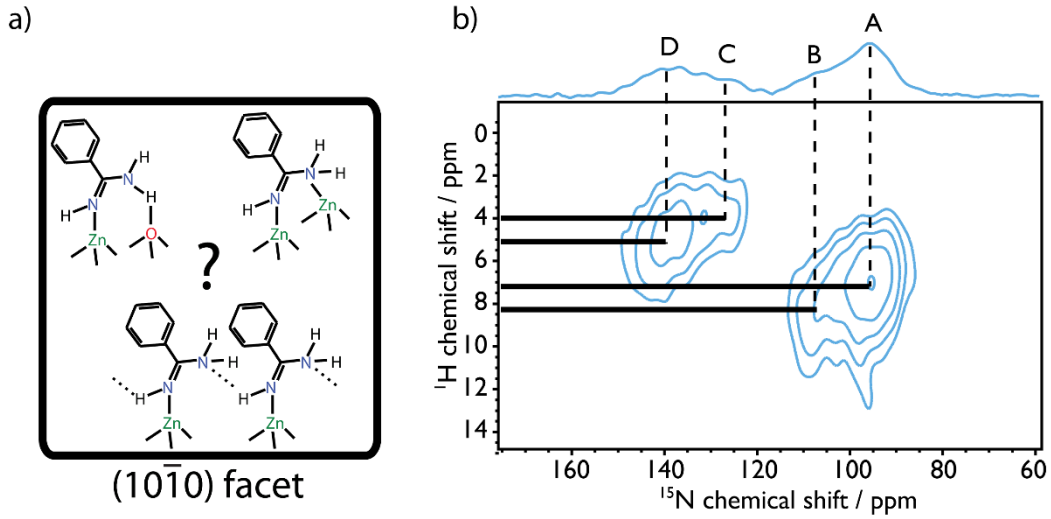

Figure 4-3. a) Possible neutral-ligand binding modes on the (**$10\bar{1}0$**) facets. (b) DNP-enhanced 2D ^{1}H-^{15}N FSLG-HETCOR NMR spectrum of ZnO-BA-NPL3, recorded at ~100 K using a MAS frequency of 12 kHz and a mixing time of 100 µs.

Isotropic chemical shifts hold rich information about the electronic environment of the nucleus under study. Benzamidine, the ligand used for the synthesis of NPLs, binds to ZnO surface sites through its basic N atoms. Hence in Chapter 3, using ^{1}H-^{15}N CPMAS NMR experiments the presence of bimodal ligand binding specific to the polar and non-polar facets of ZnO, for platelets NPL-1,2,3 and 8, respectively, was shown. But, to gain insights into the more intricate interactions between neighbouring nuclei in a system, for instance hydrogen-bonding interactions, heteronuclear dipolar correlation experiments must be recorded. Recording these experiments for NPL surface ligand at ^{15}N NA (~0.4%) requires unrealistic experimental times. However, using the enhancements provided by DNP, NA 2D ^{1}H-^{15}N heteronuclear dipolar correlation experiments were recorded at a 100 µs mixing time for NPL-1 and NPL-8. A representative spectrum of the experiment performed for NPL-1 is shown in Figure 4-3 b). The correlations observed in these experiments are between ligand ^{15}N atoms and their nearest ^{1}H's. Peaks B and C in the ^{15}N CPMAS NMR spectrum correspond to two anionic forms of the ligand on the polar facets of ZnO NPLs. Whereas, Peaks A and D

correspond to the amino and imino nitrogens of the neutral ligand on the $(10\bar{1}0)$ non-polar facets (Chapter 3).

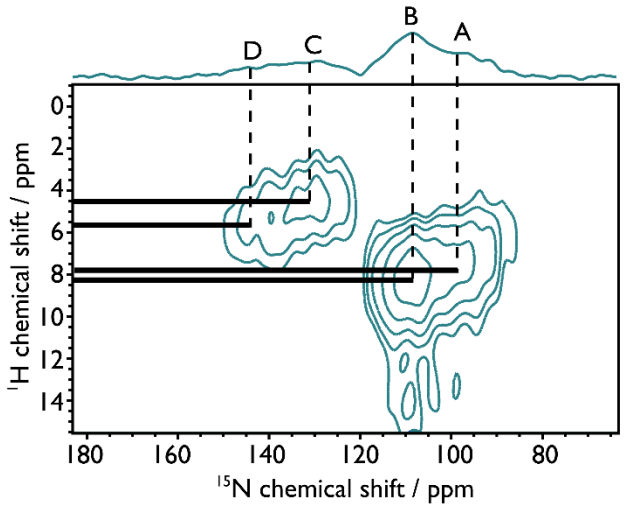

Figure 4-4. DNP-enhanced 2D ^{1}H-^{15}N FSLG-HETCOR[224] NMR spectrum of NPL-8, recorded at ~100 K using a MAS frequency of 12 kHz and a mixing time of 100 μs.

On the non-polar facets, it was clear from the ^{15}N isotropic chemical shift of imino nitrogen at 140 ppm that neutral benzamidine acts as an L-type ligand via lone pair donation through its more basic imino nitrogen atom, as seen in Figure 4-3a). However, binding of the amino nitrogen atom could possibly take place through: i) amino lone pair donation to surface zinc, ii) hydrogen-bond formation between amine protons and surface oxygen, or iii) amine acting as hydrogen-bond acceptors to adjacent benzamidine imino ^{1}H's (structures shown in Figure 4-3 a). From the spectrum in Figure 4-3 b, it can be seen that a contour cross peak between imino nitrogen at 140 ppm and ^{1}H at $\delta\{^{1}H\} \sim 5.1$ ppm is present, whereas amino nitrogen at 90 ppm correlates with higher-shifted ^{1}H at $\delta\{^{1}H\} \sim 7$ ppm. For free benzamidine pro-ligand, the ^{1}H chemical shift of N-H protons measured in $CDCl_3$ is observed at 5.5 ppm[198]. For the platelets, the observed high chemical shift at 7 ppm for amino protons of the surface-bound neutral ligand indicates that these are involved in hydrogen-bonding. Interestingly, the amino proton peak is relatively broad, showing a distribution of chemical shifts possibly due to a varied extent of hydrogen-bonding of the ligand on the surface. Therefore, on non-polar facets of the ZnO-BA-NPLs, the imino nitrogen from the neutral form of the ligand is bound to Zn sites via its lone pair (acting as an L-type ligand) and protons from the amine are involved in hydrogen-bonding, likely with

surface O sites. In the equivalent spectrum of NPL-8 (Figure 4-4), the center of the ^{1}H chemical shift of the correlation to peak B is observed at $\delta\{^{1}H\}$ ~8.0 ppm. Note that in Complex 2, the molecular complex containing the neutral ligand, both the amine and the imine nitrogen atoms act as hydrogen-bond donors (Figure 4-17). Hence, unlike the neutral ligand on the NPL surface, in Complex 2 the equivalent ^{1}H-^{15}N heteronuclear dipolar correlation experiment (Figure 4-5) shows high shifted protons attached to both the amino and imino nitrogen atoms.

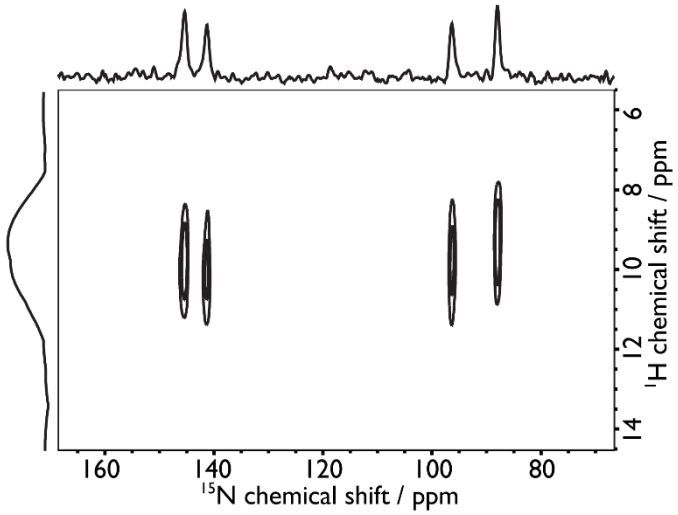

Figure 4-5. DNP-enhanced 2D ^{1}H-^{15}N FSLG-HETCOR NMR spectrum of Complex 2, recorded at ~100 K using a MAS frequency of 12 kHz and a mixing time of 500 μs.

On the polar (0001) facets of NPL-1, ^{15}N peak C associated with anionic form of ligand, correlates with ^{1}H at $\delta\{^{1}H\}$ ~ 3.9 ppm. Whereas peak B associated with another anionic form of the ligand, correlates with ^{1}H at $\delta\{^{1}H\}$ ~ 8.3 ppm. For the latter, the high-shifted ^{1}H correlation indicates involvement in hydrogen-bonding. Thus, it can be inferred that there exist two anionic forms of the BA ligand capping polar (0001) facets: a μ_2-coordinated structure similar to that of Complex 1, the molecular complex containing anionic ligand geometry (anionic BA C, Figure 4-7a); and the other, involved in hydrogen-bonding but with an unknown coordination mode/configuration on the surface. In order to find the structure corresponding to this other anionic form of the ligand on the surface, isotropic magnetic shieldings were determined for various modeled structures using density functional theory (DFT) calculations.

4.2.5 Determining the 'other' anionic form of BA ligand

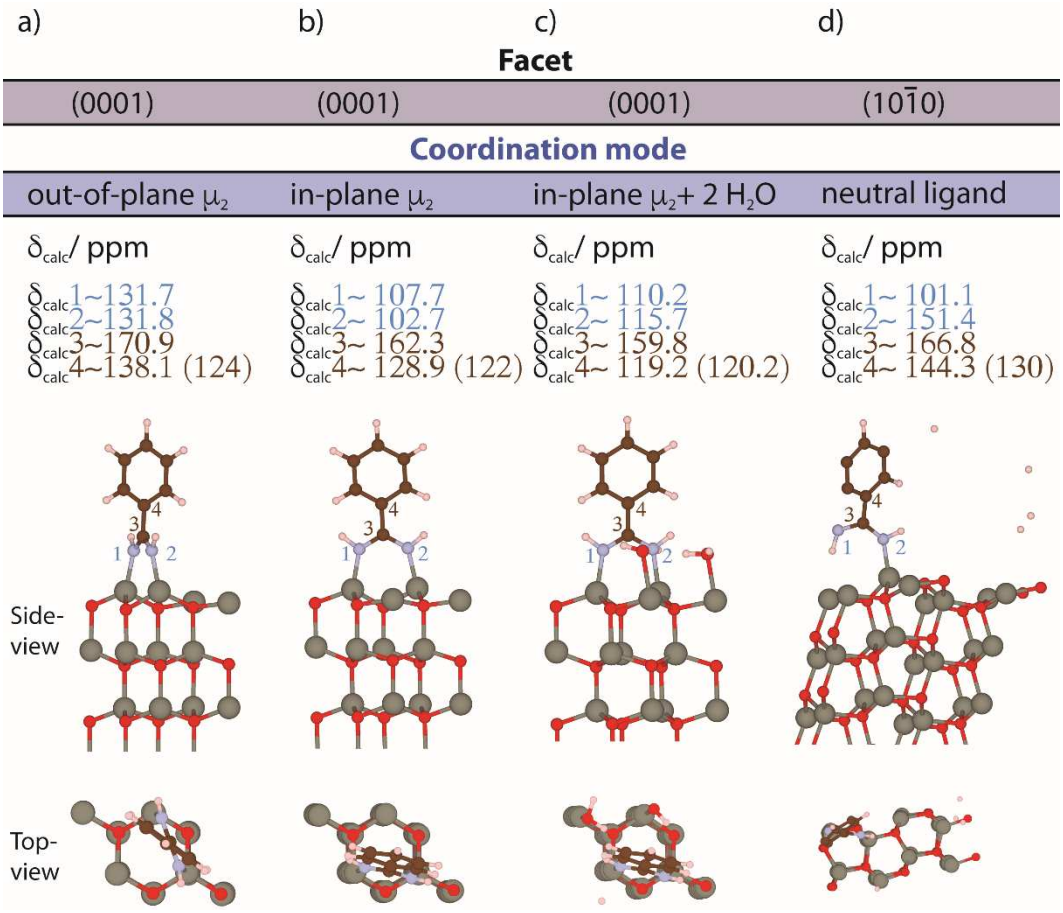

Figure 4-6. Side view and top view of geometry optimized structures on the (0001) facet of a) out-of-plane-μ_2 coordination, b) in-plane-μ_2 coordination, c) out-of-plane-μ_2 coordination with one water molecule, and on the (10$\bar{1}$**0**) facet of d) neutral ligand coordination. In each figure, the amidine ^{15}N's (1 and 2), amidine ^{13}C (3) and ipso ^{13}C (4) have been labelled and the corresponding calculated NMR shifts have been mentioned above.

DFT calculations were performed, using PWSCF and GIPAW modules within Quantum ESPRESSO[225,226] package, to calculate NMR parameters of modeled structures. Surfaces were built with Atomic Simulation Environment[227], a python library, using a periodic slab model for wurtzite zinc oxide. The number of layers of ZnO used for the calculations was optimized to ensure that the top and bottom facets don't interact with each other, using the magnetic shielding values of atoms from two facets. The plot of magnetic shielding values of surface hydroxyl ^{17}O as a function of the number of ZnO unit cell layers is depicted in Figure 4-10. It was found that six ZnO layers were needed to ensure convergence of magnetic shielding, i.e., top and bottom atoms don't interact with each other (through the bulk). It must be noted that NPL-1

(the smallest and also highly mono-dispersed NPLs) also has six zinc oxide unit cells along z, as measured from PXRD Scherrer analysis. Moreover, a 60 Å vacuum was set-up between slabs repeating in the z-direction to prevent spurious interactions between these slabs. To save computation time, 1×1 x-y slab with one ZnO unit cell along the z-direction was modeled for the calculation of layer of vacuum needed, and the magnetic shielding of surface ^{67}Zn and ^{17}O were plotted as a function of vacuum between repeating slabs, shown in Figure 4-11. While the values converge at ~15 Å vacuum between the layers, for the ZnO surface slab model with 6 ZnO unit cells, a 60 Å vacuum was set-up to ensure no interaction between repeating images along the z-direction. For calculation of NMR parameters, Generalized Gradient Approximation from Perdew–Bruker–Ernzerhof (GGA-PBE) functional[121] was used. Also, a plane-wave basis set with a kinetic energy cutoff of 100 Ry and Monkhorst–Pack grid of 2x2x1 were used. Pseudopotentials (psp) for GIPAW were described by norm-conserving Trouiller-Martins psp's[122] obtained from Davide Ceresoli's website[228] (H, C, N, O) or using appropriate psp available in the QE library[229] and converting them to GIPAW psp's using atomic code[230](Zn). It is worth noting that experimental NMR parameters were obtained from experiments performed at 100 K, thus any dynamical effects can be quite reasonably neglected. Hence, it is appropriate to consider a frozen and more stable configuration.

A basic introduction to the DFT GIPAW method was given in Chapter 1, Section 0. DFT GIPAW calculations output isotropic magnetic shielding value σ_{iso} which must be converted into experimental isotropic chemical value δ_{iso} with the equation[124]:

$$\delta_{iso}^{calc} = -\alpha\left(\sigma_{iso}^{calc} - \sigma_{ref}\right)$$

where α and σ_{ref} are parameters determined from linear regression of computed to experimental values for a set of known structures. As the first step, optimized geometry of the molecular complex, Complex 2 (Figure 4-7b), with a known crystal structure (Chapter 3) was used as a reference for the calculations of ^{15}N and ^{13}C NMR chemical shifts (Table 4-1, Entry 1 and 2). Moreover, the ^{13}C and ^{15}N NMR spectra for Complex 2 showed narrow peak-widths (f.w.h.m. ~ 1ppm), thus providing an accurate value for comparison with calculations (Chapter 3). The calculated ^{15}N (Figure 4-8) and ^{13}C

(Figure 4-9) chemical shifts (ppm) were obtained using the best fit of isotropic magnetic shielding and experimental chemical shifts for Complex 2. Deviation of α from its ideal value of 1 are generally ascribed to the limitations of the chosen DFT functional. As shown in supplementary material, excellent correlation is observed with correlation coefficients of R=0.99 and R=1 for ^{15}N and ^{13}C, respectively.

Figure 4-6d shows relaxed geometry of neutral ligand on the $(10\bar{1}0)$ facets, and corresponding calculated chemical shifts. The calculated isotropic chemical shifts $\delta_{calc}\{^{15}N\}$ ~151.4 ppm and 101.1 ppm for imine and amine nitrogens, respectively, were in the same range as experimental shifts of ^{15}N peaks D and A. The objective was to determine the origin of difference in ^{15}N isotropic chemical shifts of peaks B and C, both stemming from anionic BA ligands. This ~20 ppm chemical shift difference could result from different binding modes, inter-ligand interactions, hydrogen-bonding, or anisotropic interactions. Subsequently, geometry optimizations of some ligand placements on the dominant (0001) facet were carried out, and Figure 4-6 a), b), and c) show the corresponding relaxed geometries. Since the anionic form associated with ^{15}N peak C had a nitrogen atom environment similar to that in Complex 1 (Figure 4-7 a) as evidenced from the similar ^{15}N shift range, this binding mode was replicated on the modeled (0001) facet (Figure 4-6a). This structure has $\delta_{calc}\{^{15}N\}$ ~130 ppm for both the nitrogens, the same as in Complex 1. This structure in Figure 4-6a had the benzene ring out-of-plane relative to the plane formed by the amidine nitrogen atoms (referred to out-of-plane μ_2 coordination), while calculations were performed on a structure with the benzene ring in-plane (referred to in-plane μ_2, Figure 4-6b). This structure has $\delta_{calc}\{^{15}N\}$ ~108 ppm for both nitrogen atoms, and hence matched the experimental parameters obtained for the anionic form associated with ^{15}N peak B. Indeed, having the benzene ring at a large angle relative to the plane of the nitrogen atoms, as in Complex 1, seems to result in this significant difference in ^{15}N chemical shift of 20 ppm. Co-planarity between the benzene ring and the amidine nitrogens likely allows extended movement of pi-electrons in the system, and the added electron density on the nitrogens[231] likely causes shielding, and hence the relative lowering of the ^{15}N chemical shift. Other than the above-described structures, models of (0001) facet with μ_3 anionic ligand coordination (Table 4-1, Entry 3), and complete surface coverage (Table 4-1,

Entry 4) were also geometry optimized and corresponding NMR parameters were calculated, but did not match the experimental parameters obtained for ^{15}N peak B.

It was then interesting to determine how anionic in-plane μ_2-coordination participates in hydrogen-bonding to protons with $\delta\{^1H\} \sim 8.3$ ppm as observed in the ^1H-^{15}N FSLG-HETCOR NMR (Figure 4-3b) experiment. Due to constraints on the surface, it is unlikely that two ligands that are μ_2-coordinated on the surface would form hydrogen-bonds with each other. Another possible source of H-bonding on the surface could be the water/surface hydroxyl groups involved in the synthesis of these materials and have also previously been observed on ZnO NC surface[60,232]. Thus, DFT calculations were performed on a ZnO wurtzite (0001) surface with the anionic in-plane-μ_2 coordinated ligand in the presence of water molecules, as depicted in Figure 4-6c. Upon energy minimization, it was observed that indeed this structure does participate in hydrogen-bonding with N…H-O bond distance of ~2.1 Å, but with the water molecules acting as the hydrogen-bond donors.

In the crystal structure of Complex 2 (not shown), two forms of the ligand are present, i.e., strongly hydrogen-bonded (2 Å) and in comparison, weakly hydrogen-bonded (2.3 Å) N-H…O. For the former, 2 Å hydrogen-bonding case, the benzene ring is out-of-plane to the NCN plane. While, for the latter, the benzene ring is in-plane with the NCN plane. This observation is in contrast to the occurrence at the (0001) facets, i.e., hydrogen-bonded system has a benzene ring in-plane versus non-hydrogen-bonded is out-of-plane. This contrast can be explained by considering that the nitrogen atoms in case of the $(10\bar{1}0)$ facet act as hydrogen-bond donors, while, on the (0001) facets they act as hydrogen-bond acceptors as seen above. To act as a hydrogen-bond acceptor, it is likely more effective to have more electron density around the nucleus[231], thus having the benzene ring in-plane. Whereas, to be a hydrogen-bond donor, it is more effective to have less electron density[231] and thus the benzene ring, out-of-plane. It should be noted that some out-of-plane μ_2-coordination can change to in-plane μ_2-coordination upon the addition of water. Thus, an outcome of water addition to the sample is change of some out-of-plane μ_2-coordination to in-plane μ_2-coordination. (Figure 4-15)

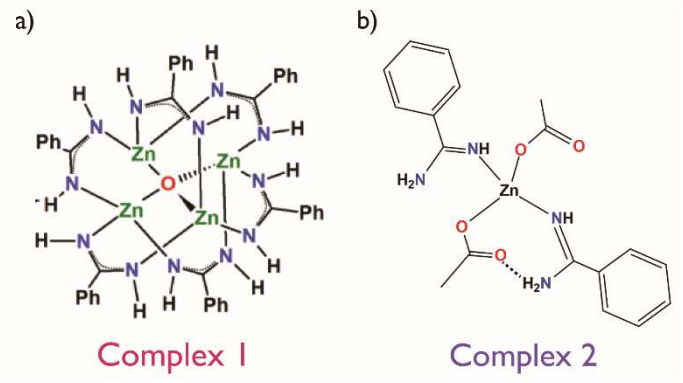

Figure 4-7. Molecular structure of a) Complex 1, and b) Complex 2.

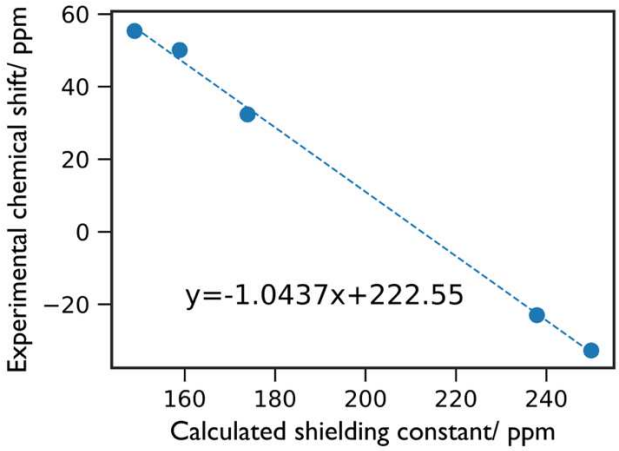

Figure 4-8. Plot of calculated isotropic chemical shielding and the experimental chemical shifts for ^{15}N in Complex 2 and the best linear fit.

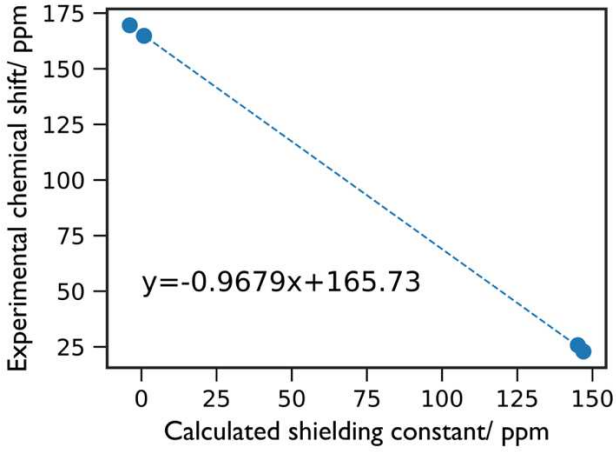

Figure 4-9. Plot of calculated isotropic chemical shielding and the experimental chemical shifts for ^{13}C in Complex 2 and the best linear fit.

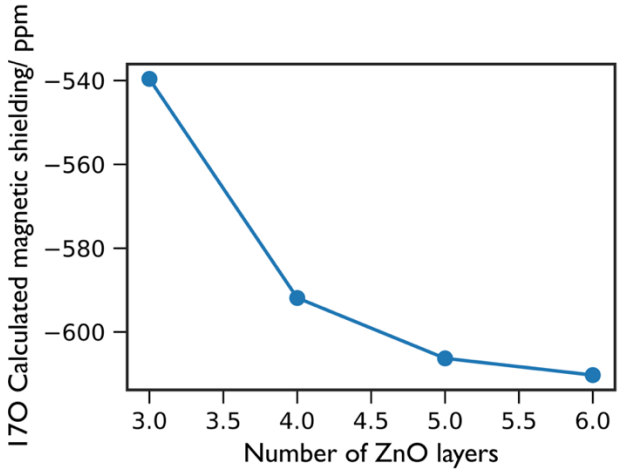

Figure 4-10. Plot of magnetic shielding values of surface hydroxyl ^{17}O as a function of the number of ZnO unit cell layers.

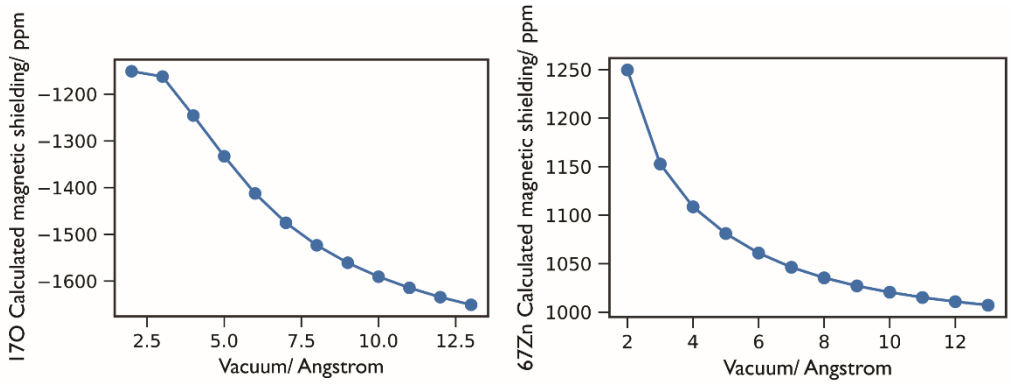

Figure 4-11. Plot of magnetic shielding values of surface ^{17}O and ^{67}Zn as a function of vacuum (Å) between layers of repeating slabs.

Table 4-1. Geometry optimized structures and corresponding calculated chemical shifts.

Entry	Structure	$\delta_{calc}\{^{15}N\}$ (ppm)	$\delta_{calc}\{^{13}C\}$ amidine
1	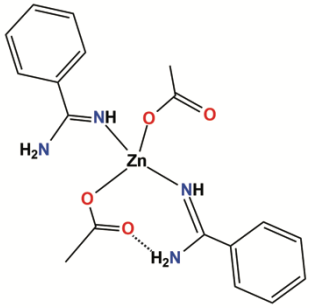 Molecular complex containing neutral ligand	**~145.6 (=NH)** **~99.2 ($-NH_2$)**	**164.9**
2	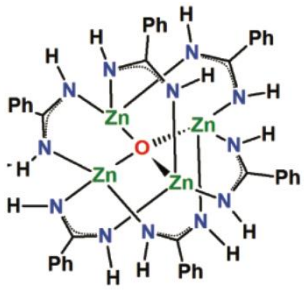 Molecular complex containing anionic ligand	**~130**	**169.4**
3	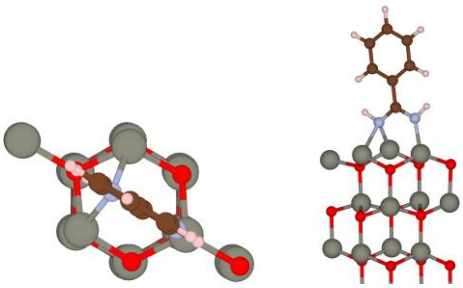	**119.8** **156.18**	**184.0**

4	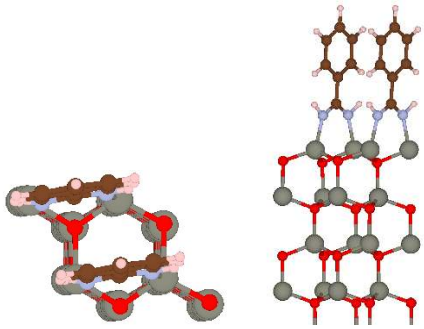	**129.2** **142.1**	**167.1**

4.2.6 Assignment confirmation by ^{15}N labeling of surface ligand

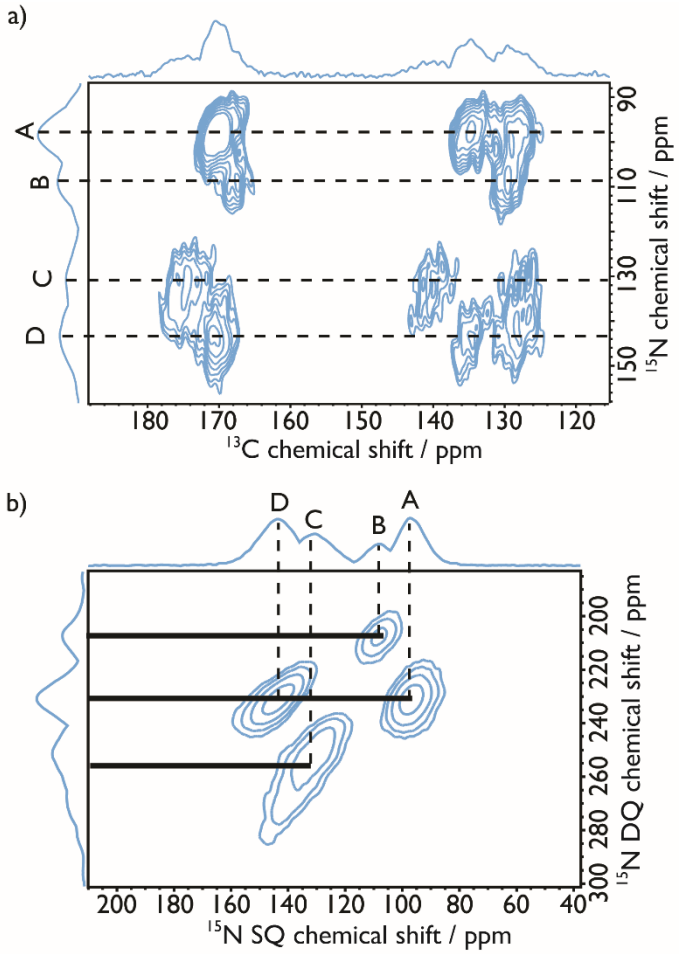

Figure 4-12. a) DNP enhanced ^{13}C-^{15}N TEDOR experiment of ^{15}N- NPL-1 recorded at 10 kHz with a 4 ms mix time, and b) DNP enhanced ^{15}N-^{15}N DQ-SQ dipolar correlation spectrum of ^{15}N- NPL-1 recorded with 24.8 ms mixing time at 13333 Hz and 100 K.

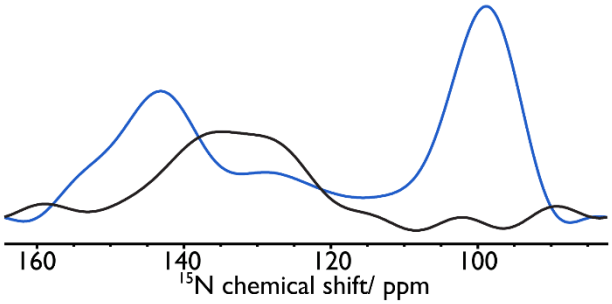

Figure 4-13. ^{15}N cross-sections at $\delta^{13}C$ ~171 ppm and $\delta^{13}C$ ~175 ppm from DNP enhanced ^{13}C-^{15}N TEDOR experiment of ^{15}N-NPL-1. (Figure 4-12, main manuscript)

In order to confirm the assignment done using DFT calculations, the platelets were synthesized with ^{15}N-labeled benzamidine. This labeled ligand was used for the synthesis of ^{15}N-labeled benzamidine capped ZnO NPLs (procedure shown in materials and methods section). The DNP enhanced ^{15}N-^{13}C transferred echo double resonance (TEDOR) experiment, which involves heteronuclear dipolar recoupling, was recorded and the corresponding spectrum for ^{15}N-NPL-1 is shown in Figure 4-12a. The benzamidine present in the NPL system broadly has two kinds of ^{13}C chemical shifts i.e., aromatic $\delta^{13}C$ ~130 ppm and amidine $\delta^{13}C$ ~170 ppm shifts. In the $^{13}C\{^{15}N\}$ TEDOR spectrum (Figure 4-12a), it can be seen that the amidine ^{13}C chemical shift associated with out-of-plane-μ_2 coordination (associated with ^{15}N peak C, $\delta^{13}C$ ~175 ppm) is highest, followed by neutral coordination (associated with ^{15}N peaks A and D, $\delta^{13}C$ ~171 ppm) and finally, the least for anionic in-plane-μ_2 coordination (associated with ^{15}N peak B, $\delta^{13}C$ ~168 ppm). This trend agrees with the calculated ^{13}C chemical shift for the three structures (Figure 4-6 a, b, and d). On the other hand, for aromatic C's, benzene ring being in-plane for anionic in-plane-μ_2 coordination (peak B), leads to a uniform electron density distribution over the entire benzene ring for it and hence the aromatic ipso $\delta^{13}C$ ~130 ppm is very similar to the rest of the aromatic carbons of the ring $\delta^{13}C$ ~130 ppm for this binding mode (Figure 4-12a). Whereas, for the out-of-plane-μ_2 coordination and neutral ligand binding, the ipso $\delta^{13}C$ ~142 ppm and ~136 ppm, respectively, is different from the remaining aromatic carbons with $\delta^{13}C$ ~130 ppm (Figure 4-12a). The calculated benzene ^{13}C chemical shift associated with the various binding modes agrees with the experiment (Figure 4-6). Thus, this observation confirms the assignment for peak B made using DFT calculations.

DNP enhanced ^{15}N homonuclear dipolar correlation experiment (Figure 4-12b) on ^{15}N-NPL-1 confirms that indeed there are only four kinds of nitrogen atoms present in the system. There are two from the neutral ligand, where the amine (peak A) and the imine nitrogen (peak D) cross-correlations on the $(10\bar{1}0)$ facet can be observed, and two auto-correlations from the two distinct forms of anionic ligands associated with peaks B and C on the (0001) facet. The chemical shift of peak C from the anionic out-of-plane-μ_2 form of ligand ranges from 115 ppm to 150 ppm. The higher chemical shifts of this range overlap with peak D, but are indeed higher-shifted peak C auto-correlations, as can be confirmed by overlaying the ^{15}N cross-sections (Figure 4-13) at $\delta^{13}C$ ~171 ppm and $\delta^{13}C$ ~175 ppm from the TEDOR experiment (Figure 4-12a).

4.2.7 Effect of polar protic solvent addition on NPL-1: insight into transition from molecular complexes to NPLs

As mentioned earlier, addition of 1 or 2 equivalents of water to the THF solution of ethyl zinc benzaminate leads to the formation of molecular complex, Complex 1, while the addition of 3 equivalents of water leads to the formation of smallest NPLs, NPL-1. NPL-1 clearly forms hexagonal NPLs as seen in the STEM HAADF image, and these smallest NPLs are the first step in the stage involving transition from molecular complexes to NPLs. Hence it can potentially be interesting to gain information on the growth mechanism of the NPLs. Therefore, the system was studied before performing any post-synthetic treatment, like the addition of solvent like water or methanol. The ^{15}N CPMAS NMR spectrum recorded before and after water addition for ^{15}N-NPL-1 changes from being dominated by peak C (anionic form) to the appearance of peaks A and D (neutral form) corresponding to the neutral form of ligand (Figure 4-14). This change in the spectrum of NPL-1 can be explained by the presence of residual anionic benzamidine on the neutral $(10\bar{1}0)$ facets. Likely due to the lack of addition of sufficient labile protons in the synthesis of NPL-1 (prepared by adding only 3 equivalents of water to the ethylzincbenzaminate complex), some of the anionic ligands on the $(10\bar{1}0)$ facets did not get protonated to form neutral benzamidine on these facets. Thus, the addition of water provides the necessary protons for converting these anionic ligands on the non-polar $(10\bar{1}0)$ facets to their neutral form as seen in Figure 4-14. It must be noted that

this change is observed only for the case of NPL-1 and not for bigger platelets, as they had sufficient water for protonation during synthesis.

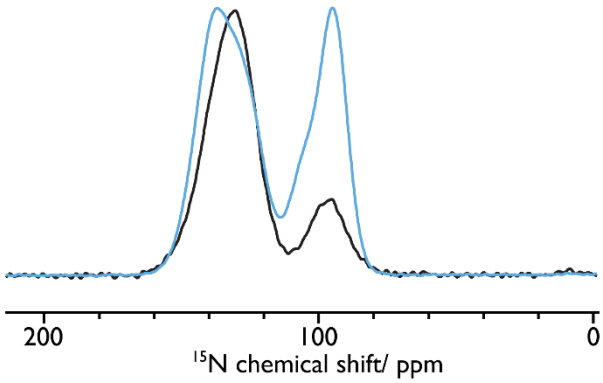

Figure 4-14. {^{1}H-}^{15}N CPMAS NMR spectra of ^{15}N-NPL-1 before any post-synthetic treatment (black) and its comparison to ^{15}N-NPL-1 after addition of water (blue) recorded at low temperature (105 K) with MAS frequency of 12 kHz and 9.4 T.

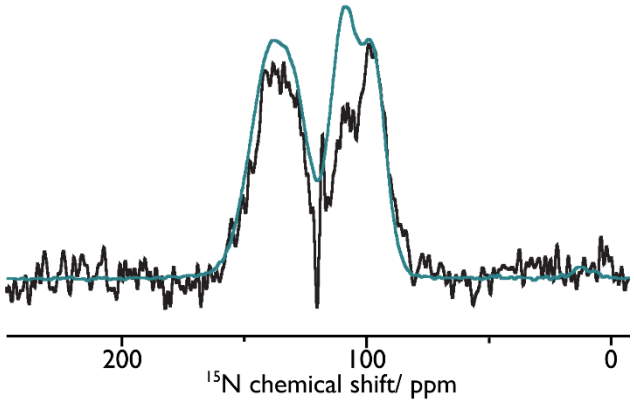

Figure 4-15. {^{1}H-}^{15}N CPMAS NMR spectra of ^{15}N-NPL-8 along with biradical solution recorded with DNP at low temperature (105 K) and its comparison to ^{15}N-NPL-8 before methanol addition recorded at RT at MAS frequency of 12 kHz and 9.4 T.

4.2.8 Presence of neutral ligand on NPL-1 (10$\bar{1}$0) facets: Gauging ligand proximities_on the surface at ^{13}C natural isotopic abundance

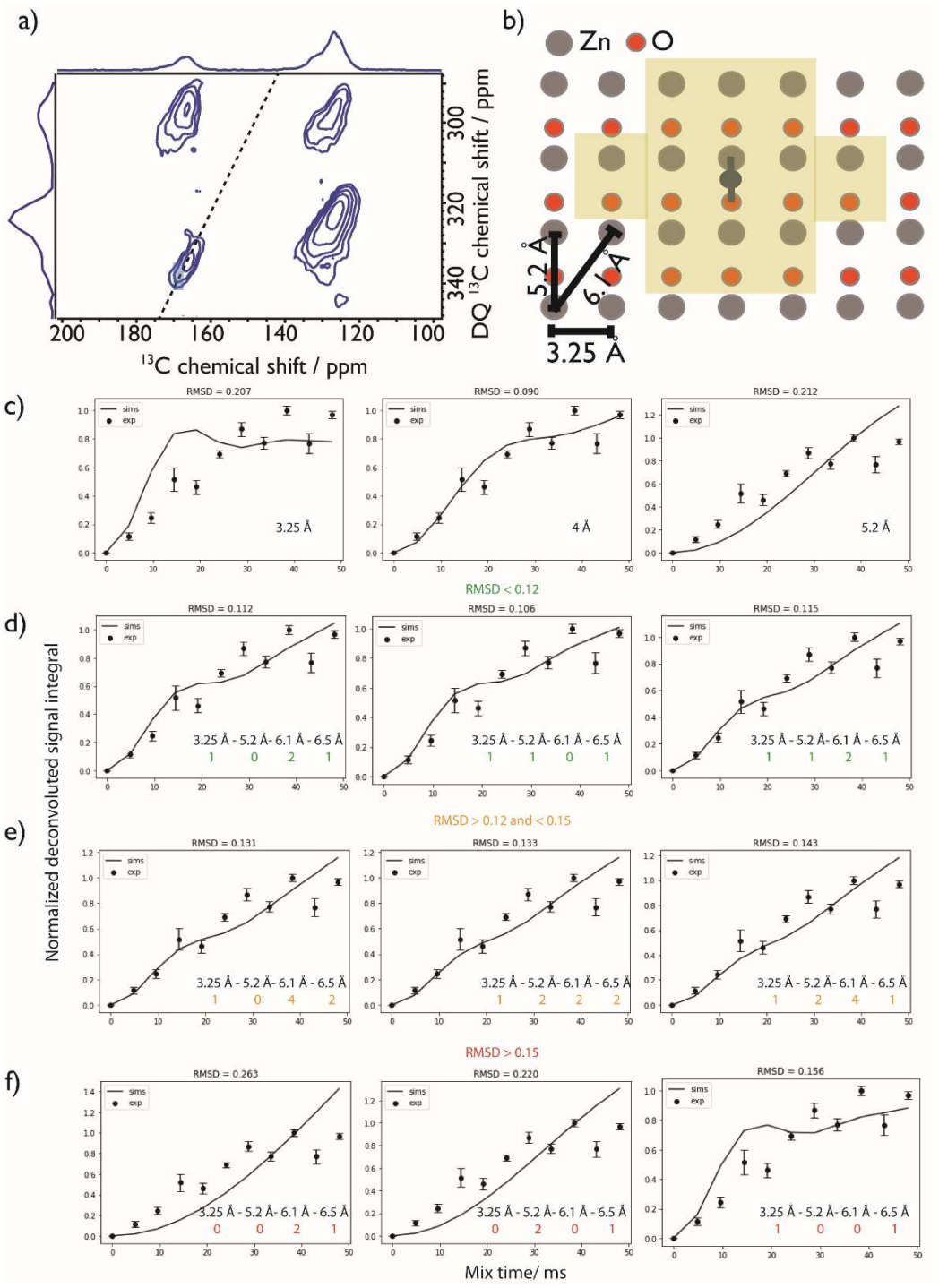

Figure 4-16. a) DNP enhanced ^{13}C DQ-SQ correlation spectrum recorded on NPL-1 with 38.4 ms mixing time at 13333 Hz and 100 K, where the intensity of the region highlighted in blue (amidine ^{13}C-^{13}C auto-

correlation) has been studied as a function of mixing time to obtain distance information. b) shows a schematic top view of the $(10\bar{1}0)$ facets of wurtzite ZnO NPLs where the highlighted (in yellow) region represents the region around the ligand (marked with a black line and dot) accessible for distance measurements, the contributions at further distances are negligible. c), d), e) and f) represent plot of relative intensity to mixing time derived for amidine ^{13}C-^{13}C auto-correlation peak (highlighted in blue) and their fit to spinevolution[156] simulations for c) single distances, combinations with d) RMSD<0.12, e) RMSD values between 0.12 and 0.15, f) RMSD>0.15, respectively, and the relative weights of each contributing distance specified in the plots. Also, RMSD values corresponding to each fit have been mentioned at the top of each figure.

The S_3 DQ-SQ recoupling sequence is used to recouple homonuclear ^{13}C dipolar couplings under MAS and is robust to perform distance measurements for spins with large CSA interactions, like aromatic carbons[107]. The intensity of polarization transfer can be studied as a function of mixing time to extract distance information. Experiments at ^{13}C NA ~1.1% are crucial because the probability of having spin pairs for ^{13}C at NA is ~0.01%. This small probability means that each spin pair is virtually isolated and hence not affected by dipolar truncation and thus in the buildup curves, an average of buildups from each of these isolated spin pairs was observed. Using the signal enhancements provided by DNP, these distance measurements were performed for ^{13}C at 1.1 % NA for the ligands on the $(10\bar{1}0)$ surface of ZnO NPLs. For this particular case, the intensity of the amidine auto-correlation peaks with $\delta\{^{13}C\}$~170 ppm (highlighted in blue, Figure 4-16a) as a function of time was used to get a measure of inter-ligand distances on the surface. Experimental details have been provided in the materials and methods section.

It must be noted that ligands on the surface can only be present at discrete values, as can be seen in Figure 4-16b which shows a schematic of ZnO $(10\bar{1}0)$ surface. The region highlighted in yellow shows the area around the central ligand (marked with a black line and dot) accessible for distance measurements, as the contributions at further distances are negligible. Thus, within the highlighted region there can be a total of 11 ligands present at a distance of 3.25 Å (2), 5.2 Å (2), 6.1 Å (4), and 6.5 Å (2) from the central ligand. Simulated buildups from all the possible distance combinations within the specified yellow region were fit to the experimental data using the least-square fitting method and RMSD's were calculated for each fit. The S3 buildup simulations for the different distances were obtained using Spinevolution[156]. Two S3 experimental datasets were recorded and the obtained buildup were fitted to simulations for all the

possible distance combinations within the specified yellow region. Thus, Table 4-2, shows for the many possible combinations of distances on the $(10\bar{1}0)$ surface, relative weights of each contributing distance and the RMSD for these fits for the two recorded datasets. It was found that both the experimental datasets had similar RMSD values for a particular fit, and hence same best fits were found from both. When the buildup was fit using a single distance, 4 ± 0.5 Å (RMSD=0.09, Figure 4-16c) was found to be the maximum average distance that fits well to the curve. It can be seen in Figure 4-16c that 5.2 Å (RMSD=0.212) and 3.25 Å (RMSD=0.207) fit poorly. Since a dipolar coupling buildup provides an average distance information for all the amidine ^{13}C pairs (~0.011%) in the system, the fact that the average distance is 4 Å shows very close approach between the ligands over-all. This fact re-affirms that the ligands on $(10\bar{1}0)$ facets are indeed placed on the surface of NPLs. In fact, even in Complex 1, a system containing densely packed ligands, the smallest distance between immediate neighboring amidine ^{13}C atoms is 4.5 Å, and thus the average dipolar coupling buildup for amidine C of this system would fit to a distance greater than 4.5 Å. Similarly, in Complex 2 the smallest distance between immediate neighboring amidine ^{13}C atoms is 5.4 Å, and thus the average of the system will be greater than 5.4 Å. Thus, an average distance of 4 Å for the amidine C buildup for NPLs signifies close approach between ligands which can only be possible on the NPL surface. However, since a single distance of 4 Å is not possible on the surface, combinations of distances were fitted to the experimental data, in order to determine a best fit.

Table 4-2. For S3 experimental dataset 1 and 2, RMSD's and relative contributions of each distance corresponding to fits for the various possible distance combinations on the surface of NPLs.

3.2	5.2	6.1	6.5	Data Set 1 RMSD	Data Set 2 RMSD	Total number of ligands
0	0	0	1	0.27	0.28	1
0	0	0	2	0.27	0.28	2
0	0	1	1	0.265	0.274	2
0	0	1	2	0.266	0.275	3
0	0	2	1	0.263	0.272	3
0	0	2	2	0.265	0.274	4
0	0	3	1	0.262	0.271	4
0	0	3	2	0.264	0.272	5
0	0	4	1	0.262	0.271	5
0	0	4	2	0.263	0.272	6
0	1	0	1	0.226	0.229	2
0	1	0	2	0.235	0.239	3
0	1	1	1	0.235	0.24	3
0	1	1	2	0.241	0.246	4
0	1	2	1	0.24	0.246	4
0	1	2	2	0.244	0.25	5
0	1	3	1	0.244	0.25	5
0	1	3	2	0.247	0.253	6
0	1	4	1	0.246	0.252	6
0	1	4	2	0.248	0.255	7
0	2	0	1	0.22	0.222	3
0	2	0	2	0.226	0.229	4
0	2	1	1	0.227	0.23	4
0	2	1	2	0.231	0.235	5
0	2	2	1	0.232	0.235	5
0	2	2	2	0.235	0.24	6
0	2	3	1	0.235	0.24	6
0	2	3	2	0.238	0.243	7
0	2	4	1	0.238	0.243	7
0	2	4	2	0.24	0.246	8
1	0	0	1	0.157	0.169	2
1	0	0	2	0.129	0.136	3
1	0	1	1	0.122	0.128	3
1	0	1	2	0.114	0.117	4
1	0	2	1	0.113	0.114	4
1	0	2	2	0.115	0.115	5

1	0	3	1	0.116	0.115	5
1	0	3	2	0.122	0.121	6
1	0	4	1	0.124	0.122	6
1	0	4	2	0.131	0.13	7
1	1	0	1	0.106	0.106	3
1	1	0	2	0.107	0.105	4
1	1	1	1	0.108	0.105	4
1	1	1	2	0.113	0.11	5
1	1	2	1	0.115	0.112	5
1	1	2	2	0.122	0.119	6
1	1	3	1	0.125	0.121	6
1	1	3	2	0.132	0.129	7
1	1	4	1	0.134	0.131	7
1	1	4	2	0.141	0.138	8
1	2	0	1	0.108	0.102	4
1	2	0	2	0.115	0.11	5
1	2	1	1	0.117	0.112	5
1	2	1	2	0.124	0.12	6
1	2	2	1	0.126	0.122	6
1	2	2	2	0.133	0.129	7
1	2	3	1	0.135	0.131	7
1	2	3	2	0.142	0.139	8
1	2	4	1	0.143	0.14	8
1	2	4	2	0.149	0.147	9

From the analysis of the data based on the possible placement of ligands on the surface, it was found that the plot fits best, i.e., has the lowest RMSD, for a distance combination of at least one 3.25 Å, along with two or three longer distances (some combination of 5.2 Å, 6.1 Å, or 6.5 Å) within the yellow region (Figure 4-16d and Table 4-2) with an RMSD < 0.12. In Figure 4-12e, it can be seen that combination of 3.25 Å along with 6 or 7 longer distances have RMSD between 0.12 and 0.15. TGA data suggests 5 ligands/nm^2 on the $(10\bar{1}0)$ facets which means ~7 ligands in the highlighted yellow region. Thus, from the fits and the TGA data, it can be concluded that on average within the highlighted region every central ligand has one 3.25 Å, along with some combination of five distances among 5.2, 6.1 and 6.5 Å present on the $(10\bar{1}0)$ facets of ZnO NPLs.

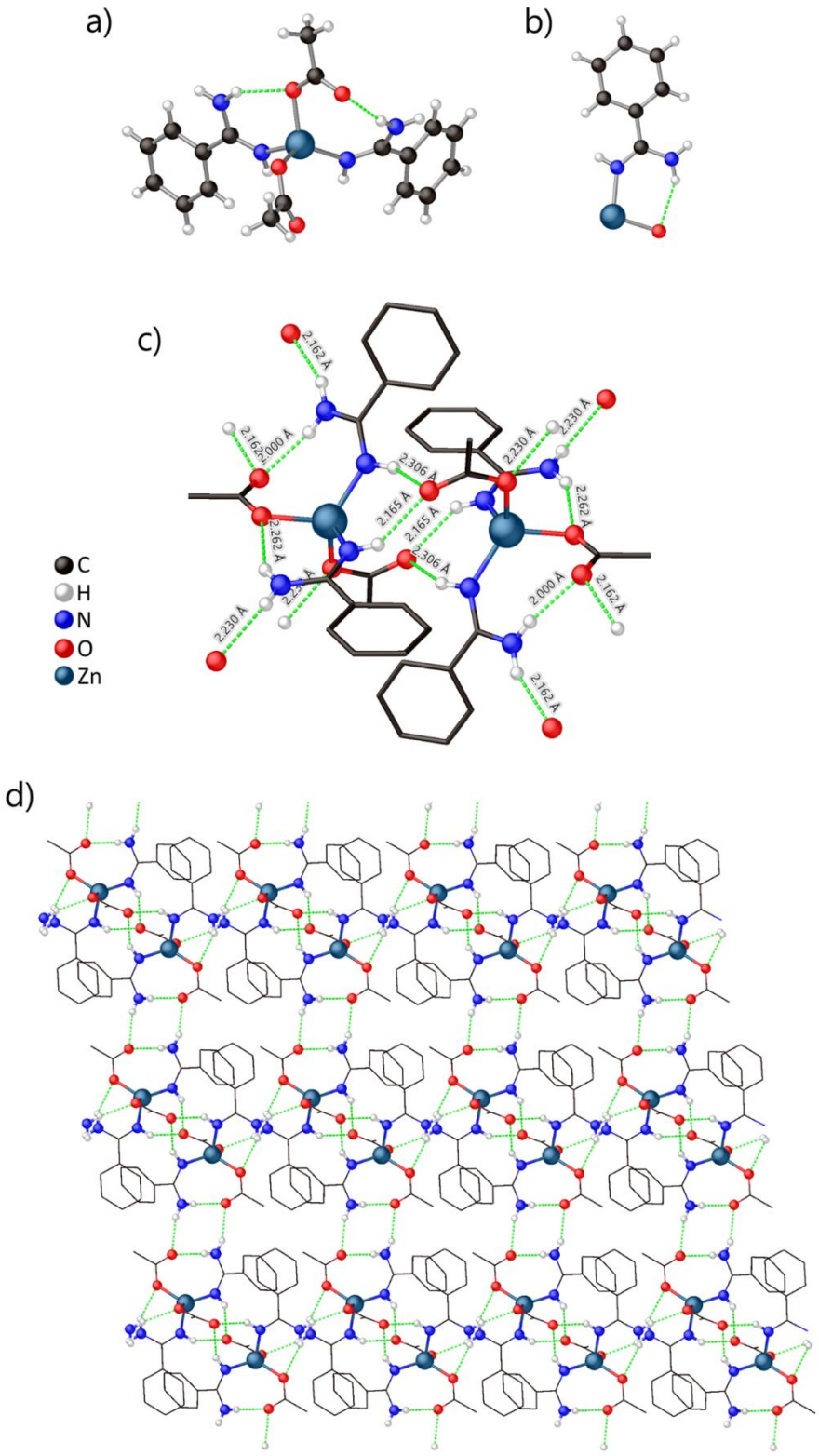

Figure 4-17. Molecular structure (a) and bza-H coordination mode (b) in Complex **2**. H-bond mediated dimers (c) and 2D supramolecular layers (d) of Complex **2**.

4.2.9 Insight into the role of ligand in the growth of NPLs

The morphology of ZnO NPLs clearly indicates the role of anionic benzamidine in capping the (0001) facet and thus propagating growth along the basal plane. Moreover, the likely presence of Zn capped $(000\bar{1})$ facets, as shown above using the HAADF STEM images of the sides complemented with the TGA data, further indicates that the Zn-ligand bond is strong and hence caps even the $(000\bar{1})$ facet where it is not expected. However, the role of neutral benzamidine ligands in the growth of the NPLs is not clear. The effect of solvent addition on the smallest platelets NPL-1 sheds light on this. The addition of water changes the anionic form of the ligand to the neutral form for the smallest platelets NPL-1. The fact that these neutral ligands are actually present on the $(10\bar{1}0)$ facets and not in the form of some complex is supported by the distance measurements. From this observation, it can be concluded that the neutral form of ligand was not present when the NPLs had formed (as evidenced from HAADF STEM images of NPL-1). Thus, the neutral form of the ligand does not actively participate in directing the morphology of the NPLs.

4.3 Conclusion

The ultra-thin ZnO NPLs synthesized by OSSOM-II approach, a modified version of the OSSOM approach, were analyzed in detail. The HAADF STEM images of the side of the NPLs suggested the presence of Zn terminated $(000\bar{1})$ facets using. Moreover, the organic-inorganic interface of these materials was studied using DNP enhanced ssNMR complemented with DFT calculations to unravel the ligand binding and arrangement on the two facets present in the ZnO NPL morphology. The $(10\bar{1}0)$ non-polar facets are stabilized by the neutral form of the ligand with the =N bound to the Zn and the NH_2 protons involved in hydrogen-bonding to the oxygen from the surface. Also, insights into the arrangement of ligands on the $(10\bar{1}0)$ non-polar have been provided, showing ~66% surface coverage, close-packing, and long-term ligand stability. The polar 0001 facets have an anionic in-plane-μ_2 coordination and angular binding modes stabilizing the surface. The observations in this work provided insights into the role of ligands in the growth of these NPLs. Thus, this study provides an overall

view of the interface of these materials, and will thus help facilitate the future chemistry of stable designer nano-objects.

4.4 Materials and methods

4.4.1 DNP NMR spectroscopy

The experiments were performed on a Bruker DNP-SSNMR AVANCE III 9.4 T 400 MHz spectrometer equipped with a gyrotron and transmission line capable of providing ~5 W of 264 GHz microwave irradiation at the sample. These experiments were performed on a low-temperature 3.2 mm MAS probe at sample temperatures of ~105 K or at RT, as stated in the corresponding figure caption. Experiments were acquired using ^{1}H $\pi/2$ pulses of 100 kHz, ^{13}C $\pi/2$ pulses of 50 kHz, ^{15}N $\pi/2$ pulses of ~40 kHz, ^{15}N and ^{13}C CP spin-locking at ~40 kHz and ~50 kHz, respectively. 100 kHz of SPINAL-64 heteronuclear ^{1}H decoupling was used throughout the 10 and 15 ms signal detection periods for ^{13}C and ^{15}N CP experiments, respectively, with direct spectral widths of 40 kHz. These low temperature (~105 K) experiments used optimized experimental repetition delays of 3.4 s, 1.5 s, 3 s and 3.7 s for NPL-1,2,3,8, respectively. CP times and ramp corresponding to DNP-enhanced {^{1}H-}^{15}N CPMAS NMR spectra with ^{15}N spin-locking at ~40 kHz is 3 ms with corresponding ramped (80-100%) ^{1}H CP at ~60 kHz for NPL-1 and 8.

S3 experimental details

Experiments were performed at a spinning speed of 13.333 kHz, and spectra were recorded with 10 sampling points between 4.8 to 48.001 ms of recoupling times. Two sets of data were recorded to ensure the reproducibility of the build-up curves. Each point in the buildup curve was recorded as 2D in 6 hours. The correlation spectrum peak intensity of the correlation along the diagonal for amidine carbon (highlighted in blue, Figure 4-16 a) was used to analyze benzamidine/ benzamidinate ligand placement on the ZnO surface. The amidine peak contains ligands majorly from the $(10\bar{1}0)$ facets, as the intensity of the peaks from (0001) facet is not strong enough for distance measurements. After deconvolution based on the ^{13}C chemical shift range of neutral

ligand (derived from X-TEDOR experiment), the intensity of this correlation peak at each recoupling time was plotted against the recoupling time to obtain a plot characteristic of the distances between ligands on the $(10\bar{1}0)$ facet.

4.4.2 ^{15}N labelling

A suspension of $PhC(OMe)NH_2^+Cl^-$ (prepared by the Pinner reaction of benzonitrile with HCl and methanol in ether solvent) in water and ether was stirred, and $NaHCO_3$ was added to it in small portions. When carbon dioxide evolution stopped, the solvent was removed using a rotary evaporator. The residue was distilled to give $PhC(NH)OCH_3$. A solution of this in methanol was stirred, and $^{15}NH_4Cl$ was added. The mixture was heated at 46 ℃ for 6 hours, and the methanol solvent was removed. The solid was dried under vacuum and collected to give ^{15}N labeled benzamidine hydrochloride (one ^{15}N per molecule on average).

Chapter 5
Mixed Ligand Shell Nanoparticles

5.1 Introduction

5.1.1 Mixed ligand shell nanoparticles

Mixed ligand shells on nanoparticles (NPs) have been extensively studied as these are found to improve NP properties such as solubility[233], catalysis[234], and cation capturing ability[235] and are useful in bio-applications such as drug delivery or targeted therapies[236,237]. However, characterization of the ligand shell of these NPs is still an evolving area of research. Several techniques have attempted to characterize the surface of mixed ligand shell NPs, each with its strengths and shortcomings. A review by Ong et al. [238] describes these aspects in detail for the various microscopy, spectroscopy, and simulation techniques used for mixed-ligand shell characterization. Figure 5-1 shows the various possible ligand morphologies on the surface of NPs. In particular, microscopy techniques such as the scanning tunneling microscope (STM)[239] and cryogenic transmission electron microscopy (cryo-TEM)[240] have been previously used to characterize mixed-ligand shells. However, these techniques can be used to characterize only a few kinds of systems and the sample preparation and image interpretation are not straightforward. Spectroscopy techniques such as nuclear magnetic resonance (NMR)[241,242] and mass spectrometry[243] have also been used for this purpose. For example, Liu et al.[241] exploited the sensitivity of ^{1}H NMR shifts to their surrounding environment and showed that the change in ^{1}H chemical shift with percentage ligand shell composition is characteristic of the ligand shell morphology. However, the use of this method is limited by the kind of ligands used for the ligand

shell. In the work mentioned above, two ligands, one aromatic-based and one aliphatic, were present in the ligand shell. Thus, the two ligands had sufficiently different chemical shifts, and hence the changes in ^{1}H chemical shifts could be observed directly. Moreover, the presented method requires comparing several different relative concentrations in the ligand shell and assumes that the ligand shell morphology remains the same despite the change in relative ligand concentrations.

To date, several strategies have been presented to characterize the ligand shell on mixed-ligand shell NPs[238,240,241,244]. However, a universal or fairly standard method to characterize the ligand shell morphology for a mixture of ligands, which can either arrange randomly or form random[245], striped[246], patches[247] and Janus[248,249] morphologies, remains elusive. While most of the studies mentioned above have been performed on gold NPs, in this work, the ligand shell morphology on the surface of ZnO NPs was characterized using dynamic nuclear polarization (DNP)-enhanced solid-state NMR (ssNMR). A method is presented to quantify the percentage of X ligands in the vicinity of Y for an X-Y mixed ligand shell on the surface of ZnO NPs prepared by an organometallic approach. A first quantitative use of the widely used transferred echo double resonance (TEDOR) heteronuclear dipolar recoupling pulse sequence[250,251] to characterize the ligand shell of mixed-ligand NPs. This approach is illustrated on ligand shells on the surface of ZnO NPs, which include three samples containing two ligands, specifically, di-phenyl phosphate (DPP) in combination with hexanoate (HA), phenyl acetate (PhAA), and phenyl propanoate (PhPAA). The enhancements provided by DNP allow the acquisition of these experiments at natural isotopic abundance (NA). A strength of this method is that the characterization of a single ligand mixture (i.e, sample containing only one relative concentration) is sufficient to determine the percentage proximity between hetero-ligands.

5.1.2 The strategy

In order to obtain information about the surface ligand morphology of mixed ligand NPs, the following aspects about the ligand shell need to be known: 1) the relative ratio of the two ligands, say ligand A and B, present on the surface; 2) for various possible ligand morphologies, the % boundary between the hetero-ligands; 3) for ligand A, an

estimation of the percentage of neighboring ligand A and B; 4) for ligand B, an estimation of neighboring ligand A and B. These details about homoligand and hetero-ligand proximities can be used to map the ligand shell morphology. To obtain this information, the following experiments can be performed:

1) The relative amounts of the two ligands, say A and B, present on the surface of the NPs, can be obtained using quantitative NMR experiments like the quantitative multiple cross-polarization (multiCP) experiment by Schmidt-Rohr and co-workers[252]. If the two ligands possess sufficiently well resolved ^{1}H chemical shifts, quantitative information can be extracted from the ^{1}H NMR spectrum as well.

2) The size of NPs can be obtained from TEM or PXRD experiments. Subsequently, the relative ratio of two ligands i.e., the % of hetero-ligands in the vicinity to each other which is different for the various ligand morphologies (random, striped, patches, or Janus) (***Figure*** 5-1) can be estimated theoretically.

3) Recording heteronuclear dipolar correlation experiments such as TEDOR experiments to obtain the percentage of hetero-ligand A present next to ligand B. Comparing this to the theoretical percentage vicinity for each ligand shell morphology as calculated in Step 2) can lead to a better understanding of the ligand shell morphology.

4) Furthermore, additional information about homoligand proximities can help provide a complete picture of the mixed ligand shell. To do this, homonuclear dipolar recoupling experiments can be performed.

Based on the relative amount of the two ligands and the size of the NPs, the expected percentage of hetero-ligands in the vicinity with one another can be determined for the various kinds of ligand morphologies, which include random, striped, patches, and Janus, as shown in Figure 5-1. For equal amounts of both kinds of ligands, the percentage of A ligands in vicinity to B ligands are close to 10% for Janus, 100% for random and between 10 to 100% for patched and striped ligand morphologies, respectively. Hence, from the measurement of % heteroligand proximity it is difficult to differentiate between the patched and striped domains. For the system under study

in this work, the amount of DPP ligands in the vicinity with hetero-ligands (PhAA/PhPAA/HA) will be determined, and the obtained value will be compared to the expected theoretical value for each ligand shell morphology. Hence the ligand shell morphology can be determined.

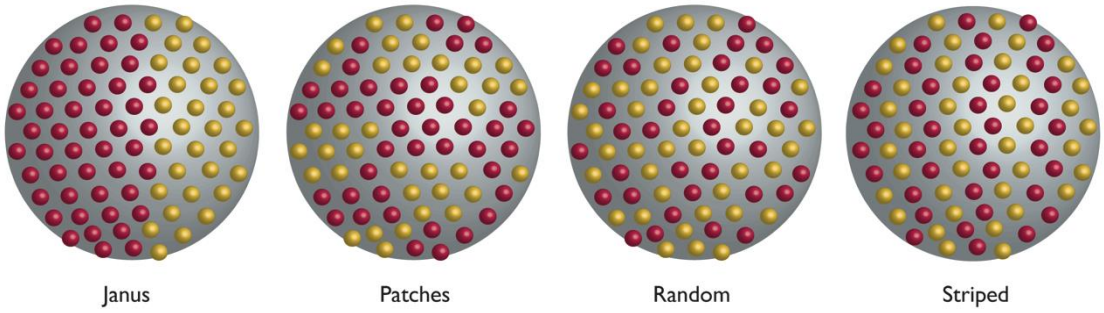

Figure 5-1. Ligand morphologies on the surface of NPs, including Janus, Patches, Random, and Striped.

Now, to determine proximities between the two kinds of ligands, in this case, phosphate-based (DPP) and carboxylate based (COO-) ligands in the system, ^{31}P-^{13}C dipolar recoupling experiments were performed using the heteronuclear dipolar recoupling sequence TEDOR, depicted in Figure 5-2. This sequence can be used to obtain the distance between hetero-atoms in the vicinity of each other through dipolar coupling measurements. Another closely related pulse sequence that could have possibly been used in this work was the rotational-echo double-resonance (REDOR) pulse sequence. However, in REDOR, experiments with and without REDOR pulses need to be recorded and thus the experimental times are twice as long. Therefore, in this work, ^{13}C{^{31}P} TEDOR experiments were performed. The ^{31}P atom is present only on one of the ligands, i.e., DPP, while ^{13}C atoms are present on both DPP and the carboxylate-based ligands (PhAA/PhPAA/HA). In the ^{13}C{^{31}P} TEDOR experiments described here-in, any NMR peaks that appear corresponding to the carboxylate-based hetero-ligands correspond to those present in the direct vicinity with DPP ligands.

In the case of the system described herein, the pulse sequence involves creating transverse ^{13}C magnetization using CP, followed by its evolution into antiphase ^{13}C coherence with respect to ^{31}P for a time period $t_{mix}/2$. The two pairs of 90° pulses on ^{13}C and ^{31}P channels transfer this antiphase ^{13}C magnetization to ^{31}P and back to ^{13}C, labeled in t_1 with ^{31}P chemical shifts. Application of a second REDOR sequence

reconverts this antiphase ^{13}C magnetization to observable in-phase ^{13}C magnetization, subsequently labeled in ^{13}C chemical shifts in t_2. Thus, at the end of each TEDOR sequence, for each crystallite in powder sample, a cross-peak intensity modulated as a function of mixing time, t_{mix}, as $\sin^2(\omega t_{mix}/2)$ was obtained, where ω is the dipolar coupling between ^{13}C and ^{31}P. Moreover, the applied phase cycling removes all coherences which contain only ^{13}C-spin operators after the first REDOR mixing period and only terms that depend on transverse ^{31}P spin operators are kept. Thus, in the $^{13}C\{^{31}P\}$ TEDOR experiments, any signal that appears corresponding to the carboxylate-based hetero-ligands comes from the ligands present in direct vicinity to the ^{31}P containing DPP ligands.

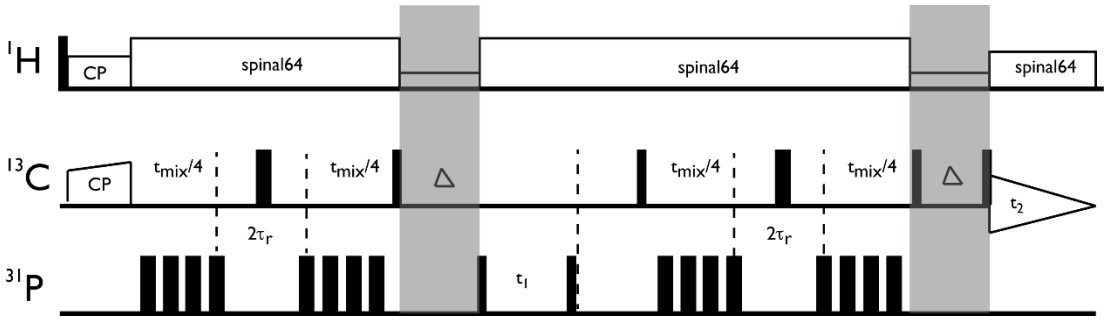

Figure 5-2. z-filtered TEDOR pulse sequence. Narrow and wide solid rectangles represent π/2 and π pulses, respectively. During REDOR, two π pulses per rotor period are applied on the ^{31}P channel and phase cycled according to the xy-4 scheme.

The enhancements provided by DNP allow the acquisition of these experiments at NA. The advantages of performing experiments at NA have been described in Chapter 1. At NA, ^{31}P is 100% abundant while ^{13}C is 1.1%. Thus, in $^{13}C\{^{31}P\}$ TEDOR experiments performed in this work, spin systems consisted of one ^{13}C atom surrounded by multiple ^{31}P atoms.

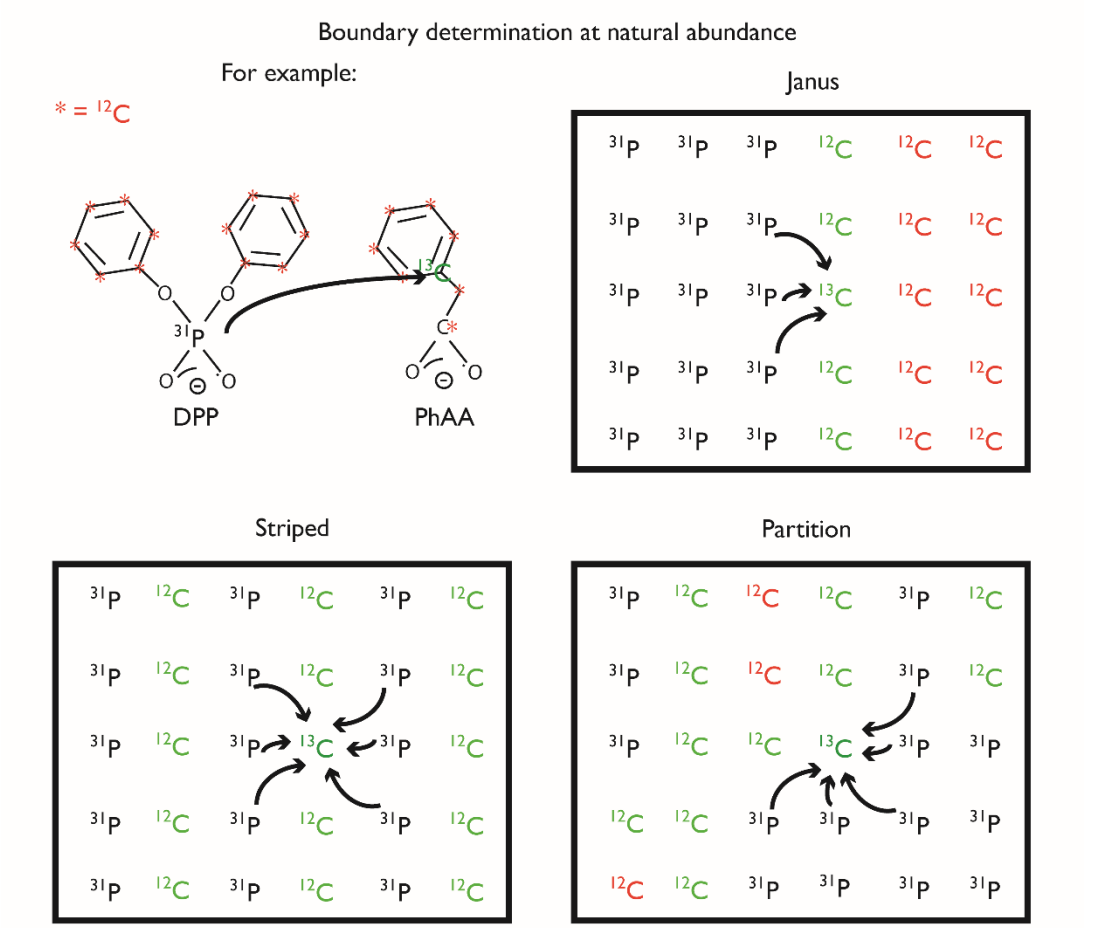

Figure 5-3. Schematic showing ligand distribution for Janus, striped and patched morphologies. The ^{31}P highlighted in the figure corresponds to the DPP ligand, while the $^{13}C/^{12}C$ represent carboxylate hetero-ligands. The green and red $^{13}C/^{12}C$ represent hetero-ligands present in vicinity to and farther from DPP ligands, respectively. In each case, schematic of polarization transfer at NA from ^{31}P to ^{13}C has been depicted.

The case in which multiple DPP ligands surround a carboxylate-based hetero-ligand (PhAA/PhPAA/HA) is analogous to a spin system with a single ^{13}C surrounded by multiple ^{31}P simultaneously transferring their polarization. Schematic representation of this transfer for the various possible ligand morphologies is shown in Figure 5-3. $^{13}C\{^{31}P\}$ TEDOR would give signal corresponding to carboxylate-based hetero-ligands that are present in direct vicinity with DPP ligands. Thus, the boundary between the hetero-ligands can be tracked via $^{13}C\{^{31}P\}$ TEDOR. Similarly, for the case of multiple DPP bundled together, if the DPP ipso ^{13}C buildup is tracked, then it forms a spin system with one ^{13}C in the presence of one ^{31}P at ~2.6 Å (intra-ligand) and other ^{31}Ps at longer distances (inter-ligand) from surrounding DPP ligands. The presence of multiple nuclei transferring polarization to a single nucleus can be understood using

equations 5.1.1 and 5.1.2. For N_i ^{31}P nuclei transferring polarization to a single ^{13}C of type *i*, the equation describing this polarization transfer can be written as follows[106]:

$$V_{i1}(t_{mix}) = \Lambda_i(1 - [\mathrm{J}_0(\sqrt{2}\mathrm{D}_{i1}\mathrm{t}_{mix})]^2)\prod_{k=2}^{N_i}(1 + [\mathrm{J}_0(\sqrt{2}\mathrm{D}_{ik}\mathrm{t}_{mix})]^2)$$

$$V_{i2}(t_{mix}) = \Lambda_i(1 - [\mathrm{J}_0(\sqrt{2}\mathrm{D}_{i2}\mathrm{t}_{mix})]^2)\prod_{k=2}^{N_i}(1 + [\mathrm{J}_0(\sqrt{2}\mathrm{D}_{ik}\mathrm{t}_{mix})]^2)$$

.

.

.

$$V_{iN_i}(t_{mix}) = \Lambda_i(1 - \left[\mathrm{J}_0\left((\sqrt{2}\mathrm{D}_{iN_i}\mathrm{t}_{mix}\right)\right]^2)\prod_{k=2}^{N_i}(1 + [\mathrm{J}_0(\sqrt{2}\mathrm{D}_{ik}\mathrm{t}_{mix})]^2) \qquad \textbf{5.1.1}$$

In this equation, Λ_i is given by:

$$\Lambda_i = \frac{1}{2^{N_i}}\mathrm{V}_i(0)\lambda_i \exp(-\Gamma_i \mathrm{t}_{mix}) \qquad \textbf{5.1.2}$$

$\mathrm{D_{i1}}$ is the dipolar coupling between ^{13}C of type *i* and the 1st ^{31}P among N_i ^{31}Ps surrounding this carbon in these equations. $\mathrm{V}_i(0)$ is the reference cross-polarization intensity, λ_i is the amplitude scaling factor, and Γ is the transverse relaxation rate for the ^{13}C site being analyzed. In this work, using the TEDOR pulse sequence, a method is presented to quantify the boundary between hetero-ligands in mixed ligand shell NPs.

5.2 Synthesis and core structure analysis

5.2.1 General synthesis of mixed ligand shell ZnO NPs using modified OSSOM approach

Model mixed-ligand shell ZnO NPs were prepared according to the modified one-pot two-step OSSOM approach. In a general synthesis, 0.5 mmol of DPP (0.125 g) and 0.5 mmol of selected carboxylic acid (i.e., 68 mg of phenylacetic acid; 75 mg of phenylpropanoic acid and 58 mg of hexanoic acid, respectively) were dissolved in THF (10 mL) and the solution was cooled to -78°C under N_2 atmosphere. $ZnEt_2$ (0.5 mL of a 2 M solution in hexane, 1 mmol) was then added dropwise under vigorous stirring. After a few minutes, the reaction mixture was allowed to gradually warm to room temperature (RT) and stirred for an additional 6 h. In the second step, the resulting reaction mixture was exposed to air to initiate transformations toward ZnO NPs and stirred for an additional 5-7 days at an ambient temperature. Subsequently, the liquid residual was evaporated in vacuo. Then the NPs were redispersed in THF and were precipitated using hexane, centrifuged, and washed again with hexane.

While this method worked for ZnO-DPP-PhAA and ZnO-DPP-PhPAA, the desired result was not obtained for HA. Thus, for ZnO-DPP-HA, the respective ethylzinc derivatives of DPP and HA were prepared separately and eventually mixed.

5.2.2 Transmission electron microscopy (TEM)

The TEM images in Figure 5-4 show that the synthesized NPs in ZnO-DPP and ZnO-DPP-HA samples have a ~5 nm diameter.

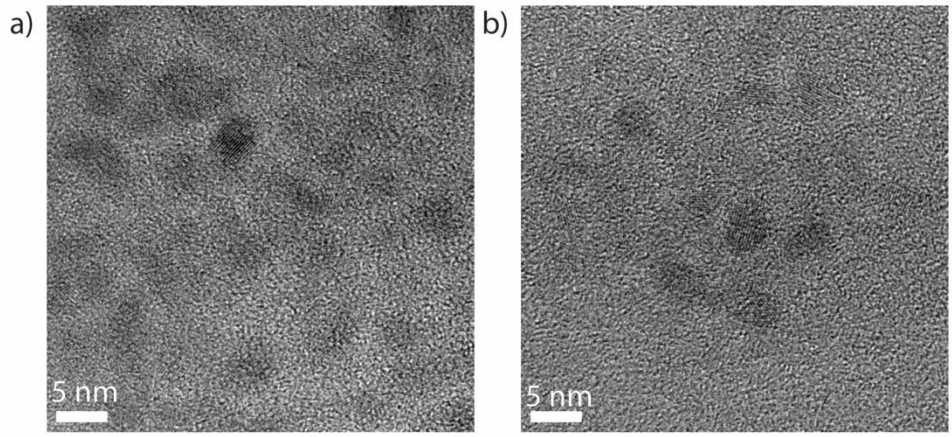

Figure 5-4 TEM image of a) ZnO-DPP and b) ZnO-DPP-HA

5.3 Spectral assignment and an initial understanding of the ligand-shell

5.3.1 ^{13}C and ^{31}P peak assignment

The $\{^1H\text{-}\}^{13}C$ and $\{^1H\text{-}\}^{31}P$ cross polarization magic angle spinning (CPMAS) NMR experiments were recorded at RT, 100 K, and at 105 K under DNP conditions. The corresponding spectra and assignments for samples ZnO-DPP-PhAA, ZnO-DPP-PhPAA, and ZnO-DPP-HA, are shown in Figure 5-5. 10 mM AsympolPOK[253] solution in 6:3:1 d_8-glycerol:D_2O:H_2O was used for the DNP experiments, and $\varepsilon_{on/off}$ ~10 was obtained for all samples.

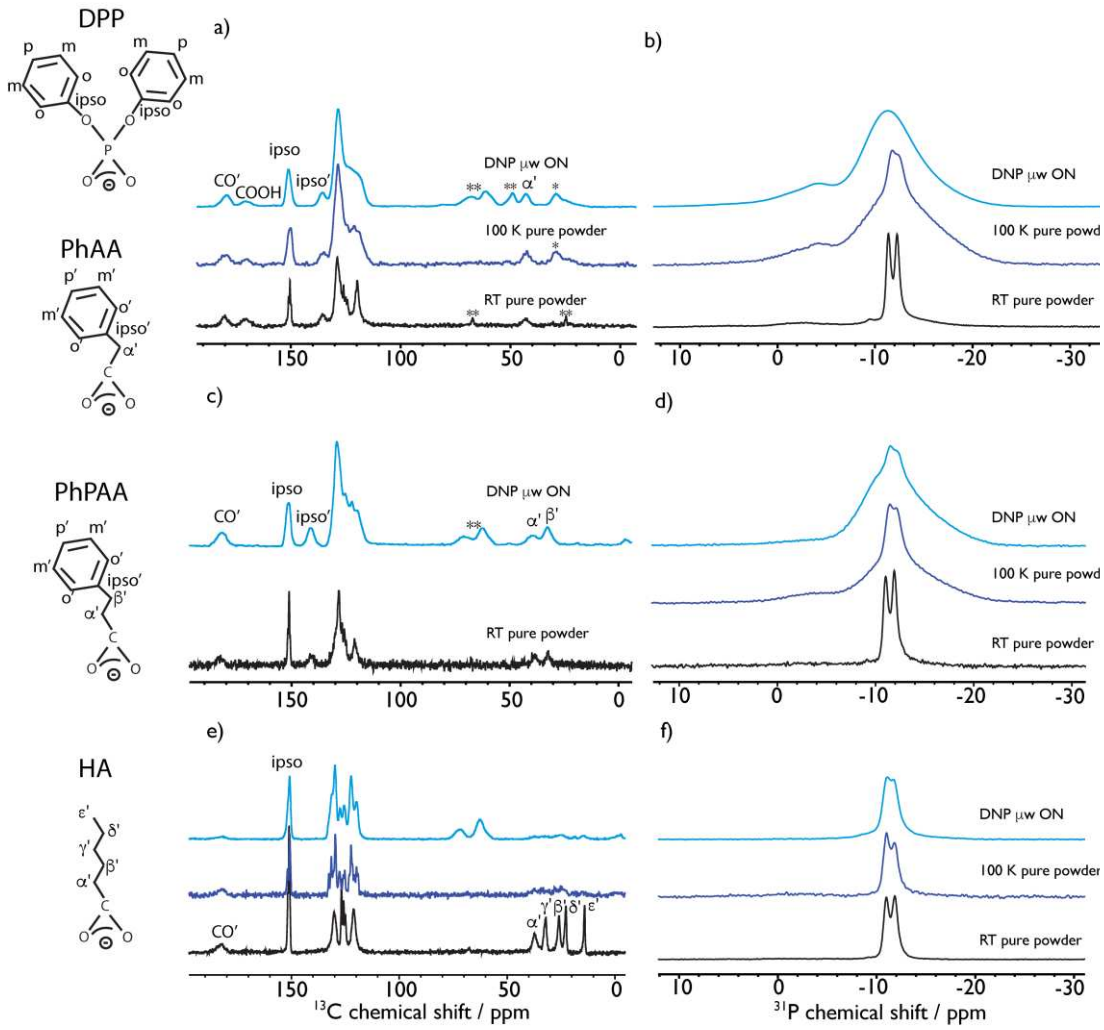

Figure 5-5. {^{1}H-}^{13}C CPMAS NMR and {^{1}H-}^{31}P CPMAS NMR spectra of ZnO NPs capped by DPP-PhAA (a, b), DPP- PhPAA (c, d), and DPP-HA (e, f) recorded at RT, 100K and under DNP conditions at 100 K. Experiments were performed at a MAS frequency of 20 kHz for pure powder at RT and 10 kHz for pure powder at 100 K and for the sample under DNP conditions. Also, the chemical structures of DPP, PhAA, PhPAA, and HA are shown, and also the assignment of ^{13}C peaks has been shown. These are 180 ppm carboxylate species, 151 ppm DPP ipso carbon, 115-140 ppm o- m- p- C of DPP and carboxylate ligands and ipso C of carboxylate ligands, peaks in 0-50 ppm range have been assigned to aliphatic C atoms.

Free DPP-H has $\delta^{31}P \sim -10$ ppm[31], free DPP^{-} anion has $\delta^{31}P \sim -9$ ppm[254], while DPP-R has $\delta^{31}P \sim -11.6$ ppm[255]. On the other hand, DPP^{-} anion bound to dimetallic species experiences shielding compared to free DPP^{-} anion with $\delta^{31}P \sim -9$ ppm, and generally have $\delta^{31}P$ lower than -11 ppm[254,256]. {^{1}H-}^{31}P CPMAS NMR spectra for all three samples at RT show two peaks, at $\delta^{31}P \sim -11$ and ~ -12 ppm, similar to mono-ligand DPP stabilized ZnO (ZnO-DPP), which correspond to μ_2 and μ_3 coordination modes of ligand on the NP surface, as seen in Chapter 2. Thus, the $\delta^{31}P$ chemical shifts obtained

for ZnO-DPP-X samples (X=PhAA/PhPAA/HA) indicate that the DPP^- is Zn-bound, as discussed earlier.

As shown in Figure 5-5, the DPP ligand has ^{13}C peaks only in the aromatic region, both PhAA and PhPAA in aliphatic, aromatic, and carboxylate regions, and HA in aliphatic and carboxylate regions. $\{^1H\text{-}\}^{13}C$ CPMAS NMR spectra for all three samples show characteristic well separated DPP ipso ^{13}C peaks at $\delta^{13}C$ ~151 ppm. The ipso ^{13}C peaks for PhAA and PhPAA appear at $\delta^{13}C$ ~135 ppm and 141 ppm, respectively. The rest of the aromatic ^{13}C peaks for DPP, PhAA, and PhPAA appear in the 115-135 ppm range and hence are convoluted in the spectrum of ZnO-DPP-PhAA and ZnO-DPP-PhPAA samples. On the other hand, the spectrum of ZnO-DPP-HA is well resolved, as DPP and HA do not have any overlapping peak regions. In the region where carboxylate peaks are expected, i.e., greater than $\delta^{13}C$ ~ 160 ppm, for all three samples, a peak at $\delta^{13}C$ ~ 182 ppm is observed; however, for the case of ZnO-DPP-PhAA, an extra peak at $\delta^{13}C$ ~ 170 ppm is seen. To understand the origin of this peak at 170 ppm, a DNP-enhanced 2D $^1H\text{-}^{13}C$ heteronuclear dipolar correlation experiment with 1 ms mixing time was performed, and the spectrum is shown in Figure 5-6. It can be seen that the carboxyl species at $\delta^{13}C$ ~ 170 ppm has correlation peaks to ^1H at 8.7 ppm, whereas $\delta^{13}C$ ~ 182 ppm has correlations to δ ^1H ~3.7 ppm from PhAA aliphatic groups. This shows that $\delta^{13}C$ ~ 170 ppm is a -COOH group.

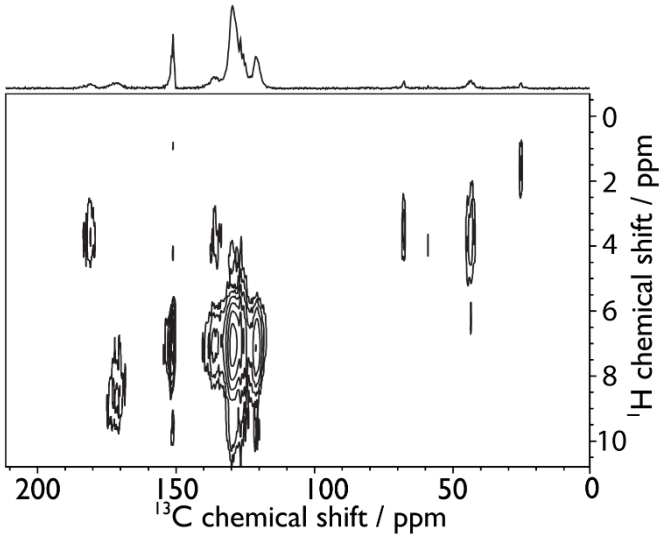

Figure 5-6. DNP-enhanced 2D $^1H\text{-}^{13}C$ FSLG-HETCOR NMR spectrum of ZnO-DPP-PhAA, recorded at ~105 K.

5.3.2 Comparison between RT, 100 K, and DNP-NMR spectra

The appearance of narrow peaks in the ^{13}C spectrum can result from ligand dynamics in a regime that does not interfere with proton decoupling or a well-organized structure like pi-stacking. In the case of dynamics in a regime that does not interfere with decoupling, lower temperatures broaden the peaks significantly due to freezing of the ligand in various conformations, leading to a distribution in chemical shifts. In the case of pi-stacking, the peaks would not change significantly due to a "crystalline" structure of the ligands. In this section, the changes in the ^{13}C and ^{31}P spectra observed upon cooling have been analyzed and explained. A further study is still required to confirm the preliminary conclusions. Comparing samples at RT and 100 K, as in Figure 5-5, it was observed that changes in DPP in ZnO-DPP-HA were similar to changes observed in the mono-ligand stabilized ZnO-DPP sample as seen in Chapter 2. For these samples, the ^{31}P spectrum does not change at 100 K or at 100 K with radical solution (required for DNP). However, some changes are observed in the ^{13}C spectrum. Figure 5-5e shows a comparison of the $\{^{1}H\text{-}\}^{13}C$ CPMAS NMR spectrum of ZnO-DPP-HA at RT, 100K and at 100 K with radical solution. For ZnO-DPP-HA, at RT, other than the characteristic ipso DPP peak at $\delta^{13}C$ ~151 ppm, three well-resolved peaks of approximately the same intensity are observed. These peaks could be a result of benzene ring flips at RT. Whereas at 100 K, for ^{13}C peaks, the appearance of resolved features is observed, consistent with the population of a favored structure, possibly through the formation of pi-stackings. However, the lower temperature does not affect the ^{31}P CPMAS NMR spectrum for these samples. This could also be because of the formation of pi-stacking at these temperatures. Thus, the ^{31}P peaks of ZnO-DPP and ZnO-DPP-HA are narrow at RT likely due to benzene ring flips, and at 100 K likely due to the formation of pi-stacking.

For the case of ZnO-DPP-PhAA and ZnO-DPP-PhPAA some mixing is expected due to the presence of phenyl groups in all these ligands. For these samples, significant peak broadening can be observed in $\{^{1}H\text{-}\}^{31}P$ CPMAS NMR spectra between RT and 100K as seen in Figure 5-5b and Figure 5-5d. In these cases, the presence of hetero-ligands among DPP could possibly be interrupting the DPP pi-stacking at 100 K. Subsequently, two explanations can be provided for the ^{31}P peak broadening: 1) when pi-stacking is

present at low temperature, it helps to get ^{1}H decoupling to work and thus to obtain narrow lines. Thus, imperfect ^{1}H decoupling due to intermediate to slow ring flip motions could lead to peak broadening. 2) Due to the absence of pi-stacking at low temperature, DPP could freeze in various conformations. If the ^{31}P chemical shift is sensitive to a change in DPP conformation, this could lead to broad peaks. This is also supported by the slight broadening of ^{13}C peaks of DPP at 100 K observed using TEDOR at short mixing times, as discussed in Section 5.4.1. In contrast, similarities in $\{^{1}H\text{-}\}^{31}P$ and $\{^{1}H\text{-}\}^{13}C$ CPMAS NMR spectra at RT and 100 K for mixed-ligand ZnO-DPP-HA and mono-ligand ZnO-DPP samples show that DPP and HA do not mix very well.

5.3.3 Quantitative measurements – multiCP experiments

Quantitative multiCP experiments[252] by Schmidt-Rohr and co-workers were recorded for the samples and the deconvoluted spectra along with peak intensities are shown in Figure **5-7**. The ratio of half of the DPP ipso ^{13}C peak intensity ($\delta\{^{13}C\} \sim 151$ ppm) (since DPP has two phenyl moieties per molecule) and the most resolved and least broad (since these are least affected by the spectral noise) ^{13}C peaks of PhAA, PhPAA and HA were determined and are given in ***Table* 5-1**.

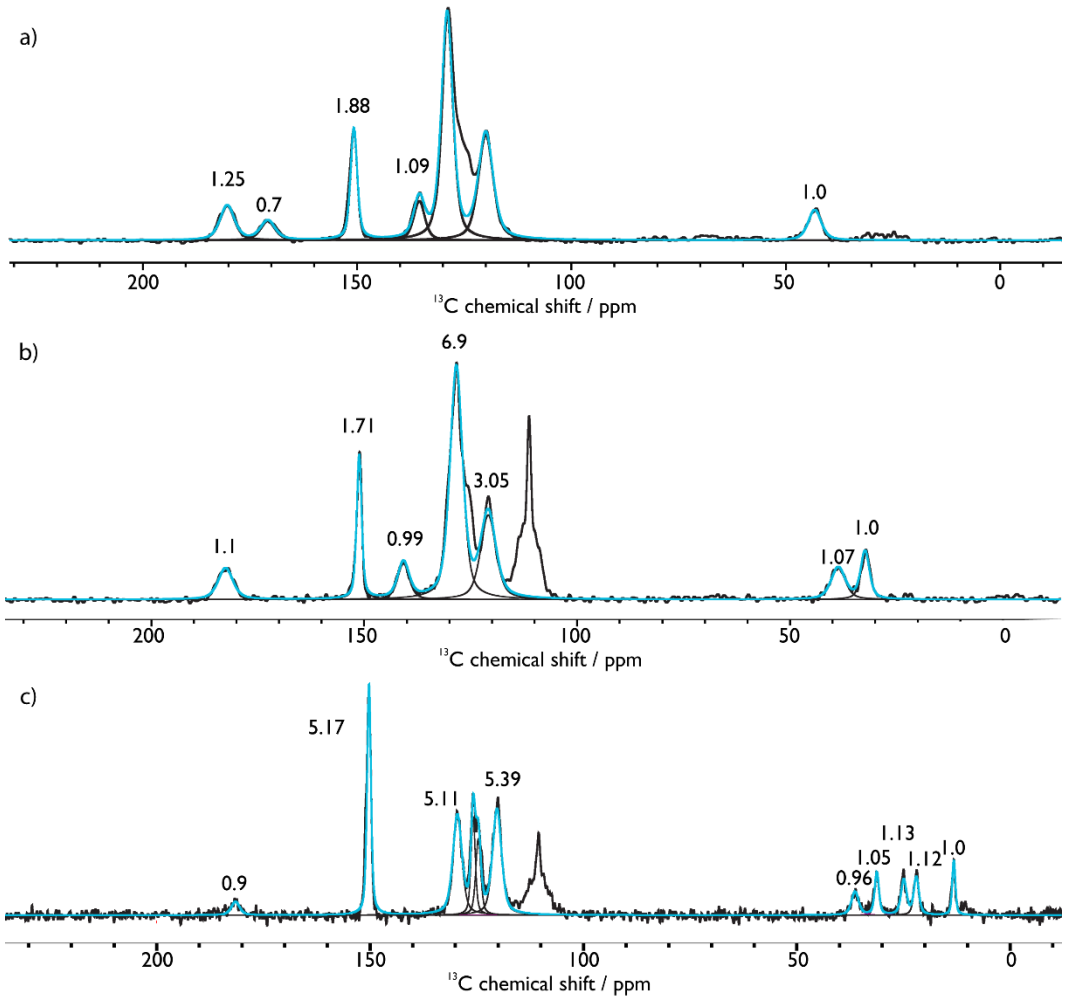

Figure 5-7. Deconvoluted quantitative ^{13}C after 7×1.1 ms multiCP for ZnO NPs capped by a) DPP-PhAA, b) DPP-PhPAA, and c) DPP-HA recorded at RT.

Table 5-1. Relative ratios of the two ligands in different DPP-X mixed ligand samples where X=PhAA, PhPAA and HA.

DPP-X	DPP	X
DPP-PhAA	0.94	1
DPP-PhPAA	0.85	1
DPP-HA	2.58	1

5.4 Quantitative analysis of the mixed ligand shell

5.4.1 Spin echo and TEDOR measurements

1D $^{13}C\{^{31}P\}$ TEDOR experiments with ^{13}C detection were recorded at different mixing times and the corresponding spectra and obtained buildup curves for various ^{13}C sites in DPP and hetero-ligands (PhAA/PhPAA/PhPAA) are shown in **Figure 5-8**. For the case of DPP-PhAA and DPP-PhPAA, the ^{13}C peaks in the aromatic region are convoluted for the two ligands. Spectra from experiments recorded at short mixing times (< 3.5 ms) clearly show DPP ^{13}C peak buildup, as these times are too short for inter-ligand transfer to nearby hetero-ligands. Thus, from the TEDOR spectra at mixing times < 3.5 ms, well resolved DPP aromatic peaks can be obtained for these samples. Comparison of aromatic peak widths between the three hetero-ligand samples (**Figure 5-8** a, b, and c) show that the DPP ^{13}C peaks are relatively narrow for ZnO-DPP-HA (similar to the peak widths obtained from ZnO-DPP, chapter 2), while broader for ZnO-DPP-PhAA and ZnO-DPP-PhPAA. This broadening is in accordance with the loss of pi-stacking at 100 K (as suggested in Section 5.3.2) for the case of possibly intimately mixed ligand shell between DPP and the hetero-ligand (PhAA/PhPAA).

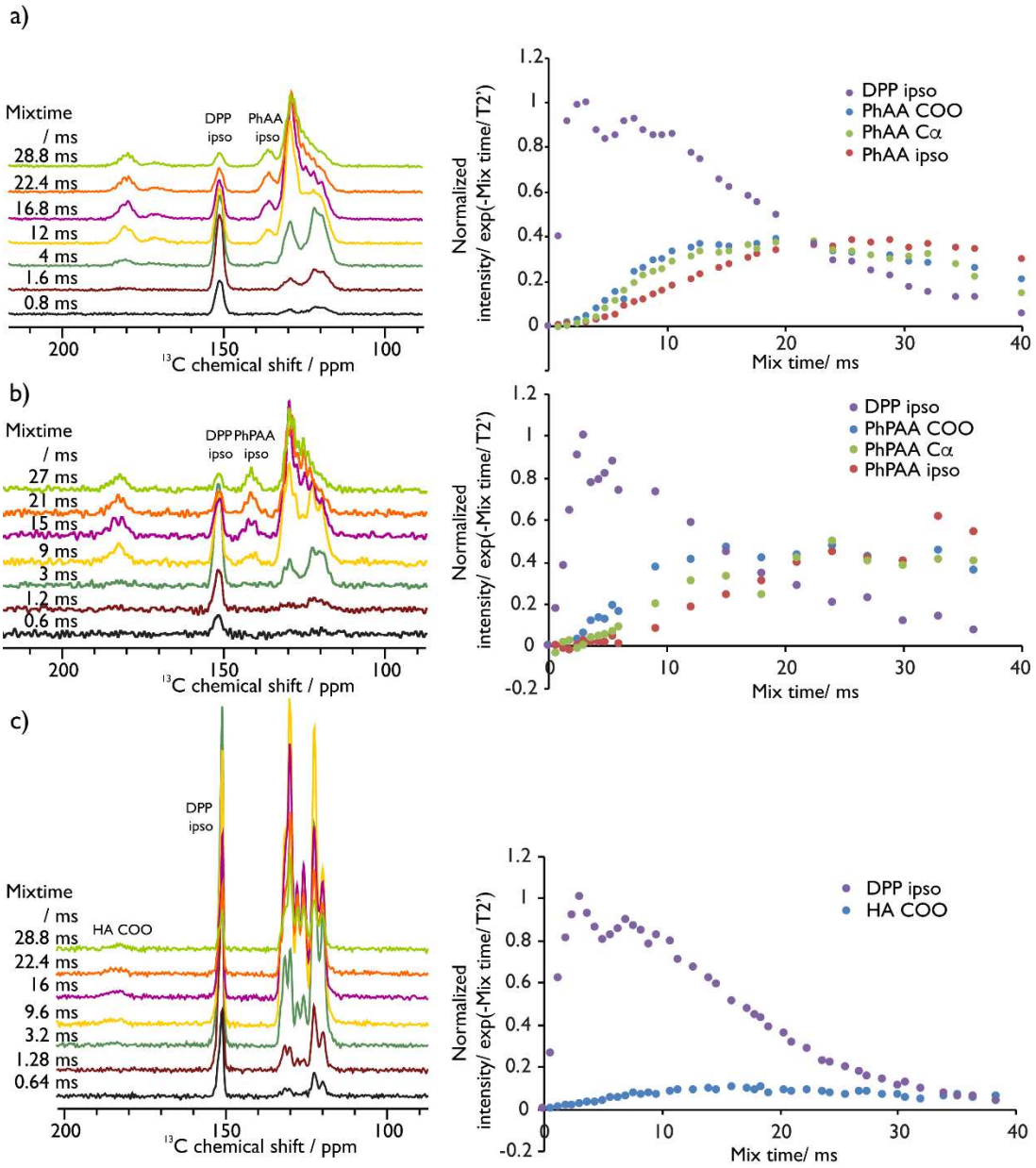

Figure 5-8. Spectra obtained from experimental 1D $^{13}C\{^{31}P\}$ TEDOR experiments with ^{13}C detection, at various mixing times and the corresponding buildups (after accounting for relaxation under echo) for the ipso ^{13}C of DPP ($\delta\{^{13}C\} \sim 151$ ppm) and a) carboxylate, C_α, and ipso ^{13}C of PhAA for sample ZnO-DPP-PhAA at 10 kHz MAS, b) carboxylate, C_α, C_β, and ipso ^{13}C of PhPAA for sample ZnO-DPP-PhPAA at 13.333 kHz MAS, and c) carboxylate ^{13}C of HA for sample ZnO-DPP-HA at 12.5 kHz MAS.

5.4.2 Buildup analysis

In the buildups, the decay is due to transverse relaxation and can be determined using a CP echo experiment with variable echo-time. To fit these buildups, the analytical expressions in Equations 5.1.1 and 5.1.2, described in Section 5.1.2, were used. It must be noted that while ^{31}P is present only in DPP, ^{13}Cs are present in both DPP and the hetero-ligand. Depending on the ligand shell morphology on the surface, the DPP will either be surrounded by other DPP or by hetero-ligand. This information can be obtained by tracking the $^{13}C\{^{31}P\}$ TEDOR, i.e., the buildup of ^{13}C peaks of DPP and hetero-ligand obtained from the TEDOR spectra. For the DPP ipso ^{13}C peak buildup, simultaneous contributions from intra ^{31}P at 2.6 Å and several inter-ligand ^{31}P-^{13}C interactions of about ~6 Å are expected. Equation 5.4.1 can be used to fit the ipso DPP buildup as follows:

$$V_i(t_{mix}) = \Lambda_i(1-[\mathrm{J_0}(\sqrt{2}\mathrm{D}_{intra}\mathrm{t}_{mix})]^2)(1+[\mathrm{J_0}(\sqrt{2}\mathrm{D}_{inter}\mathrm{t}_{mix})]^2)^n + n*\Lambda_i(1-[\mathrm{J_0}(\sqrt{2}\mathrm{D}_{inter}\mathrm{t}_{mix})]^2)(1+[\mathrm{J_0}((\sqrt{2}\mathrm{D}_{intra}\mathrm{t}_{mix})]^2)(1+[\mathrm{J_0}(\sqrt{2}\mathrm{D}_{inter}\mathrm{t}_{mix})]^2)^{n-1} \quad \textbf{5.4.1}$$

where *n* is the number of neighboring DPPs present around the DPP containing the ^{13}C at NA, D_{intra} is the dipolar coupling between the ^{13}C and the ^{31}P present in the same molecule, and D_{inter} is the dipolar coupling between the ^{13}C and ^{31}Ps from neighboring DPPs. Note that at NA, neighboring DPPs have ^{12}Cs that are not NMR active. And Λ_i is given by:

$$\Lambda_i = \frac{1}{2^{n+1}}\mathrm{V}_i(0)\lambda_i \exp(-\Gamma_i \mathrm{t}_{mix}) \quad \textbf{5.4.2}$$

Γ_i, the transverse relaxation rate, was measured using the spin-echo experiment. $V_i(0)$ is the reference cross-peak intensity. λ_i describes the amplitude scaling of cross-peaks, which can come from experimental imperfections, higher order CSA and ^{13}C-^{13}C, ^{1}H-^{13}C, and ^{1}H-^{31}P dipolar coupling effects, and possible systematic deviations associated with the description of experimental data using the approximate model[106].

Among the terms described above in Equations 5.4.1 and 5.4.2, D_{intra} (696.4 Hz (from 2.6 Å)) and Γ_i (from spin echo experiments, $1/T_2'$; Table 5-2., Table 5-3., Table 5-4.) are already known. Thus, D_{inter} and n were varied to fit the DPP ipso buildup curve.

Similarly, to fit the hetero-ligand C buildup, which shows transfer between DPP and these ligands, Equations 5.4.1 and 5.4.2 can be used, except for changing D_{intra} to the analogous $D_{inter\text{-}close}$. Here, $D_{inter\text{-}close}$ is the dipolar coupling between hetero-ligand (PhAA/PhPAA/HA) ^{13}C, and ^{31}P from the nearest DPP. While D_{inter} represents coupling to ^{31}Ps from DPP that are present at longer distances.

$$V_i(t_{mix}) = \Lambda_i(1-[J_0(\sqrt{2}D_{inter-close}t_{mix})]^2)(1+[J_0(\sqrt{2}D_{inter}t_{mix})]^2)^n + n * \Lambda_i(1-[J_0(\sqrt{2}D_{inter}t_{mix})]^2)(1+[J_0((\sqrt{2}D_{inter-close}t_{mix})]^2)(1+[J_0(\sqrt{2}D_{inter}t_{mix})]^2)^{n-1} \quad \textbf{5.4.3}$$

5.4.3 Distance estimates

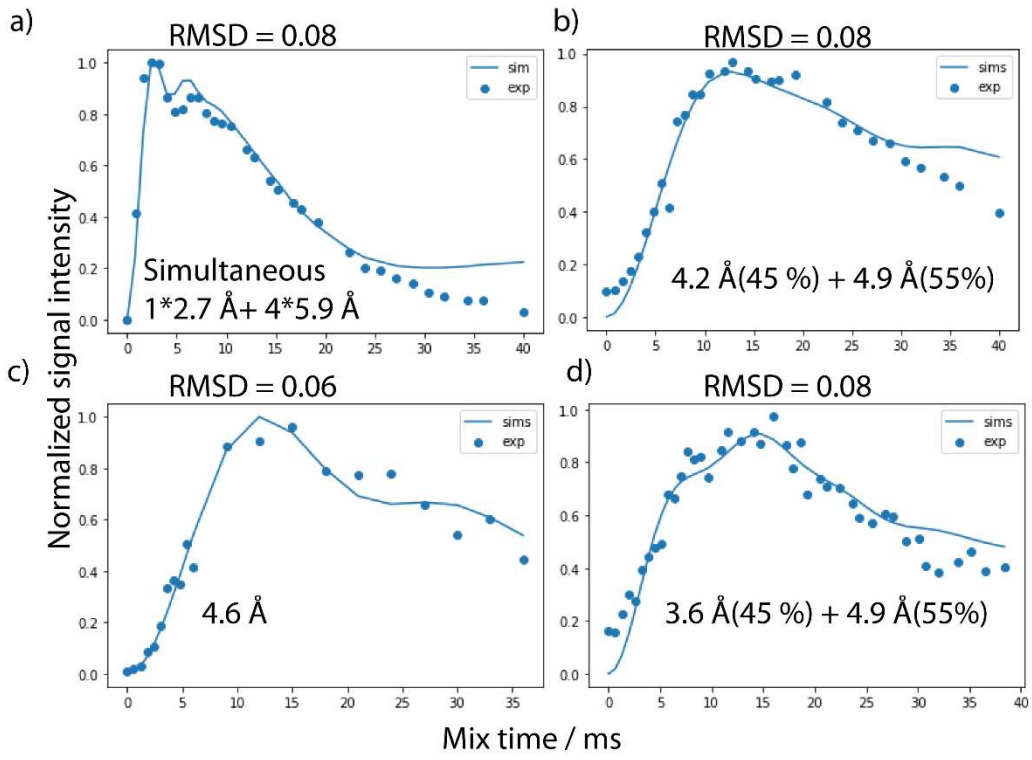

Figure 5-9. TEDOR buildup curves for transfer from DPP ^{31}P to a) DPP ipso C, b) PhAA COO-, c) PhPAA COO-, and d) HA COO- and their fits to various distances/combinations (mentioned in the plots). The RMSD of these fits have been mentioned on the top of each plot.

The quantification of the ligand shell does not require rigorous distance measurements, however, an idea of the distances leading to the buildup curves is required. This is because it needs to be understood whether the maxima obtained in the buildup curves are just from the immediate neighbors or from ligands at farther distances as well. If farther distances contribute to the buildup, then this contribution needs to be removed from the maxima of the buildup because the idea here is to find the immediate boundary between the two kinds of ligands. The DPP ^{31}P to ipso ^{13}C buildup, fits to a 2.7 Å intra and four 5.9 Å inter-ligand distances contributing simultaneously, Figure 5-9a. The hetero-ligand buildup between DPP ^{31}P and carboxylate ^{13}C of PhAA, PhPAA and HA fit to average distance combinations of 4.2 (45%) + 4.9 (55%) Å, 4.6 Å, and 3.6 (45%) + 4.9 (55%)Å, respectively. Even for the systems where two distance contributions are present, the obtained distances are not long enough to belong to farther neighbors, as these would be expected around at least 6.5 Å, for (0001)-like facets. Thus, it can be concluded that all the distances contributing to the maxima of the buildup curve are from the nearby hetero-ligand neighbors of DPP. For the fitting of hetero-ligand buildup curves, the effect of multiple neighboring DPP's was not taken into account. While the number of neighboring DPP's does not affect the maxima of the buildup, it does affect the exact distance measurement. Furthermore, thermogravimetric analysis (TGA) data needs to be recorded and the surface ligand density needs to be measured to ensure that it agrees with these distance measurements.

5.4.4 Quantification

After accounting for transverse relaxation under an echo, except for factor λ_i from Equations 5.4.1 and 5.4.2, the rest of the equation leads to the same maxima for the buildup curve (recorded as a function of t_{mix}), irrespective of the value of n, D_{intra} , and D_{inter}. Thus, if λ_i is the same or its value is known for two ^{13}C sites, their maxima can be directly compared to obtain quantitative information about the boundary between the two kinds of ligands. For the experiments described herein, among the factors that possibly affect λ_I, ^{13}C-^{13}C, ^{1}H-^{13}C, and ^{1}H-^{31}P can be neglected because of experiments at ^{13}C NA, absence of strong ^{1}H-^{13}C and ^{1}H-^{31}P interactions in the case of COO^{-}, ipso C peaks, and in DPP, respectively. In the case of aliphatic ^{13}C peaks, the ^{1}H-^{13}C dipolar

couplings need to be considered. Whereas, experimental imperfections and higher-order CSA terms need to be accounted for in all cases.

Experimental imperfections and systematic deviations

Experimental imperfections are expected to be the same for the intra and inter ligand $^{13}C\{^{31}P\}$ TEDOR. All DPP ipso ^{13}Cs always have an intra ^{31}P at 2.7 Å i.e, this transfer represents the maximum possible transfer efficiency under the given set of experimental conditions. Whereas hetero-ligand (PhAA/PhPAA/HA) ^{13}Cs would have a ^{31}P nearby depending on the ligand shell morphology. Thus, in this case, at NA every ^{13}C may or may not have a neighboring ^{31}P depending on the ligand shell morphology. Therefore, the $^{13}C\{^{31}P\}$ TEDOR buildup for DPP ipso ^{13}C can be used as a reference to account for the effect of experimental imperfections. The buildup maxima of the DPP ipso ^{13}C peak (S_{max}(ipso)) divided by the reference CP intensity S_0 (ipso) for the ipso ^{13}C would give the transfer efficiency (TE_{EI}), accounting for the experimental imperfections and systematic deviations of $^{13}C\{^{31}P\}$ TEDOR and can be used for both intra and inter-ligand systems.

Chemical shift anisotropy

Among the various sites present in the system, the aromatic ^{13}Cs have a chemical shift anisotropy (CSA) ~100 ppm and aliphatic ^{13}Cs have a CSA of ~20 ppm, measured from sideband fitting at various MAS rates (data not shown). To account for the effect of CSA on the maximum of the buildup curves for these sites, Spinevolution[156] simulations were performed, Figure 5-10. In all the simulations a 100 ppm ^{31}P CSA was used for all the simulations as DPP ^{31}P CSA was found to be ~100 ppm from sideband analysis (data not shown). It can be seen from Figure 5-10 that CSA scales the maxima of the buildup curve by the same amount irrespective of the distance between the ^{31}P-^{13}C spin pair. Since the carboxylate and aromatic peaks possess ~100 ppm CSA, the scaling factor due to CSA, TE_{CSA}, is 1. Whereas, to scale the aliphatic peaks, a factor of 1.4 scaling is required.

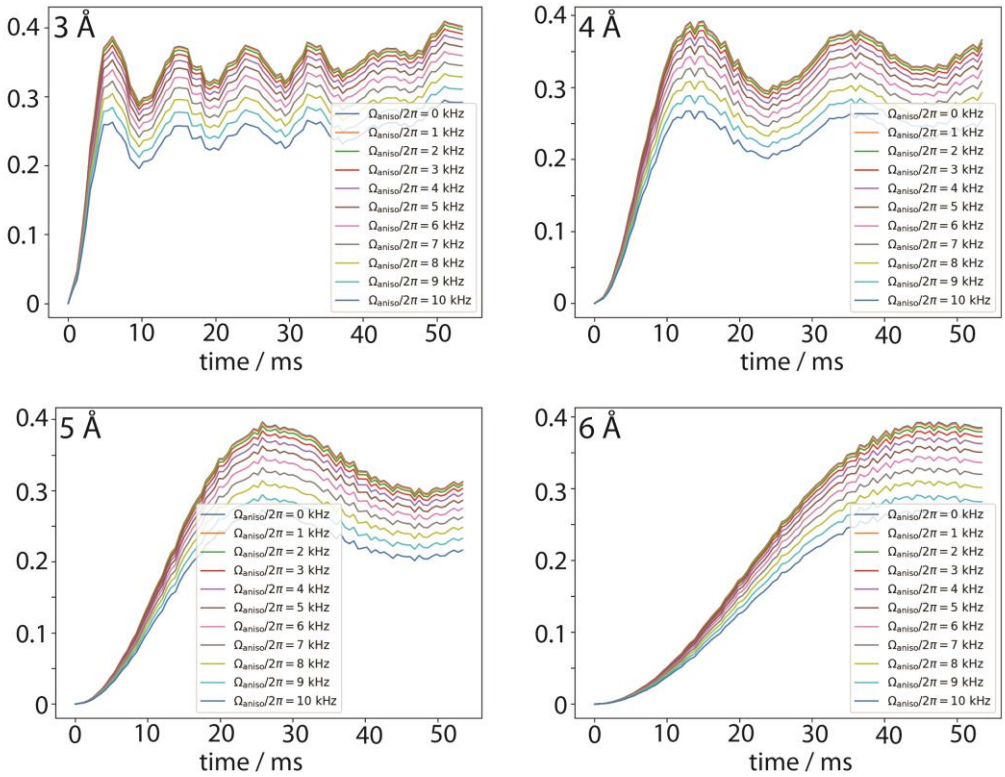

Figure 5-10. Spinevolution[156] simulations showing the effect of ^{13}C CSA (varied between 0 to 100 ppm in 10 ppm steps) on the maxima of the ^{13}C TEDOR buildup curves for ^{31}P-^{13}C spin pairs 3, 4, 5, and 6 Å apart. In all the simulations a 100 ppm ^{31}P CSA was used.

Quantification

Thus, after accounting for relaxation under echo obtained by dividing the buildup curve by $\exp(-\Gamma_i t_{mix})$, the maxima of the ipso ^{13}C buildup curve can be divided by the ipso ^{13}C reference CP intensity to get the TE_{EI} (ipso). Depending on the CSA of the ^{13}C being analyzed, multiplying the TE by the reference CP intensity of hetero-ligand ^{13}C peak (S_0 * TE_{EI} (ipso)*TE_{CSA}) would give the $^{13}C\{^{31}P\}$ TEDOR between DPP and the hetero-ligand in a case where each ^{13}C has a ^{31}P nearby, i.e., a 100% boundary between the hetero-ligands. Dividing the maxima of the TEDOR buildup for hetero-ligand ^{13}C S_{max}(hetero) by (S_0 * TE_{EI} (ipso)*TE_{CSA}) would give the % hetero-ligands in the vicinity of DPP.

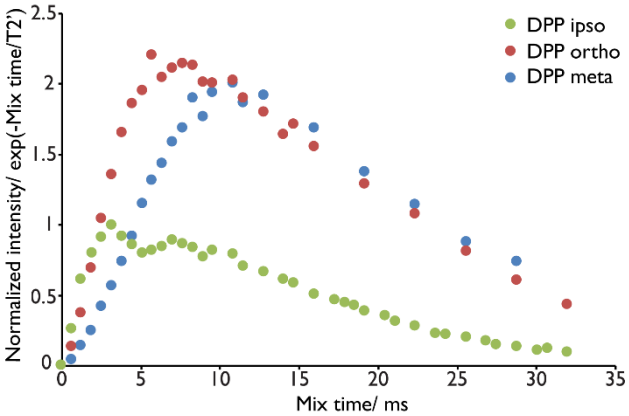

Figure 5-11. ^{13}C detected 1D $^{13}C\{^{31}P\}$ TEDOR buildup of DPP ipso, ortho and meta ^{13}C peaks for ZnO-DPP-HA.

Another critical aspect of quantification was ensuring that the buildup maxima does not get affected by the distance between the ^{31}P and the ^{13}C. From the Spinevolution simulations shown in Figure 5-10, it can be seen that for the same CSA values, the buildup maxima is the same for 3, 4, 5, and 6 Å distances which was also confirmed by experiments. Since the DPP aromatic region in ZnO-DPP-HA TEDOR buildups was most well separated, shown in Figure **5-8**c, thus the buildup of the DPP ipso (2.7 Å), ortho (3.15 Å), and meta (4.6 Å) peaks were analysed and compared. From the spectra recorded at various mixing times, shown in Figure **5-8**c, it can be seen that the ^{13}C peak at $\delta^{13}C$ 151 ppm builds up the fastest and hence must belong to the closest carbon to DPP phosphorus, followed by $\delta^{13}C$ ~120 ppm, $\delta^{13}C$ ~132 ppm, and $\delta^{13}C$ ~127 ppm in that order. Thus, $\delta^{13}C$ 151 ppm was assigned to ipso ^{13}C, $\delta^{13}C$ ~120 ppm to ortho, $\delta^{13}C$ ~132 ppm to meta, and $\delta^{13}C$ ~127 ppm to para. After accounting for the relaxation under spin-echo and comparing the maxima to the reference CP intensities (not shown), it was found that indeed the maxima per spin pair is the same for the short and long distances as shown in Figure 5-11. The maxima for ortho and meta peaks are twice that for ipso because there are twice as many of these ^{13}Cs present in the system.

5.4.5 Percentage inter-ligand boundaries in the mixed ligand shell

The above-described analysis was performed on the three mixed-ligand systems, DPP-PhAA, DPP-PhPAA and DPP-HA and is shown in Table 5-2., Table 5-3., and Table 5-4. These tables show the measured T_2' ($1/\Gamma_i$) values from the spin-echo experiments, the reference cross-peak intensity from CP (S_0), the maximum of the TEDOR buildup curve (**Figure 5-8**) (S_{max}), the transfer efficiency (TE) and the % hetero-ligands that see DPP for various ^{13}C sites present in the system. Based on the hetero-ligand (PhAA/PhPAA/HA) ipso carbon and/or carboxylate peak buildup, the % hetero-ligands in close proximity to DPP was found to be ~85%, ~82%, and ~49% for the DPP-PhAA, DPP-PhPAA, and DPP-HA systems, respectively. Considering the relative amounts of the ligands obtained from quantitative multiCP experiments (Section 5.3.3), 85% of PhAA would be 0.85 PhAA, which is (0.85/0.94*100=) 90.4% of the total DPP present. Thus, these percentages are equivalent to ~90.4%, ~96.4%, and ~18.9% DPP in DPP-PhAA, DPP-PhPAA, and DPP-HA systems, respectively. These percentages indicate an intimately mixed random ligand shell morphology for the DPP-PhAA and DPP-PhPAA case. Whereas, even though ~49% of HA ligands are present in the vicinity to DPP, this makes only ~20% of DPP that are around HA, and the rest ~80% DPP form a homoligand shell on the surface. These results are also in accordance with the disruption of pi-stacking at 100 K for the DPP-PhAA and DPP-PhPAA case because of intimate hetero-ligand mixing, as discussed in Section 5.3.2.

Thus, for these samples, the ~90% boundary between the PhAA/PhPAA and DPP ligands points to the presence of random mixed ligand shell morphologies on these NPs. Further, homonuclear dipolar recoupling experiments will be performed to support these results. For DPP-HA case, the applied synthetic procedure leads to a 2.58:1 ligand ratio on the NP surface even though a 1:1 DPP: heteroligand ratio was used in the starting reagents. This shows that for DPP-HA mixture, further optimization of the synthetic procedure is required.

It must be noted that the % vicinity obtained from the aliphatic CH_2 peak buildups in the case of PhAA and PhPAA are deemed less reliable because of the following reasons: a) the presence of C-H interactions, which might affect the scaling factor, λ_i. b) the fast relaxation rates, with T_2' values of ~18 ms. In this range, the buildup maxima

is highly sensitive to the accurate value of T_2' and thus makes the analysis unreliable. Moreover, for the case of HA among the aliphatic and carboxylate sites, only carboxylate sites have been compared to DPP. It is because, at ~105 K, the freezing of HA chains leads to significant peak broadening and thus the aliphatic peaks become highly convoluted. It prevented the separate analysis of each aliphatic site to obtain quantitative information. Thus, only the carboxylate site was used for the analysis.

Table 5-2. The T_2' ($1/\Gamma_i'$) values measured from spin-echo experiments, reference cross-peak intensity from CP (S_0), the maximum of TEDOR buildup curve (S), the transfer efficiency (S/S_0) and the % PhAA that see DPP for the various ^{13}C sites present in the system. In the row showing the values of 'S', the values in brackets correspond to mixing times at the maxima of the buildup curves.

	DPP ipso ^{13}C	**PhAA ^{13}COO-**	**PhAA $^{13}C\square$**	**PhAA ipso ^{13}C**
T_2' (ms)	57.2	53.4	18	46.4
S_0	1.0000	0.6845	0.5768	0.5055
$S_{max}=S/\exp(-t_{mix}/T_2')$	0.1250 (3.2)	0.0697 (18.4)	0.0594 (18.4)	0.0551 (26.4)
$\%TE_{EI}=S_{max}/S_0$	12.5 %			
% PhAA-DPP= $S_{max}/(S_0 * TE_{EI}$ (ipso)$*TE_{CSA})$		81.4 %	65.8 %	87.3 %

S_0= reference cross-polarization intensity

Table 5-3. The T_2' ($1/\Gamma_i'$) values measured from spin-echo experiments, reference cross-peak intensity from CP (S_0), the maximum of TEDOR buildup curve (S), the transfer efficiency (S/S_0) and the % PhPAA that see DPP for the various ^{13}C sites present in the system. In the row showing the values of 'S', the values in brackets correspond to mixing times at the maxima of the buildup curves.

	DPP ipso ^{13}C	**PhPAA $^{13}COO^-$**	**PhPAA ^{13}C□**	**PhPAA ^{13}C□**	**PhPAA ipso ^{13}C**
T_2' (ms)	53.8	41	13	16	36
S_0	1.0000	0.6788	0.4572	0.7685	0.5770
$S=S_{expmax}/exp(-t_{mix}/T_2')$	0.1952 (3)	0.1061 (15)	0.0516 (27)	0.0615 (27)	0.0932 (27)
$\%TE_{EI}=S_{max}/S_0$	19.5%				
% PhPAA-DPP= $S_{max}/(S_0 * TE_{EI} * TE_{CSA})$		80.1%	41.3%	29.3%	82.9%

Table 5-4. The T_2' ($1/\Gamma_i'$) values measured from spin-echo experiments, reference cross-peak intensity from CP (S_0), the maximum of TEDOR buildup curve (S), the transfer efficiency (S/S_0) and the % HA that see DPP for the various ^{13}C sites present in the system. In the row showing the values of 'S', the values in brackets correspond to mixing times at the maxima of the buildup curves.

	DPP ipso ^{13}C	**HA $^{13}COO^-$**
T_2' (ms)	106.4	36.6
S_0	1.0000	0.1273
$S=S_{expmax}/exp(-t_{mix}/T_2')$	0.1865 (3)	0.0116 (12)
$\%TE_{EI}=S_{max}/S_0$	18.6 %	
% HA that sees DPP= $S_{max}/(S_0 * TE_{EI} * TE_{CSA})$		48.8 %

5.4.6 Important considerations

A few considerations must be noted for the quantitative use of this method:

1) The information obtained from NMR in general, and hence this method, is an ensemble average of various spin systems present in the sample being studied. Thus, if there are significant variations in the ligand shell morphologies between NPs present in the system, then the obtained quantitative information can lead to incorrect conclusions.

2) For a particular nucleus, at least one peak in the spectrum should be well resolved for both the ligands present in the mixed-ligand shell.

3) As described in the section above, fast T_2' relaxation leads to higher uncertainties in the quantitative measurements. Hence, the T_2' values for the peaks being studied should be sufficiently greater than the maxima of buildup curves for the dipolar coupling being tracked.

4) If in the buildup curves for hetero-ligand transfer, a combination of distances is observed, then the analysis of the buildup curves becomes more informative but simultaneously more complicated to analyze as observed signal is a combination of the nearest heteroligands as well as the ones possibly present in the second neighboring shell.

5.5 Conclusion

An in-depth analysis of the mixed ligand shell of ZnO NPs prepared by the OSSOM approach was performed. Three samples were studied, which included DPP in combination with HA, PhAA, and PhPAA ligands on the surface of ZnO NPs. The chemical shifts in the corresponding ^{13}C and ^{31}P spectra for the samples were assigned and the changes in the spectra between RT and 100 K were explained. Subsequently, TEDOR heteronuclear dipolar correlation experiments were performed on these samples and quantitative analysis of the mixed-ligand shell using this pulse sequence was presented. Thus, for these samples, the % of hetero-ligand PhAA/PhPAA/HA in vicinity to DPP were determined. For DPP-PhAA and DPP-PhPAA systems with ~1:1

ligand ratio, these experiments showed an ~90% boundary between the PhAA/PhPAA and DPP ligands. This observation points to the presence of random mixed ligand shell morphologies on these NPs. For DPP-HA, the applied synthetic procedure leads to a 2.5:1 ligand ratio on the NP surface even though a 1:1 DPP: heteroligand ratio was used in the starting reagents. This shows that for DPP-HA mixture, further optimization of the synthetic procedure is required. The TEDOR buildup analysis shows that ~50% of HA ligands are in the vicinity of DPP. However, since the applied synthetic procedure needs standardization, it is unclear whether the % boundary arises from a uniform ligand morphology throughout the sample or from a combination of different ligand shell morphologies. Furthermore, a complementary analysis from homonuclear dipolar correlation experiments will be performed to support these results.

5.6 Materials and methods

5.6.1 DNP NMR spectroscopy

Experiments were acquired using ^{1}H $\pi/2$ pulses of 100 kHz, ^{31}P $\pi/2$ pulses of 50 kHz, ^{31}P and ^{13}C CP spin-locking at ~50 kHz was applied for 2.5 and 3 ms, respectively. 100 kHz of SPINAL-64[160] heteronuclear ^{1}H decoupling was used throughout the 20 and 40 ms signal detection periods for ^{31}P and ^{13}C CP experiments, respectively, with direct spectral widths of 50 kHz. Optimized experimental repetition delays of 2.6, 4, and 3 s for the ZnO-DPP-PhAA, ZnO-DPP-PhPAA, ZnO-DPP-HA, respectively.

Conclusions and outlook

In this work, novel applications of dynamic nuclear polarization (DNP)-enhanced solid-state nuclear magnetic resonance (ssNMR) for the advanced characterization of ligand shells on the surface of nanoparticles (NPs) have been presented. Functional groups and local proximities were analyzed to improve understanding of key areas concerning NPs, specifically zinc oxide (ZnO) NPs. These include studies of ligand shells a) for comparison between synthetic techniques (sol-gel and organometallic approaches), b) to unravel the role of the ligand in the formation and stabilization of a unique controlled hexagonal nanoplatelet (NPL) morphology, and c) to determine the ligand shell morphology on mixed ligand shell NPs.

Firstly, diphenyl phosphate (DPP) ligand-capped ZnO NPs prepared by a sol-gel method and the OSSOM approach were compared in terms of ligand binding modes and arrangement on the surface of NPs. For this purpose, ^{31}P and ^{13}C CPMAS NMR spectra were studied over time, and also homonuclear ^{31}P dipolar recoupling experiments were performed to analyze inter-ligand proximities and binding modes on the surface of these NPs. It was shown that the surface of OSSOM-prepared NPs had a highly-ordered surface ligand arrangement that remained stable under storage and upon addition of a competitive ligand (glycerol). Conversely, ZnO NPs produced via a sol-gel method exhibit multiple coordination modes of DPP ligands and a time-dependent surface restructuring process with a displacement of most ligands from the surface, indicating a corrugated surface morphology.

Defining binding modes and determining ligand arrangement on surfaces through DNP-NMR led to the investigation of the growth of interesting ZnO NPLs. Firstly, the OSSOM-II approach employed in the synthesis of ultra-thin hexagonal ZnO NPLs was described. Subsequently, the role of the specific ligand, benzamidine, in the stabilization of the polar and non-polar facets was examined using ^{1}H-^{15}N CPMAS

NMR spectra, and a complete assignment of the peaks was obtained with the help of DFT calculations. HRTEM revealed unique structural motifs, and their presence was attributed to the likely formation of unusual Zn terminated $(000\bar{1})$ facets. ^{1}H-^{15}N dipolar recoupling experiments revealed hydrogen bonding interactions on the polar and non-polar interfaces. Notably, ^{13}C homonuclear dipolar recoupling experiments, which are generally challenging due to lack of sensitivity, were recorded at ^{13}C NA for ligands on NPL surfaces. From these experiments, insights into the arrangement of ligands on the $(10\bar{1}0)$ non-polar have been obtained, showing ~66% surface coverage, close-packing, and long-term ligand stability. Additionally, changes in the NMR spectra of the smallest NPLs upon water addition showed that neutral ligand was not present during the growth of the NPLs and hence likely does not play an active role in the growth process.

Finally, the ligand shell morphology, namely, Janus, random, and stripe-like, of mixed ligand shell NPs were analyzed. For this, quantitative application of the well-known transferred echo double resonance (TEDOR) pulse sequence was presented on three samples which included DPP in combination with three different carboxylate-based hetero-ligands. Specifically, $^{13}C\{^{31}P\}$ TEDOR was recorded, where the buildup of hetero-ligand ^{13}C polarization originates from carboxylate-based hetero-ligands in proximity to DPP ligands. Subsequently, using DPP ipso ^{13}C buildup as a reference, the percentage of hetero-ligand near DPP could be determined, which provides insights into the ligand shell morphology. In detail, for the DPP-PhAA and DPP-PhPAA systems for which all ligands are aromatic, $^{13}C\{^{31}P\}$ TEDOR buildup analysis suggested the formation of random mixed ligand shell morphology. Further complementary experiments such as ^{31}P homonuclear dipolar recoupling experiments will be performed to support these conclusions. For the DPP-HA system containing an aromatic and aliphatic ligand, to draw any conclusive results from the $^{13}C\{^{31}P\}$ TEDOR buildup analysis, further optimization of the applied synthetic method is required.

Furthermore, for a better understanding of the NP systems described herein, future work may involve:

1) **Improved enhancements.** The significant DNP enhancements obtained on the hexagonal NPL samples allowed the acquisition of ^{13}C homonuclear dipolar correlation

experiments, and hence inter-ligand distance measurements on $(10\bar{1}0)$ facets. Improved enhancements might allow these experiments for (0001) facets. Thus, applications of methods such as improved radicals and MAS experiments at temperatures << 100 K, i.e., using cryogenic helium for spinning and cooling, can be applied to gain further information about the interfaces of these materials.

2) **^{17}O NMR.** Another source of information about the interfaces of these materials is ^{17}O NMR. When ligand/adsorbed species are present on the surface of these NPs, the bonding valencies of surface species are satisfied, and hence it is likely that the chemical shift of these surface atoms is similar to that of core atoms. However, removing these adsorbed/bound molecules (for example, by heating at sufficiently high temperatures) will lead to surface species with unsatisfied valencies and hence a change in their chemical shift, allowing a clear differentiation between bulk and surface atoms for such NPs. Thus obtained chemical shifts of ^{17}O surface atoms can be studied in combination with computational modeling techniques. This analysis can provide detailed information regarding the atomic-level structure of the facets of these materials.

The methods presented in this work for surface ligand characterization can be extended to other hybrid materials with an internal crystalline core and surface species. Capping ligands control NP growth and modulate surface properties such as functionality, size, morphology, and stability. Thus, a deeper understanding of the capping ligands' role helps optimize the synthesis process and design NPs with desired properties. For instance, for lead halide perovskites which are promising alternatives to conventional silicon-based solar cells, it has been shown that ligand plays a crucial role in the stoichiometry, crystal structure, and surface passivation of lead halide perovskite NPs and hence on device stability[257,258]. Similarly, the role of ligands in the surface chemistry of many other organic-inorganic hybrid materials such as Au, CdSe, TiO_2 NPs, has been shown to be critical[259]. Moreover, for biopolymer-based nanoparticles used for drug loading and drug release[260,261], and bone mineral particles with a hydroxyapatite core and an amorphous surface layer[262,263], an understanding of their interface is essential for their therapeutic applications. Systems with membranes such

as ion-exchange membranes in fuel cells[264] or ion-exchange membranes used in water purification[265] are also interesting systems with potential applications of this work.

In this work, DNP-NMR has been presented as a powerful tool for the characterization of ligand shells on the surface of NPs. Specifically, the use of samples with natural isotopic abundances, enabled by DNP, especially for ^{13}C (NA 1.1%) and ^{15}N (NA 0.37%), allowed the measurement of NMR spectra for low NA nuclei from ligands on the surface of NPs (for instance ^{15}N CPMAS NMR in the case of benzamidine capped NPLs). DNP-NMR also allowed probing proximities and accurate (by enabling the acquisition of multiple data points) local long-range distance measurements between ligands on the NP surfaces.

In conclusion, this thesis covers extensive methodology and applications of DNP-NMR for the characterization of ligand shell coordination chemistry and arrangement on the surface of NPs. The methods provided herein are envisaged to facilitate a better understanding of the interfaces of hybrid materials.

Bibliography

1. Kagan, C. R., Lifshitz, E., Sargent, E. H. & Talapin, D. V. Building devices from colloidal quantum dots. *Science.* **353**, 6302 (2016).
2. Talapin, D. V., Lee, J. S., Kovalenko, M. V. & Shevchenko, E. V. Prospects of colloidal nanocrystals for electronic and optoelectronic applications. *Chem. Rev.* **110**, 389–458 (2010).
3. Kramer, I. J. & Sargent, E. H. The architecture of colloidal quantum dot solar cells: materials to devices. *Chem. Rev.* **114**, 863–82 (2014).
4. Litvin, A. P. *et al.* Colloidal quantum dots for optoelectronics. *J. Mater. Chem. A* **5**, 13252–13275 (2017).
5. Bisri, S. Z., Piliego, C., Gao, J. & Loi, M. A. Outlook and emerging semiconducting materials for ambipolar transistors. *Adv. Mater.* **26**, 1176–1199 (2014).
6. Kovalenko, M. V *et al.* Prospects of Nanoscience with Nanocrystals. *ACS Nano* **9**, 1012–1057 (2015).
7. Carenco, S. Describing inorganic nanoparticles in the context of surface reactivity and catalysis. *Chem. Commun.* **54**, 6719–6727 (2018).
8. Zhang, J., Mou, L. & Jiang, X. Surface chemistry of gold nanoparticles for health-related applications. *Chemical Science* **11**, 923–936 (2020).
9. Bai, S., Wang, L., Li, Z. & Xiong, Y. Facet-Engineered Surface and Interface Design of Photocatalytic Materials. *Advanced Science* **4**, 1600216(2017).
10. Owen, J. The coordination chemistry of nanocrystal surfaces. *Science* **347**, 615-616 (2015).
11. Boles, M. A., Ling, D., Hyeon, T. & Talapin, D. V. The surface science of nanocrystals. *Nature Materials* **15**, 141–153 (2016).
12. Morkoç, H. & Özgür, Ü. *Zinc Oxide: Fundamentals, Materials and Device Technology*. (Wiley-VCH, Weinheim, 2008).
13. Klingshirn, C. F. ZnO: Material, physics and applications. *ChemPhysChem* **8**, 782–803 (2007).
14. Djurišić, A. B. & Leung, Y. H. Optical properties of ZnO nanostructures. *Small* **2**, 944–961 (2006).
15. Kumar, S. G. & Rao, K. S. R. K. Zinc oxide based photocatalysis: tailoring surface-bulk structure and related interfacial charge carrier dynamics for better environmental applications. *RSC Adv.* **5**, 3306–3351 (2015).
16. Carofiglio, M., Barui, S., Cauda, V. & Laurenti, M. Doped zinc oxide nanoparticles: Synthesis, characterization and potential use in nanomedicine. *Applied Sciences* **10**, 5194 (2020).
17. Constantinoiu, I. & Viespe, C. Zno metal oxide semiconductor in surface acoustic wave sensors: A review. *Sensors* **20**, 1–20 (2020).
18. Şerban, I. & Enesca, A. Metal Oxides-Based Semiconductors for Biosensors Applications. *Frontiers in Chemistry* **8**, 354 (2020).
19. Nunes, D. *et al.* Metal oxide nanostructures for sensor applications. *Semiconductor Science and Technology* **34**, 043001 (2019).

20. Chen, F., Guan, Z. & Tang, A. Nanostructure and device architecture engineering for high-performance quantum-dot light-emitting diodes. *This J. is Cite this J. Mater. Chem. C* **6**, 10958 (1095).
21. Sushma, C. & Girish Kumar, S. Advancements in the zinc oxide nanomaterials for efficient photocatalysis. *Chemical Papers* **71**, 2023–2042 (2017).
22. Paczesny, J. *et al.* Towards Organized Hybrid Nanomaterials at the Air/Water Interface Based on Liquid-Crystal/ZnO Nanocrystals. *Chem. - A Eur. J.* **21**, 16941–16947 (2015).
23. Paczesny, J. *et al.* Photoactive Langmuir-Blodgett, Freely Suspended and Free Standing Films of Carboxylate Ligand-Coated ZnO Nanocrystals. *ACS Appl. Mater. Interfaces* **8**, 13532–13541 (2016).
24. Grala, A. *et al.* 'Clickable' ZnO nanocrystals: the superiority of a novel organometallic approach over the inorganic sol–gel procedure. *Chem. Commun.* **52**, 7340–7343 (2016).
25. Wolska-Pietkiewicz, M. *et al.* From Well-Defined Alkylzinc Phosphinates to Quantum-Sized ZnO Nanocrystals. *Chem. - A Eur. J.* **23**, 11856–11865 (2017).
26. Chwojnowska, E., Wolska-Pietkiewicz, M., Grzonka, J. & Lewiński, J. An organometallic route to chiroptically active ZnO nanocrystals. *Nanoscale* **9**, 14782-14786 (2017).
27. Grala, A. *et al.* Remarkable water-soluble ZnO nanocrystals: from 'click' functionalization to a supramolecular aggregation enhanced emission phenomenon. *Mater. Chem. Front.* **2**, 1104–1111 (2018).
28. Wolska-Pietkiewicz, M. *et al.* Safe-by-Design Ligand-Coated ZnO Nanocrystals Engineered by an Organometallic Approach: Unique Physicochemical Properties and Low Toxicity toward Lung Cells. *Chem. - A Eur. J.* **24**, 4033–4042 (2018).
29. Cieślak, A. M. *et al.* Ultra long-lived electron-hole separation within water-soluble colloidal ZnO nanocrystals: Prospective applications for solar energy production. *Nano Energy* **30**, 187–192 (2016).
30. Pavliuk, M. V. *et al.* Hydrogen evolution with nanoengineered ZnO interfaces decorated using a beetroot extract and a hydrogenase mimic. *Sustain. Energy Fuels* **1**, 69–73 (2017).
31. Lee, D. *et al.* Disclosing Interfaces of ZnO Nanocrystals Using Dynamic Nuclear Polarization: Sol-Gel versus Organometallic Approach. *Angew. Chemie Int. Ed.* **58**, 17163–17168 (2019).
32. Neetha, M., Rohit, K. R., Saranya, S. & Anilkumar, G. Zinc-Catalysed Multi-Component Reactions: An Overview. *ChemistrySelect* **5**, 1054–1070 (2020).
33. Borysiewicz, M. A. ZnO as a Functional Material, a Review. *Crystals* **9**, 505 (2019).
34. Alavi, M. & Nokhodchi, A. An overview on antimicrobial and wound healing properties of ZnO nanobiofilms, hydrogels, and bionanocomposites based on cellulose, chitosan, and alginate polymers. *Carbohydrate Polymers* **227**, (2020).
35. Huang, X., Zheng, X., Xu, Z. & Yi, C. ZnO-based nanocarriers for drug delivery application: From passive to smart strategies. *International Journal of Pharmaceutics* **534**, 190–194 (2017).
36. Li, W. N. *et al.* Hydrothermal synthesis of structure- And shape-controlled manganese oxide octahedral molecular sieve nanomaterials. *Adv. Funct. Mater.* **16**, 1247–1253 (2006).

37. Xu, L. *et al.* 3D flowerlike α-nickel hydroxide with enhanced electrochemical activity synthesized by microwave-assisted hydrothermal method. *Chem. Mater.* **20**, 308–316 (2008).
38. Jonca, J. *et al.* Shape-controlled ZnO nanostructures for gas sensing applications. in *Procedia Engineering* **87**, 907–910 (2014).
39. Xu, L. *et al.* ZnO with Different Morphologies Synthesized by Solvothermal Methods for Enhanced Photocatalytic Activity. *Chem. Mater* **21**, 2875 (2009).
40. Abrahams, S. C. & Bernstein, J. L. *Relneasurement of the Structure of Hexagonal ZnO*. *Acta Cryst* **25**, 1233-1236 (1969).
41. Wolska-Pietkiewicz, M. *et al.* From Well-Defined Alkylzinc Phosphinates to Quantum-Sized ZnO Nanocrystals. *Chem. - A Eur. J.* **23**, 11856–11865 (2017).
42. Kahn, M. L. *et al.* Size- and shape-control of crystalline zinc oxide nanoparticles: A new organometallic synthetic method. *Adv. Funct. Mater.* **15**, 458–468 (2005).
43. Orchard, K. L., Shaffer, M. S. P. & Williams, C. K. Organometallic route to surface-modified ZnO nanoparticles suitable for in situ nanocomposite synthesis: Bound carboxylate stoichiometry controls particle size or surface coverage. *Chem. Mater.* **24**, 2443–2448 (2012).
44. Spanhel, L. & Anderson, M. A. *Semiconductor Clusters in the Sol-Gel Process: Quantized Aggregation, Gelation, and Crystal Growth in Concentrated ZnO Colloids*. *J. Am. Chem. Soc* **113**, 2826-2833(1991).
45. Meulenkamp, E. A. *Synthesis and Growth of ZnO Nanoparticles*. (1998).
46. Jolivet, J. P., M. Henry, and J. Livage. Metal Oxide Chemistry and Synthesis: From Solution to Solid State.2003.Wiley.
47. Lifshitz, I. M. & Slyozov, V. V. The kinetics of precipitation from supersaturated solid solutions. *J. Phys. Chem. Solids* **19**, 35–50 (1961).
48. Elektrochemie, C. W. Theorie der alterung von niederschlägen durch umlösen (Ostwald-reifung). *Zeitschrift für Elektrochemie, Berichte der Bunsengesellschaft für physikalische Chemie* **65**, 581-591 (1961)
49. Pike, S. D., White, E. R., Shaffer, M. S. P. & Williams, C. K. Simple phosphinate ligands access zinc clusters identified in the synthesis of zinc oxide nanoparticles. *Nat. Commun.* **7**, 1-11 (2016).
50. Heuer-Jungemann, A. *et al.* The Role of Ligands in the Chemical Synthesis and Applications of Inorganic Nanoparticles. *Chemical Reviews* **119**, 4819-4880 (2019).
51. Marchetti, A. *et al.* Understanding Surface and Interfacial Chemistry in Functional Nanomaterials via Solid-State NMR. *Adv. Mater.* **29**, 1605895 (2017).
52. Coppel, Y. *et al.* Full characterization of colloidal solutions of long-alkyl-chain-amine- stabilized Zno nanoparticles by NMR spectroscopy: Surface state, equilibria, and affinity. *Chem. - A Eur. J.* **18**, 5384-5393 (2012).
53. Valdez, C. N., Schimpf, A. M., Gamelin, D. R. & Mayer, J. M. Low capping group surface density on zinc oxide nanocrystals. *ACS Nano* **8**, 9463-9470 (2014).
54. Peng, Y.-K. *et al.* Trimethylphosphine-Assisted Surface Fingerprinting of Metal Oxide Nanoparticle by 31 P Solid-State NMR: A Zinc Oxide Case Study. *J. Am. Chem. Soc.* **138**, 2225-2234 (2016).
55. Champouret, Y., Coppel, Y. & Kahn, M. L. Evidence for Core Oxygen Dynamics and Exchange in Metal Oxide Nanocrystals from in Situ 17O MAS

NMR. *J. Am. Chem. Soc.* **138**, 16322-16328 (2016).
56. Spataro, G., Champouret, Y., Florian, P., Coppel, Y. & Kahn, M. L. Multinuclear solid-state NMR study: A powerful tool for understanding the structure of ZnO hybrid nanoparticles. *Phys. Chem. Chem. Phys.* **20**, 12413–12421 (2018).
57. Bracht, H. *et al.* Interstitial-Mediated Diffusion in Germanium under Proton Irradiation. *Phys. Rev. lett.* **103**, 255501 (2009).
58. Bang, J. & Chang, K. J. Cite as. *Appl. Phys. Lett* **92**, 132109 (2008).
59. Wang, M. *et al.* Identification of intrinsic hydrogen impurities in ZnO with 1H solid-state nuclear magnetic resonance spectroscopy. *Chem. Phys. Lett.* **627**, 7–12 (2015).
60. Wang, L. Q. *et al.* Probing hydrogen in ZnO nanorods using solid-state H1 nuclear magnetic resonance. *Appl. Phys. Lett.* **90**, 173115 (2007).
61. Park, J. K., Kwon, H.-J. & Lee, C. E. NMR Observation of Mobile Protons in Proton-Implanted ZnO Nanorods. *Scientific reports* **6**, 1-8 (2016).
62. Champouret, Y., Coppel, Y. & Kahn, M. L. Evidence for Core Oxygen Dynamics and Exchange in Metal Oxide Nanocrystals from In Situ 17 O MAS NMR. *J. Am. Chem. Soc* **138**, 57 (2016).
63. Gory Spataro, G., Champouret, Y., Florian, P., Coppel, Y. & Kahn, M. L. Multinuclear solid-state NMR study: a powerful tool for understanding the structure of ZnO hybrid nanoparticles †. *Phys. Chem. Chem. Phys* **20**, 12413 (2018).
64. Zheng, A., Huang, S.-J., Liu, S.-B. & Deng, F. This journal is c the Owner Societies. *Phys. Chem. Chem. Phys* **13**, 14889–14901 (2011).
65. Peng, Y.-K. *et al.* Trimethylphosphine-Assisted Surface Fingerprinting of Metal Oxide Nanoparticle by 31 P Solid-State NMR: A Zinc Oxide Case Study. (2016). doi:10.1021/jacs.5b12080
66. Howarth, A. J. *et al.* Best practices for the synthesis, activation, and characterization of metal−organic frameworks. *Chemistry of Materials* **29**, 26–39 (2017).
67. Mourdikoudis, S., Pallares, R. M. & Thanh, N. T. K. Characterization techniques for nanoparticles: Comparison and complementarity upon studying nanoparticle properties. *Nanoscale* **10**, 12871–12934 (2018).
68. Pecher, O., Carretero-Gonzalez, J., Griffith, K. J. & Grey, C. P. Materials' methods: NMR in battery research. *Chemistry of Materials* **29**, 213–242 (2017).
69. Meier, B. H., Riek, R. & Böckmann, A. Emerging Structural Understanding of Amyloid Fibrils by Solid-State NMR. *Trends in Biochemical Sciences* **42**, 777–787 (2017).
70. Chiti, F. & Dobson, C. M. Protein misfolding, amyloid formation, and human disease: A summary of progress over the last decade. *Annual Review of Biochemistry* **86**, 27–68 (2017).
71. Iadanza, M. G., Jackson, M. P., Hewitt, E. W., Ranson, N. A. & Radford, S. E. A new era for understanding amyloid structures and disease. *Nature Reviews Molecular Cell Biology* **19**, 755–773 (2018).
72. Walker, T. G. Fundamentals of spin-exchange optical pumping. in *Journal of Physics: Conference Series* **294**, 012001 (Institute of Physics Publishing, 2011).
73. Duckett, S. B. & Mewis, R. E. Application of para hydrogen induced polarization techniques in NMR spectroscopy and imaging. *Acc. Chem. Res.* **45**, 1247–1257 (2012).

74. Lawler, R. G. *et al. Chemically Induced Dynamic Nuclear Polarization (CIDNP). II. The Radical-Pair Model C\(n\lx\m)\2gnm(Hf)(Nn-Nm) (1). Accounts Chem. Res* **5**, (1972).
75. Overhauser, A. W. Polarization of nuclei in metals. *Phys. Rev.* **92**, 411–415 (1953).
76. Carver, T. R. & Slichter, C. P. Polarization of nuclear spins in metals [15]. *Phys. Rev.* **92**, 212–213 (1953).
77. Becerra, L. R., Gerfen, G. J., Temkin, R. J., Singel, D. J. & Grisn', R. G. *Dynamic Nuclear Polarization with a Cyclotron Resonance Maser at 5 T*. **71**, (1993).
78. Becerra, L. R. *et al.* A Spectrometer for Dynamic Nuclear Polarization and Electron Paramagnetic Resonance at High Frequencies. *J. Magn. Reson. Ser. A* **117**, 28–40 (1995).
79. Gerfen, G. J. *et al.* High frequency (140 GHz) dynamic nuclear polarization: Polarization transfer to a solute in frozen aqueous solution. *J. Chem. Phys.* **102**, 9494–9497 (1995).
80. Weis, V., Bennati, M., Rosay, M., Bryant, J. A. & Griffin, R. G. High-Field DNP and ENDOR with a Novel Multiple-Frequency Resonance Structure. *Journal of Magnetic Resonance* **140**, 293–299 (1999).
81. Barnes, A. B. *et al.* Dynamic nuclear polarization at 700 MHz/460 GHz. *J. Magn. Reson.* **224**, 1–7 (2012).
82. Rosay, M., Blank, M. & Engelke, F. Instrumentation for solid-state dynamic nuclear polarization with magic angle spinning NMR. *J. Magn. Reson.* **264**, 88–98 (2016).
83. waves., J. D.-I. and millimeter & 1985, undefined. Propagation and mode coupling in corrugated and smooth-wall circular waveguides. *books.google.com*
84. Allen, P. J., Creuzet, F., De Groot, H. J. M. & Griffin, R. G. Apparatus for low-temperature magic-angle spinning NMR. *J. Magn. Reson.* **92**, 614–617 (1991).
85. Matsuki, Y. *et al.* Helium-cooling and -spinning dynamic nuclear polarization for sensitivity-enhanced solid-state NMR at 14 T and 30 K. *J. Magn. Reson.* **225**, 1–9 (2012).
86. Matsuki, Y., Nakamura, S., Fukui, S., Suematsu, H. & Fujiwara, T. Closed-cycle cold helium magic-angle spinning for sensitivity-enhanced multi-dimensional solid-state NMR. *J. Magn. Reson.* **259**, 76–81 (2015).
87. Bouleau, E. *et al.* Pushing NMR sensitivity limits using dynamic nuclear polarization with closed-loop cryogenic helium sample spinning. *Chem. Sci.* **6**, 6806–6812 (2015).
88. Lee, D., Bouleau, E., Saint-Bonnet, P., Hediger, S. & De Paëpe, G. Ultra-low temperature MAS-DNP. *J. Magn. Reson.* **264**, 116–124 (2016).
89. Kessenikh, A., Lushchikov, V., … A. M.-S. P.-S. S. Proton polarization in irradiated polyethylenes. *Soviet Phys.-Solid State* (1963)
90. Hwang, C. F. & Hill, D. A. Phenomenological model for the new effect in dynamic polarization. *Phys. Rev. Lett.* **19**, 1011–1014 (1967).
91. Mentink-Vigier, F. *et al.* Fast passage dynamic nuclear polarization on rotating solids. *J. Magn. Reson.* **224**, 13–21 (2012).
92. Thurber, K. R. & Tycko, R. Theory for cross effect dynamic nuclear polarization under magic-angle spinning in solid state nuclear magnetic resonance: The importance of level crossings. *J. Chem. Phys.* **137**, 084508 (2012).

93. Song, C., Hu, K. N., Joo, C. G., Swager, T. M. & Griffin, R. G. TOTAPOL: A biradical polarizing agent for dynamic nuclear polarization experiments in aqueous media. *J. Am. Chem. Soc.* **128**, 11385–11390 (2006).
94. Sauvée, C. *et al.* Highly Efficient, Water-Soluble Polarizing Agents for Dynamic Nuclear Polarization at High Frequency. *Angew. Chemie Int. Ed.* **52**, 10858–10861 (2013).
95. Matsuki, Y. *et al.* Dynamic nuclear polarization with a rigid biradical. *Angew. Chemie - Int. Ed.* **48**, 4996–5000 (2009).
96. Mentink-Vigier, F. *et al.* Computationally Assisted Design of Polarizing Agents for Dynamic Nuclear Polarization Enhanced NMR: The AsymPol Family. *J. Am. Chem. Soc.* **140**, 11013–11019 (2018).
97. Mathies, G. *et al.* Efficient Dynamic Nuclear Polarization at 800 MHz/527 GHz with Trityl-Nitroxide Biradicals. *Angew. Chemie Int. Ed.* **54**, 11770–11774 (2015).
98. Wisser, D. *et al.* BDPA-Nitroxide Biradicals Tailored for Efficient Dynamic Nuclear Polarization Enhanced Solid-State NMR at Magnetic Fields up to 21.1 T. *J. Am. Chem. Soc.* **140**, 13340–13349 (2018).
99. Michaelis, V. K., Corzilius, rn, Smith, A. A. & Griffin, R. G. Dynamic Nuclear Polarization of 17 O: Direct Polarization. *J. Phys. Chem. B* **117**, 14894-14906 (2013).
100. De Paëpe, G. Dipolar Recoupling in Magic Angle Spinning Solid-State Nuclear Magnetic Resonance. *Annu. Rev. Phys. Chem. is online* **63**, 661–84 (2012).
101. Smith, A. N., Märker, K., Hediger, S. & De Paëpe, G. Natural Isotopic Abundance 13C and 15N Multidimensional Solid-State NMR Enabled by Dynamic Nuclear Polarization. *Journal of Physical Chemistry Letters* **10**, 4652–4662 (2019).
102. Hohwy, M., Rienstra, C. M., Jaroniec, C. P. & Griffin, R. G. Fivefold symmetric homonuclear dipolar recoupling in rotating solids: Application to double quantum spectroscopy. *J. Chem. Phys.* **110**, 7983–7992 (1999).
103. Ladizhansky, V. & Vega, S. Polarization transfer dynamics in Lee-Goldburg cross polarization nuclear magnetic resonance experiments on rotating solids. *J. Chem. Phys.* **112**, 7158–7168 (2000).
104. Fyfe, C. A. & Lewis, A. R. Investigation of the Viability of Solid-State NMR Distance Determinations in Multiple Spin Systems of Unknown Structure. *J. Phys. Chem. B* **104**, 48-55 (2000).
105. Hodgkinson, P. & Emsley, L. The Accuracy of Distance Measurements in Solid-State NMR. *J. Magn. Reson.* **139**, 46–59 (1999).
106. Jaroniec, C. P., Filip, C. & Griffin, R. G. 3D TEDOR NMR experiments for the simultaneous measurement of multiple carbon-nitrogen distances in uniformly 13C,15N-labeled solids. *J. Am. Chem. Soc.* **124**, 10728–10742 (2002).
107. Märker, K. *et al.* Welcoming natural isotopic abundance in solid-state NMR: probing π-stacking and supramolecular structure of organic nanoassemblies using DNP. *Chem. Sci.* **8**, 974–987 (2017).
108. Lesage, A. *et al.* Surface enhanced NMR spectroscopy by dynamic nuclear polarization. *J. Am. Chem. Soc.* **132**, 15459–15461 (2010).
109. Rossini, A. J. *et al.* Dynamic nuclear polarization surface enhanced NMR spectroscopy. *Acc. Chem. Res.* **46**, 1942–1951 (2013).
110. Lee, D. *et al.* Untangling the Condensation Network of Organosiloxanes on

Nanoparticles using 2D 29Si–29Si Solid-State NMR Enhanced by Dynamic Nuclear Polarization. *J. Am. Chem. Soc.* **136**, 13781–13788 (2014).
111. Rankin, A. G. M., Trébosc, J., Pourpoint, F., Amoureux, J. P. & Lafon, O. Recent developments in MAS DNP-NMR of materials. *Solid State Nuclear Magnetic Resonance* **101**, 116–143 (2019).
112. Berruyer, P. *et al.* Three-Dimensional Structure Determination of Surface Sites. *J. Am. Chem. Soc.* **139**, 849-855 (2016).
113. Gullion, T. Introduction to rotational-echo, double-resonance NMR. *Concepts Magn. Reson.* **10**, 277–289 (1998).
114. Schaefer, J. 'Development of REDOR rotational-echo double-resonance NMR' by Terry Gullion and Jacob Schaefer [J. Magn. Reson. 81 (1989) 196-200]. *Journal of Magnetic Resonance* **213**, 421–422 (2011).
115. Piveteau, L. *et al.* Structure of Colloidal Quantum Dots from Dynamic Nuclear Polarization Surface Enhanced NMR Spectroscopy. *J. Am. Chem. Soc* **137**, 1 (2015).
116. Hanrahan, M. P. *et al.* Probing the Surface Structure of Semiconductor Nanoparticles by DNP SENS with Dielectric Support Materials. *J. Am. Chem. Soc.* **141**, 15532–15546 (2019).
117. Hope, M. A. *et al.* Surface-selective direct 17O DNP NMR of CeO2 nanoparticles. *Chem. Commun.* **53**, 2142–2145 (2017).
118. Nagashima, H. *et al.* Observation of Low-γQuadrupolar Nuclei by Surface-Enhanced NMR Spectroscopy. *J. Am. Chem. Soc.* **142**, 10659–10672 (2020).
119. Hohenberg, P. & Kohn, W. Inhomogeneous electron gas. *Phys. Rev.* **136**, B864 (1964).
120. Kohn, W. & Sham, L. J. Self-consistent equations including exchange and correlation effects. *Phys. Rev.* **140**, A1133 (1965).
121. Perdew, J. P., Burke, K. & Ernzerhof, M. Generalized gradient approximation made simple. *Phys. Rev. Lett.* **77**, (1996).
122. Troullier, N. & Martins, J. L. Efficient pseudopotentials for plane-wave calculations. *Phys. Rev. B* **43**, (1991).
123. Pickard, C. J. & Mauri, F. All-electron magnetic response with pseudopotentials: NMR chemical shifts. *Phys. Rev. B - Condens. Matter Mater. Phys.* **63**, 2451011–2451013 (2001).
124. Charpentier, T. The PAW/GIPAW approach for computing NMR parameters: A new dimension added to NMR study of solids. *Solid State Nucl. Magn. Reson.* **40**, 1–20 (2011).
125. Bonhomme, C. *et al.* First-principles calculation of NMR parameters using the gauge including projector augmented wave method: A chemists point of view. *Chemical Reviews* **112**, 5733–5779 (2012).
126. Klingshirn, C. ZnO: Material, Physics and Applications. *ChemPhysChem* **8**, 782–803 (2007).
127. Ludi, B., Transactions, M. N.-D. & 2013, undefined. Zinc oxide nanoparticles: chemical mechanisms and classical and non-classical crystallization. *Dalton Transactions* **42**, 12554-12568 (2013)
128. Kumar, S. G. & Rao, K. S. R. K. Zinc oxide based photocatalysis: Tailoring surface-bulk structure and related interfacial charge carrier dynamics for better environmental applications. *RSC Advances* **5**, 3306–3351 (2015).
129. Meulenkamp, E. A. Synthesis and growth of ZnO nanoparticles. *J. Phys. Chem.*

B **102**, 5566–5572 (1998).
130. Pacholski, C., Kornowski, A. & Weller, H. Self-assembly of ZnO: From nanodots to nanorods. *Angew. Chemie - Int. Ed.* **41**, 1188–1191 (2002).
131. Fu, Y. S. *et al.* Stable aqueous dispersion of ZnO quantum dots with strong blue emission via simple solution route. *J. Am. Chem. Soc.* **129**, 16029–16033 (2007).
132. Yang, M., Sun, K. & Kotov, N. A. Formation and assembly-disassembly processes of ZnO hexagonal pyramids driven by dipolar and excluded volume interactions. *J. Am. Chem. Soc.* **132**, 1860–1872 (2010).
133. Tokumoto, M. S., Pulcinelli, S. H., Santilli, C. V. & Briois, V. Catalysis and temperature dependence on the formation of ZnO nanoparticles and of zinc acetate derivatives prepared by the sol-gel route. *J. Phys. Chem. B* **107**, 568–574 (2003).
134. Voigt, M., Klaumünzer, M., Thiem, H. & Peukert, W. Detailed analysis of the growth kinetics of ZnO nanorods in methanol. *J. Phys. Chem. C* **114**, 6243–6249 (2010).
135. Caetano, B. L., Santilli, C. V., Meneau, F., Briois, V. & Pulcinelli, S. H. In situ and simultaneous UV-vis/SAXS and UV-vis/XAFS time-resolved monitoring of ZnO quantum dots formation and growth. *J. Phys. Chem. C* **115**, 4404–4412 (2011).
136. Layek, A. *et al.* A generalized three-stage mechanism of ZnO nanoparticle formation in homogeneous liquid medium. *J. Phys. Chem. C* **116**, 24757–24769 (2012).
137. Schindler, T., Walter, J., Peukert, W., Segets, D. & Unruh, T. In Situ Study on the Evolution of Multimodal Particle Size Distributions of ZnO Quantum Dots: Some General Rules for the Occurrence of Multimodalities. *J. Phys. Chem. B* **119**, 15370–15380 (2015).
138. Sakohara, S., Ishida, M. & Anderson, M. A. Visible luminescence and surface properties of nanosized ZnO colloids prepared by hydrolyzing zinc acetate. *J. Phys. Chem. B* **102**, 10169–10175 (1998).
139. Segets, D. *et al.* Experimental and theoretical studies of the colloidal stability of nanoparticles-a general interpretation based on stability maps. *ACS Nano* **5**, 4658–4669 (2011).
140. Zobel, M., Neder, R. B. & Kimber, S. A. J. Universal solvent restructuring induced by colloidal nanoparticles. *Science (80-.).* **347**, 292–294 (2015).
141. Schindler, T. *et al.* A Combined SAXS/SANS Study for the in Situ Characterization of Ligand Shells on Small Nanoparticles: The Case of ZnO. *Langmuir* **31**, 10130–10136 (2015).
142. Gong, M. *et al.* All-Printable ZnO Quantum Dots/Graphene van der Waals Heterostructures for Ultrasensitive Detection of Ultraviolet Light. *ACS Nano* **11**, 4114–4123 (2017).
143. Monge, M., Kahn, M. L., Maisonnat, A. & Chaudret, B. Room-Temperature Organometallic Synthesis of Soluble and Crystalline ZnO Nanoparticles of Controlled Size and Shape. *Angew. Chemie - Int. Ed.* **42**, 5321–5324 (2003).
144. Coppel, Y. *et al.* Self-assembly of ZnO nanoparticles - An NMR spectroscopic study. *Eur. J. Inorg. Chem.* **2012**, 2691–2699 (2012).
145. Hall, D. A. *et al.* Polarization-enhanced NMR spectroscopy of biomolecules in frozen solution. *Science (80-.).* **276**, 930–932 (1997).
146. Lee, D., Hediger, S. & Paëpe, G. De. High-Field Solid-State NMR with Dynamic

Nuclear Polarization. in *Modern Magnetic Resonance,* 1–17 (2017).
147. Piveteau, L. *et al.* Resolving the Core and the Surface of CdSe Quantum Dots and Nanoplatelets Using Dynamic Nuclear Polarization Enhanced PASS-PIETA NMR Spectroscopy. *ACS Cent. Sci.* **4**, 1113–1125 (2018).
148. Benoit, D. N. *et al.* Measuring the grafting density of nanoparticles in solution by analytical ultracentrifugation and total organic carbon analysis. *Anal. Chem.* **84**, 9238–9245 (2012).
149. Al-Johani, H. *et al.* The structure and binding mode of citrate in the stabilization of gold nanoparticles. *Nat. Chem.* **9**, 890–895 (2017).
150. Pang, Z., Zhang, J., Cao, W., Kong, X. & Peng, X. Partitioning surface ligands on nanocrystals for maximal solubility. *Nat. Commun.* **10**, 1–8 (2019).
151. Wolska-Pietkiewicz, M. *et al.* Alkylzinc diorganophosphates: Synthesis, structural diversity and unique ability to incorporate zincoxane units. *Dalt. Trans.* **45**, 18813–18816 (2016).
152. Lin, W. *et al.* A general approach to study the thermodynamics of ligand adsorption to colloidal surfaces demonstrated by means of catechols binding to zinc oxide quantum dots. *Chem. Mater.* **27**, 358–369 (2015).
153. Burger, A., Srikantharajah, R., Peukert, W. & Hirsch, A. Individualization and Stabilization of Zinc Oxide Nanorods by Covalent Functionalization with Positively Charged Catechol Derivatives. *Chem. - A Eur. J.* **23**, 17257–17268 (2017).
154. Teymoori, G., Pahari, B., Stevensson, B. & Edén, M. Low-power broadband homonuclear dipolar recoupling without decoupling: Double-quantum 13C NMR correlations at very fast magic-angle spinning. *Chem. Phys. Lett.* **547**, 103–109 (2012).
155. Teymoori, G., Pahari, B. & Edén, M. Low-power broadband homonuclear dipolar recoupling in MAS NMR by two-fold symmetry pulse schemes for magnetization transfers and double-quantum excitation. *J. Magn. Reson.* **261**, 205–220 (2015).
156. Veshtort, M. & Griffin, R. G. SPINEVOLUTION: A powerful tool for the simulation of solid and liquid state NMR experiments. *J. Magn. Reson.* **178**, 248–282 (2006).
157. Nicholas, N. J., Franks, G. V. & Ducker, W. A. Selective adsorption to particular crystal faces of ZnO. *Langmuir* **28**, 7189–7196 (2012).
158. Spanhel, L. & Anderson, M. A. Semiconductor Clusters in the Sol-Gel Process: Quantized Aggregation, Gelation, and Crystal Growth in Concentrated ZnO Colloids. *J. Am. Chem. Soc.* **113**, 2826–2833 (1991).
159. Takahashi, H. *et al.* Rapid Natural-Abundance 2D ^{13}C-^{13}C Correlation Spectroscopy Using Dynamic Nuclear Polarization Enhanced Solid-State NMR and Matrix-Free Sample Preparation. *Angew. Chemie Int. Ed.* **51**, 11766–11769 (2012).
160. Fung, B. M., Khitrin, A. K. & Ermolaev, K. An Improved Broadband Decoupling Sequence for Liquid Crystals and Solids. *J. Magn. Reson.* **142**, 97–101 (2000).
161. Baldus, M., Geurts, D. G., Rediger, S. & Meier, B. H. Efficient 15 N- 13 C polarization transfer by adiabatic-passage Hartmann-Hahn cross polarization. *Journal of Magnetic Resonance - Series A* **118**, 140–144 (1996).
162. Lee, M. & Goldburg, W. I. Nuclear-magnetic-resonance line narrowing by a

rotating rf field. *Phys. Rev.* **140**, A1261 (1965).
163. Burda, C., Chen, X., Narayanan, R. & El-Sayed, M. A. *Chemistry and properties of nanocrystals of different shapes*. *Chemical Reviews* **105**, (2005).
164. El-Sayed, M. A. Small Is Different: Shape-, Size-, and Composition-Dependent Properties of Some Colloidal Semiconductor Nanocrystals. *Acc. Chem. Res.* **37**, 326–333 (2004).
165. Jun, Y., Choi, J. & Cheon, J. Shape control of semiconductor and metal oxide nanocrystals through nonhydrolytic colloidal routes. *Angew. Chem. Int. Ed. Engl.* **45**, 3414–39 (2006).
166. Soon, G. K. & Hyeon, T. Colloidal chemical synthesis and formation kinetics of uniformly sized nanocrystals of metals, oxides, and chalcogenides. *Acc. Chem. Res.* **41**, 1696–1709 (2008).
167. Yin, Y. & Alivisatos, A. P. Colloidal nanocrystal synthesis and the organic–inorganic interface. *Nature* **437**, 664–670 (2005).
168. Nasilowski, M., Mahler, B., Lhuillier, E., Ithurria, S. & Dubertret, B. Two-Dimensional Colloidal Nanocrystals. *Chem. Rev.* **116**, 10934–10982 (2016).
169. Li, Q. & Lian, T. Exciton Spatial Coherence and Optical Gain in Colloidal Two-Dimensional Cadmium Chalcogenide Nanoplatelets. *Acc. Chem. Res.* **52**, 2684–2693 (2019).
170. Berends, A. C. & de Mello Donega, C. Ultrathin One- and Two-Dimensional Colloidal Semiconductor Nanocrystals: Pushing Quantum Confinement to the Limit. *J. Phys. Chem. Lett.* **8**, 4077–4090 (2017).
171. Shu, Y. *et al.* Quantum Dots for Display. *Angew. Chemie Int. Ed.* **59**, 22312-22323 (2020).
172. Erdem, T. & Demir, H. V. Colloidal nanocrystals for quality lighting and displays: Milestones and recent developments. *Nanophotonics* **5**, 74–95 (2016).
173. Grim, J. Q. *et al.* Continuous-wave biexciton lasing at room temperature using solution-processed quantum wells. *Nat. Nanotechnol.* **9**, 891–895 (2014).
174. Cha, J. J. *et al.* Two-Dimensional Chalcogenide Nanoplates as Tunable Metamaterials via Chemical Intercalation. *Nano Lett.* **13**, 5913–5918 (2013).
175. Ye, C., Bando, Y., Shen, G. & Golberg, D. Thickness-dependent photocatalytic performance of ZnO nanoplatelets. *J. Phys. Chem. B* **110**, 15146–15151 (2006).
176. Yu, J., Low, J., Xiao, W., Zhou, P. & Jaroniec, M. Enhanced Photocatalytic CO 2 -Reduction Activity of Anatase TiO 2 by Coexposed {001} and {101} Facets. *J. Am. Chem. Soc.* **136**, 8839–8842 (2014).
177. Wang, Y., Zhou, Y., Zhang, Y. & Buhro, W. E. Magic-Size II–VI Nanoclusters as Synthons for Flat Colloidal Nanocrystals. *Inorg. Chem.* **54**, 1165–1177 (2015).
178. Knüsel, P. N. *et al.* Experimental Evidence for Two-Dimensional Ostwald Ripening in Semiconductor Nanoplatelets. *Chem. Mater.* **32**, 3312–3319 (2020).
179. Meerbach, C. *et al.* Halide-Assisted Synthesis of Cadmium Chalcogenide Nanoplatelets. *Chem. Mater.* **32**, 566–574 (2020).
180. Christodoulou, S. *et al.* Chloride-Induced Thickness Control in CdSe Nanoplatelets. *Nano Lett.* **18**, 6248–6254 (2018).
181. Puzder, A. *et al.* The effect of organic ligand binding on the growth of CdSe nanoparticles probed by Ab initio calculations. *Nano Lett.* **4**, 2361–2365 (2004).
182. Bealing, C. R., Baumgardner, W. J., Choi, J. J., Hanrath, T. & Hennig, R. G. Predicting nanocrystal shape through consideration of surface-ligand

interactions. *ACS Nano* **6**, 2118–2127 (2012).
183. Ithurria, S. & Dubertret, B. Quasi 2D colloidal CdSe platelets with thicknesses controlled at the atomic level. *J. Am. Chem. Soc.* **130**, 16504–16505 (2008).
184. Zhu, C. *et al.* Facet-Dependent On-Surface Reactions in the Growth of CdSe Nanoplatelets. *Angew. Chemie Int. Ed.* **58**, 17764–17770 (2019).
185. Tessier, M. D., Javaux, C., Maksimovic, I., Loriette, V. & Dubertret, B. Spectroscopy of single CdSe nanoplatelets. *ACS Nano* **6**, 6751–6758 (2012).
186. Wang, A. *et al.* Dominant Polar Surfaces of Colloidal II-VI Wurtzite Semiconductor Nanocrystals Enabled by Cation Exchange. *J. Phys. Chem. Lett.* **11**, 4990–4997 (2020).
187. Cunningham, P. D., Coropceanu, I., Mulloy, K., Cho, W. & Talapin, D. V. Quantized Reaction Pathways for Solution Synthesis of Colloidal ZnSe Nanostructures: A Connection between Clusters, Nanowires, and Two-Dimensional Nanoplatelets. *ACS Nano* **14**, 3847-3857 (2020).
188. He, S. *et al.* Enhancement of visible light photocatalysis by grafting ZnO nanoplatelets with exposed (0001) facets onto a hierarchical substrate. *Chem. Commun.* **47**, 10797–10799 (2011).
189. Hong, J. Il *et al.* Magnetism in dopant-free ZnO nanoplates. *Nano Lett.* **12**, 576–581 (2012).
190. Cao, B. & Cai, W. From ZnO nanorods to nanoplates: Chemical bath deposition growth and surface-related emissions. *J. Phys. Chem. C* **112**, 680–685 (2008).
191. Song, J. *et al.* Epitaxial ZnO nanowire-on-nanoplate structures as efficient and transferable field emitters. *Adv. Mater.* **25**, 5750–5755 (2013).
192. Qiu, Y., Chen, W. & Yang, S. Facile hydrothermal preparation of hierarchically assembled, porous single-crystalline ZnO nanoplates and their application in dye-sensitized solar cells. *J. Mater. Chem.* **20**, 1001–1006 (2010).
193. Jing, Z. & Zhan, J. Fabrication and gas-sensing properties of porous ZnO nanoplates. *Adv. Mater.* **20**, 4547–4551 (2008).
194. Phuruangrat, A., Thongtem, S. & Thongtem, T. Ultrasonic-assisted synthesis and photocatalytic performance of ZnO nanoplates and microflowers. *Mater. Des.* **107**, 250–256 (2016).
195. Illy, B., Shollock, B. A., MacManus-Driscoll, J. L. & Ryan, M. P. Electrochemical growth of ZnO nanoplates. *Nanotechnology* **16**, 320–324 (2005).
196. Krupiński, P., Kornowicz, A., Sokołowski, K., Cieślak, A. M. & Lewiński, J. Applying Mechanochemistry for Bottom-Up Synthesis and Host-Guest Surface Modification of Semiconducting Nanocrystals: A Case of Water-Soluble β-Cyclodextrin-Coated Zinc Oxide. *Chem. - A Eur. J.* **22**, 7817–7823 (2016).
197. Lewiński, J. *et al.* From uncommon ethylzinc complexes supported by ureate ligands to water-soluble ZnO nanocrystals: A mechanochemical approach. *ACS Sustain. Chem. Eng.* **9**, 1540-1549 (2021).
198. Bordwell, F. G. & Ji, G. Z. Effects of Structural Changes on Acidities and Homolytic Bond Dissociation Energies of the H-N Bonds in Amidines, Carboxamides, and Thiocarboxamides. *J. Am. Chem. Soc.* **113**, 8398–8401 (1991).
199. Prochowicz, D., Sokołowski, K. & Lewiński, J. Zinc hydroxides and oxides supported by organic ligands: Synthesis and structural diversity. *Coord. Chem. Rev.* **270**–**271**, 112–126 (2014).

200. Pietrzak, T., Justyniak, I., Kubisiak, M., Bojarski, E. & Lewiński, J. An In-Depth Look at the Reactivity of Non-Redox-Metal Alkylperoxides. *Angew. Chemie - Int. Ed.* **58**, 8526–8530 (2019).
201. Leszczyński, M. K., Justyniak, I. & Lewiński, J. Toward Factors Affecting the Degree of Zinc Alkyls Oxygenation: A Case of Organozinc Guanidinate Complexes. *Organometallics* **36**, 2377–2380 (2017).
202. Lewiński, J., Kościelski, M., Suwałła, K. & Justyniak, I. Transformation of ethylzinc species to zinc acetate mediated by O 2 activation: Reactive oxygen-centered radicals under control. *Angew. Chemie - Int. Ed.* **48**, 7017–7020 (2009).
203. Lewiński, J. *et al.* Oxygenation of alkylzinc complexes with pyrrolylketiminate ligand: Access to alkylperoxide versus oxo-encapsulated complexes. *Chem. Commun.* **119**, 215–217 (2009).
204. Lewiński, J. *et al.* Oxygenation of a Me2Zn/α-diimine system: A unique zinc methylperoxide cluster and evidence for its sequential decomposition pathways. *Angew. Chemie - Int. Ed.* **47**, 7888–7891 (2008).
205. Lewiński, J., Sliwiński, W., Dranka, M., Justyniak, I. & Lipkowski, J. Reactions of [ZnR2(L)] complexes with dioxygen: a new look at an old problem. *Angew. Chem. Int. Ed. Engl.* **45**, 4826–9 (2006).
206. Leszczyński, M. K., Justyniak, I., Zelga, K. & Lewiński, J. From ethylzinc guanidinate to [Zn10O4]-supertetrahedron. *Dalt. Trans.* **46**, 12404–12407 (2017).
207. Zelga, K. *et al.* Synthesis, structure and unique reactivity of the ethylzinc derivative of a bicyclic guanidine. *Dalton Trans.* **41**, 5934–8 (2012).
208. Terlecki, M., Justyniak, I., Leszczyński, M. & Lewiński, J. Effect of the proximal secondary sphere on the self-assembly of octahedral zinc-oxo clusters supported by organic ligands. *Chem. Commun.* Submitted
209. CARVER, T. R. & SLICHTER, C. P. *Polarization of Nuclear Spins in Metals*. *Physical Review* **92**, 212 (1953).
210. Gerfen, G. J. *et al.* High frequency (140 GHz) dynamic nuclear polarization: Polarization transfer to a solute in frozen aqueous solution. *J. Chem. Phys.* **102**, 9494–9497 (1995).
211. Rankin, A. G. M., Trébosc, J., Pourpoint, F., Amoureux, J.-P. & Lafon, O. Recent developments in MAS DNP-NMR of materials. *Solid State Nucl. Magn. Reson.* **101**, 116–143 (2019).
212. Semenov, V. A., Samultsev, D. O. & Krivdin, L. B. Theoretical and experimental study of 15N NMR protonation shifts. *Magn. Reson. Chem.* **53**, 433–441 (2015).
213. Pawley, G. S. Unit-cell refinement from powder diffraction scans. *J. Appl. Crystallogr.* **14**, 357–361 (1981).
214. Wejrzanowski, T. *et al.* Quantitative methods for nanopowders characterization. *Appl. Surf. Sci.* **253**, 204–208 (2006).
215. Terlecki, M.; Justyniak, I.; Leszczyński, M.; Lewiński, J. Effect of the Proximal Secondary Sphere on the Self-Assembly of Octahedral Zinc-Oxo Clusters Supported by Organic Ligands. *Chem. Commun. Submitt.*
216. Shim, J. & Bashir, R. An organometallic route to chiroptically active ZnO nanocrystals. *Nanoscale* **9**, 14743–15162 (2017).
217. Lee, D. *et al.* Disclosing Interfaces of ZnO Nanocrystals Using Dynamic Nuclear Polarization: Sol-Gel versus Organometallic Approach. *Angew. Chemie Int. Ed.* **58**, 17163–17168 (2019).

218. Lim, S. J., Ma, L., Schleife, A. & Smith, A. M. Quantum dot surface engineering: Toward inert fluorophores with compact size and bright, stable emission. *Coordination Chemistry Reviews* **320**–**321**, (2016).
219. Tang, C., Spencer, M. J. S. & Barnard, A. S. Activity of ZnO polar surfaces: An insight from surface energies. *Phys. Chem. Chem. Phys.* **16**, (2014).
220. Lee, D., Hediger, S. & De Paëpe, G. Is solid-state NMR enhanced by dynamic nuclear polarization? *Solid State Nucl. Magn. Reson.* **66**, 6–20 (2015).
221. Piveteau, L. *et al.* Resolving the Core and the Surface of CdSe Quantum Dots and Nanoplatelets Using Dynamic Nuclear Polarization Enhanced PASS−PIETA NMR Spectroscopy. **14**, 52 (2020).
222. Viger-Gravel, J. *et al.* Frozen Acrylamide Gels as Dynamic Nuclear Polarization Matrices. *Angew. Chemie - Int. Ed.* **56**, 8726–8730 (2017).
223. Takahashi, H. *et al.* Optimization of an absolute sensitivity in a glassy matrix during DNP-enhanced multidimensional solid-state NMR experiments. *J. Magn. Reson.* **239**, 91–99 (2014).
224. Van Rossum, B. J., Förster, H. & De Groot, H. J. M. High-Field and High-Speed CP-MAS 13 C NMR Heteronuclear Dipolar-Correlation Spectroscopy of Solids with Frequency-Switched Lee-Goldburg Homonuclear Decoupling. *Journal of Magnetic Resonance* **124**, 516–519 (1997).
225. Giannozzi, P. *et al.* QUANTUM ESPRESSO: a modular and open-source software project for quantum simulations of materials Related content QUANTUM ESPRESSO: a modular and open-source software project for quantum simulations of materials. *J. Phys. Condens. Matter* **21**, 395502 (2009).
226. Giannozzi, P., Baroni, S. & Bonini, N. Advanced capabilities for materials modelling with Quantum ESPRESSO. *Journal of physics: Condensed matter* **29**, 465901 (2017).
227. Hjorth Larsen, A. *et al.* The atomic simulation environment - A Python library for working with atoms. *Journal of Physics Condensed Matter* **29**, (2017).
228. Davide Ceresoli - Pseudopotentials. Available at: https://sites.google.com/site/dceresoli/pseudopotentials.
229. PSLibrary - QUANTUMESPRESSO - QUANTUMESPRESSO. Available at: http://www.quantum-espresso.org/pseudopotentials/pslibrary.
230. QUANTUMESPRESSO - QUANTUMESPRESSO. Available at: http://www.quantum-espresso.org/.
231. Szatyłowicz, H., Krygowski, T. M. & Zachara-Horeglad, J. E. Long-Distance Structural Consequences of H-Bonding. How H-Bonding Affects Aromaticity of the Ring in Variously Substituted Aniline/Anilinium/Anilide Complexes with Bases and Acids †. (2007). doi:10.1021/ci600502w
232. Wang, M. *et al.* Identification of intrinsic hydrogen impurities in ZnO with 1H solid-state nuclear magnetic resonance spectroscopy. *Chem. Phys. Lett.* **627**, (2015).
233. Centrone, A. *et al.* The role of nanostructure in the wetting behavior of mixed-monolayer- protected metal nanoparticles. *Proc. Natl. Acad. Sci. U. S. A.* **105**, 9886–9891 (2008).
234. Ghosh, A., Basak, S., Wunsch, B. H., Kumar, R. & Stellacci, F. Effect of composition on the catalytic properties of mixed-ligand-coated gold nanoparticles. *Angew. Chemie - Int. Ed.* **50**, 7900–7905 (2011).
235. Cho, E. S. *et al.* Ultrasensitive detection of toxic cations through changes in the

tunnelling current across films of striped nanoparticles. *Nat. Mater.* **11**, 978–985 (2012).
236. Kim, C.-K., Ghosh, P. & Rotello, V. M. Multimodal drug delivery using gold nanoparticles. *Nanoscale* **1**, 61-67 (2008).
237. Wang, H. X., Xiong, M. H., Wang, Y. C., Zhu, J. & Wang, J. N-acetylgalactosamine functionalized mixed micellar nanoparticles for targeted delivery of siRNA to liver. *J. Control. Release* **166**, 106–114 (2013).
238. Ong, Q., Luo, Z. & Stellacci, F. Characterization of Ligand Shell for Mixed-Ligand Coated Gold Nanoparticles. *Accounts of Chemical Research*, **50**, 1911-1919 (2017).
239. Jackson, A. M., Myerson, J. W. & Stellacci, F. Spontaneous assembly of subnanometre-ordered domains in the ligand shell of monolayer-protected nanoparticles. *Nat. Mater.* **3**, 330–336 (2004).
240. Wang, Y., Zeiri, O., Neyman, A., Stellacci, F. & Weinstock, I. A. Nucleation and Island Growth of Alkanethiolate Ligand Domains on Gold Nanoparticles. *ACS Nano* **6**, 629-640 (2012).
241. Liu, X., Yu, miao, Kim, H., mameli, marta & stellacci, F. Determination of monolayer-protected gold nanoparticle ligand-shell morphology using NMR. *Nat. Commun.* **3**, 1-9 (2012).
242. Şologan, M. *et al.* Patchy and Janus Nanoparticles by Self-Organization of Mixtures of Fluorinated and Hydrogenated Alkanethiolates on the Surface of a Gold Core. *ACS Nano* **10**, 9316–9325 (2016).
243. Harkness, K. M., Balinski, A., McLean, J. A. & Cliffel, D. E. Nanoscale phase segregation of mixed thiolates on gold nanoparticles. *Angew. Chemie - Int. Ed.* **50**, 10554–10559 (2011).
244. Liao, S., Luo, Z., Metternich, J. B., Zenobi, R. & Stellacci, F. Quantification of surface composition and segregation on AuAg bimetallic nanoparticles by MALDI MS †. **12**, 22639 (2020).
245. Luo, Z., Hou, J., Menin, L., Ong, Q. K. & Stellacci, F. Evolution of the Ligand Shell Morphology during Ligand Exchange Reactions on Gold Nanoparticles. *Angew. Chemie - Int. Ed.* **56**, 13521–13525 (2017).
246. Centrone, A., Hu, Y., Jackson, A. M., Zerbi, G. & Stellacci, F. Phase separation on mixed-monolayer-protected metal nanoparticles: A study by infrared spectroscopy and scanning tunneling microscopy. *Small* **3**, 814–817 (2007).
247. Romano, F., Sanz, E. & Sciortino, F. Phase diagram of a tetrahedral patchy particle model for different interaction ranges. *J. Chem. Phys.* **132**, 174502 (2010).
248. Singh, C. *et al.* Entropy-Mediated Patterning of Surfactant-Coated Nanoparticles and Surfaces. *Phys. Rev. Lett.* **99**, 226106 (2007).
249. Kim, H. *et al.* Synthesis and characterization of Janus gold nanoparticles. *Adv. Mater.* **24**, 3857–3863 (2012).
250. Hing, A. W., Vega, S. & Schaefer, J. Transferred-echo double-resonance NMR. *J. Magn. Reson.* **96**, 205–209 (1992).
251. Hing, A. W., Vega, S. & Schaefer, J. Measurement of heteronuclear dipolar coupling by transferred-echo double-resonance NMR. *J. Magn. Reson. - Ser. A* **103**, 151–162 (1993).
252. Johnson, R. L. & Schmidt-Rohr, K. Quantitative solid-state 13C NMR with signal enhancement by multiple cross polarization. *J. Magn. Reson.* **239**, 44–49

(2014).
253. Mentink-Vigier, ric *et al.* Computationally Assisted Design of Polarizing Agents for Dynamic Nuclear Polarization Enhanced NMR: The AsymPol Family. *J. Am. Chem. Soc.* **140**, 11013-11019 (2018).
254. Tanase, T., Yun, J. W. & Lippard, S. J. *Zinc-Containing Carboxylate-Bridged Heterodimetallic Complexes and Their Reactions with Phosphodiester Ligands*. *Inorganic Chemistry* **35**, 3585-3594 (1996).
255. Nilsson, J., Kraszewski, A. & Stawinski, J. Reinvestigation of the 31 P NMR evidence for the formation of diorganyl phosphoropyridinium intermediates. *Journal of the Chemical Society, Perkin Transactions* **2**, 2263-2266 (2001).
256. Yun, J. W., Tañase, T., Pence, L. E., Lippard, S. J. & Proc, B. *Carboxylate-and Phosphodiester-Bridged Dinuclear Magnesium(II) Complexes4) (a*. *J. A. Proc. Natl. Acad. Sci. U.S.A* **117**, (1995).
257. Kazes, M., Udayabhaskararao, T., Dey, S. & Oron, D. Effect of Surface Ligands in Perovskite Nanocrystals: Extending in and Reaching out. *Acc. Chem. Res.* **54**, 151 (2021).
258. Raja, S. N. *et al.* Encapsulation of Perovskite Nanocrystals into Macroscale Polymer Matrices: Enhanced Stability and Polarization. *ACS Appl. Mater. Interfaces* **8**, 35523–35533 (2016).
259. Heuer-Jungemann, A. *et al.* The Role of Ligands in the Chemical Synthesis and Applications of Inorganic Nanoparticles. *Chemical Reviews* **119**, 4819-4880 (2019).
260. Sundar, S., Kundu, J. & Kundu, S. C. Biopolymeric nanoparticles. *Sci. Technol. Adv. Mater.* **11**, 014104 (2010).
261. Kumar, A. *et al.* The surface chemistry of a nanocellulose drug carrier unravelled by MAS-DNP. *Chem. Sci.* **11**, 3868–3877 (2020).
262. Kaflak, A., Chmielewski, D. & Kolodziejski, W. Solid-state NMR study of discrete environments of bone mineral nanoparticles using phosphorus-31 relaxation. *J. Appl. Biomed.* **14**, 321–330 (2016).
263. Von euw, stanislas *et al.* Bone mineral: new insights into its chemical composition. *Scientific Reports* **9**, 1-11 (2019)
264. Danks, T. N., Slade, R. C. T. & Varcoe, J. R. Alkaline anion-exchange radiation-grafted membranes for possible electrochemical application in fuel cells. *J. Mater. Chem.* **13**, 712–721 (2003).
265. Chakrabarty, T. *et al.* Stable ion-exchange membranes for water desalination by electrodialysis. *Desalination* **282**, 2–8 (2011).